INAUGURAL - DISSERTATION

zur

Erlangung der Doktorwürde

der

Naturwissenschaftlich-Mathematischen Gesamtfakultät

der

Ruprecht-Karls-Universität Heidelberg

vorgelegt von

Diplom-Chemikerin Marta Zajaczkowski-Fischer

aus Krakau (Polen)

Tag der mündlichen Prüfung: 29.10.2010

Second Generation Model Complexes for the Enzyme Purple Acid Phosphatase

Gutachter: Prof. Dr. Peter Comba
Prof. Dr. Roland Krämer

Für meine Eltern

Acknowledgements - Danksagungen

Zu allererst möchte ich Herrn Prof. Dr. Peter Comba danken für die faszinierende und anspruchsvolle Themenstellung, die dieser Arbeit zugrunde liegt. Ich habe die wissenschaftliche Freiheit bei der Ausarbeitung sehr geschätzt, aber auch die immer gewährte Anleitung und Hilfe an den kritischen Punkten dieses Unternehmens. Unheimlich dankbar bin ich auch für die vielen Möglichkeiten, Konferenzen zu besuchen und natürlich für den ermöglichten Aufenthalt in Brisbane, Australien. Nicht zu vergessen sind die vier Skiseminare, die ich immer sehr genossen habe.

Furthermore, I´d like to say „thank you“ to Prof. Dr. Graeme Hanson for his advice, help and hospitality during my stay at the University of Queensland, Brisbane and beyond. I really enjoyed working with you, but I also appreciate you as a friend. Thank you very much for reading and correcting this thesis. I hope that my English was not too bad.

Thank you to Prof. Lawrence Gahan for including me into his group during my stay in Brisbane and his interest in and suggestions for my work. I hope I could contribute to your research in some way. Thank you to Prof. Paul Bernhardt for his help with the bulk electrolysis and fruitful discussions. A huge thank you to Dr. Chris Noble for his assistance with the EPR measurements and advice in the simulation of the spectra. Without you I would have been lost! Thanks to all the people that helped me at the UQ, including Dr. Tri Le for NMR assistance – especially for all the 2D experiments, George Blazak for microanalysis measurements and a lot of nice chats, Graham MacFarlane for ESI measurements, David Rosolen for assistance with UV/vis measurements, Paul Malek Mirzayans for helping me with the microwave reactor, Kristian Dalle for being a wonderful lab mate and our climbing sessions, Rebecca Buchholz for introducing me into the world of kinetic experiments, and Michelle Zee, Bianca McCarthy, Darryl Angus, Dr. Kieran Hadler, Fernandy Ely and Dr. Eleanor Leung for their friendship. Thanks to all you lovely people at the CAI (former CMR) for making me feel so welcome and for your help with all kinds of issues. Special thanks to Barbara Rash for all the nice chats and her good wishes.

Ein herzliches Dankeschön auch an meine lieben AK-Kollegen in Heidelberg! Ich habe mich wirklich wohlgefühlt bei Euch und werde Euch vermissen. Vor allem Danke an Dr. Bodo Martin für seine unermüdliche Hilfe bei computertechnischen und –chemischen Fragestellungen aller Art (unterstützt durch Sacha Hausberg – Danke für alles!!!) und Dr.

Marion Kerscher für Diskussionsfreude und Unterstützung beim experimentellen Part, sowie für die Korrektur der Arbeit – ich weiß es zu schätzen, dass Du dich durch das Pamphlet gekämpft hast! Danke an die weltbeste Laborpartnerin und mittlerweilen gute Freundin Nina Dovalil für „einfach Alles“. Ohne Dich hätte ich bestimmt nicht mehr Spaß gehabt als in der Geschlossenen. Danke Euch allen die mich während der vier Jahre im AK Comba begleitet, ermutigt und unterstützt haben, die mit mir Kaffee und Bier getrunken haben, Sinn und Unsinn geredet haben und für den alltäglichen „normalen Wahnsinn“ in 503. Vielen Dank auch an die Nachbarn, den AK Linti, die dazu nach bestem Wissen und Gewissen beigetragen haben. Vor allem danke ich Philipp Butzug, Thomas Zessin und Prof. Linti für Aufnahme und Lösen der Kristallstrukturen, die in dieser Arbeit enthalten sind. Danke, liebe Marlies und liebe Karin, für die großartige Hilfe in allen administrativen Angelegenheiten und unsere netten Gespräche. Ohne Euch würde der Laden nicht laufen! Desweiteren danke ich auch den Mitarbeitern der chemischen Institute in Heidelberg für vielfältige Hilfe und Unterstützung: PD. Dr. Markus Enders und Beate Termin für die NMR-Experimente, Dr. Gross und seinem Team für die Massenspektren, den Angehörigen des Elementaranalytischen Labors und den zahlreichen Mitarbeitern im Hintergrund. Extra Dank an meine vier Forschis, Carolin Lang, Kerstin Mayer, Jakob Striffler und Reida Rutte, für Eure gute Arbeit und den Einsatz den Ihr gezeigt habt.

Für die finanziellen Mittel in Form eines Stipendiums des Graduiertenkollegs 850 danke ich der Deutschen Forschungsgemeinschaft und für diverse Reisekostenzuschüsse danke ich herzlich der HGS MathComp und der Graduiertenakademie.

Zuletzt danke ich meinen Eltern und meinem Mann Sven für die seelisch-moralische und auch finanzielle Unterstützung während des Studiums und der Doktorarbeit. Ich liebe Euch.

Abstract

The present thesis is concerned with the development and characterization of new diferric purple acid phosphatase (PAP) model systems, which include functional groups that are meant to act as a second coordination sphere in phosphoester hydrolysis. A short review on purple acid phosphatases, including the postulated reaction mechanisms in phosphoester hydrolysis, and published PAP model complexes is given in Chapter 2. Furthermore, important data regarding published bridged diferric complexes are presented, in order to have a basis for interpretation of the analytical data in the results part.

In Chapter 3, the results on the new model complexes are presented and discussed. At first, the cyclam-based ligand **L**$^{\mathbf{1}}$ and its coordination chemistry are described (Chapter 3.1). The most important findings are the following: Ligand **L**$^{\mathbf{1}}$ predominantly forms a μ-oxo bridged diferric complex when reacted with $[FeCl_4]^-$ *in situ*. This complex, called **K**$^{\mathbf{1}}$, can readily coordinate phosphate and inactive phosphoesters, also in partly aqueous solution. Interestingly, the inactive phosphodiester diphenylphosphate (DPP) coordinates in a monodentate mode to one Fe^{III}, whereas the monoesters *para*-nitrophenylphosphate (pNPP) and 1-naphthylphosphate (1-NP) bind in a bridging mode to both Fe^{III} centers. The monodentate coordination of DPP is encouraging in terms of the intended reactivity in phosphoester hydrolysis, as this coordination mode is believed to be the active one, leading to a terminal hydroxide as a possible nucleophile.

Chapter 3.2 deals with the phenolate-based ligands **HL**$^{\mathbf{2}}$ and $\mathbf{H_3L^3}$ and their coordination chemistry. These ligands are derivatives of the published HBPMP ligand and incorporate amino and amido functional groups as second coordination sphere mimics. Diferric complexes, called **K**$^{\mathbf{2}}$ and **K**$^{\mathbf{3}}$, are obtained by *in situ* reaction of the ligands with a ferric salt. A spectrophotometric pH titration was performed and revealed the pH dependent species distribution and the corresponding pK_a values of the complex solutions. **K**$^{\mathbf{2}}$ has three equilibria between pH 4.6 and 11, where the second equilibrium is the deprotonation of the second coordination sphere amines. In contrast, **K**$^{\mathbf{3}}$ has only two equilibria due to the low pK_a of the amido protons. Regarding the coordination of phosphoesters, **K**$^{\mathbf{2}}$ shows a similar behavior to **K**$^{\mathbf{1}}$. DPP is coordinated monodentately to one Fe^{III}, whereas pNPP and 1-NP form bridging complexes. This is not observed with **K**$^{\mathbf{3}}$, which shows bridging coordination with

both, mono- and diesters, possibly due to the lack of hydrogen bond donors in the second coordination sphere.

The complexes **K**^{1}, **K**^{2} and **K**^{3} were tested for hydrolytic activity towards the activated phosphoester substrates bis-(2,4-dinitrophenyl)phosphate (BDNPP) and 2,4-dinitrophenyl-phosphate (DNPP). The results of these experiments are presented in Chapter 3.3. **K**^{1} and **K**^{2} are the first examples of PAP model complexes that catalyze the hydrolysis of the phophomonoester DNPP. So far, only diester hydrolysis with PAP model complexes has been reported in literature, while the inactive bridging coordination mode is observed for phosphomonoesters. We draw the fact, that **K**^{1} and **K**^{2} can hydrolyze monoesters, back to the hydrogen bonding interaction of the coordinated substrates to the remote ligand parts. A closer analysis of the reactivity of **K**^{1} towards DNPP and BDNPP, based on DFT calculations, shows that 1) BDNPP is stabilized by the interaction with the protonated cyclam in the monodentate coordination mode, 2) the hydrolysis of DNPP has a significantly lower activation barrier with the hydrogen bonding interactions than without and 3) this barrier is lower than the energy barrier to a bridging coordination mode. As a conclusion, a mechanism is proposed, where the substrate binds in a monodentate coordination mode and is subsequently attacked by a terminal hydroxide. This active species is in equilibrium with the inactive bridging complex. In the case of the diester BDNPP, the equilibrium is shifted to the active species, while the monoester DNPP is more stable in the bridging coordination mode. The hydrolysis product remains bound to **K**^{1} and inhibits catalysis.

Kurzfassung

Die vorliegende Arbeit beschäftigt sich mit der Entwicklung und Charakterisierung neuer zweikerniger Fe^{III} Komplexe als Modelle für das Enzym Purple Acid Phosphatase (PAP), die zusätzliche funktionelle Gruppen tragen, welche als zweite Koordinatiossphäre die Hydrolyse von Phosphatestern beschleunigen sollen. Eine kurze Übersicht über PAPs und die postulierten Reaktionsmechanismen in der Phosphatesterhydrolyse sowie über literaturbekannte PAP Modellsysteme wird in Kapitel 2 gegeben. Zusätzlich werden die Eckdaten von verbrückten zweikernigen Fe^{III} Komplexen im Hinblick auf die Interpretation der analytischen Daten im Ergebnisteil beschrieben.

In Kapitel 3 werden die Ergebnisse der Arbeit präsentiert und diskutiert. Zu Anfang wird der Cyclam-basierte Ligand $\mathbf{L^1}$ und seine Koordinationchemie behandelt (Kapitel 3.1). Die wichtigsten Erkenntnisse sind: Der Ligand $\mathbf{L^1}$ bildet bevorzugt einen µ-oxo-verbrückten zweikernigen Fe^{III} Komplex, genannt $\mathbf{K^1}$, wenn er mit $[FeCl_4]^-$ *in situ* umgesetzt wird. Phosphat und inaktive Phosphatester koordinieren bereitwillig an diesen Komplex. Interessanterweise werde unterschiedliche Koordinationsmodi des inaktiven Phosphatdiesters Diphenylphosphat (DPP) und der Monoester *para*-Nitrophenylphosphat (pNPP) und 1-Naphthylphosphat (1-NP) beobachtet: DPP koordiniert als monodentater Ligand an nur ein Fe^{III}, während die Monoester als verbrückende Liganden an beide Fe^{III} Zentren binden. Dieses Ergebnis ist ermutigend im Hinblick auf die beabsichtigte Aktivität in der Phosphatesterhydrolyse, da der monodentate Koordinationsmodus als die aktive Form angesehen wird und von einem terminalen Hydroxid als mögliches Nukleophil angegriffen wird.

Kpitel 3.2 beschäftigt sich mit den Phenolat-basierten Liganden $\mathbf{HL^2}$ und $\mathbf{H_3L^3}$ und deren Koordinationschemie. Diese Liganden sind Derivate des literaturbekannten HBPMP Liganden und tragen zusätzliche Amino- und Amidogruppen als zweite Koordinationssphäre. Die $\mathbf{K^2}$ und $\mathbf{K^3}$ genannten zweikernigen Fe^{III} Komplexe werden durch *in situ* Reaktion der Liganden mit einem Fe^{III} Salz erhalten. Spektrophotometrische pH Titrationen der beiden Komplexe liefern die pH-abhängige Verteilung der verschiedenen Spezies und die dazugehörigen pK_s Werte. $\mathbf{K^2}$ liegt zwischen pH 4.6 und 11 in drei Gleichgewichten vor, wobei das mittlere Gleichgewicht der Deprotonierung der zusätzlichen Aminogruppen entspricht. Im Gegensatz dazu findet man bei $\mathbf{K^3}$ nur zwei Gleichgewichte, da die zusätzlichen Amide bereits bei

niedrigen pH Werten deprotoniert werden. In Bezug auf die Koordination von Phosphatestern verhält sich **K**^{2} ähnlich wie **K**^{1}: DPP bindet monodentat an ein Fe^{III}, wohingegen pNPP und 1-NP als verbrückende Liganden an beide Fe^{III} Zentren koordinieren. Dieses Verhalten wird bei **K**^{3} nicht beobachtet; stattdessen binden sowohl Mono- als auch Diester als verbrückende Liganden. Dies ist vermutlich auf die fehlenden Wasserstoffbrücken-Donoren in der zweiten Koordinatiossphäre zurückzuführen.

Die Komplexe **K**^{1}, **K**^{2} und **K**^{3} wurden in der Hydrolyse der aktivierten Phosphatester Bis-(2,4-dinitrophenyl)phosphat (BDNPP) und 2,4-Dinitrophenylphsophat (DNPP) untersucht. Die Resultate dieser Experimente werden in Kapitel 3.3 dargestellt. **K**^{1} und **K**^{2} sind die ersten PAP Modellkomplexe, die die Hydrolyse des Monoesters DNPP katalysieren. Bisher wurde in publizierten Arbeiten mit Modellkomplexen nur Diesterhydrolyse gefunden. Bei Phosphatmonoestern wurde nur die inaktive verbrückende Koordinationsform beobachtet. Wir führen die Fähigkeit von **K**^{1} und **K**^{2}, Phosphomonoester zu hydrolysieren, auf den Einfluss der zweiten Koordinationssphäre durch Wasserstoffbrückenbindungen zu den koordinierten Substraten zurück. Eine nähere Betrachtung der Reaktivität von **K**^{1} mit DNPP und BDNPP mit Hilfe von DFT Methoden führte zu folgenden Ergebnissen: 1) BDNPP wird durch die Wasserstoffbrückenbindungen zum protonierten Cyclam in der monodentaten Koordinationsgeometrie stabilisiert, 2) die Hydrolyse von DNPP hat mit den Wechselwirkungen zwischen Substrat und zweiter Koordinatiossphäre eine deutlich niedrigere Aktivierungsbarriere als ohne und 3) diese Barriere ist kleiner als die der Reaktion zum verbrückenden Substrat. Zusammenfassend wird ein Mechanismus postuliert, bei dem das Substrat monodentat an ein Fe^{III} gebunden ist und von einem terminalen Hydroxid nukleophil angegriffen wird. In Konkurrenz dazu steht das Gleichgewicht zum inaktiven verbrückenden Koordinationsmodus. Für den Diester BDNPP liegt dieses Gleichgewicht auf der Seite der aktiven, monodentat gebundenen Spezies, während der Monoester DNPP in der verbrückenden Koordination stabiler ist. Nach der Hydrolyse verbleibt das Produkt koordiniert am Komplex und verhindert eine katalytische Reaktion.

Table of Contents

Ligand Structures and Abbreviations

The following ligands are relevant for the present thesis:

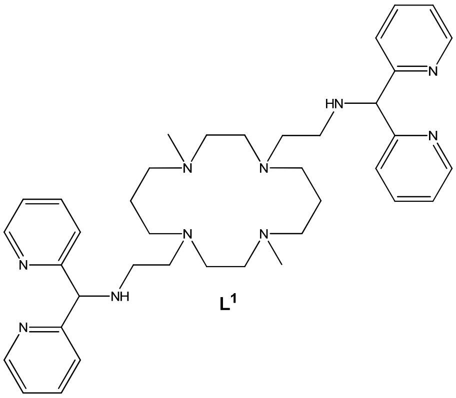
L^1

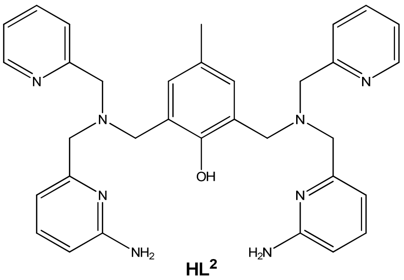
HL^2

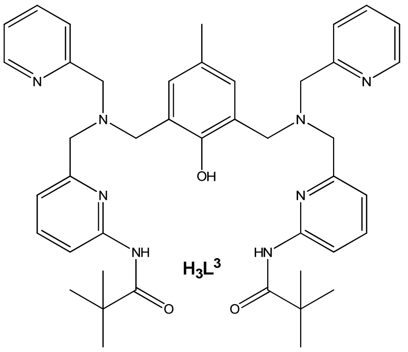
H$_3$L^3

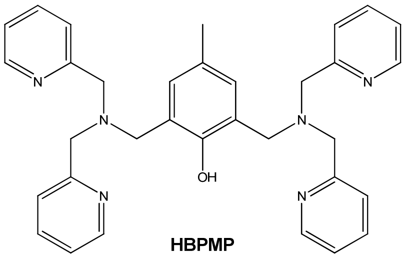
HBPMP

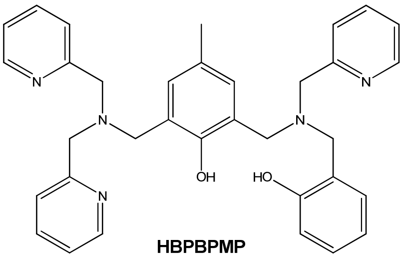
HBPBPMP

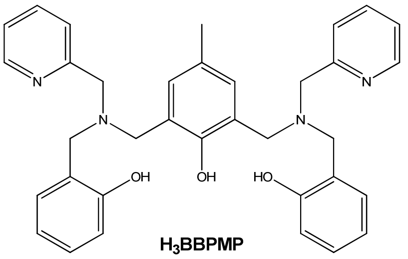
H$_3$BBPMP

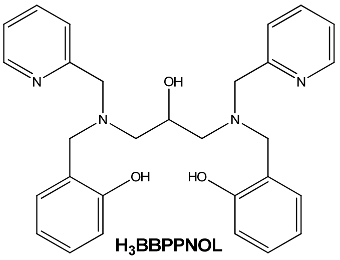
H$_3$BBPPNOL

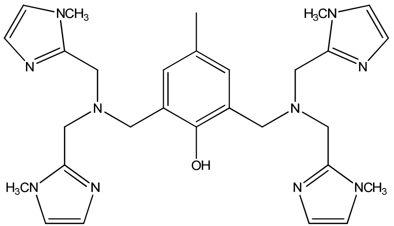
HBIMP

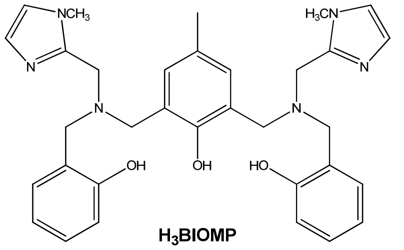
H$_3$BIOMP

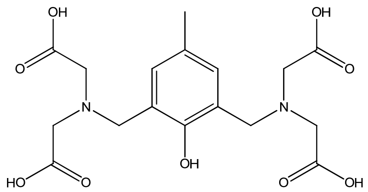
HXTA

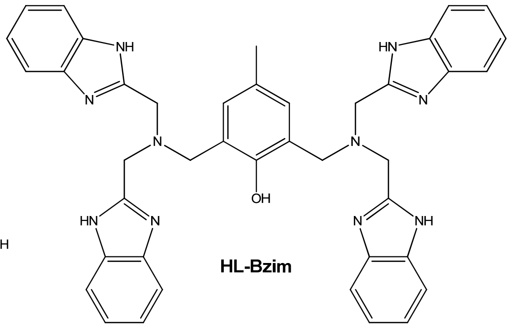
HL-Bzim

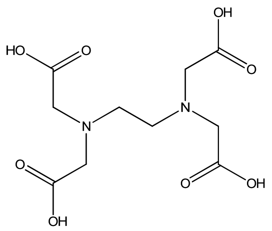
H$_4$EDTA

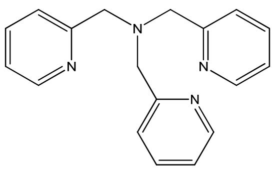
TPA

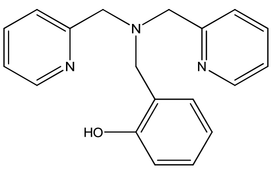
HDP

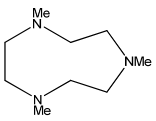
Me$_3$tacn

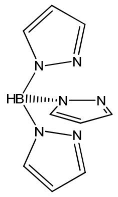
HB(pz)$_3$

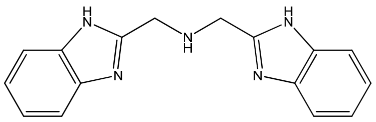
BBA

Chapter 1:

Introduction and Objective

“As I look at a living organism, I see reminders of many questions that need to be answered. […] How do I feel things? How are nerves build and how do they function? […] How do the enzymes in my body break up the food that I eat, burn it to keep me warm and permit me to do work, and build new tissues for me from the food fragments?”

(Prof. Linus Pauling, Nature 1948, *161*, 707-709.)

A huge diversity of living organisms and, therein, even more complex metabolic processes confront mankind with a multitude of problems. Malfunctions of these processes are very likely and numerous and usually lead to diseases, which are, of course, not desirable. Whereas in past times and also nowadays, treatment of many diseases was based on mere trial and error approaches, a deep understanding of enzymatic and metabolic processes can lead to a well-directed development of therapeutic agents. One example is osteoporosis, a bone-degenerative disease that is associated with elevated levels of a certain enzyme, purple acid phosphatase. In the present thesis, this enzyme is the main research target. A detailed knowledge, of how the enzyme catalyzes the hydrolysis of phosphoesters and which factors influence its activity, would help to find new approaches for drug design. On the other hand, the question about modes of action itself is highly interesting. Identifying the methods for high turnover rates is a very attractive target for chemical synthesis and industrial applications.

Different approaches are used to gain insight into enzymatic reactions. Whereas crystallization of enzymes in their resting state or with additional substrate mimics, i.e. inhibitors, gives rather static information about general structures and geometric features, spectroscopy and kinetic analysis of reactions are more useful in terms of reactivity and mechanisms. Another interesting tool is site-directed mutagenesis, where individual amino acid residues are selectively replaced. By this, the influence of certain positions in the active site can be studied in detail. A more chemical approach is the design and investigation of small molecules mimicking enzymes. These simplified systems can fulfill different roles. Structural models aim at reproducing the geometric features of the enzyme´s active site, usually as a first step to identify crucial aspects. The spectroscopic data of an enzyme provide more information about reactivity and structures in solution. Therefore, spectroscopic models target on reflecting these data as accurately as possible. The final goal is the development of functional models, showing the same reactivity as the natural prototype. It is not necessary that the mimetic has the same structural setup as the enzyme to perform well. A nice example is the superoxide dismutase mimetic M40403, a mononuclear seven-coordinated Mn^{II} complex (different structure than enzyme) that has equivalent or superior catalytic activity to that of the native enzyme. Nevertheless, the direct copy of a feature found in enzymes can lead to the desired result of high activity and selectivity.

The present thesis is concerned with the development and investigation of a new type of diferric complexes mimicking purple acid phosphatases, which are designed to enable hydrogen bonding interactions between bound substrates and the surrounding second coordination sphere. A main purpose is to build functional PAP mimics, i.e. catalysts that have the ability of hydrolyzing phosphomonoesters. So far, only diesters could be hydrolyzed by PAP mimetics, whereas the actual function of PAP is the hydrolysis of monoesters.

Based on recent results, it is proposed that a monodentate coordination of phosphoester substrates is highly desirable in terms of activity and efficiency of the catalyst. In the natural PAP systems, an extended hydrogen bonding network holds the substrates in place and optimizes the geometric arrangement of reactants. The aim of the present work was therefore, to mimic this kind of interaction in small diferric complexes, which shall result in an active coordination mode for both, phosphomono- and diesters. The synthesized complexes are characterized spectroscopically, and their reactivity towards hydrolysis of the activated phosphoesters (2,4-dinitrophenyl)phosphate (DNPP) and bis-(2,4-dinitrophenyl)phosphate (BDNPP) are investigated. DFT calculations on structures, properties and reaction pathways help to understand the observations.

Chapter 2:

State of Knowledge

2.1. *Enzymatic Modes of Action*

Since many years, enzymes are known to catalyze biological reactions, but the mechanistic principles behind the observed high activity are still up to debate. First attempts to explain this observation were made by Emil Fischer in 1894. He found that yeast reacts with stereoisomeric hexoses in different ways and concluded that the enzymes present in yeast and their substrates, the different sugars, must fit perfectly to each other to result in high reactivity (lock and key principle, see Figure 2.1).[1] Similar observations were summarized by Pauling in 1948, concerning the interactions in serological reactions and crystallization processes.[2]

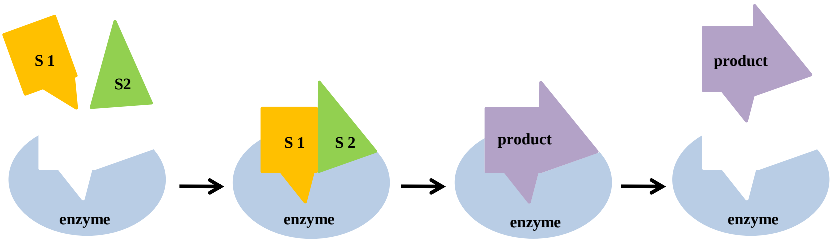

Figure 2.1: Schematic representation of the lock and key principle in an enzymatic activity.

This principle was adapted to the knowledge on chemical reactions in the following years, leading to the hypothesis that enzymes are not complementary to the reactants but to the activated complex (i.e. the transition state) that is formed during reaction (Figure 2.2).[2, 3] Stabilization of these transition states results in lowering of the activation energy of a reaction and therefore in a faster conversion of the substrate to products.

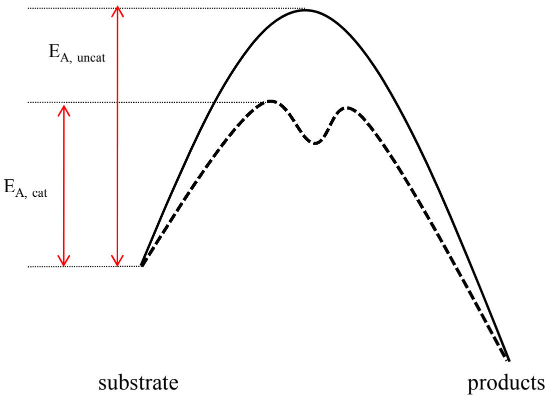

Figure 2.2: Schematic energy profiles of catalyzed (dashed line) vs. uncatalyzed reactions (solid line).

The reverse phenomenon, i.e. lowering the activation energy by destabilizing the substrates, is called “entatic state”[4] (from entasis, *greek* = tension) which means “a state of an atom or group which, due to its binding in a protein, has its geometric or electronic condition adapted for function”.[5] By this, the substrates are forced into a structure that is already close to the structure of the transition state. Nice examples are redox reactions catalyzed by heme iron proteins, where the bonds between Fe^{III} and the ligand are longer than expected. This makes it easier for the enzyme to change the redox state of the metal and therefore catalyze redox processes.[6, 7] Hydrolytic reactions, where zinc or cobalt in the enzyme´s active site facilitate ligand substitution by accepting distorted geometries, are another example.[8, 9]

These suggestions are the usually accepted modes of action for enzymes nowadays. They culminated in the recently reported design of artificial enzymes, so called “theozymes”, where functional groups have been arranged in a way that gives optimum interactions with predicted transition states to yield the best stabilization, i.e. the largest lowering in energy.[10, 11] Nevertheless, one has to pay attention to the fact that optimum transition state stabilization may lead to stabilization of the reactant structure as well. This would not necessarily result in lowering of activation barriers, but the opposite effect might be observed. And indeed, a recently published comparison of oxo-anion hole structures in enzymes and small molecules arrives at the following conclusion: The hydrogen bonding interactions between the enzyme´s H-bond donors and carbonyl groups observed in there are not optimized for the expected transition states. Evolution rather caused an arrangement, which results in lower activation energies.[12]

2.2. *Purple Acid Phosphatases*

Purple Acid Phosphatases (PAPs) belong to the enzyme family of binuclear metallohydrolases, which catalyze the hydrolysis of amides and esters of carboxylic and phosphoric acids. They contain dinuclear metal ion centers in their active sites, which can be homo- or heterovalent. Some examples, together with their metal composition and, if known, their metabolic roles are summarized in Table 2.1.[13]

Table 2.1: Examples of binuclear metallohydrolases.[13]

enzyme	metal center	metabolic roles
purple acid phosphatases	Fe(III)-Fe(II) Fe(III)-Zn(II) Fe(III)-Mn(II)	bone resorption, iron transport, ROS generation; mobilization of inorganic phosphate
ser/thr phosphatases[a]	Fe(II)-Fe(II) Fe(II)-Zn(II) Mn(II)-Mn(II)	glycogen metabolism, muscle contraction, signal transduction, neuronal activities, cell cycle progression, RNA splicing
ureases	Ni(II)-Ni(II)	hydrolysis of urea
leucine aminopeptidases	Zn(II)-Zn(II)	protein degradation, amino acid biosynthesis
3´-5´exonucleases	Mn(II)-Mn(II)	correction of errors during DNA replication
phosphotriesterase[a]	Zn(II)-Zn(II) Cd(II)-Cd(II) Zn(II)-Cd(II) Co(II)-Co(II)	removal of organophosphates as response to toxic stress

[a] *in vivo* metal composition not established

As indicated in Table 2.1, PAPs exhibit diverse metabolic roles that also depend on the organism. An important finding was that osteoporosis patients or people with bone metastases have elevated PAP concentrations.[14] Transgenic mice, in which the enzymes are over-expressed, develop a mild form of osteoporosis with increased bone resorption.[15] Knock-out mice, which completely lack the enzyme, exhibit the opposite phenotype (osteopetrosis).[16] Nowadays, PAP has become the most commonly used histochemical marker for osteoporosis.[17] Its obvious involvement in this disease makes it a very attractive target for the development of therapeutics.[18] Other functions of mammalian PAP include iron transport during pregnancy[19] and the generation of reactive oxygen species through Fenton-type chemistry.[20-22]

Plant PAP is presumably responsible for mobilizing organic phosphate esters.[23] In tomatoes, high PAP expression has been observed when phosphate starvation occurs.[24] A second role is an alkaline peroxidase type function of some forms of plant PAP. Reactive oxygen species (ROS) are produced by PAPs with peroxidase activity as a response to pathogen attack or biotic and abiotic stress.[24] The main problem of studying plant PAP activity is that a multitude of genes encode different isoforms of this enzyme.[25]

Purple acid phosphatases are the only enzymes among the group of hydrolases, where a heterovalent metal composition is crucial for activity. They always contain Fe^{III} and a second, divalent metal ion, depending on the source.[13, 26] Mammalian PAP, for example, uses Fe^{II},[27-29] whereas plant PAP contains Zn^{II} or Mn^{II}.[30-33] This is not the only difference: Mammalian PAP is a rather small monomeric enzyme with ≈ 38 kDa,[27-29] while most plant PAPs are homodimeric proteins with two subunits of ≈ 55 kDa each, connected via disulfide bridges.[30-32] Also, heterodimeric forms of plant PAP have been reported.[24] Fungal PAP is supposed to exist in a monomeric form with a molecular weight of ≈ 85 kDa and its metal ion composition is not yet known.[34, 35] No bacterial PAP has been characterized so far, but there is evidence that PAPs only occur in a limited number of microorganisms.[36] Nevertheless, independent of the type, the active site amino acids in all PAPs are conserved, as shown in Figure 2.3.[37] The two metal ions are bridged by an aspartate and surrounded by six more amino acids that form two sites of different hardness. As one would expect, Fe^{III} is bound to the hard site, the divalent metal ion M to the soft one. Typical metal-metal distances observed in crystal structures are in the range of 3.1 to 3.3 Å for Fe^{III}-Zn^{II} in red kidney bean PAP,[13] 3.3 Å for Fe^{III}-Mn^{II} in sweet potato PAP[13] and 3.1 to 3.5 Å for mammalian PAP.[13] These are in good agreement with the values obtained from EXAFS studies.[38, 39] The proposed bridging and terminal aqua, hydroxo and oxo ligands, which indicate how the resting state of the enzyme might look like, are supported by various spectroscopic studies (CD/MCD, CW and pulsed

EPR, Mössbauer, UV/vis)[40-43] as well as X-ray crystallography.[44, 45] Depending on the metal ion composition and pH value, different bridging units are observed: The $Fe^{III}Fe^{II}$ core in mammalian PAP is only weakly coupled at pH 4.9, according to EPR and magnetization measurements. Most probably, a μ-hydroxo bridge is present in this case. The EPR spectrum shows a broad anisotropic signal with effective g values < 2.0, which has been assigned to the $S = ½$ state of the antiferromagnetically coupled $Fe^{III}Fe^{II}$ pair.[40] In contrast, $Fe^{III}Mn^{II}$ centers from sweet potato PAP are strongly coupled at this pH. This is consistent with a μ-oxo bridge.[33]

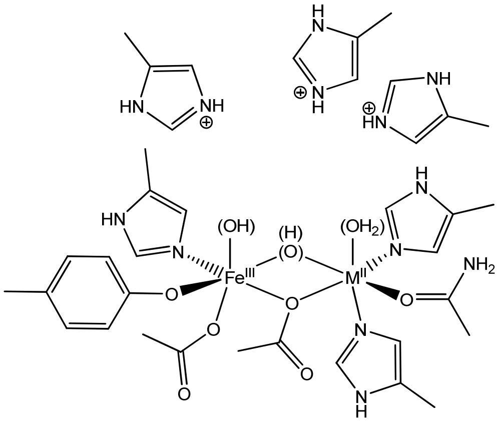

Figure 2.3: Schematic representation of the active site of PAPs at physiological pH; $M^{II} = Fe^{II}, Zn^{II}, Mn^{II}$.[44, 45]

Acid dissociation constants determined by spectrophotometric titrations have been assigned to aqua ligands coordinated to the metal ions. Water coordinated to the Fe^{III} site has pK_a values between 3.8 and 4.8,[41, 43] whereas Zn^{II}-bound aqua ligands give rise to pK_as around 9.5.[45] The additional protonated histidine residues shown in Figure 2.3 represent the second coordination sphere of the enzyme and together with the asparagine amido group are able to build up an extensive hydrogen bonding network.[46, 47]

The term "purple acid phosphatase" originates from the acidic to neutral pH optimum for PAP catalyzed reactions[17, 48, 49] and a tyrosine-to-Fe^{III} CT, which is responsible for the purple colour ($\lambda_{max} = 510 - 560$ nm; $\varepsilon = 3000 - 4000\ M^{-1}cm^{-1}$) of the enzyme.[50-52] In the case of mammalian PAP, the ferrous ion can be reversibly oxidized to a ferric ion, resulting in an inactive enzyme.[53, 54] This process is accompanied by a change in colour from pink ($\lambda_{max} \approx 515$ nm) to purple ($\lambda_{max} \approx 560$ nm).[50, 52] It is proposed that redox switching from active to inactive states is an *in vivo* regulation of PAP activity,[53] facilitated by low redox potentials for the $\mathrm{Fe^{III}Fe^{II}}$ / $\mathrm{Fe^{III}Fe^{III}}$ couple ($E_{1/2}$ = 306 mV vs. NHE, i.e 92 mV vs. SCE).[53, 54] The plant PAP´s $\mathrm{Fe^{III}Zn^{II}}$ center is missing any redox activity.[13]

PAPs catalyze, among others, the hydrolysis of phosphomonoesters.[13, 26] Phosphodiesters were generally found to be unaffected. Only small diester substrates, like the methyl derivative of pNPP, which are biologically irrelevant, are hydrolyzed by PAPs.[55] Different reaction mechanisms have been proposed so far and there is an ongoing debate about the various suggestions.[13, 37, 55-57] The most important questions to solve concern the mode of substrate coordination (monodentate vs. bridging), the nature of the attacking nucleophile (μ-hydroxide vs. terminal hydroxide or water/hydroxide bound in the second coordination sphere) and the reaction type (concerted vs. stepwise). The possible pathways are summarized in Scheme 2.1.[56]

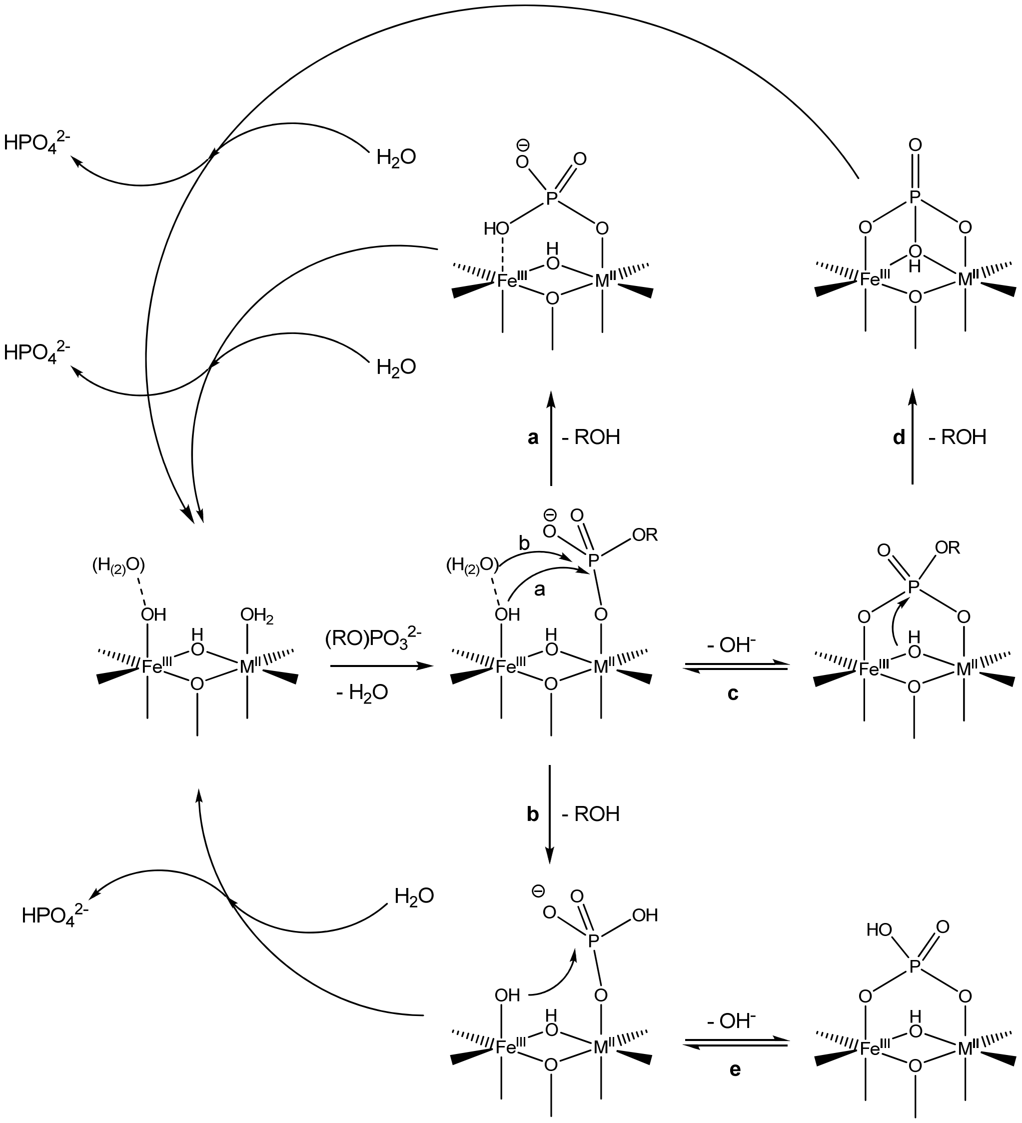

Scheme 2.1: Possible pathways for PAP catalyzed phosphoester hydrolysis; $\mathrm{M^{II}} = \mathrm{Fe^{II}}, \mathrm{Zn^{II}}, \mathrm{Mn^{II}}$.

Early publications about red kidney bean PAP and uteroferrin (pig uterus PAP) propose a monodentate binding mode of the substrate at the divalent metal and subsequent attack of an Fe^{III}-bound terminal hydroxide via pentacoordinate, associative-type phosphorous intermediates or transition states, which is consistent with pathway **a** in Scheme 2.1.[41, 45] Later on,[56] spectroscopic studies on bovine spleen PAP showed that the CT bands observed in UV/vis spectra and EPR signals associated with Fe^{III} are only slowly affected during reaction of the enzyme with phosphate. Based on these findings, mechanistic suggestions were made that support the monodentate binding mode of substrate, but argue against an Fe^{III}-bound terminal hydroxide as nucleophile. A reasonable explanation is that this hydroxide acts only as a base, which deprotonates a water molecule bound in the second coordination sphere of the enzyme. The resulting “free” hydroxide can then attack the substrate (pathway **b**), giving rise to a monodentate phosphate as product.[56] Different inhibition processes are discussed; they all include formation of bridging substrate or product coordination modes (equilibria **c** and **e** in Scheme 2.1).[41, 45] Pathway **d** was therefore excluded, which is further justified by the low nucleophilicity of μ-hydroxides. Labeling studies with [^{18}O]-phosphate demonstrated successive oxygen exchange between enzyme-bound phosphate and water.[58] This result supports the existence of equilibrium **e** with nucleophilic substitution at the bound phosphate, as indicated by the reaction arrow, instead of simple replacement of the Fe^{III}-bound terminal hydroxide. The latter process is discussed to be less plausible due to slow ligand exchange at trivalent metal ion sites, which would also favor path **b** over path **a**.

A few years ago, an eight step mechanism was published, which is based on X-ray structures in conjunction with spectroscopic studies of different enzyme-inhibitor complexes as well as kinetic data for phosphoester hydrolysis.[37] Schenk and co-workers suggest a pre-coordination of the substrate in the second coordination sphere, followed by monodentate and, subsequently, bridging coordination. The attacking nucleophile would then be a μ-hydroxide, which is rather asymmetrically bound (“quasi-terminal”) and therefore believed to be more active. This proposal was originally made by Wang et. al.[38] and resembles the previously excluded pathway **d** in Scheme 2.1. The product of such a reaction would be a phosphate bound in a tripodal way. Although this coordination mode was only observed in sweet potato PAP, which has an $Fe^{III}Mn^{II}$ active site, the mechanistic proposal was attributed to red kidney bean PAP, which has Zn^{II} as divalent metal ion in its native form.

Stopped-flow experiments on phenyl phosphate hydrolysis by the native $Fe^{III}Fe^{II}$ form and the artificial $Fe^{III}Mn^{II}$ derivative of uteroferrin were reported recently.[59] In the native form, they show that hydrolysis of the substrate occurs definitely faster than perturbation of the CT bands of Fe^{III}, which again supports monodentate substrate binding and non-Fe^{III}-bound hydroxide as nucleophile (pathway **b**). With the Mn^{II} derivative, the ratio of hydrolysis vs. Fe^{III} involvement rate is smaller by one to two orders of magnitude, but still catalysis is faster than formation of bridging substrate.

It is likely that, depending on the metal composition in the PAP active site and the substrate used, different mechanisms operate.[60] Nevertheless, a non-bridging coordination mode of the substrate and a hydroxide bound in the second coordination sphere as nucleophile seems to be more plausible, especially when the recently reported stopped-flow experiments are considered.[59]

In PAPs[37, 45, 59] as well as in many other enzymes,[61-63] the second coordination sphere is believed to play a crucial role for catalytic efficiency. Possible functions include preorganisation, orientation and activation of substrates, stabilization of transition states as well as acceleration of product release by hydrogen bonding and its role as a proton source. Krebs *et al.* already suggested in 1996 that the substrate is bound by the divalent metal and two protonated histidine residues (His_{216} and His_{113} in Figure 2.4a; the numbering Scheme corresponds to rat bone PAP) and is by that optimally aligned for an in-line attack of the Fe^{III}-bound hydroxide.[45] During reaction, the negative charges of the pentacoordinate intermediate or transition state are likely to be balanced by the protons, resulting in over-all stabilization. In 2010, Schenk *et al.* also included hydrogen bonding interactions into their considerations: A water molecule positioned in the second coordination sphere (which is deprotonated by Fe^{III}-bound hydroxide) is believed to act as nucleophile (see Figure 2.4a).[59] More interactions were found in X-ray structures of PAPs with inhibitors, like sulfate, which are also bound by an extensive hydrogen bonding network.[37]

Site-directed mutagenesis studies, where the mentioned histidines were replaced by other amino acids, gave more insight into the function of the second coordination sphere. Rat bone PAP and its mutants were examined in acid phosphatase activity (AcP) as well as in activity towards generation of reactive oxygen species (ROS).[21] The relative activities are presented in Figure 2.4b. All mutations reported in this paper lead to significantly lower AcP activity, while ROS activity remained nearly unaffected.

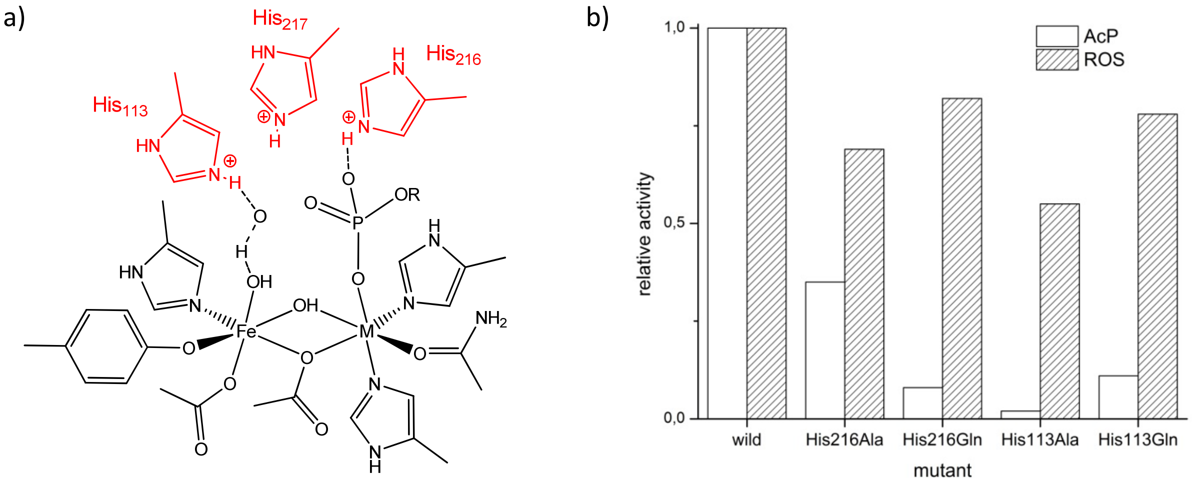

Figure 2.4: Numbering (a) and effects of replacement (b) of second coordination sphere amino acids in PAPs.

No definite mechanistic conclusions can be drawn from these results, but it becomes clear that the two metabolic roles of mammalian PAP involve different reaction mechanisms. Also, hydrogen bonding seems to be crucial for AcP activity, although the glutamines in the His$_x$Gln mutants are technically capable of hydrogen bonding interactions but still lead to lower activity. This is clarified by experiments with another mutant, where His$_{113}$ is replaced by an asparagine, which is the shorter analogue of glutamine.[64] This mutant shows a three-time larger activity than the wild-type enzyme. Probably, in this case an optimum geometry for hydrogen bonding is achieved.

2.3. *PAP Model Systems*

Small molecules mimicking enzymatic reactions have been widely used to gain a better understanding of possible pathways and mechanisms in enzymes. They do not only serve as a means to an end, but are themselves meant to act as therapeutics or catalysts. In fact, the field of “biomimetic chemistry” was mainly established in order to use obvious natural principles in chemical laboratories, especially for selectivity in chemical reactions (bioinspired catalysis), and not for a deeper understanding of natural processes.[65] This latter ambition was rather developed over time, when one realized that this deep understanding is often required to identify which motifs lead to high reactivity and selectivity.

When thinking about hydrolase mimetics, the need for accelerating this type of reactions is not obvious at first. Hydrolysis is in general not a difficult problem under laboratory conditions. Things become more complicated when physiological conditions are required. Of course, enzymes are perfectly developed for high performance at nearly neutral pH and ambient temperature, but their use has some limitations. Expression and purification of enzymes is time consuming and economically disadvantageous. Storage problems are another factor. The most problematic fact is that very complex analytical work has to be done on enzymatic systems. So it is desirable to have small, stable molecules that can catalyze hydrolysis under mild conditions. A major application target is the degradation of nerve agents and organophosphate pesticides, which are mainly phosphotriesters.[66, 67] This highly toxic class of compounds is generally quite stable and may accumulate over time.

In contrast, the scope of PAP mimetics is not the acceleration of hydrolysis, but the elucidation of the enzymatic mechanism. Osteoporosis, as well as some other diseases, have been proposed to be greatly affected by PAPs,[14] therefore a profound understanding of the mode of action will lead to new approaches in the for development of therapeutics.

Up to date, a variety of model systems for PAPs has been published.[13, 68-70] First structural models were built from relatively simple mononucleating ligands (see Figure 2.5 for structures and Table 2.2 for data and references) and resulted in symmetric diferric complexes, which imitate the inactive, diferric form of mammalian PAP. Good agreement was achieved regarding magnetic properties and geometric features (see Chapter 2.4 for more details on diferric systems).

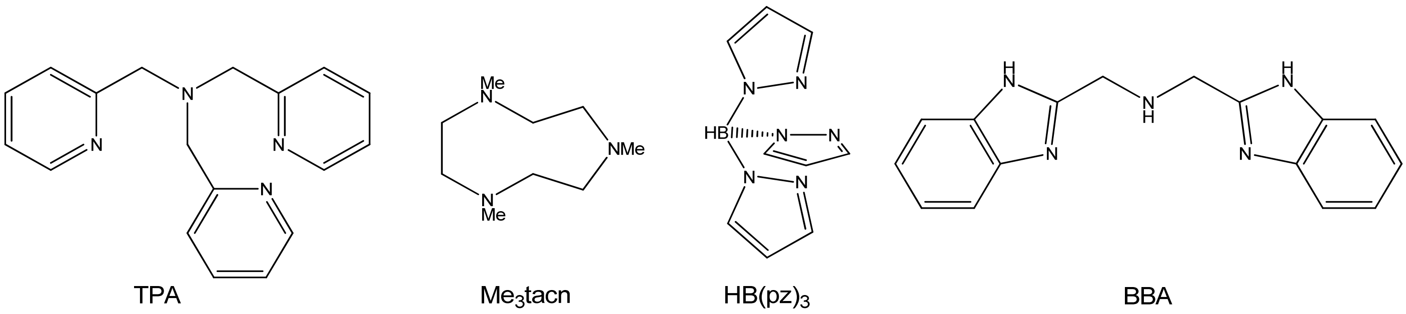

Figure 2.5: Mononucleating ligands for simple PAP model systems.

Table 2.2: Magnetic and geometric parameters of oxidized mammalian PAP and diferric model complexes.

parameter	ox. PAP[51]	a	b	c	d
-J [cm^{-1}]*	≥ 150	119	119	121	117
d(Fe-Fe) [Å]	3.50	3.24	3.12	3.15	3.08
Fe-O-Fe [°]	122.1	127.9	119.7	123.5	118.7
d(Fe-O) [Å]	2.00	1.80	1.80	1.78	1.80

* $H = -2JS_AS_B$; a = $[Fe_2(TPA)_2O(OBz)]^{3+}$;[71] b = $[Fe_2(Me_3tacn)_2O(OAc)_2]^{2+}$;[72] c = $[Fe_2(HB(pz)_3)_2O(OAc)_2]$;[73] d = $[Fe_2(BBA)_2O(OBz)_2]^{3+}$.[74]

In 1988, Que et al. reported a nice example of a spectroscopic model, where the tyrosinate-Fe^{III} feature of the natural enzymes was mimicked.[75] Using the tripodal ligand *N*-(*o*-hydroxybenzyl)-*N*,*N*-bis-(2-pyridylmethyl)amine (HDP) and benzoic acid as co-ligand, a μ-oxo-μ-benzoato bridged diferric complex was obtained (Figure 2.6).

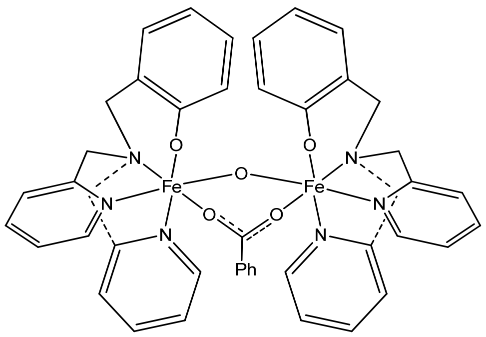

Figure 2.6: Spectroscopic PAP model complex based on ligand HDP.[75]

For the first time, the high molar extinction coefficient for the phenolate-to-iron CT transition observed in the enzyme was nearly reproduced by a model complex (λ = 552 nm; ε = 3300 $M^{-1}cm^{-1}$/Fe vs. λ = 550 nm; ε = 4000 $M^{-1}cm^{-1}$ in the oxidized enzyme).

A major challenge towards functional PAP model complexes is the introduction of heterodimetallic sites. With mononucleating ligands this task could not be performed. A big success was then the development of dinucleating ligands, where a bridging donor atom is included in the ligand backbone. The main motifs used thereby are shown in Figure 2.7 (upper part).[69] Many different ligands were synthesized based on these linkers, at first with four equal residues $\mathbf{R}^x$ leading to symmetric systems. Examples included ligands based on linker **A** with residues **2** (HBIMP),[76] **3** (HL-Bzim)[77] or **5** (HXTA).[78] Starting from ferrous salts, all reactions under anaerobic conditions resulted in heterovalent di-iron complexes with weak exchange coupling (-J ≈ 2-7 cm^{-1}), which is in good agreement with the reduced form of mammalian PAP (-J = 7-10 cm^{-1}).[51] Also, the reduction potentials for the $Fe^{III}_2/Fe^{III}Fe^{II}$ couples have been reported for the complexes with Hbimp and HXTA ligands: They are 435 mV and -286 mV vs. SCE, respectively. In contrast, the redox potential of mammalian PAP is 92 mV vs. SCE.[53, 54] These model complexes obviously do not reproduce the electrochemical properties of the enzyme. The symmetric ligand HBPMP (linker **A** with four picolyl residues **1**) was used for the synthesis of heterodimetallic complexes, e.g. $Fe^{III}Zn^{II}$,[79, 80] $Fe^{III}Cu^{II}$,[81, 82] $Fe^{III}Co^{II}$ [83] and $Fe^{III}Ni^{II}$,[83] resulting in very similar asymmetric structures.

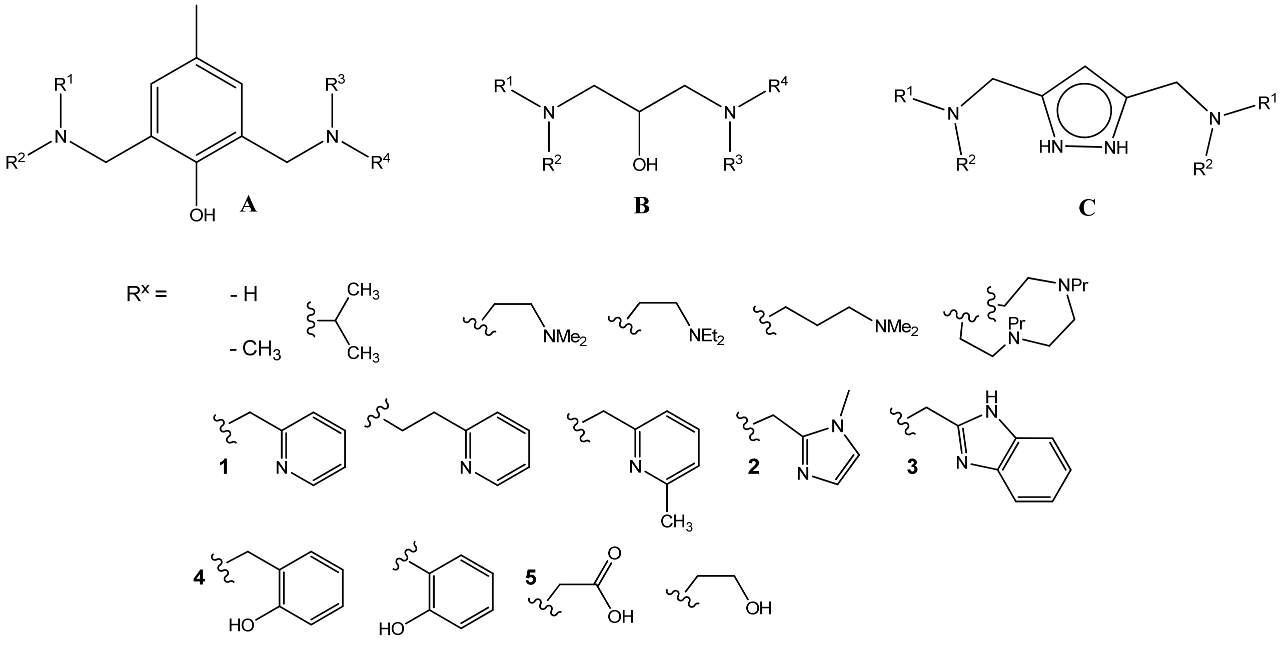

Figure 2.7: Variety of dinucleating ligands used for PAP model complexes.[69]

The next big achievement was the development of synthetic protocols giving rise to non-symmetric ligands with two or more different coordinating residues. Based on the HSAB principle, sites of non-equivalent hardness (different number of N- and O-donors, see Figure 2.7, bottom) resulted in selective coordination of di- and trivalent metals, respectively. The first complex of this type was presented by Bernhard *et al.* in 1994.[84] The ligand was based on linker **A** in combination with three picolyl (**1**) and one methylphenolate (**4**) residues (Figure 2.8; H_2BPBPMP = 2-bis[{(2-pyridylmethyl)-aminomethyl}-6-{(2-hydroxybenzyl)-(2-pyridylmethyl)}-aminomethyl]-4-methylphenol). The phenolate containing site is the hard one and therefore Fe^{III} preferably binds there. The softer bis-pyridyl site is coordinated to the divalent metal ion. In the reported case, Fe^{II} is used as divalent metal ion. The geometric features of this complex determined by X-ray crystallography and some spectroscopic and magnetic properties are very close to the ones of the enzyme´s active site: the metal-metal distance is 3.42 Å vs. 3.52 Å in the reduced form of the enzyme.[51] In the UV/vis spectrum, the phenolate-to-Fe^{III} CT transition is found at λ = 535 nm (ε = 1700 $M^{-1}cm^{-1}$). Also, the oxidation potential of 220 mV vs. SCE fits better to the enzyme´s redox potential than those for the symmetric complexes mentioned above. Asymmetry is also nicely visible in the bond lengths from the two iron centers to the bridging phenolate, where a significant difference of 0.124 Å is observed. This leads to the conclusion that both iron ions are in localized valence states. Later on, the heterovalent di-iron complex of H_2BPBPMP was used to elucidate the redox regulation of enzymatic activity in mammalian PAP. It was shown that the product of hydrolysis (i.e. phosphate) is able to promote the oxidation of the complex.[85]

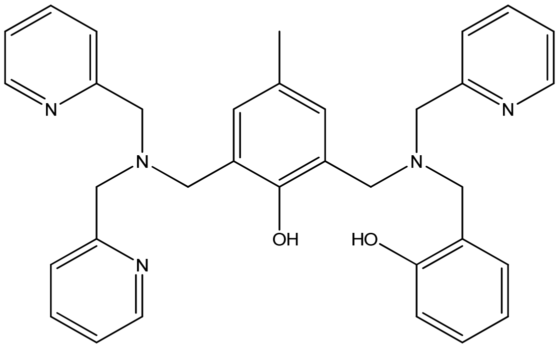

Figure 2.8: Asymmetric dinucleating ligand H_2BPBPMP.

H_2BPBPMP was also used to synthesize a variety of heterodinuclear complexes. Their catalytic properties in the hydrolysis of the activated diester substrate bis-(2,4-dinitrophenyl)-

phosphate (BDNPP) are summarized in Table 2.3.[69] Looking at the effects of different metal compositions on catalysis can give important hints about the reaction mechanism. For example, the Michaelis-Menten constant K_M, which can be interpreted as a measure of substrate affinity, strongly depends on the divalent ion: whereas Mn^{II} results in the lowest K_M (2.1 mM, i.e. best affinity), complexes with Co^{II} have an almost 50-fold higher K_M (50-fold lower affinity). In contrast, substitution of the trivalent metal ($Fe^{III} \rightarrow Ga^{III}$) has almost no effect on K_M, but leads to slightly increased turnover rates. These findings suggest that a) the substrate is only bound to the divalent metal ion during catalysis and b) the nucleophile is likely bound to the trivalent metal ion. The pH dependencies of all catalysts were measured and all resulted in bell-shaped profiles. The observed pK_as and the pH at which maximum activity occurs are all quite similar to each other. Interestingly, both pK_as are affected by a change of the divalent and the trivalent metal ion. This indicates a significant interaction between the metal ions. However, when changing the divalent metal ion, the effect is larger for the second pK_a.

Table 2.3: Catalytic properties of different complexes with the asymmetric, dinucleating ligand $H_2BPBPMP$.[69]

catalyst	pH_{max}	$pK_a(I)$[a]	$pK_a(II)$[a]	k_{cat} $[s^{-1}]*10^{-3}$	K_M [mM]	k_{cat}/K_M $[s^{-1}M^{-1}]$
$[Fe^{III}Fe^{II}BPBPMP(\mu\text{-}OAc)_2]^{+}$[86]	6.0	4.74	7.54	3.00	13.0	0.23
$[Fe^{III}Zn^{II}BPBPMP(\mu\text{-}OAc)_2]^{+}$[87]	6.1	4.80	7.50	0.73	8.1	0.09
$[Fe^{III}Mn^{II}BPBPMP(\mu\text{-}OAc)_2]^{+}$[88]	6.7	5.80	7.76	0.45	2.1	0.21
$[Fe^{III}Cu^{II}BPBPMP(\mu\text{-}OAc)_2]^{+}$[89]	7.0	5.20	8.50	1.77	11	0.16
$[Fe^{III}Ni^{II}BPBPMP(\mu\text{-}OAc)_2]^{+}$[90]	6.0	4.91	8.34	0.45	3.85	0.12
$[Fe^{III}Co^{II}BPBPMP(\mu\text{-}OAc)_2]^{+}$[91]	7.0	5.20	8.80	1.42	93	0.02
$[Ga^{III}Zn^{II}BPBPMP(\mu\text{-}OAc)_2]^{+}$[60]	6.8	5.35	8.55	1.41	7.15	0.20
$[Ga^{III}Co^{II}BPBPMP(\mu\text{-}OAc)_2]^{+}$[91]	7.5	5.70	8.90	1.87	88	0.02

[a] The assignment of the dissociation constants is depicted in Scheme 2.2.

Based on known pK_a values for metal ion bound water molecules and supported by spectrophotometric titrations of the complexes, the following mechanistic proposal was made

(Scheme 2.2): The first pK_a value belongs to water that is bound to the trivalent metal ion. Its deprotonation leads to formation of a suitable nucleophile for substrate hydrolysis. At a pH lower than the second pK_a value, at first, a water molecule is bound to the divalent metal which can easily be substituted by the substrate. Deprotonation of the water at higher pH leads to formation of a hydroxo ligand, which is more difficult to substitute. This diprotic model is a good explanation for the observed pH profiles, with an aqua-hydroxo complex of the following constitution being the active species: $[LM^{III}(OH)(\mu\text{-}OH)M^{II}(OH_2)]$ (middle structure in Scheme 2.2). The bridging hydroxide was included in this model as it was found in several X-ray structures of these complexes.[92] It is most probably inert, because bridging hydroxides are known to be poor nucleophiles.

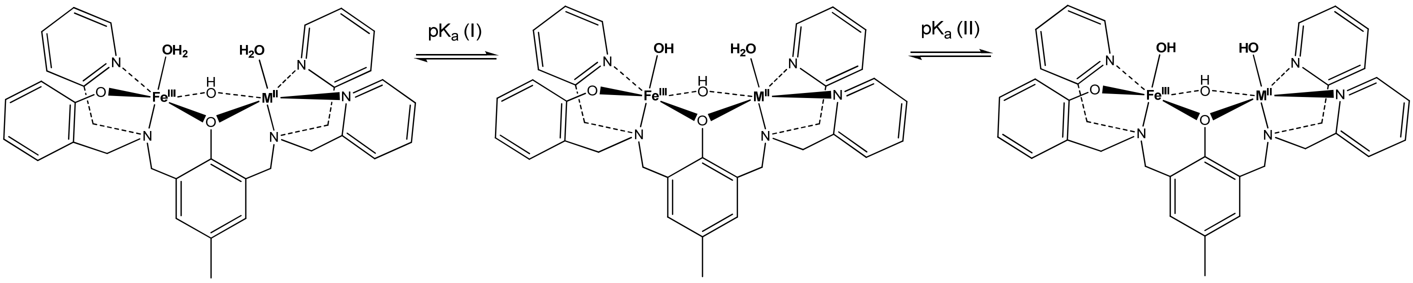

Scheme 2.2: Kinetically relevant protonation equilibria in H_2BPBPMP-based model complexes.

Some mechanistic investigations regarding the hydrolysis of activated phosphoesters were conducted with the $Fe^{III}Zn^{II}$ derivative of H_2BPBPMP.[92] UV/vis spectra of the complex with an excess of the diester BDNPP showed almost no change in the phenolate-to-Fe^{III} CT band, suggesting that no interaction between the substrate and Fe^{III} occured. When DNPP, the monoester analogue of BDNPP (and therefore the reaction product of the first hydrolysis step) is used as substrate, a hypsochromic shift of the mentioned band is observed but, apart from the background activity, no hydrolysis can be seen. This is interpreted as a bridging coordination of the monoester, which represents an inhibitory state. The coordination of DNPP is rather weak and it can be easily replaced by BDNPP, showing perfectly recovered hydrolytic activity. Based on these results, the following catalytic cycle was proposed (Scheme 2.3):[92]

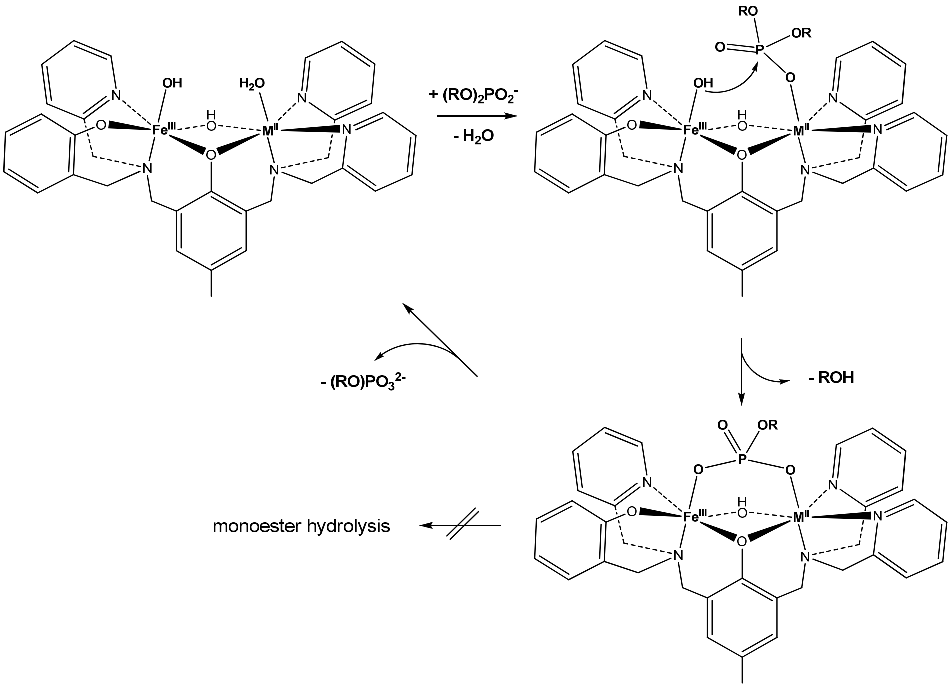

Scheme 2.3: Proposed catalytic cycle for PAP model complexes.[92]

This pathway has also been investigated by DFT calculations,[93] using a simplified system, where the phenolate ring had been cut resulting in a 3-pentanol bridged ligand. Dimethyl phosphate (DMP) was used as simple phosphodiester substrate. Starting from monodentately coordinated DMP on Zn^{II} and a hydroxo ligand on Fe^{III}, the reaction proceeds to a pentacoordinated phosphorane structure via a transition state which is close to the intermediate. The activation barrier for this process is 12.3 kcal/mol, which is a rather small value. From this intermediate, two other structures are found before reaching the product state. The energy values for these do not indicate a second transition state, but this can be explained with a very flat energy surface in combination with the inaccuracy of DFT methods. In comparison to the previously calculated uncatalyzed DMP hydrolysis (32 kcal/mol), the barrier for the catalytic reaction is 2.6 times lower, which would mean an unrealistic acceleration rate of ca. 10^{14}. Unfortunately, no calculations were performed on substrate coordination or product release, which might be involved in the rate determining step. Also, the energy barrier for the attack of the bridging hydroxide at the bridging monoester would be interesting in terms of explaining the lack of reactivity.

So far, no PAP type model complexes were reported to catalyze phosphomonoester hydrolysis, which is the actual function of the enzymes.[87, 88, 90] The main problem could be the inhibitor-like bridging coordination mode together with a μ-hydroxide as nucleophile that is too weak to perform the reaction. In the enzymes, the substrate is most probably bound monodentately to the divalent metal ion, with subsequent attack of either an Fe^{III} bound hydroxide or a hydroxide located in the second coordination sphere.[41, 45, 56, 59] The goal of functional PAP mimetics should therefore be to preorganize the monoester substrate in a monodentate coordination mode. A possible way to achieve this could be the incorporation of a second coordination sphere mimic into the model systems. Only few publications are available, where this principle has been examined (see Figure 2.9 for the structures): Masuda *et al.* reported the stabilization of a terminal Cu^{II} bound hydroxide through interaction with hydrogen bond donors and shielding by bulky neopentyl groups (structure **1** in Figure 2.9).[94] Marque-Rivas and Williams *et al.* clearly showed a rate enhancement of phosphodiester hydrolysis by cooperation of double Lewis activation (2 x Zn^{II}) and the hydrogen-bonding environment provided by the used ligand (structure **2** in Figure 2.9).[95] These results encourage the development of PAP mimetics containing a second coordination sphere but no iron complexes or PAP mimetics have so far been reported, where these types of interactions were present.

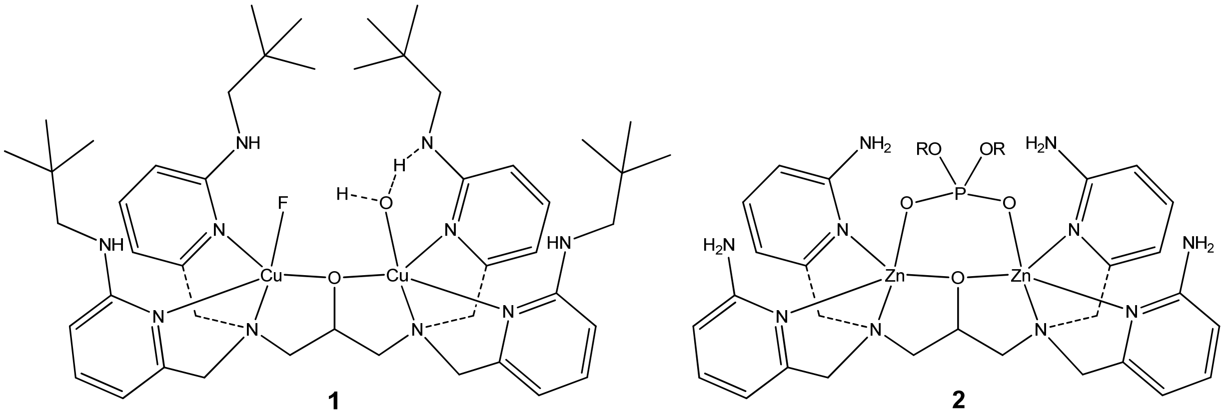

1 **2**

Figure 2.9: Examples of model complexes with a second coordination sphere.

2.4. Chemistry of Bridged Diferric Complexes

In order to simplify the envisioned study of second coordination sphere effects, we have chosen to work on diferric model complexes only. Although mammalian PAPs are reported to be exclusively active in their heterovalent state,[96] some diferric model complexes are known to catalyze phosphoester hydrolysis.[97-101] The results of these studies suggest that in the model systems the slow exchange of product is not a significant barrier to the hydrolysis reaction, whereas in the PAP enzyme systems a diferric active site would be.

Bridged diferric complexes can be formed with relatively simple, mononucleating ligands, including $EDTA^{4-}$, TPA, BBA, HDP, $HB(pz)_3^-$ and Me_3tacn (see Chapter 2.3 for ligand structures). Extensive structural and spectroscopic studies have been performed on this kind of complexes with different types of bridging groups (Figure 2.10). The complex synthesis is, generally, rather simple: Ligand solutions in MeOH or MeCN, sometimes in other solvents or with additional base, are reacted with solutions of ferric salts, like ferric perchlorate or nitrate, and subsequently co-ligands are added.[102, 103] With Me_3tacn[104] and $HB(pz)_3$,[105] an already formed diferric complex with an easily replaceable acetate bridge was used as starting material and reacted with the respective co-ligand under ligand exchange. Almost in every case, X-ray quality crystals were obtained with established crystallization methods.

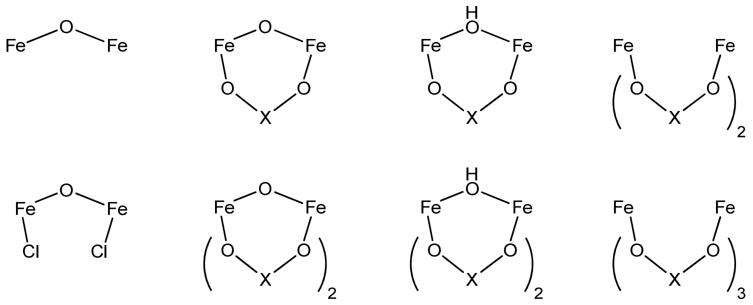

$O-X-O = HPO_4^{2-}$, $(RO)PO_3^{2-}$, $(RO)_2PO_2^-$, $(R)_2PO_2^-$, OAc^-, OBz^-, CO_3^{2-}, SO_4^{2-}, AsO_4^{3-}, CrO_4^{2-}, MoO_4^{2-}, ...

Figure 2.10: Structural variations of bridged diferric complexes relevant for this work.

Table 2.4 summarizes the obtained structural and magnetic parameters for selected complexes of the type shown above. Generally, μ-oxo bridged complexes give rise to strong antiferromagnetic coupling with $–J > 80\ cm^{-1}$. No correlation is observable between the actual J-value and structural factors like number of bridging/non-bridging co-ligands or Fe-O-Fe angles, which span a range between 123 and 175°. Different metal-metal distances result from these varying angles, lying between 3.15 and 3.57 Å.

Table 2.4: Structural and magnetic data of selected diferric complexes.

entry	complex	d(Fe-Fe) [Å]	d(Fe-O) [Å]	< Fe-O-Fe [°]	$-J^{[a]}$ [cm^{-1}]	ref.
1	$[Fe_2(A)_2O(O_2P(OPh)_2)_2]$	3.34	1.81	134.7	98	[105]
2	$[Fe_2(A)_2OH(O_2P(OPh)_2)_2]^+$	3.59	1.96/1.98	131.1	15	[106]
3	$[Fe_2(A)_2(O_2P(OPh)_2)_3]^+$	4.68	-	-	0.8	[106]
4	$[Fe_2(A)_2O(OAc)_2]$	3.15	1.78	123.6	121	[73]
5	$[Fe_2(A)_2OH(OAc)_2]^+$	3.44	1.96/1.95	123.0	17	[106]
6	$[Fe_2(B)_2O(O_3POPh)_2]$	3.20	1.82	123.2	98	[104]
7	$[Fe_2(B)_2(O_3POPh)_3]$	n.a	n.a	n.a	3.5	[104]
8	$[Fe_2(B)_2O(HPO_4)_2]$	n.a	n.a	n.a	80	[104]
9	$[Fe_2(B)_2(HPO_4)_3]$	n.a	n.a	n.a	2.9	[104]
10	$[Fe_2(C)_2O(O_2P(OPh)_2)]^+$	n.a	n.a	n.a	96	[107]
11	$[Fe_2(C)_2(O_2P(OPh)_2)_2]^{2+}$	4.82	-	-	0	[107]
12	$[Fe_2(C)_2O(OBz)]^+$	3.22	1.78/1.80	128.3	111	[75]
13	$[Fe_2(D)_2O(O_2P(OPh)_2)]^{3+}$	3.36	1.82/1.78	138.1	101	[71]
14	$[Fe_2(D)_2O(OBz)]^{3+}$	3.24	1.80/1.78	129.7	119	[71]
15	$[Fe_2(D)_2O(Cl)_2]^{3+}$	3.58	1.79	174.7	116	[108]
16	$[Fe_2(E)_2O]^{2-}$	3.57	1.80/1.79	165.0	95	[109]

A = $HB(pz_3)$; B = Me_3tacn; C = DPA; D = TPA; E = H_2EDTA; n.a = data not available; [a] $H = -2JS_AS_B$.

In contrast, μ-hydroxo bridged structures show significantly longer distances, e.g. 3.44 vs. 3.15 Å with acetate (entries 4 and 5) and 3.59 vs. 3.34 Å with diphenyl phosphate (entries 1 and 2). This is a result of longer Fe-OH bonds in comparison to Fe-O bonds. Also, the μ-hydroxo bridge is a less effective mediator of exchange coupling interactions, resulting in relatively small –J values of 15 to 17 cm^{-1}. When no μ-oxo or μ-hydroxo bridge is present in addition to the bridging co-ligands, even weaker coupling is observed with –J between 0 and 3.5 cm^{-1}. This is not only a consequence of the strongly reduced magnetic exchange, but also of long metal-metal distances (> 4.5 Å, entries 3 and 11). In summary, the three types of bridged diferric complexes (μ-oxo, μ-hydroxo and no additional bridge) have well separated ranges of values for structural and magnetic properties. Especially, the J values can give essential structural information.

Electronic and vibrational spectroscopy is also an important tool for the characterization of diferric compounds (see Table 2.5). Asymmetric and symmetric stretching frequencies from IR and raman spectra, respectively, can give information about the strength of the Fe-oxo bonds and, regarding the intensities, about the extent of symmetry in the complexes. Labeling studies support the assignment of bands. Yet, no correlation between spectroscopic and structural features is found in the examples shown. Also the definitive interpretation of UV/vis spectra is not easy in this case. In the visible region, almost no bands are present; this is due to Laporte forbidden dd transitions in high spin ferric ions. In contrast, very intense bands ($\varepsilon > 1000\ M^{-1}cm^{-1}$) can be seen in the near-UV or UV region, arising from a combination of ligand-to-metal and oxo-to-metal CT transitions. Although the number and position of these bands strongly differs from complex to complex, their presence is a good general indication for μ-oxo bridged structures.

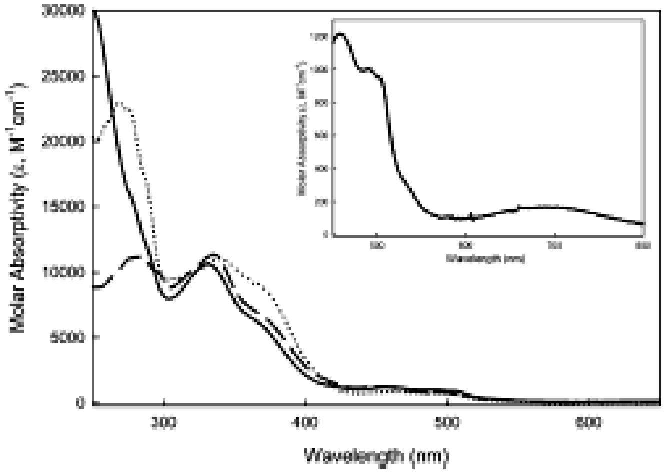

Figure 2.11: Typical UV/vis spectra of different μ-oxo bridged diferric complexes based on TPA.[110]

Table 2.5: Spectroscopic data of diferric complexes.[a]

entry	complex	LMCT λ [nm]	ν_{as} [cm^{-1}]	ν_s [cm^{-1}]
1	$[Fe_2(A)_2O(O_2P(OPh)_2)_2]$	321; 366; 500	767	478
2	$[Fe_2(A)_2OH(O_2P(OPh)_2)_2]^+$	n.a.	n.a.	n.a.
3	$[Fe_2(A)_2(O_2P(OPh)_2)_3]^+$	n.a.	-	-
4	$[Fe_2(A)_2O(OAc)_2]$	339; 358; 400; 528	751	528
5	$[Fe_2(A)_2OH(OAc)_2]^+$	n.a.	n.a.	n.a.
6	$[Fe_2(B)_2O(O_3POPh)_2]$	6 bands at 300 - 520	694	n.a.
7	$[Fe_2(B)_2(O_3POPh)_3]$	ca. 330 (sh)	-	-
8	$[Fe_2(B)_2O(HPO_4)_2]$	6 bands at 300 - 520	706	n.a.
9	$[Fe_2(B)_2(HPO_4)_3]$	ca. 325 (sh)	-	-
10	$[Fe_2(C)_2O(O_2P(OPh)_2)]^+$	350; 516[b]	n.a.	461
11	$[Fe_2(C)_2(O_2P(OPh)_2)_2]^{2+}$	380; 605[b]	-	-
12	$[Fe_2(C)_2O(OBz)]^+$	350; 522[b]	763	494
13	$[Fe_2(D)_2O(O_2P(OPh)_2)]^{3+}$	322; 360; 446; 480;496; 518	778	454
14	$[Fe_2(D)_2O(OBz)]^{3+}$	328; 368; 460; 492; 504; 534	772	497
15	$[Fe_2(D)_2O(Cl)_2]^{3+}$	320; 380; 490; 573	816	363
16	$[Fe_2(E)_2O]^{2-}$	307; 343; 403; 455; 477; 544	838	409

[a] see Table 2.4 for references and ligand abbreviations; [b] phenolate-to-Fe CT transitions from HDP ligand; n.a. = data not available.

Electrochemical studies were performed on a series of diferric μ-oxo bridged TPA complexes with a multitude of bridging oxo-anions, like acetate, phosphates, vanadate, molybdate, as well as with chloride as non-bridging terminal co-ligand.[111] Their redox potentials for the $Fe^{III}_2/Fe^{III}Fe^{II}$ couples cover a range of almost 600 mV. With diphenyl phosphate, the highest redox potential was obtained (-64 mV vs. SCE), whereas the carbonate bridged complex had the lowest (-624 mV vs. SCE). Almost all complexes showed a reversible redox behavior, apart from the phosphate and carbonate bridged species. In the case of phthalate bridging, a quasi-reversible reduction was observed. By choosing the right type of co-ligand, it is therefore possible to stabilize the heterovalent state in μ-oxo bridged di-iron complexes. Nevertheless, the question remains if stability is retained under aerobic conditions Reduced Uf (uteroferrin, a form of mammalian PAP) is reported to slowly undergo autoxidation, having a redox potential of 92 mV vs. SCE,[53, 54] and Uf-phosphato complexes (-130 mV vs. SCE)[53] are oxidized even faster, whereas with molybdate as co-ligand, an air-stable form of reduced Uf is obtained (254 mV vs. SCE).[53] Regarding the redox potentials, a substantial aerobic stability of the heterovalent states in the cited complexes is not expected.

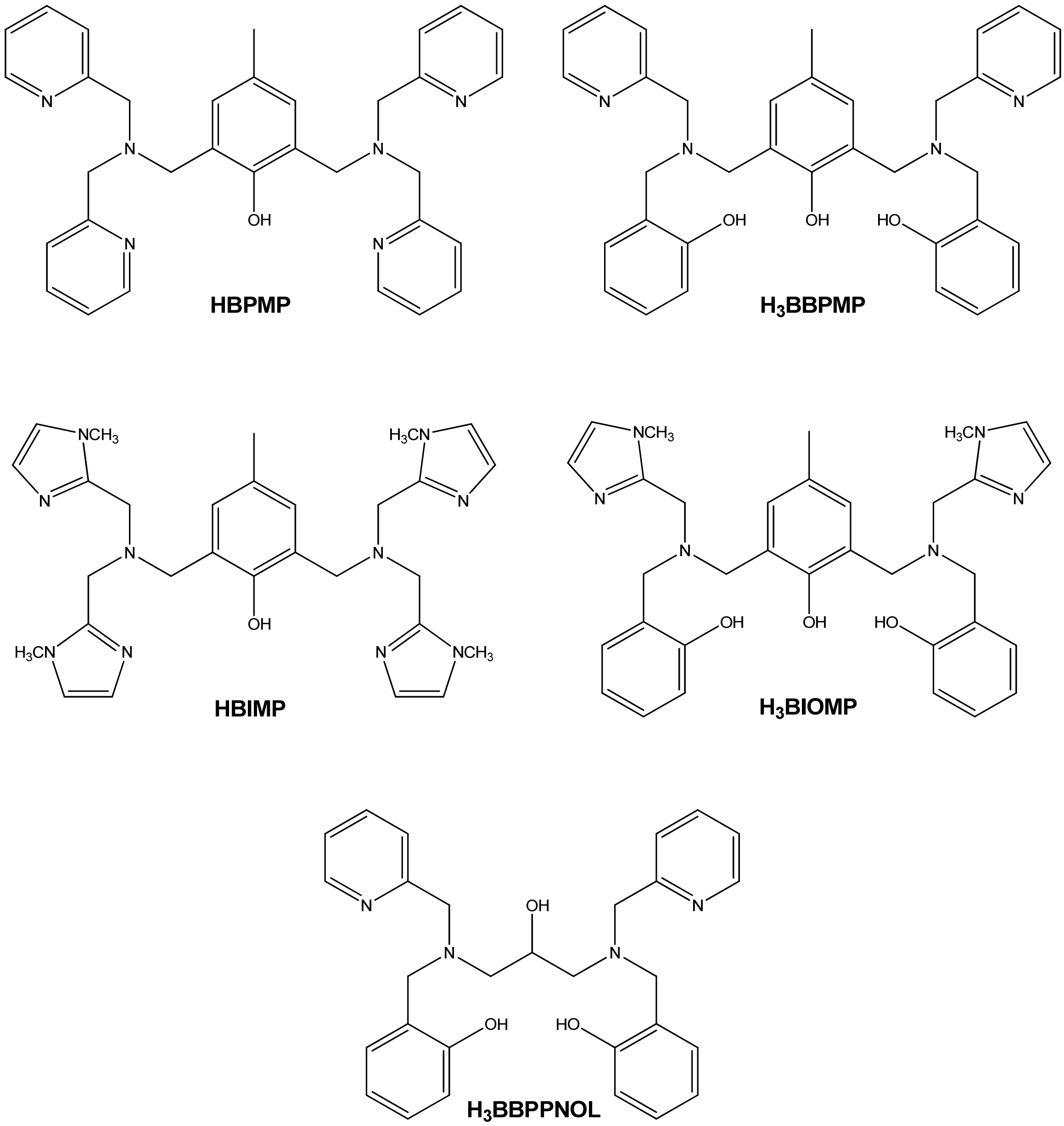

Figure 2.12: Dinucleating ligands used for diferric complexes.[69]

When dinucleating ligands of the type presented in Figure 2.12 are used, usually triply bridged structures are obtained. One bridge arises from the ligand itself; mainly, phenolate or alcoholate type ligand backbones are used. The other bridges are built up by additional co-ligands of the same kind as presented in Figure 2.10. As the core structures in these kinds of complexes do not vary much, the magnetic properties are very similar. The coupling constants for antiferromagnetic coupling –J lie in the range of 5 to 15 cm^{-1}, which is typical for phenoxo/alkoxo/hydroxo bridges.[112, 113] The number of coordinated phenolates is reflected in the actual value, as the trans effect of phenolate ligands elongates the Fe-O-Fe bonds and therefore weakens the interaction, resulting in rather small –J values in the mentioned range.[112] UV/vis spectra of diferric complexes with phenolate-based ligands are dominated by the relatively broad phenolate-to-iron CT transitions, which are in the range between λ = 500 - 700 nm with extinction coefficients of ε = 1000 – 2000 $M^{-1}cm^{-1}$. Additional $p_{\pi} - d_{\sigma*}$ type transitions are present in the range between λ = 300 – 400 nm (ε = 2500 – 5000 $M^{-1}cm^{-1}$).[112-115] Mixed-valent $Fe^{III}Fe^{II}$ complexes usually have bands in the same regions, but with significantly smaller extinction coefficients ($\varepsilon \approx 500$ $M^{-1}cm^{-1}$) due to the presence of only one ferric ion per complex.[115] The reported redox potentials span a wider range, depending on which dinuclating ligand is used and the nature of the co-ligands. Several examples are given in Table 2.6, (see Figure 2.12 for ligand structures).

Table 2.6: Redox potentials of diferric complexes with dinucleating ligands (in mV vs. SCE; n.a = data not available).

co-ligand // ligand	BPMP	BBPMP	BIMP	BIOMP	BBPPNOL
OAc^-	690[116]	-190[115]	435[76]	155[113]	-230[114]
$O_2P(OPh)_2^-$	n.a	-200[112]	n.a	n.a	60[112]

When ferrous salts are used as precursors under anaerobic conditions, all presented ligands can form heterovalent complexes.[115, 116] As solids, these complexes are quite stable against oxidation. Their solution behavior is well reflected by their redox potentials. Some trends can be seen regarding the type of ligand and co-ligands. The complexes with BPMP and BIMP have very positive redox potentials, and in fact, only the heterovalent states are stabilized and obtained, even when ferric salts are used as precursors.[76, 115] The di-phenol derivatives, BBPMP and BIOMP result in complexes with redox potentials that are 880 and

280 mV lower, respectively, and therefore the homovalent, diferric states are obtained in solution under aerobic conditions.[112, 113, 115] The co-ligands only show marginal effects in the BBPMP case, whereas with BBPPNOL as ligand, a change from acetate to diphenyl phosphate results in a positive shift of the redox potential of almost 300 mV. Still, this value is not high enough to yield air-stable heterovalent complexes. In summary, the integration of more than one phenolate into the coordination sphere results in complexes with low redox potentials and rather stabilizes their diferric state than the heterovalent one.

Chapter 3:

Results and Discussion

3.1. Preliminary Considerations

The aim of this work is to explore the effects of a second coordination sphere on the activity towards hydrolysis of phosphoesters, especially monoesters. Suitable ligand systems must be found that have the following prerequisites: A coordination sphere is required that can bind two metal centers in an appropriate distance, which is between approximately 3.2 and 4 Å.[13] At least one free coordination site per metal is needed in order to provide the possibility of substrate and nucleophile coordination. As the used substrates, BDNPP and DNPP, are relatively bulky due to their 2,4-dinitrophenol groups, enough space must be provided around the metals to prevent a large steric strain.

There are some difficulties associated with the incorporation of a second coordination sphere into the ligand system. Important considerations include which kind of atoms to use and at what distance to the metal center to place them. In natural systems, mainly histidine residues with their protonated imidazoles fulfill this role. Enzyme X-ray structures of red kidney bean PAP[37, 45] and mammalian PAP[46, 117, 118] reveal metal – second coordination sphere distances between 4.9 and 6.3 Å, depending on which co-ligand is used and how this is bound to the active site. Usually, the ligand backbone with its amino acid residues is relatively flexible, so these deviations are not unexpected.

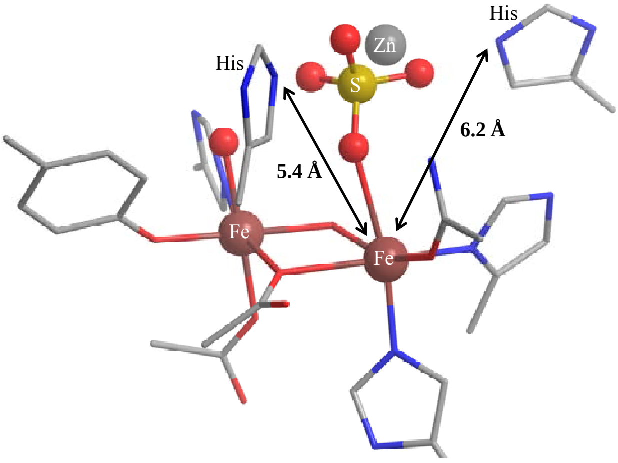

Figure 3.1: Distances between metal and second coordination sphere in rat PAP with sulfate.[117]

Only one X-ray structure of a purple acid phosphatase with a monodentately bound substrate mimic exists, which is proposed to be an artifact of the crystallization method as additional zinc is present in the second coordination sphere.[117] In this case, the distances from the coordinated metal to the closest protonated histidine residues are 5.40 and 6.20 Å, respectively (Figure 3.1). To further explore an appropriate distance between the metal ions and a second coordinaton sphere, the following model was established (see Figure 3.2): Two metal ions were connected via a μ-oxo bridge in a distance of 3.4 Å. A phosphate anion was coordinated to one of these metals forming an angle of 150° between metal, oxygen and phosphorous atoms. Hydrogen atoms were added to the oxygen atoms at a distance of 1.1 Å and additional nitrogen atoms, representing the second coordination sphere, were attached to them. Finally, the distance between the metals and the second coordination sphere nitrogen atoms was measured and resulted in values between 6 and 6.5 Å. Of course, this procedure is not very accurate but at least gives an idea about the geometric features that are needed to ensure interactions between a bound substrate and the remote ligand parts.

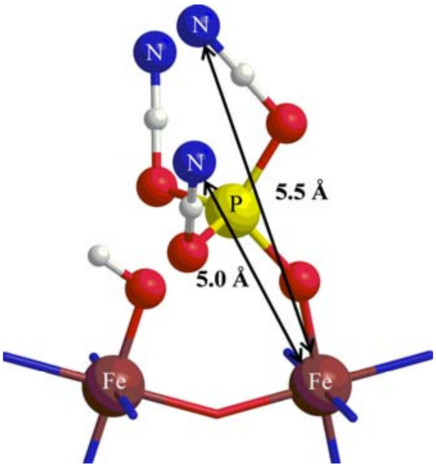

Figure 3.2: Modeling the appropriate distances between metal and second coordination sphere.

Regarding the choice of metal, we focused on diferric systems as a first approach. Some $Fe^{III}Fe^{II}$ complexes are known with redox potentials that are high enough to stabilize the heterovalent state under anaerobic conditions,[76, 115] but most of them are only air-stable in their homovalent, diferric form.[112, 113, 115] Although it is known that no activity is observed for mammalian PAP´s in their diferric state,[53, 54] this is not necessarily the case for model complexes. Certainly, no direct comparison of reactivities and kinetic data can be expected due to this difference, but this is not the aim of our work.

Based on these ideas, the development of new ligand systems for PAP model complexes was performed and will be described in the following chapters.

3.2. The Cyclam-based Ligand L^1

3.2.1. Synthesis and Properties of Ligand L^1

The retrosynthetic approach for ligand **L**^{1} is depicted in Scheme 3.1. Based on 1,4,8,11-tetraazacyclotetradecane (cyclam), the desired molecule is synthesized in six steps. An important step is the selective alkylation of two cyclam nitrogen atoms that are situated trans to each other. The resulting key intermediate 1,8-dimethylcyclam[119] is shown in the scheme.

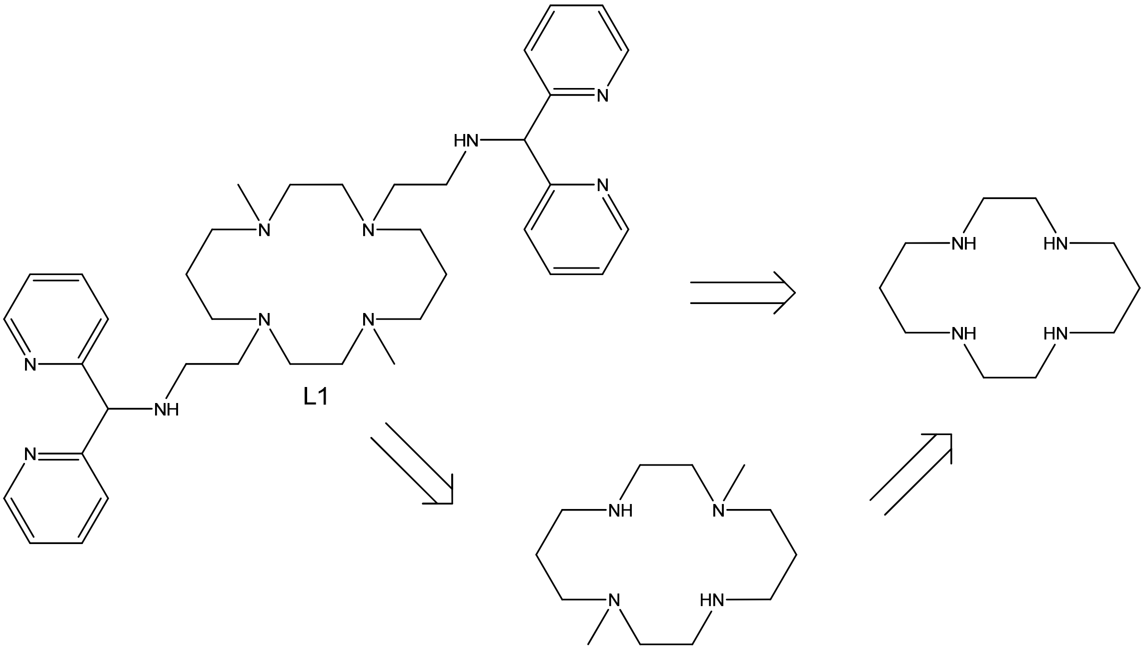

Scheme 3.1: Retrosynthesis of ligand **L**^{1}.

Different considerations gave rise to the development of ligand **L**^{1}. Cyclam was chosen as a linker between the two coordination sites due to its high basicity (pK_a=11),[120] that favors protonation of the nitrogen atoms over coordination of a metal ion. The protonated cyclam is designed as a second coordination sphere mimic. Another important feature is the conformational flexibility, which should allow varying metal-metal distances in the desired dinuclear complex. In a postulated mechanism by Schenk et. al.,[37] the catalytic cycle shows different binding modes of substrate and product. A flexible model system should be able to reproduce this behavior more accurately than a rigid one. The two coordinating units are connected to the cyclam platform via two trans-disposed nitrogen atoms. On one hand, this is crucial to ensure an appropriate distance. On the other, this cyclam substitution pattern is well known in the literature and therefore easy to adopt.[119] The use of ethylene bridges between cyclam and the coordination sites derives from *N*-tosylaziridine as a building block. This reacts selectively with the secondary amines in 1,8-dimethylcyclam via nucleophilic ring opening. The coordination site of the ligand resembles the known ligand di-(2pyridyl)methylamine (abbr. as dipa or dpma).[121, 122] Almost all well-established PAP model systems have chosen bis-(2-pyridylmethyl)amine (also known as bis-(picolyl)amine) as a coordinating unit.[69] In our case, the introduction of such a group was not feasible (see Scheme 3.2). Usually, bis-(2-picolyl)amine is reacted with a primary chloro- or bromoalkane in a nucleophilic substitution reaction. The latter are not directly accessible from cyclam. Another possible route would involve a fourfold alkylation reaction of two primary amines. Such a reaction is not favored from an entropic point of view. Therefore, this type of coordination site was not further considered.

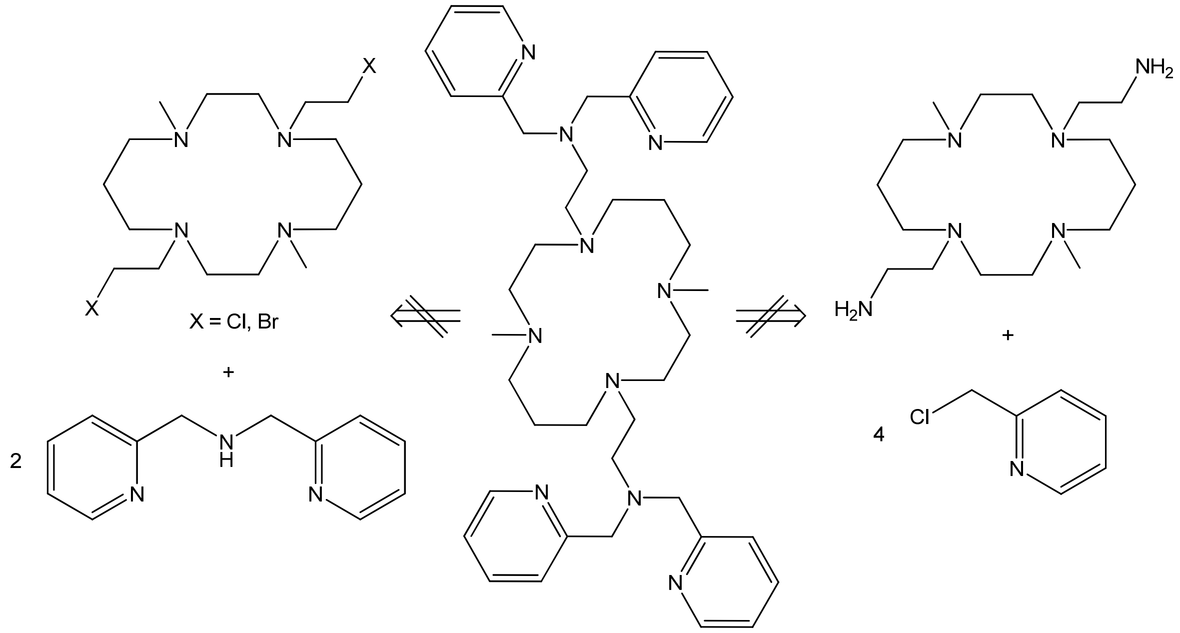

Scheme 3.2: Failed routes to a bis-(picolyl)amine substituted ligand.

A successful approach is the reaction of two equivalents di-(2-pyridyl)methylchloride with the primary amines in structure **6** (Scheme 3.3). The resulting donor set is also superior regarding the coordination chemistry with Fe^{III}. The coordination of two dipa-type units to one ferric ion in ligand **L**^{1} is unlikely, as Fe^{III}(dipa)$_2$ complexes were shown to be unstable.[121] They are reduced to Fe^{II}(dipa)$_2$. In contrast, Fe^{III} complexes with only one dipa ligand and additional co-ligands (like chloride) are easily accessible and stable.[122] Therefore, the desired uptake of two Fe^{III} per ligand should be favored. Scheme 3.3 shows the complete synthetic route to **L**^{1}:

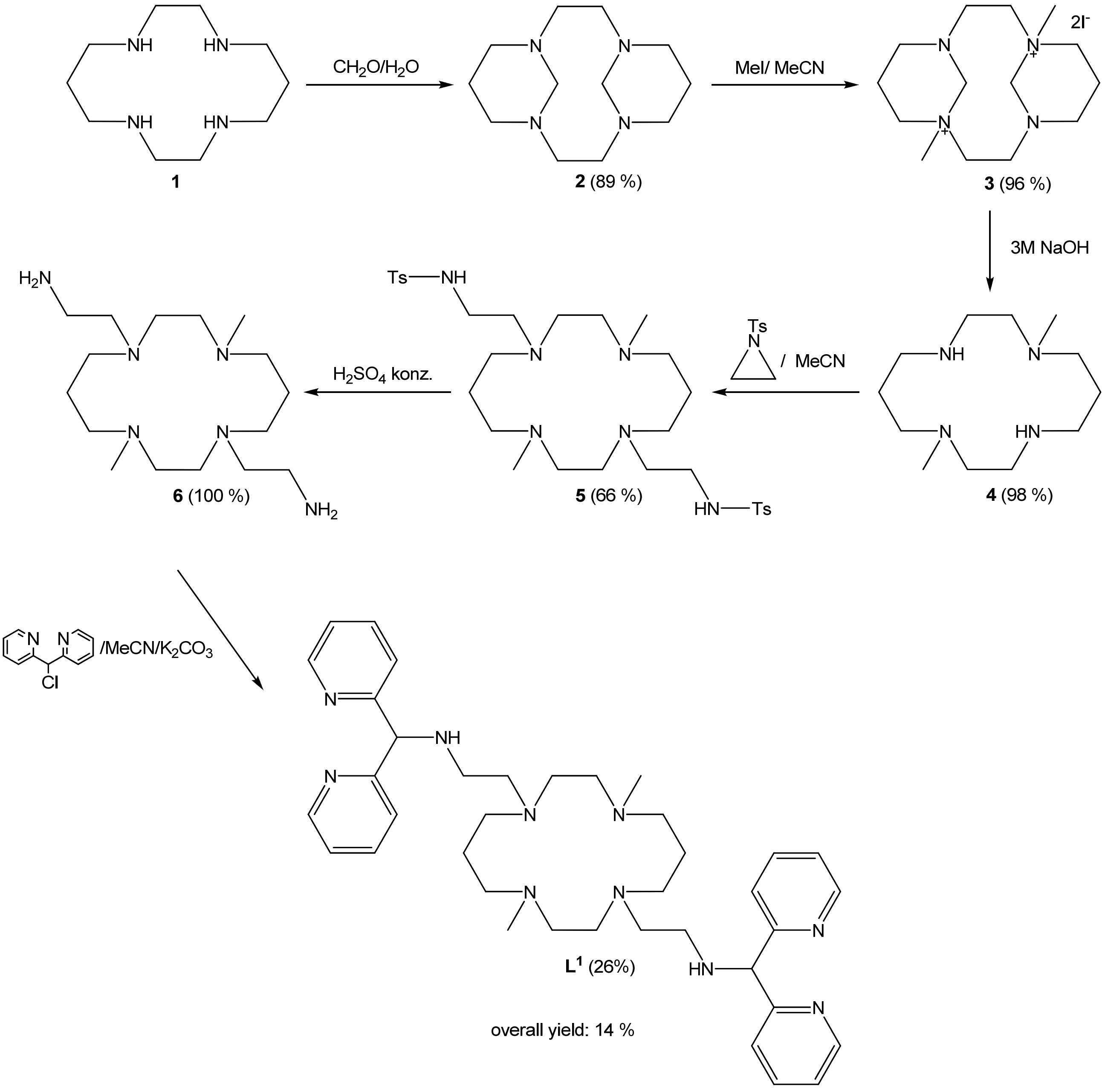

Scheme 3.3: Synthesis of ligand **L**^{1}.

The first step is the reaction of cyclam with formaldehyde in aqueous solution. The resulting product is the doubly methylene-bridged cyclam **2**, which is obtained as a white powder in 89% yield (lit. 96%). Nucleophilic substitution with methyliodide in acetonitrile gives the bis-methylated salt **3** in 96% yield (lit. 90%). Hydrolytic cleavage in 3M aqueous NaOH removes the methylene bridges to yield 98% 1,8-dimethylcyclam **4** (lit. 100%).[119]

The next step involves the reaction of *N*-tosylaziridine **9** with the secondary amines of 1,8-dimethylcyclam **4**. *N*-Tosylaziridine is synthesized from 2-aminoethanol in two steps in 61% yield (lit. 49%, see Scheme 3.4).[123, 124] The selective nucleophilic ring-opening of aziridine by secondary amines is the key step of the presented synthetic route.[125] After recrystallization of the crude reaction mixture, the product 1,8-dimethyl-4,11-bis-(2-tosylaminoethyl)cyclam **5** is obtained in 66% yield. The protecting groups are cleaved off subsequently by refluxing in conc. H_2SO_4 for 48h to give 1,8-dimethyl-4,11-bis-(2-aminoethyl)cyclam **6** (quantitative yield). At last, **6** is reacted with di-(2-pyridyl)methylchloride **12** and potassium carbonate as base in dry acetonitrile. **12** is synthesized from di-(2-pyridyl)ketone in two steps in 75% yield (lit. 52%, see Scheme 3.5).[126] The crude reaction mixture is purified by column chromatography and subsequent recrystallisation in hot hexane. **L**^{1} is obtained as a pale yellowish powder in 26% yield. The overall yield over six steps is 14%.

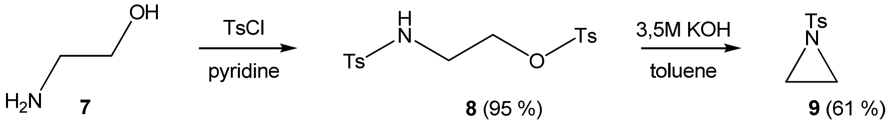

Scheme 3.4: Synthesis of *N*-tosylaziridine.[123, 124]

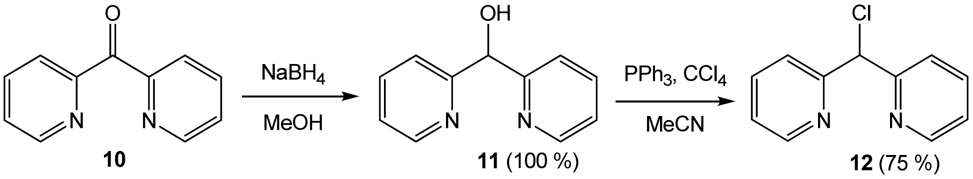

Scheme 3.5: Synthesis of di-(2-pyridyl)methylchloride.[126]

As already mentioned, the cyclam moiety of **L^1** is likely to induce a high flexibility to the ligand. In order to investigate this assumption, a conformational search is performed using MacroModel[127] (see Chapter 4.5 for details). Two starting points were chosen, a transoid ligand structure and a cisoid one. The resulting lowest-energy conformers are shown in Figure 3.3 (with 685.03 kJ/mol for the cisoid and 687.26 kJ/mol for the transoid structure):

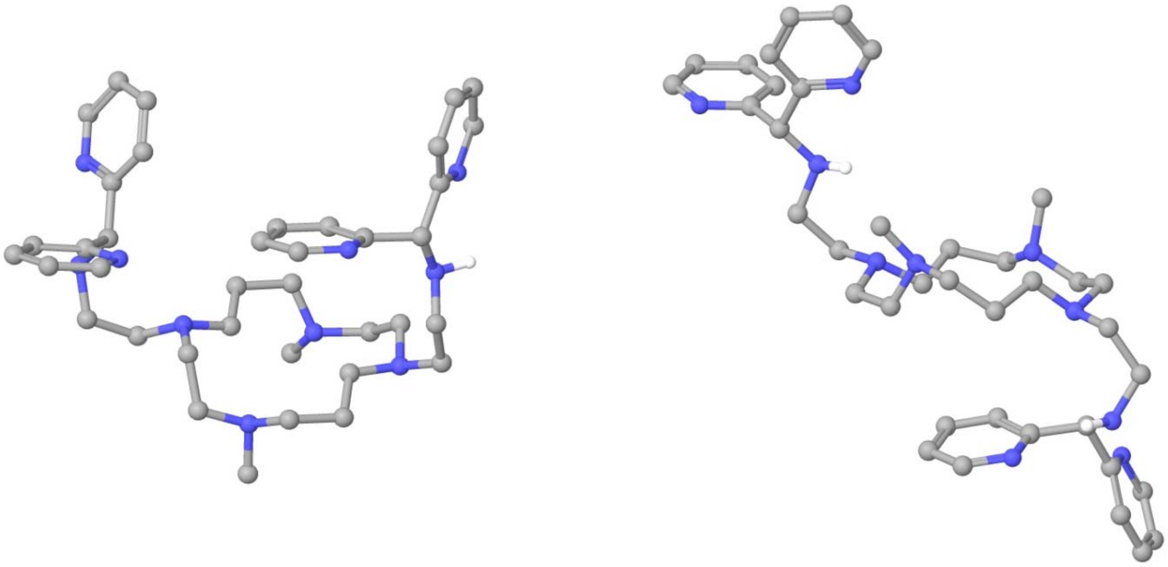

Figure 3.3: Lowest-energy conformers from a conformational search on **L^1**.

All other conformers have a maximum deviation in energy of ca. 8 kJ/mol. Most of them adopt very diverse geometries. Interestingly, starting from the cisoid structure, also transoid conformers are found and vice versa. These findings strongly support the anticipated high flexibility of **L^1**.

The crystal structures of **L^1** and [**H$_2$L^1**]$^{2+}$ are shown in Figure 3.4. A transoid structure is favored in a crystal lattice, yielding C_i symmetry (triclinic space group) in the non-protonated and C_{2h} symmetry (monoclinic space group) in the protonated ligand. A cisoid structure would lead to lower symmetry and less favorable crystal packing. The protonated ligand (Figure 3.4 b) shows small deviations from the free ligand structure: the dipa-units are rotated such that the two pyridines face the doubly-protonated cyclam ring. The cyclam part is in an all-chair conformation in both structures.

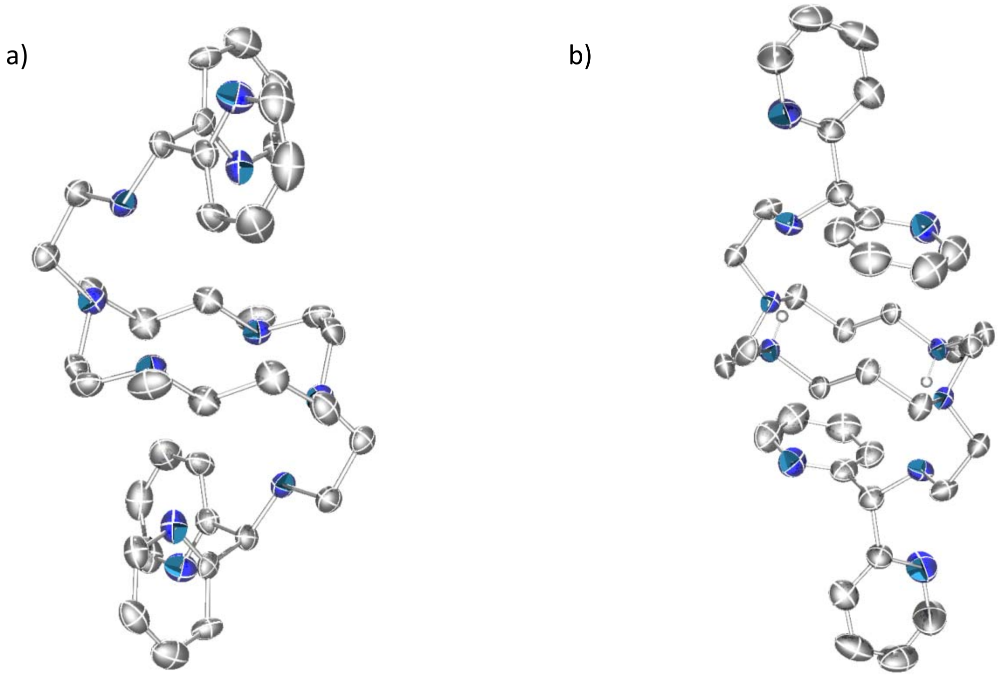

Figure 3.4: Ortep plots of the X-ray structures of a) $\mathbf{L^1}$ and b) $[\mathbf{H_2L^1}]^{2+}$ (hydrogen atoms are omitted for clarity, except for the two cyclam-nitrogen protons in b); ellipsoids are drawn at 50% probability level).

3.2.2. Fe^{III} Coordination Chemistry of L^1

3.2.2.1. Coordination Chemistry of L^1 in MeCN

The coordination chemistry of ligand $\mathbf{L^1}$ with Fe^{III} in MeCN solution was investigated thoroughly using various techniques, i.e. UV/vis, NMR and EPR spectroscopy, high resolution mass spectrometry and cyclic voltammetry. In addition, density functional theory calculations gave insight into structures and properties of the complexes.

All complexation reactions and experiments were carried out under aerobic conditions, unless otherwise stated, and no absolutely water-free MeCN is required. Tetraethylammonium tetrachloroferrate $[FeCl_4](NEt_4)$ **13** is used as the Fe^{III} source in all reactions with $\mathbf{L^1}$ because of its good solubility in organic solvents and the non-lewis-acidity of the tetrachloroferrate anion. ESI-MS predominantly showed peaks of the protonated ligand and only small peaks of complexes when a lewis-acidic iron salt, like ferric nitrate, was used. The tetrachloroferrate salt was synthesized by mixing anhydrous $FeCl_3$ and tetraethylammonium chloride in ethanol (see Scheme 3.6). The product was obtained as a yellow powder in 76% yield.[128]

$$FeCl_3 + NEt_4Cl \xrightarrow{EtOH} \underset{\textbf{13}\ (76\ \%)}{[FeCl_4](NEt_4)} \downarrow$$

Scheme 3.6: Synthesis of the non-lewis-acidic iron salt tetraethylammonium tetrachloroferrate.

UV/vis and ^1H-NMR titrations of the ligand with $[FeCl_4](NEt_4)$ were performed to gain insight into the *in situ* formation of complexes. Samples with 0 to 2 eq Fe^{III} vs. **L^1** were prepared and ^1H-NMR spectra were measured (see Figure 3.5). Upon addition of Fe^{III}, the signals between 7 and 8.5 ppm (pyridine protons), as well as the signal at 5 ppm (C*H* between the pyridines and the secondary amine) broaden and eventually start to disappear, but the chemical shifts remain the same. With 1 eq of Fe^{III}, the intensity of these signals is approximately halved, compared to the metal-free ligand spectrum. As reference for integration, the tetraethylammonium signals at 1.22 and 3.20 ppm are used. When adding 2 eq of Fe^{III}, the mentioned signals completely disappear. In the aliphatic region, it is clearly visible that the cyclam signals between 2 and 2.5 ppm are broadened and also slightly shifted, but they are still present even with 2 eq of Fe^{III}. The conclusions from this experiment are the following: one ligand **L^1** takes up two ferric ions; they are coordinated via the pyridines and secondary amines, as anticipated. The cyclam moiety is not involved in metal coordination, otherwise the corresponding NMR signals would also disappear.

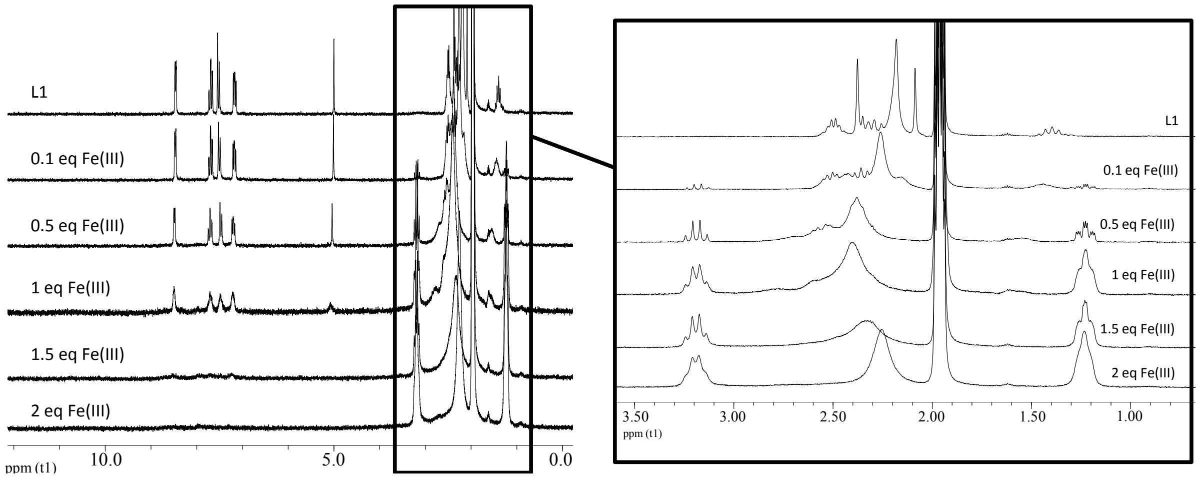

Figure 3.5: ^1H-NMR titration of **L^1** (5 mM) with $[FeCl_4](NEt_4)$ in MeCN-d_3.

The UV/vis titration of **L^1** with Fe^{III} (Figure 3.6 a) reveals more important details. The two bands at λ = 330 nm (shoulder; ε = 21120 M^{-1}cm^{-1}) and λ = 378 nm (ε = 16450 M^{-1}cm^{-1}) increase linearly. They are assigned to oxo-to-iron CT transitions.[102, 103] Interestingly, the spectra with 1 and 2 eq of Fe^{III} (bold lines) look almost alike, with only small differences due to negligible amounts of uncoordinated Fe^{III} in the upper bold spectrum (evolving band at λ = 310 nm; visible in the uppermost spectrum with 2.4 eq of Fe^{III}, i.e. Fe^{III} in excess). This suggests that only one species is formed, independent of the amount of Fe^{III} added.

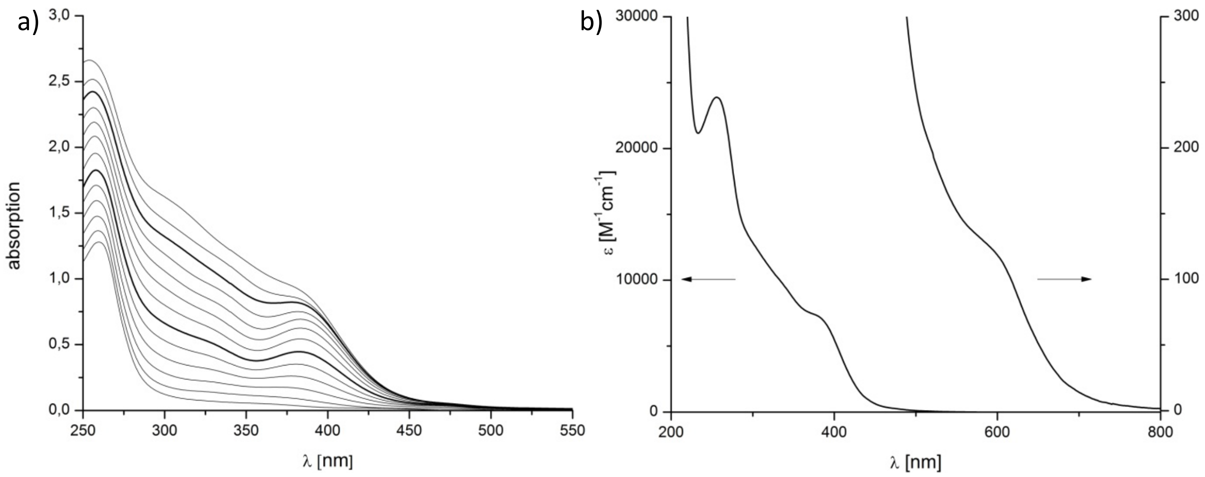

Figure 3.6: a) UV/vis titration of **L^1** (0.05 mM) with [FeCl$_4$](NEt$_4$) (in steps of 0.2 eq; bold lines represent 1 and 2 eq, respectively) and b) detailed UV/vis spectrum of **L^1** with two equivalents of [FeCl$_4$](NEt$_4$) in MeCN.

The UV/vis spectrum of **L^1** with two eq of Fe^{III} is shown in Figure 3.6 b. In addition to the two intense bands in the UV region, a third band in the visible area at λ = 600 nm (shoulder, ε = 120 M^{-1}cm^{-1}) can be observed. It corresponds to a dd transition of a high-spin ferric ion ($^6A_1 \rightarrow {}^4T_2$), which is spin- and Laporte forbidden and therefore should have a low extinction coefficient.[129] In this case, the CT bands at lower wavelengths lead to an increased intensity of this transition due to the overlap of these bands.

The intense bands in the UV region are very similar to oxo-to-iron charge transfer bands reported in the literature.[102, 103] Therefore, it can be concluded, that a μ-oxo bridged di-Fe^{III} complex is formed predominantly, independent of how many equivalents of Fe^{III} are present in solution. High resolution ESI mass spectra in MeCN confirm the presence of an oxo-unit in the complex molecule: All peaks with two Fe^{III} also contain exactly one oxygen, most probably as O^{2-}. Figure 3.7 shows the experimental and calculated isotope pattern of the main peak at *m/z* = 921.19821 (calc. *m/z* = 921.19838 for $[HL^1Fe^{III}_2Cl_4O]^+$) and the next intense signal at *m/z* = 883.22483 (calc. *m/z* = 883.22465 for $[L^1Fe^{III}_2Cl_3O]^+$). The two peaks at [M-2] and [M-1] represent a typical isotope pattern of species with two iron.

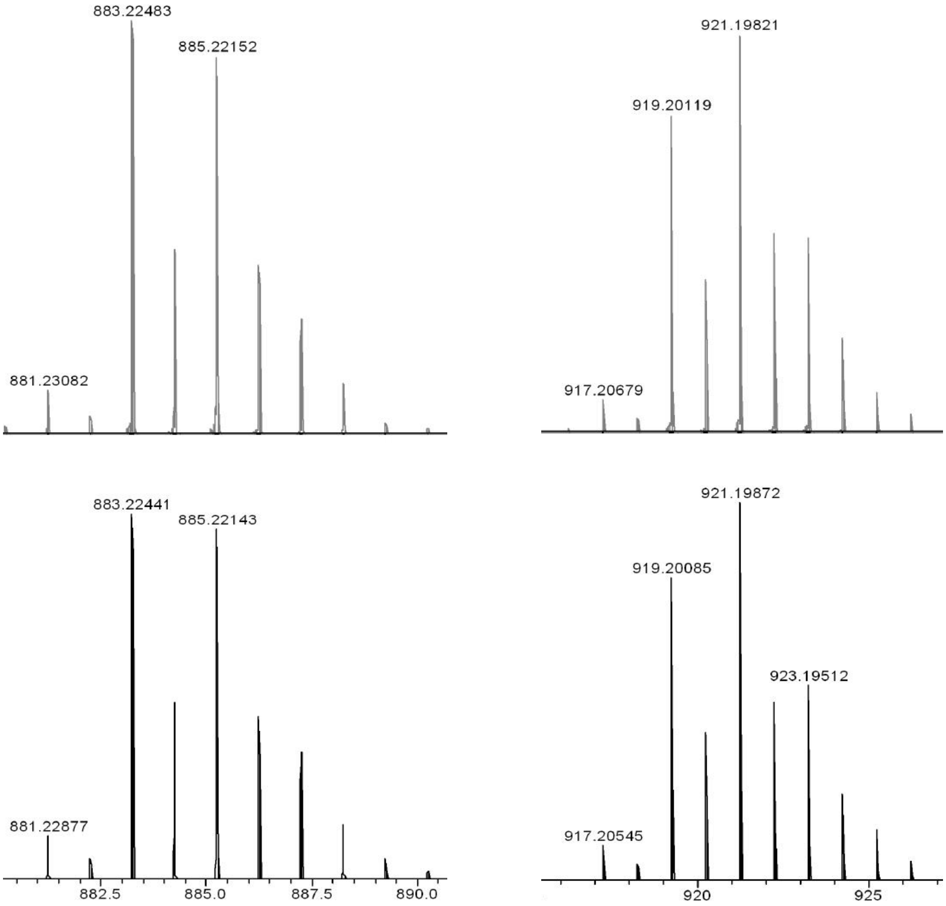

Figure 3.7: Isotope patterns of experimental (top) and calculated mass spectra (bottom) of $[L^1Fe^{III}_2Cl_3O]^+$ (left) and $[HL^1Fe^{III}_2Cl_4O]^+$ (right).

In mass spectra of solutions with **L^1** and only one eq of Fe^{III}, the main peak is the protonated ligand $[HL^1]^+$ at *m/z* = 651.46085 (calc. *m/z* = 651.46057). Other species present are, surprisingly, a mononuclear Fe^{II} complex at *m/z* = 741.35714 (calc. *m/z* = 741.35709 for $[L^1Fe^{II}Cl]^+$) as well as different dinuclear species also appearing in spectra with two eq of Fe^{III}. It is likely that the mononuclear Fe^{II} complex is a minor impurity, but well ionized during measurement. Mononuclear Fe^{III} species are not observed at all.

It is not fully understood why **L^1** only forms dinuclear complexes with Fe^{III}, or more exactly, with $[FeCl_4]^-$. The best explanation so far is based on the observation that ferric chloride forms μ-oxo bridged dimers when reacted with additional chloride in wet basic solutions (see Scheme 3.7 a).[130] Due to its cyclam part **L**^{1} is a strong bas and a basic environment is present during the addition of tetrachloroferrate to pre-dissolved **L**^{1}. It can be assumed that tetrachloroferrate reacts in a similar way with base as ferric chloride does in Scheme 3.7 a, namely tetrachloroferrate should be an intermediate in this reaction. The resulting diferric species can then react with **L**^{1} under partial ligand exchange (chloride vs. pyridine/amine) to form a μ-oxo bridged diferric complex (**K**^{1} in Scheme 3.7 b). Monomeric Fe^{III} should not be present under these conditions and therefore, no mononuclear Fe^{III} complex of **L**^{1} is observed.

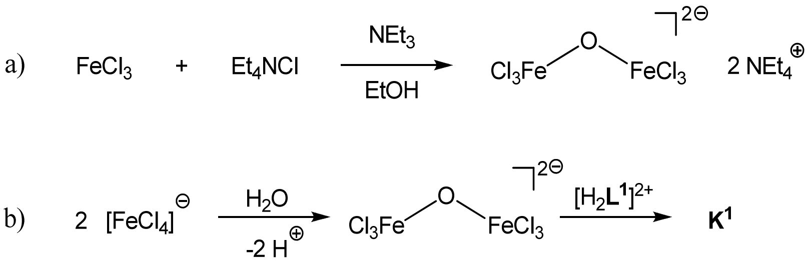

Scheme 3.7: Reactions of ferric ions in basic solution.

Based on these observations and for simplicity, a solution containing **L**^{1} and two eq of Fe^{III} is called “**K**^{1}” from now on. Scheme 3.8 shows the postulated structure of this complex. The ferric ions are coordinated by two pyridines and one secondary amine of **L**^{1}, each. Two chloro ligands and a μ-oxo bridge complete the octahedral coordination of the metal ions. The cyclam is likely to be protonated (see Scheme 3.7 b). The result is a twofold positively charged complex.

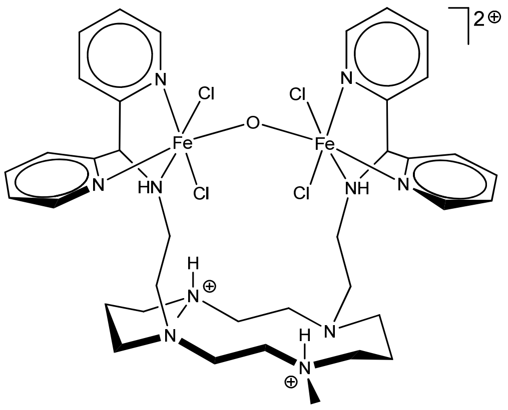

Scheme 3.8: Postulated structure of **K**^{1}.

In order to explore the magnetic properties of **K^1**, molar susceptibilities were measured using ^{1}H-NMR as described by Evans.[131] The theory behind these experiments is, that the frequency shift Δf of a signal from a diamagnetic substance (e.g. the solvent), caused by a paramagnetic compound dissolved in it, is proportional to the paramagnetic susceptibility $X_{\mathrm{para,subst}}$ of the compound (see eq. 3.1).

$$X_{para,subst} = \frac{3\Delta f}{4\,\pi * f * c} + X_{dia,solv} + X_{dia,subst} \qquad \text{(eq. 3.1)}$$

The effective magnetic moment μ_{eff} is then calculated as

$$\mu_{eff} = 2.828 * \sqrt{X_{para,subst} * T} \qquad \text{(eq. 3.2)}$$

The results of these experiments are summarized in Table 3.1. In the two last columns, the expected spin state and the theoretical spin-only value for μ_{eff} are shown.

Table 3.1: Results of Evans-NMR experiments with **K^1** in MeCN-d_3.

sample	exp. μ_{eff} [B.M.] per complex unit	expected spin state S	calc. μ_{eff} [B.M.] for expected spin state
K^1 (c_{eff} = 2 mM)	4.97	2	4.90
L^1 + 1 eq of Fe$^{\mathrm{III}}$ assuming only dinuclear complexes (c_{eff} = 1 mM)	3.69	2	4.90
L^1 + 1 eq of Fe$^{\mathrm{III}}$ assuming only mononuclear complexes (c_{eff} = 2 mM)	2.49	5/2	5.92

The observed spin state of $\mathbf{K}^1$ at room temperature is S = 2. A fully uncoupled system with two high spin ferric ions would result in μ_{eff} = 11.83 B.M. per complex and can therefore be excluded. On the other hand, the proposed μ-oxo bridged dinuclear Fe^{III} complex would be strongly antiferromagnetically coupled ($J \approx$ -100 to -150 cm^{-1}), and therefore have an S = 0 ground state. At room temperature, higher spin states may be populated. Which spin states contribute to μ_{eff} in this case cannot be analyzed on the basis of the available experimental data. Therefore, it cannot be excluded that a small fraction of non-coupled Fe^{III} is present. The Evans experiment with $\mathbf{L}^1$ and only one eq of Fe^{III} reveals some interesting facts: assuming the formation of only mononuclear complexes, a μ_{eff} value of 5.92 would be expected (S = 5/2, high spin ferric ion). The observed lower value of μ_{eff} = 2.49 at the resulting effective complex concentration c_{eff} suggests that this interpretation is wrong. If only dinuclear complexes were present (i.e. the effective complex concentration c_{eff} is halved), the same spin state as for $\mathbf{K}^1$ would be expected (S = 2). The experimental value is even smaller than that. Therefore, the ferric ions in this sample are proposed to be coupled. The deviation between the effective magnetic moments can be explained by a small excess of “free” Fe^{III} in $\mathbf{K}^1$ due to small errors during the sample preparation, leading to a larger than expected value of μ_{eff}. These observations strongly support the idea, that $\mathbf{L}^1$ forms predominantly one species, which is the dinuclear complex $\mathbf{K}^1$, independent of the amount of Fe^{III}, as already concluded from the UV/vis titration.

EPR spectra of $\mathbf{K}^1$ in MeCN at 1.7 K show a moderately intense signal at g_{eff} = 4.3 (see Appendix 2 for spectra), which is typical for octahedral high-spin Fe^{III}. It is clearly different to the signal of $[FeCl_4](Net_4)$ in MeCN. Usually, this kind of signal is very strong, leading to the interpretation that there is only a relatively small amount of uncoupled Fe^{III} present. This is consistent with the Evans-NMR data.

3.2.2.2. *Redox Properties of K^1*

Although we focus our experiments on the homovalent redox state of $\mathbf{K}^1$, a reduction to the heterovalent $Fe^{III}Fe^{II}$ complex of $\mathbf{L}^1$ would be desirable. Cyclic voltammetry (CV) experiments were conducted in order to explore the redox behavior of $\mathbf{K^1}$ and find a suitable method for the reduction. Figure 3.8 presents the results.

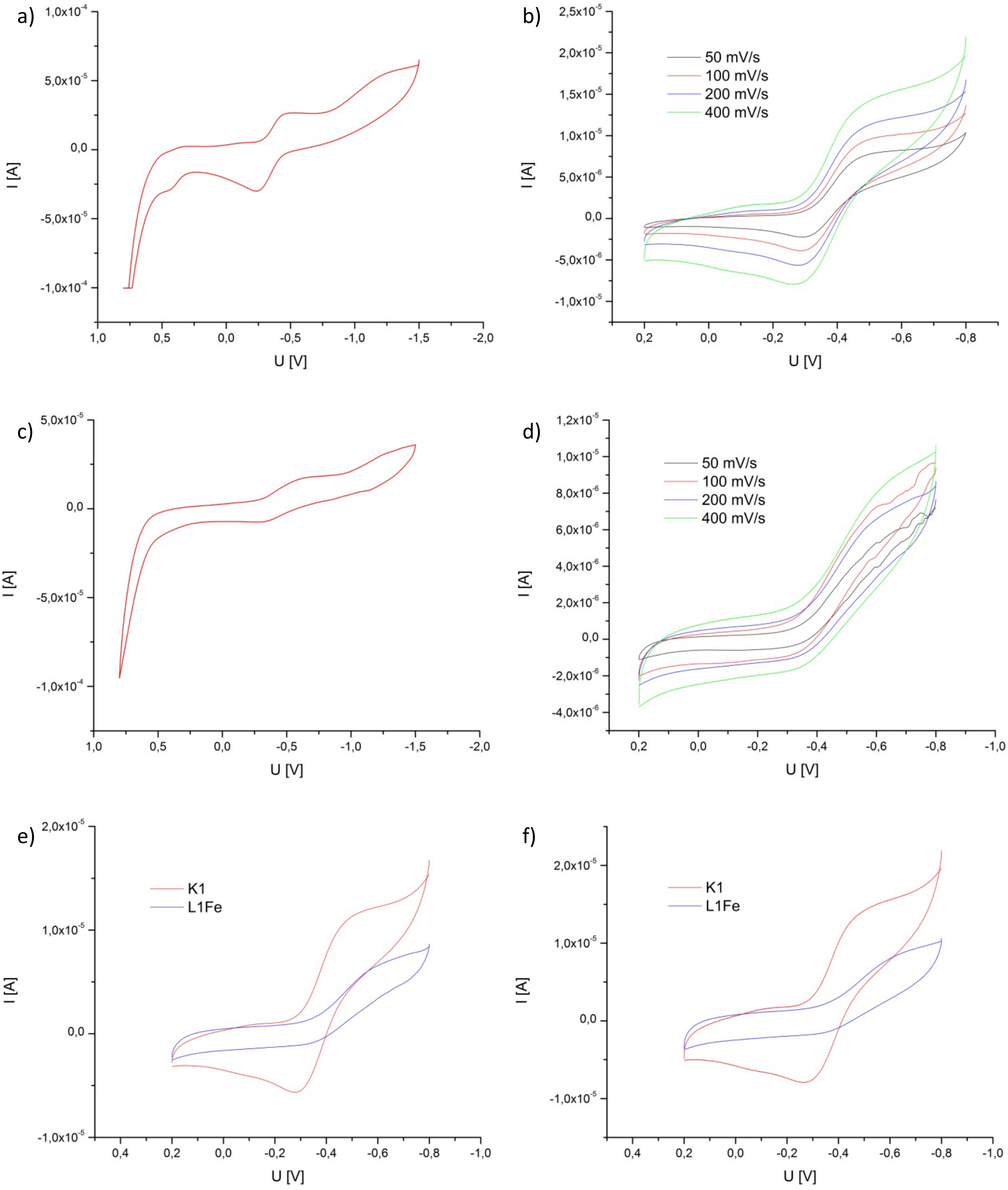

Figure 3.8: CVs of $\mathbf{K^1}$ and $\mathbf{L^1Fe}$: a) $\mathbf{K^1}$ full sweep and b) $\mathbf{K^1}$ at different chart speed; c) $\mathbf{L^1Fe}$ full sweep and d) $\mathbf{L^1Fe}$ at different chart speed; overlay of $\mathbf{K^1}$ and $\mathbf{L^1}$ Fe at e) 200 mV/s and f) 400 mV/s; all recorded in MeCN with 0.1M NBu_4ClO_4 vs. Ag/Ag^+, with $E_{1/2}$ ($FeCp_2$) = 0.08 V.

The observed reversible redox potential of **K^1** (Figure 3.8 a) at $E_{1/2}$ = -0.39 V (-0.09 V vs. SCE, ΔE = 217 mV) can be attributed to an $Fe^{III}_2/Fe^{III}Fe^{II}$ couple. The oxidation branch shows an additional, irreversible peak around 0.45 V (0.75 V vs. SCE) which might be due to an oxidation to Fe^{IV}. The scans at different speed do not show special features. As expected, the peak height rises at higher scanning speed. We also recorded CVs of **L^1** with only one eq of Fe^{III} (**L^1**Fe) and compared them to the results of **K^1** (Figure 3.8 c-f). The oxidation and reduction peaks are less intense but in comparison to the CVs of **K^1** (see Figure 3.8 e and f) clearly appear at the same potential. No additional peaks are observable so that it can be concluded that one species is formed, which is the dinuclear complex.

The reversible redox behavior of **K^1** indicates that a one-electron reduction to the heterovalent complex should be possible. At the time scale of the CV experiments, the reduced, i.e. heterovalent $Fe^{III}Fe^{II}$ species is stable. Cobaltocene was chosen as the reducing agent ($E_{1/2}$ = -0.95 V vs. SCE; 10 fold excess) under anaerobic conditions, as it is a powerful one-electron reductant. In the EPR spectra (4.8 – 50 K) no changes could be observed after reaction of **K^1** with cobaltocene. The only signal in both, **K^1** and the reduction product, was that at g_{eff} = 4.3, assigned to high spin Fe^{III}. The UV/vis spectra differ only in the relative intensities of the the absorption bands, their position remains the same (Figure 3.9). HR-ESI MS showed no mass peaks belonging to a heterovalent species, but the known peaks of **K^1**. We assume that the reaction was not successful. A possible explanation is that both complexes are too bulky (pyridine groups are shielding the ferric ions in **K^1** and the cyclopentadienyl ligands in cobaltocene) and, therefore, the metal centers cannot directly interact in an outer-sphere electron transfer reaction. As a consequence, bulk electrolysis was applied in order to reduce **K^1** to the heterovalent complex. Solutions of **K^1** in MeCN or MeCN/DMF mixtures were held at a constant potential of -0.3 V (vs. SCE) for one hour under argon. EPR spectra at liquid nitrogen temperature (140 K) show striking changes (see Appendix 3 for spectra): Whereas the spectrum of **K^1** consists of the usual g_{eff} = 4.3 signal for high spin Fe^{III} and an additional small peak at g_{eff} = 2.1, a freshly reduced solution spectrum is dominated by the previously small signal at g_{eff} = 2.1, which might be due to an S = ½ species. An antiferromagnetically coupled $Fe^{III}Fe^{II}$ complex would result in exactly this spin state. Moreover, the charge Q that was transferred during electrolysis corresponds to one equivalent of electrons. However, when the solution is left standing for a while, the EPR signal at g_{eff} = 2.1 disappears. Also, no adequate mass peaks could be identified in the HR-ESI-MS. UV/vis spectra of the electrolyzed solution have the same appearance as reported for the cobaltocene reaction mixture. Our interpretation of these results is that the desired heterovalent complex is formed, but cannot be stabilized even though anaerobic conditions were used. A disproportionation reaction of the reduced, heterovalent species into diferric and diferrous complexes is likely, with subsequent decomposition of the diferrous complex.

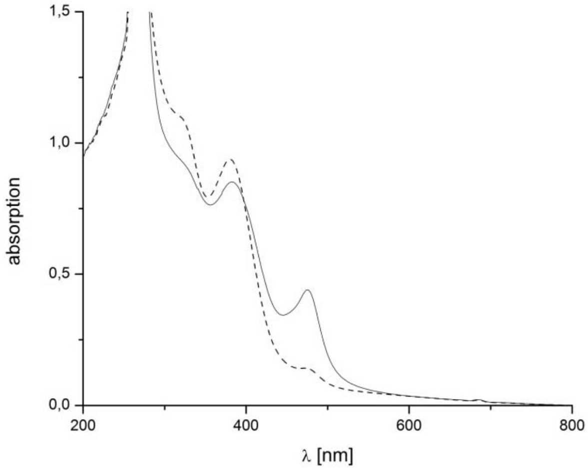

Figure 3.9: UV/vis spectrum of **K**^{1} (dashed line) and **K**^{1} with cobaltocene (solid line) in DMF (0.33 mM).

3.2.2.3. *Coordination Chemistry of L^1 in Aqueous Media*

In order to explore the behavior of **K**^{1} at different pH values, experiments were extended to MeCN/aqueous buffer mixtures (1:1). **K**^{1} was prepared in MeCN and subsequently, a multicomponent buffer, containing MES, HEPES and CHES, was added, the pH of which had been adjusted by aqueous NaOH. At first, UV/vis spectra at pH 5 were measured and compared to the spectrum of **K**^{1} in MeCN (see Figure 3.10 a). The two oxo-to-iron CT bands at 330 and 378 nm disappear and new bands at 360 and 466 nm arise. There are different possibilities to interpret these changes: As the band at 466 nm may also be assigned to a LMCT ($\varepsilon \approx 4000\ M^{-1}cm^{-1}$), the two new bands can be regarded as shifted due to ligand exchange at the coupled dinuclear Fe^{III} complex. In MeCN, chloride is the most likely co-ligand, which is exchanged by water and/or hydroxide upon addition of aqueous buffer. Another possibility is that a completely new species is formed, e.g. uncoupled dinuclear or mononuclear Fe^{III} complexes. Comparison of our spectra to literature-known species supports the first suggestion, as the band at 466 nm is typical for μ-oxo bridged diferric systems with water or hydroxide as co-ligands.[132]

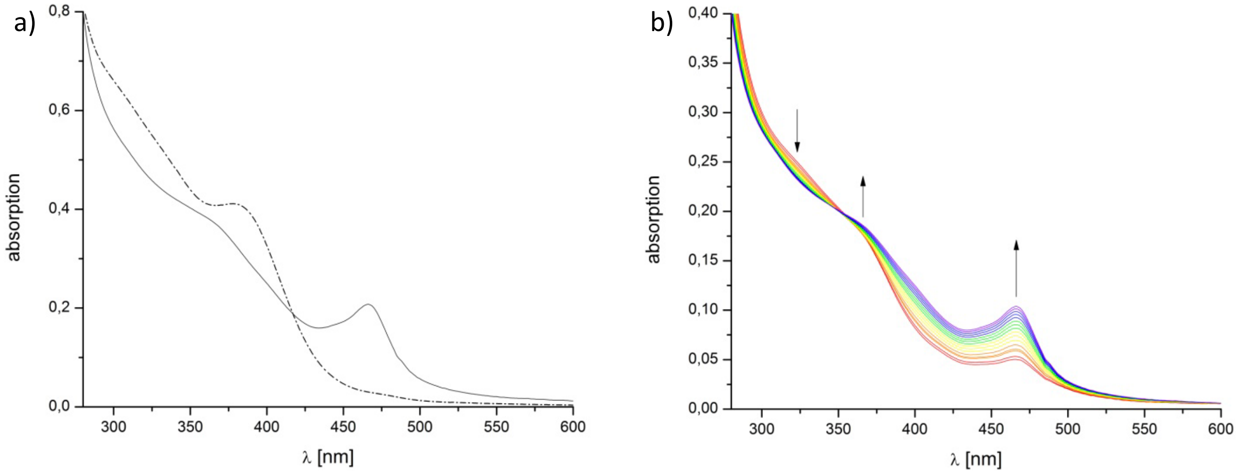

Figure 3.10: a) UV/vis spectra of **K**^{1} (0.05 mM) in MeCN (dashed line) and MeCN/buffer pH 5 (solid line) and b) time-resolved UV/vis spectra (1/30 sec) of **K**^{1} (0.025 mM) in MeCN/buffer pH 5 at 0 to 30 min after mixing.

Time-resolved UV/vis spectra, which were recorded in the first 30 min after addition of the buffer solution, show an isosbestic point around 350 nm (see Figure 3.10 b). Only small changes can be observed in the region between 300 and 380 nm, whereas the formation of the LMCT band at 466 nm is the predominant feature in the spectrum. Interestingly, the oxo-to-iron CT transition at 378 nm is not visible, although the measurement was already started approximately 10 sec after mixing. There is a very fast process leading to the loss of this band. This behavior is in contrast to the slow spectral changes observed over 30 min. A combination of the assumptions described above might help to interpret these results: when reacting with water, the μ-oxo bridged diferric complex is hydrolyzed to a non-bridged di-hydroxo species, which explains the disappearance of the band at 378 nm. Subsequently, the assumed exchange of co-ligands (chloride to aqua/hydroxo) takes place. In the meantime, the μ-oxo bridge is slowly re-established and the new oxo-to-iron CT bands rise.

This proposal is supported by EPR spectroscopy: the high spin Fe^{III} signal at $g_{eff} = 4.3$ observed in MeCN solutions of **K**^{1} at first gains intensity and then completely disappears over time when buffer is added, and no other signal is observed at 1.7 K. Obviously, an EPR-silent species is formed, which very likely is the anticipated μ-oxo bridged diferric complex with an $S = 0$ ground state. In addition, the effective magnetic moment μ_{eff} of **K**^{1} in MeCN/buffer is significantly smaller than in pure MeCN (3.77 vs. 4.97 B.M.). This suggests either a more strongly coupled dimer or, more likely, smaller fractions of non-coupled species.

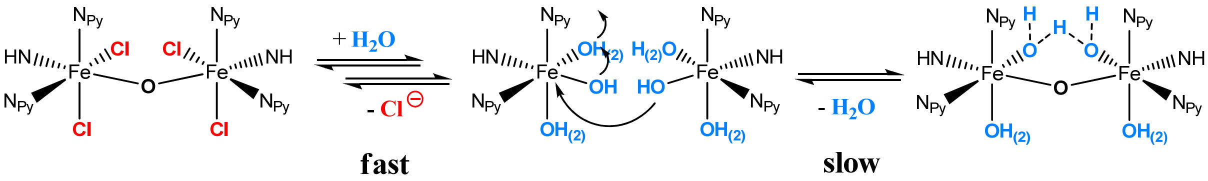

Scheme 3.9: Proposed reactions after addition of buffer to **K^1** solution in MeCN.

In summary, the species most likely existing, when **K^1** is prepared in MeCN/buffer mixtures, is a μ-oxo bridged diferric complex. Dependent on the pH of the buffer, aqua and/or hydroxo co-ligands should present. The exact distribution of species remains unclear, as spectrophotometric titrations did not give suitable results. The UV/vis spectra were not changed significantly upon variation of the pH value. Unfortunately, the CT absorptions of **K^1** are not very sensitive to pH changes. Other techniques must be used to explore the pH dependent properties of **K^1** (see Chapter 3.4.1 for more information).

An interesting question that arises, when considering that **K^1** is dissolved in a MeCN/buffer mixture, is whether MeCN hydrolysis is possible. Usually, nitriles are quite resistant against hydrolysis.[133] Only when coordinated to metal ions, a nucleophilic attack of a metal bound hydroxide leads to a fast conversion of MeCN to acetamide.[132, 134] In our case, the use of a 1:1 mixture of buffer and MeCN should prevent the coordination of MeCN and favor binding of aqua/hydroxo co-ligands, as Fe^{III} is known to be rather oxophilic. Nevertheless, the observed CT band at 466 nm might be arising from coordinated acetamide, which is the product of MeCN hydrolysis. We recorded a time-resolved UV/vis spectrum of **K^1** with acetamide in excess in MeCN/buffer pH 5 (see Appendix 4 for spectrum and details). The resulting spectrum is similar to that in Figure 3.10 b, showing the characteristic CT band at 466 nm. However, this band is growing slower in the experiment with acetamide, suggesting that it does not belong to a **K^1**acetamide complex. A weak shoulder at 488 nm can be observed in both cases, with and without additional acetamide, which is in a typical range for diferric complexes with a bridging acetamide.[132] From these results, we conclude that MeCN hydrolysis is probably occurring with **K^1** in MeCN/buffer mixtures, although very slow.

3.2.2.4. Coordination of Phosphate and Phosphoesters to K^1

As the purpose of **K^1** is to act as a PAP mimic, it is crucial to know how substrates and products interact with the complex. Important information includes the number of coordinated molecules, their coordination mode (monodentate vs. bridging) and possible interactions with the protonated cyclam moiety, as well as the number and nature of additional co-ligands (μ-oxo vs. μ-hydroxo vs. terminal hydroxo). These data should contribute to the understanding of the mechanism of phosphoester hydrolysis. The products of phosphoester hydrolysis are the corresponding alcohol and inorganic phosphate or a phosphomonoester. As substrate mimics, the inactive phosphoesters pNPP (*para*-nitrophenylphosphate), 1-NP (1-naphthylphosphate) and DPP (diphenylphosphate) were chosen (see Scheme 3.10). pNPP is used as a substrate in enzymatic reactions, because enzymes are usually more active than model compounds. This is also the case with **K^1**, which showed no detectable catalytic activity with pNPP.

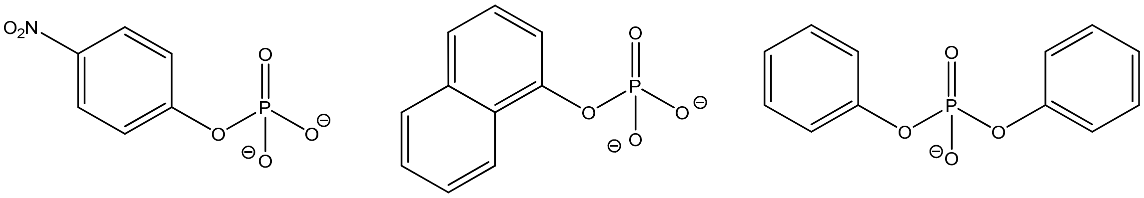

Scheme 3.10: Substrate mimics *p*-nitrophenylphosphate pNPP (left), 1-naphthylphosphate 1-NP (middle) and diphenylphosphate DPP (right).

A good tool for the investigation of phosphorous containing compounds is ^{31}P-NMR. Inorganic phosphate as well as mono- and diesters can easily be distinguished due to their typical chemical shifts. Quantitative information can be obtained by using an internal standard, which delivers data about species distribution. In order to gain insight into the number of coordinated substrate molecules per **K^1** unit, ^{31}P-NMR spectra were recorded with different equivalents of **K^1** vs. phosphorous compound. Due to the paramagnetic character of **K^1**, the ^{31}P signals of coordinated compounds are massively broadened and therefore not visible. Therefore, the loss of intensity of the uncoordinated substrate is proportional to the magnitude of coordination and consequently, the number of coordinated molecules per complex. The results for phosphate, pNPP and DPP at pH 5 (in MeCN/buffer) as well as pNPP at pH 10 are summarized in Table 3.2. Interestingly, two molecules of pNPP are bound to **K**^{1} at pH 5, whereas in the other cases only one substrate molecule is coordinated. This finding suggests different coordination modes, dependent on the substrate and the pH used. Further spectroscopic studies are needed for a reasonable interpretation of the stoichiometries found.

Table 3.2: Results from ^{31}P-NMR titrations of substrate mimics (5 mM in MeCN-d_3/buffer D_2O 1:1) with **K**^{1}.

substrate mimic	pH	chemical shift [ppm]	no. of coord. molecules
phosphate	5	-0.17	1
pNPP	5	-4.50	2
pNPP	10	-0.66	1
DPP	5	-10.59	1

In contrast to these results, species found in HR-ESI mass spectra of **K**^{1} with phosphate or pNPP (in large excess) always contain two substrate molecules. One should not over-interpret this, as weak adducts can form during ionization. Moreover, **K**^{1} itself in MeCN/buffer is not easy to detect due to protonation of the cyclam ring. The resulting high positive charge requires an appropriate number of counter-ions to generate only singly or doubly positively charged species. Therefore, two phosphate or pNPP molecules are necessary. The observed ESI-MS species are summarized in Table 3.3. Again, no mononuclear species or free ligand peaks are observed. A remarkable fact is that each peak also contains exactly one “free” oxygen. In Table 3.3, it is written as hydroxide, but this assignment is not sure. No conclusions can be drawn yet regarding the number and coordination mode of possible oxo, hydroxo or aqua co-ligands.

Table 3.3: Species observed in HR-ESI-MS of **K^1** with phosphate or pNPP in MeCN/buffer (pH 5).

species	calc. m/z	exp. m/z	peak height [%]
$[HL^1Fe^{III}_2(HPO_4)_2(OH)]^{2+}$	486.12812	486.12784	100
$[H_2L^1Fe^{III}_2(HPO_4)_2(OH)(ClO_4)]^{2+}$	536.10629	536.10619	5
$[HL^1Fe^{III}_2(HPO_4)_2(OH)Cl]^+$	1007.22508	1007.22480	11
$[HL^1Fe^{III}_2(HPO_4)_2(OH)(ClO_4)]^+$	1071.20474	1071.20482	15
$[HL^1Fe^{III}_2(pNPP)_2(OH)]^{2+}$	607.14450	607.14412	100
$[LiL^1Fe^{III}_2(pNPP)_2(OH)]^{2+}$	610.14859	610.14830	47
$[L^1Fe^{III}_2(pNPP)_2(OH)]^+$	1213.28166	1213.28025	31
$[HL^1Fe^{III}_2(pNPP)_2(OH)Cl]^+$	1249.25784	1249.25757	45

EPR spectra were recorded at low temperatures (1.6 to 16 K) in MeCN/buffer mixtures in order to elucidate the spin state of **K^1**/phosphate, pNPP or DPP complexes. As already mentioned, without any additional substrate mimic, an EPR-silent species is formed, most probably a μ-oxo bridged complex. Mixtures of **K^1** and the inactive diester DPP in excess (c(**K^1**) = 0.5 mM; c(DPP) = 10 mM) show only a moderately intense signal at $g_{eff} = 4.3$, which belongs to high spin ferric ions. This signal is constant over time and decreases with increasing temperature. It seems that also in this case, mainly an EPR-silent species is present. Upon addition of pNPP or phosphate (same concentrations as in the DPP experiment), a complex signal develops over time at pH = 5. Coupled diferric systems have various possible spin states between S = 0 and 5, which are populated depending on the type and strength of exchange coupling as well as the temperature (see Appendix 5 a for schematic energy diagram). Measurements at variable temperatures (VT) revealed a dependence of signal intensity, which at first grew with increasing temperature and then slowly decreased again (Figure 3.11). This behavior is typical for antiferromagnetically coupled systems with S = 0 as the ground state.[135] Maximum intensity was obtained at 2.4 ± 0.2 and 3.5 ± 1.0 K for **K^1** with pNPP and phosphate, respectively. This results in exchange coupling constants of J = -1.67 ± 0.14 and -2.43 ± 0.69 cm^{-1} (1 K = 0.694 cm^{-1}).

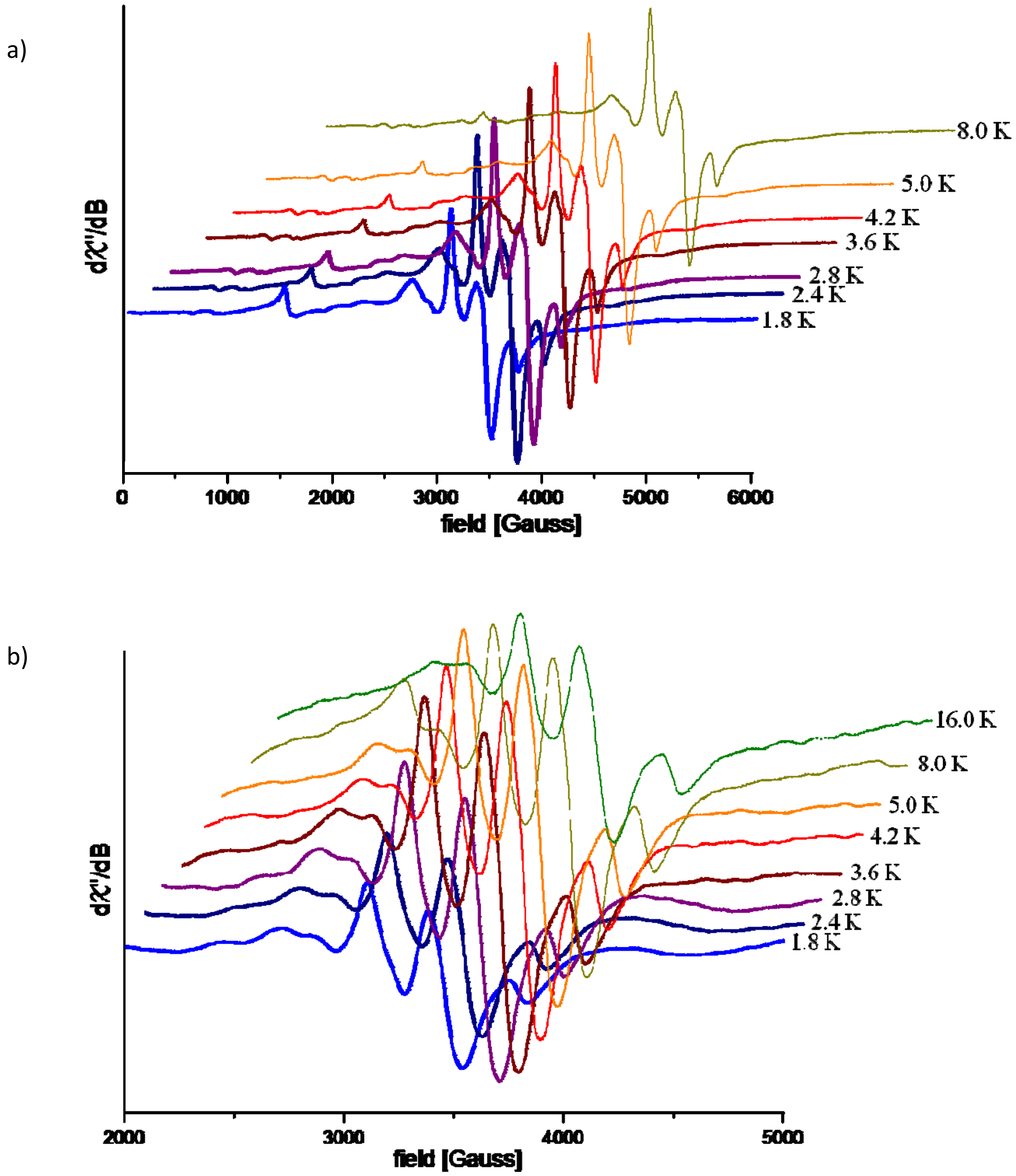

Figure 3.11: VT X-band EPR spectra of a) $\mathbf{K}^1$pNPP (9.376664 GHz) and b) $\mathbf{K}^1$phosphate (9.37824 GHz).

A first attempt to simulate the spectra with XSophe,[136] neglecting the Fe^{III}-Fe^{III} interactions and treating the system as one Fe^{III} with S = 3, lead to a reasonable match. However, several features, including the relative intensities of the smaller signals between 2000 and 3000 as well as around 3800 Gauss, were not correctly reproduced. Therefore, we decided to adopt a full description of the system, using Molecular Sophe (MoSophe)[137] for the simulation. The total spin Hamiltonian H_{total} is composed of the sum of individual spin Hamiltonians for an isolated paramagnetic center H_{Ai} and the interaction Hamiltonian H_{Aij}

(eq. 3.3).[135, 138-140] Although the interaction Hamiltonian used in the simulation defines positive J* values for antiferromagnetic coupling, all reported J values in this work are based on the Hamiltonian $H_{Aij} = -2J_{Aij} * S_{Ai} * S_{Aj}$ with $J = -2J^*$ and, therefore, negative J values indicate antiferromagnetically coupled systems. For a first guess, the same zero-field splitting value D was used as in the XSophe simulation. Based thereon, the Fe^{III}-Fe^{III} distance was approximated to be around 4.7 Å for **K^1**pNPP and 4.5 Å for **K^1**phosphate, using the relation between the dipole-dipole zero-field splitting D_{dd} and the dipole-dipole coupling constant J_{dd}.[137] The J value was taken from the VT experiments. These parameters were refined, together with the isotropic g-factor, the rhombicity parameter E and orthorhombic line widths. Euler angles, relating the relative orientation of the fine structure parameters D and E on the two metal centers, were included and further improved the simulation. The recorded and simulated spectra of **K^1** with pNPP and phosphate, respectively, are shown in Figure 3.12. Parameters obtained from the simulations are presented in Table 3.4.

$$H_{total} = \sum_{i=1}^{N} H_{Ai} + \sum_{i,j=1;i\neq j}^{N} H_{Aij}.. \qquad \text{(eq. 3.3)}$$

with

$$H_{Ai} = \vec{S}D\vec{S} + \beta\vec{B}g\vec{S} \qquad \text{(eq. 3.4)}$$

and

$$H_{Aij} = \overrightarrow{S_{Ai}}J^*_{Aij}\overrightarrow{S_{Aj}} \qquad \text{(eq. 3.5)}$$

Table 3.4: Simulated parameters for **K^1** with pNPP and phosphate (MoSophe).

parameter	**K^1** + pNPP	**K^1** + phosphate
g_{iso}[a]	1.99	2.01
D [cm^{-1}][a]	$185 * 10^{-4}$ [b]	$217 * 10^{-4}$ [c]
E/D[a]	0.33	0.33
d (Fe-Fe) [Å]	4.60[d]	4.57[e]
J_{iso} [cm^{-1}]	-2.40	-3.80

[a] equal for both Fe^{III} centers; [b],[c] The D tensors are rotated by β = ± 35 and ± 40°; [d] The positions of Fe(1) and Fe(2) are 0/0/0 and 4.60/0/0; [e] The positions of Fe(1) and Fe(2) are 0/0/0 and 4.57/0/0.

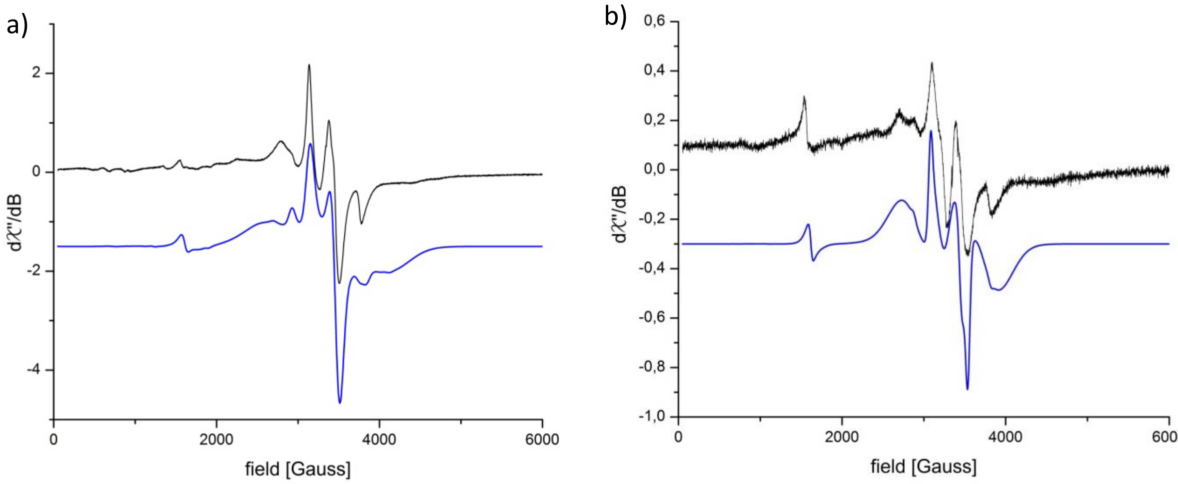

Figure 3.12: Experimental (black) and simulated (blue) X-band EPR spectra of **K**^{1} (0.5 mM in MeCN/buffer pH 5) with a) pNPP and b) phosphate (10 mM each); spectra were recorded at 9.376664 and 9.37824 GHz at 2.4 and 1.7 K, respectively.

The combination of EPR simulations and DFT calculations is a powerful method to gain structural information about molecules in solution. In our case, additional information is given by the magnetic interaction between the two Fe^{III} centers, leading to well-determined values for the coupling constant J and metal-metal distance d (simulated parameters, see Table 3.4). DFT calculations can provide calculated values for both. The latter can be estimated from geometry optimized structures, whereas J values are determined using the broken symmetry formalism.[141]

Three different structures are plausible for complexes of **K**^{1} with pNPP at pH 5: when two pNPP molecules are coordinated to each complex, as known from the ^{31}P-NMR titrations described above, one free coordination site at each Fe^{III} remains, which can be occupied by a bridging oxo-group (μ-O), a bridging hydroxide (μ-OH) or two terminal hydroxides. The geometry-optimized structures (for computational details see Chapter 4.5) are shown in Figure 3.13 and the corresponding parameters are listed in Table 3.5 and compared to experimentally obtained values of similar complexes (see Chapter 2.4 for details and references). It appears that the observed EPR signal for the **K**^{1}pNPP complex belongs to a species, where no other bridge than the two pNPP molecules is present, mainly due to the obtained coupling constant J. The estimated Fe^{III}-Fe^{III} distance of 4.68 Å fits to the value used in the simulation of the EPR spectrum (4.60 Å). Moreover, the simulated Euler angle of $\beta = \pm 35°$ almost resembles the rotation of the N-Fe^{III}-OH axes relative to the z-axis (perpendicular to the Fe^{III}-Fe^{III} axis) in the calculated structure (Figure 3.14).

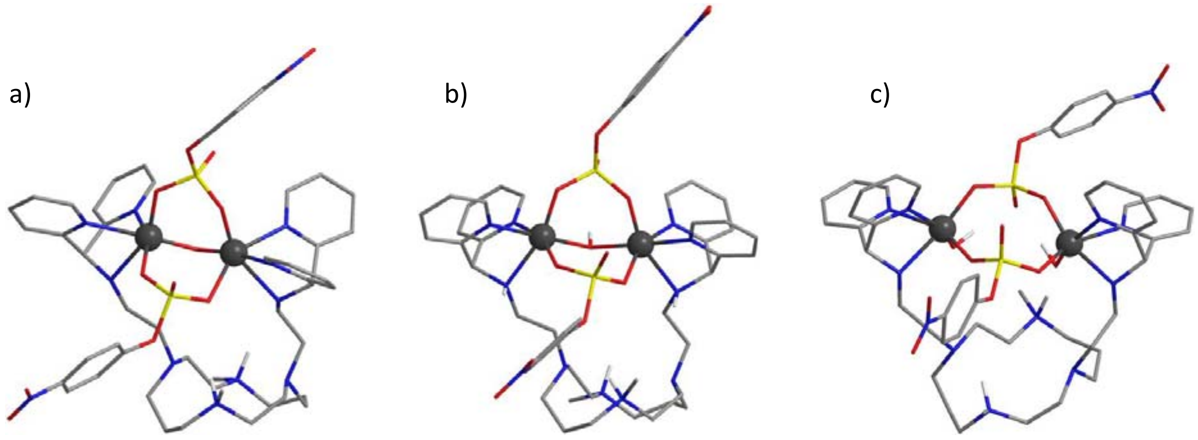

Figure 3.13: Geometry-optimized structures of **K**^{1} with two pNPP and a) μ-oxo, b) μ-hydroxo and c) two terminal hydroxo ligands; non-polar hydrogen atoms are omitted for clarity; light grey = carbon, white = hydrogen, blue = nitrogen, red = oxygen, yellow = phosphorous, dark grey = iron.

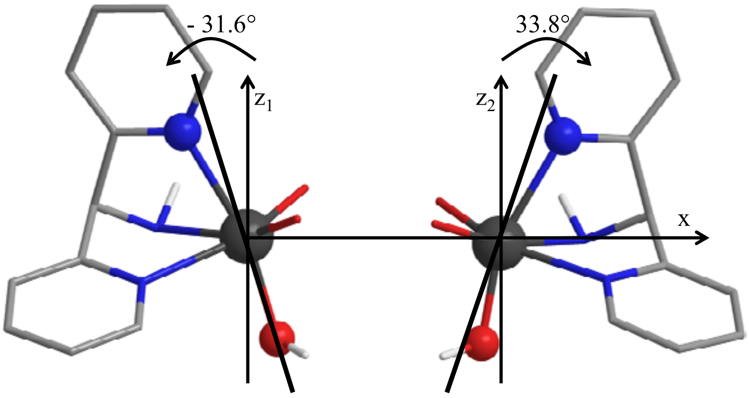

Figure 3.14: Rotation of the N-Fe-OH axes with respect to the cartesian axes.

Table 3.5: Calculated parameters for μ-oxo, μ-hydroxo and non-bridged **K**^{1} with pNPP in comparison with literature-known parameters[a] of diferric complexes

parameter	μ-oxo	μ-hydroxo	non-bridged
J_{calc} [cm^{-1}]	-67.35	-10.24	-3.11
J_{lit} [cm^{-1}]	-70 to -125	-10 to -20	0 to -3.5
d (Fe-Fe)$_{calc}$ [Å]	3.20	3.65	4.68
d (Fe-Fe)$_{lit}$ [Å]	3.15 to 3.60	3.45 to 3.60	4.60 to 4.85

[a] see Table 2.4 in Chapter 2.4 for details and references.

In order to further probe the magnetic properties of **K^1**pNPP, Evans-NMR measurements were performed. The magnetic moment significantly rises to μ_{eff} = 4.71 B.M. (vs. 3.77 B.M for **K^1** in MeCN/buffer without pNPP). This indicates a less strongly coupled species, which is consistent with the parameters obtained by EPR. Nevertheless, the low J-value of -1.67 cm^{-1} for the bis-hydroxo species (value from the VT EPR experiments) should result in a much higher magnetic moment, as the S=5 state should be populated at temperatures higher than 74 K and the Evans-NMR measurements were done at ambient temperature. This leads to the conclusion that a significant amount of **K^1** is still present in the strongly coupled, μ-oxo bridged form (see Scheme 3.11). As such a species occupies an S=0 spin state at very low temperatures, no additional EPR signals are expected. The postulated formal hydrolysis of the μ-oxo bridge includes a deprotonation step of a μ-hydroxo intermediate. Therefore, the shown equilibrium should be driven towards the μ-oxo side at high pH values. This can indeed be observed by EPR spectroscopy: with rising pH the signal intensity decreases and no signal is observed at pH 10. The relatively long time needed to fully develop the signal (around 4 h) suggests that the equilibrium is slow.

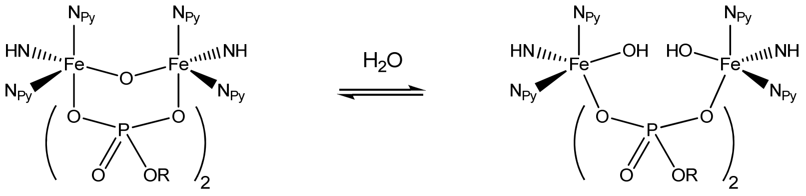

Scheme 3.11: Postulated equilibrium between μ-oxo bridged and open species of **K^1** with pNPP.

In the case of **K^1**phosphate complexes, slightly different structures can be expected. On one hand, it is known from the ^{31}P-NMR titrations that only one phosphate binds to **K^1** at pH 5. On the other hand, the simulated parameters from EPR measurements differ a bit from those of the **K^1**pNPP complex. Therefore, four different structures (Figure 3.15) were calculated with one coordinated phosphate, each. In analogy to the **K^1**pNPP species, μ-oxo and μ-hydroxo bridged phosphate complexes (Figure 3.15 a and b) were postulated and geometry-optimized. The calculated J-values of these species are too large compared to the experimental value of -2.43 cm^{-1} (Table 3.6). Figures 3.15 c and d show two possibilities for structures without additional bridges, where the phosphate is either used as a tridentate or as a bidentate ligand. This small geometric variation leads to major differences in the calculated J-values with a change from weak antiferromagnetic coupling in the tridentate coordination case to weak ferromagnetic coupling when phosphate coordinates bidentately.

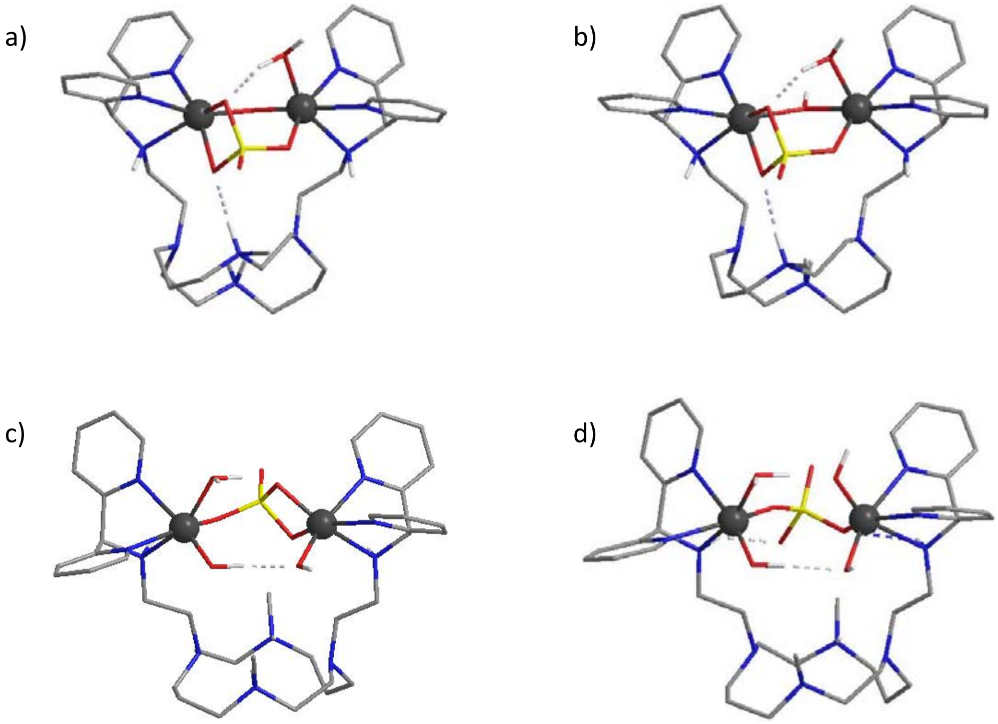

Figure 3.15: Geometry-optimized structures of $\mathbf{K^1}$ with phosphate and a) μ-oxo, b) μ-hydroxo, c) three terminal hydroxo ligands and tridentate phosphate (non-bridged 1) and d) four terminal hydroxo ligands and bidentate phosphate (non-bridged 2); non-polar hydrogen atoms are omitted for clarity; light grey = carbon, white = hydrogen, blue = nitrogen, red = oxygen, yellow = phosphorous, dark grey = iron.

Table 3.6: Calculated parameters for μ-oxo, μ-hydroxo and non-bridged $\mathbf{K^1}$ with phosphate in comparison with literature-known parameters of diferric complexes.

parameter	μ-oxo	μ-hydroxo	non-bridged 1	non-bridged 2
J_{calc} [cm^{-1}]	-68.31	-13.63	-2.61	+0.57
J_{lit} [cm^{-1}]	-70 to -125	-10 to -20	0 to -3.5	0 to -3.5
d (Fe-Fe)$_{calc}$ [Å]	3.32	3.66	4.54	4.23
d (Fe-Fe)$_{lit}$ [Å]	3.15 to 3.60	3.45 to 3.60	4.60 to 4.85	4.60 to 4.85

Again, the observed EPR signal seems to belong to a species with no additional bridge apart from phosphate. Most probably, this phosphate coordinates in a tridentate way, as shown in Figure 3.15 c. As in the case with **K^1**pNPP, it cannot be excluded that only a fraction of the molecules are present in this form and the other species is EPR-silent due to a μ-oxo bridged structure, as shown in Figure 3.15 a.

UV/vis spectra of **K^1** with the different substrate mimics (pNPP, 1-NP and DPP) as well as with phosphate as product of hydrolysis were recorded at different concentrations. The iron-oxo bands were investigated at 0.05mM **K^1** (Figure 3.16 a) and the less intense dd bands at a tenfold higher concentration (Figure 3.16 b).

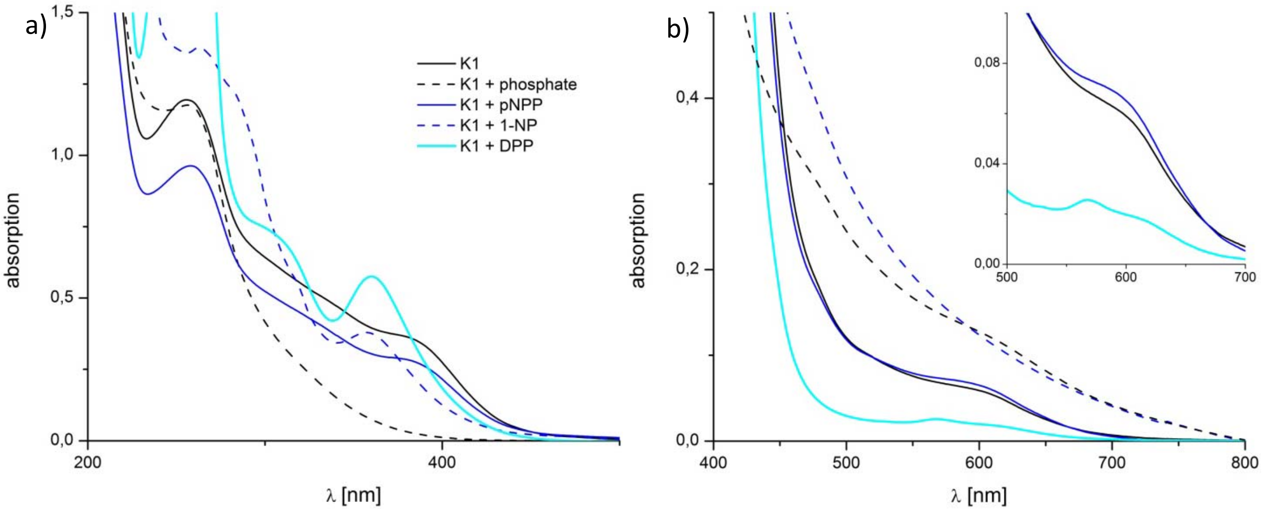

Figure 3.16: Comparison of UV/vis spectra of **K^1** with coligands in MeCN; spectra were recorded at a) 0.05 mM **K^1** and b) 0.5 mM **K^1** with one equivalent coligand each.

Whereas the spectrum of **K^1** with pNPP (dark blue) very much resembles the original spectrum of **K^1** (black), only with less intensity in the UV region, addition of 1-NP (dashed dark blue) or DPP (light blue) leads to large differences. The **K^1**DPP spectrum shows a very interesting feature in its dd region: the band is split into two peaks. This is an indication for the presence of two ferric ions with a different environment. As one equivalent of substrate was added in each experiment, the conclusion is that DPP coordinates in a monodentate way to **K^1**, leaving the other ferric ion unaffected. In all other cases only one dd band is observed. This means that these substrate mimics are bridging the two ferric ions. In constrast, the dd band of the 1-NP mixture is hardly visible. No definite conclusion can be drawn from the UV region. It seems that the two monoesters pNPP and 1-NP have a different coordination mode, as the wavelengths of the iron-oxo bands differ significantly. The iron-oxo bands of the DPP sample are very similar to the 1-NP one, only with some additional shoulders in the 1-NP spectrum, arising from the naphthyl residue. Probably, these features come from the differences in steric demand of the substrate mimics. pNPP is smaller than 1-NP, which has a similar size to DPP. It is known that the angle of the Fe-oxo-Fe unit strongly influences the spectra in the UV region.[103] This might also be the case here, as different sizes of the substrate will change the complex structure and enforce different angles. Addition of phosphate leads to a complete loss of the iron-oxo transitions. This means that the oxo bridge is lost, probably by hydrolysis into two terminal hydroxides.

As the UV/vis spectrum of $\mathbf{K^1}$ changes slowly upon the addition of buffer, time dependent UV/vis spectra were measured to investigate the behavior of $\mathbf{K^1}$/substrate mimic mixtures in partly aqueous media. pNPP was not used this time, because the hydrolysis product, *para*-nitrophenolate, has very intense absorptions that conceal all other bands even at small concentration. The spectra of $\mathbf{K^1}$ with phosphate, 1-NP and DPP are shown in Figure 3.17. Different concentrations were utilized for the different wavelength regions, as described in the figure caption. Only relatively small changes in the UV region are observed in all three cases. With phosphate, the previously present iron-oxo bands between 300 and 400 nm are hardly visible, indicating a fast hydrolysis of the μ-oxo bridge (Figure 3.17 a). In contrast, the spectra with 1-NP and DPP exhibit clearly visible shoulders in this region. With the monoester 1-NP (Figure 3.17 c), the overall intensity rises, whereas with DPP (Figure 3.17 e), an isosbestic point is formed at around 350 nm, leading to an iron-oxo band that is shifted by around 20 nm to higher wavelengths compared to 1-NP. In the visible region, the predominant feature is the already observed CT band at 470 nm in each case (see Figure 3.10 b). More interesting are the relatively weak dd bands around 600 nm. In the phosphate spectrum (Figure 3.17 b), the intensity of this band decreases over time (i.e. the shoulder becomes flatter), which can be explained by the loss of asymmetry due to the hydrolysis of the oxo bridge. The more asymmetric the environment of the ferric ions, the more intense the formally forbidden dd will bands be. The increase of the absorption band at 470 nm is due to the overall increase of intensity, visible in Figure 3.17 a. With 1-NP (Figure 3.17 d), the dd band retains its shape and is only shifted up as whole due to the shift of the whole spectrum. In the case with DPP (Figure 3.17 f), very small changes are visible regarding the dd band. In line with the spectra in pure MeCN, a split band can also be observed, although one could argue that this is due to the bad resolution of the spectrum and too low concentrations. Unfortunately, no higher concentrations can be obtained for solubility reasons.

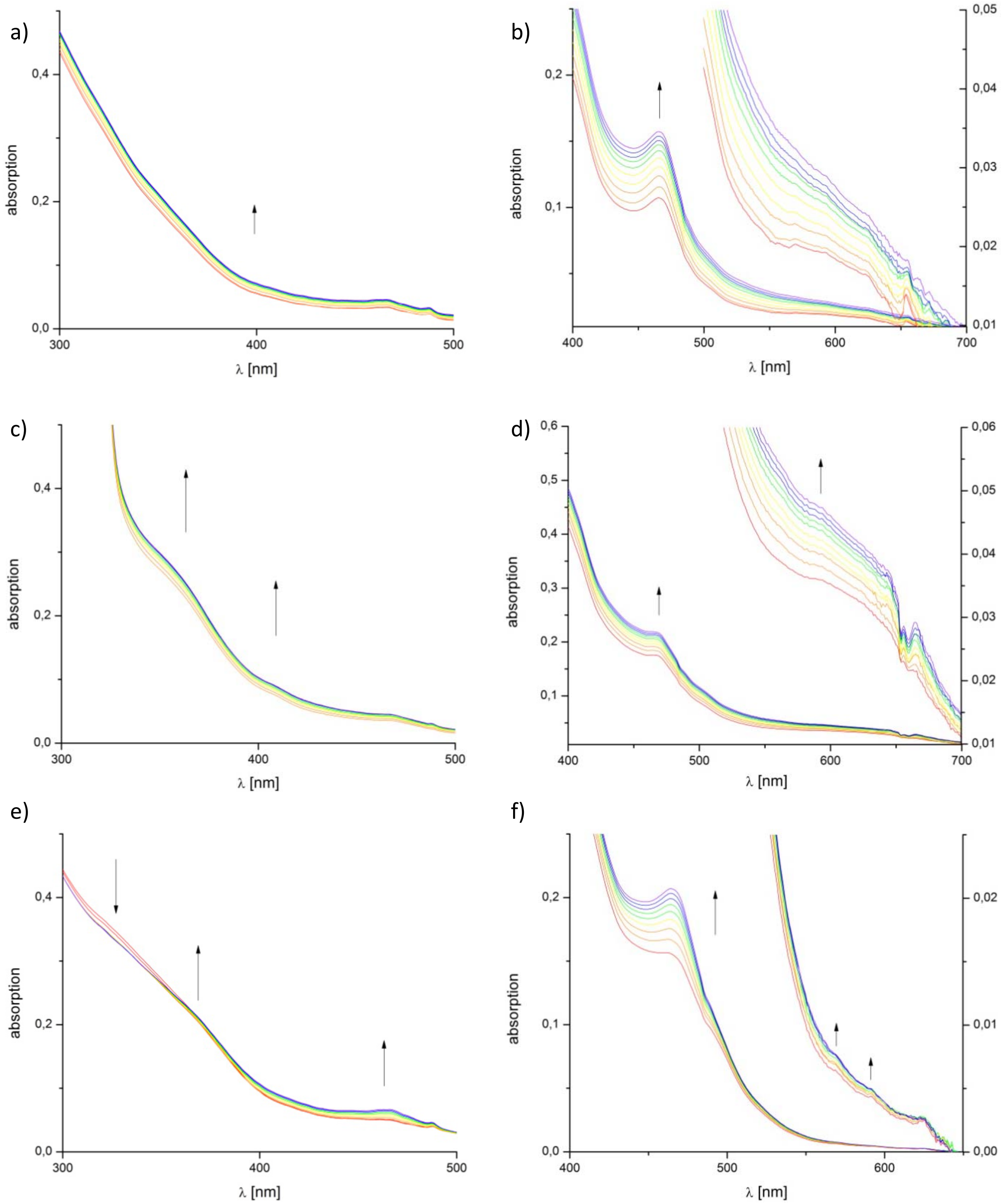

Figure 3.17: Time dependent UV/vis spectra of **K**^{1} in MeCN/buffer pH 6 with a), b) phosphate; c), d) 1-NP and e), f) DPP; left spectra (i.e. a, c and e) were recorded with 0.05 mM **K**^{1} and 1 mM coligand for 20 min, right spectra (i.e. b, d and f) with 0.25 mM **K**^{1} and 5 mM coligand for 10 min with one scan per minute each.

Nevertheless, it becomes clear that 1-NP and DPP exhibit a very different behavior, and we conclude that the monoester 1-NP is preferentially bound in a bridging coordination mode whereas the diester DPP binds monodentately.

The combination of the EPR and UV/vis results allows for a more detailed interpretation of the stoichometries observed by ^{31}P-NMR titrations at the beginning of this chapter. The proposed monodentate coordination of the relatively bulky diester DPP is in agreement with a 1:1 coordination to **K**^{1}. In the case of pNPP, the postulated hydrolysis equilibrium at low pH between the structures with a μ-oxo bridge and terminal hydroxides, respectively, leads to the possibility of ligand exchange (aqua/hydroxo vs. pNPP) and due to the smaller size of this substrate, the coordination of a second pNPP molecule is possible. However, at high pH the μ-oxo bridge is conserved and no further ligand exchange occurs. With phosphate, the sterically demanding tridentate coordination mode of this relatively small molecule prevents the coordination of a second substrate. Therefore, only 1:1 complexes are observed with **K**^{1} and phosphate.

3.2.2.5. *Solid State Coordination Chemistry of L*^{1}

When preparing solutions of **K**^{1} in MeCN at high concentrations (> 5 mM), an ochre precipitate is obtained. Elemental analysis (C, H, N, Cl and Fe) yields the following composition: $[L^1Fe^{III}_2Cl_4O] * 2\ HCl * 5\ H_2O$. The precipitate is in soluble in organic solvents, except for methanol, but soluble in water. In order to dissolve it, MeCN with 1 % water was used. This behavior can be explained by formation of polymeric structures. A reasonable possibility is a chain-type polymer **14**, intermolecularly connected via Fe-oxo-Fe units (Scheme 3.12). The pre-formed dinuclear ferric complex $[Cl_3Fe\text{-}O\text{-}FeCl_3]^{2-}$ described in Chapter 3.2.2.1 (Scheme 3.7) reacts with two ligand molecules instead of one due to the high concentration of **L**^{1}. When water is added, the μ-oxo bridges can be hydrolyzed, giving rise to monomeric **K**^{1} type complexes. HR-ESI-MS supported this proposal by showing different peaks, which were already observed for **K**^{1} solutions in MeCN. The predominant peak is *m/z* = 847.24790, which is calculated to 847.24797 for $[L^1Fe^{III}_2Cl_2O]^+$. When MeCN is used as solvent without water, no complex peaks can be identified.

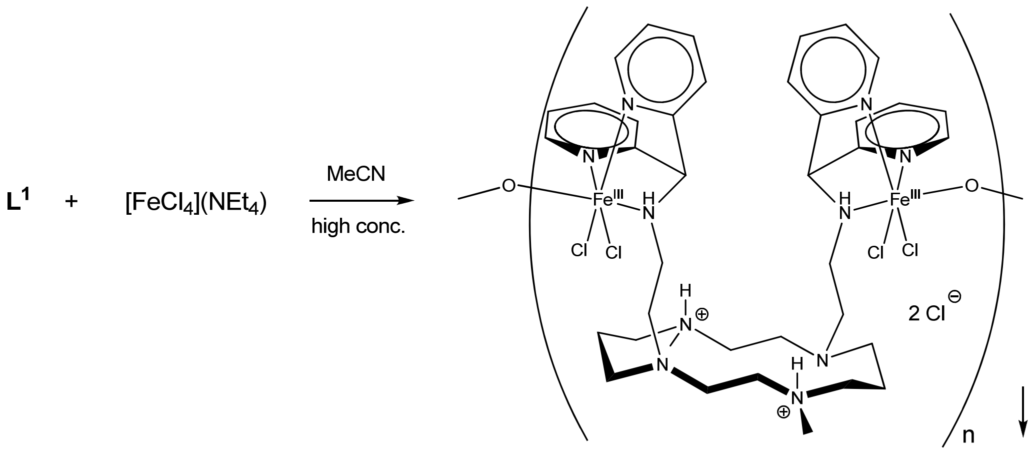

14 (67 %)

Scheme 3.12: Synthesis and possible structure of the precipitate of **K**^{1}.

UV/vis spectra were recorded in solid state, as well as in MeCN with 1 % water and are compared to solution **K**^{1} spectra in Figure 3.18. The solution spectra (dotted and solid line) are very similar with only small deviations in intensities being observed. Interestingly, the additional band at 466 nm has been previously observed, namely in the MeCN/buffer spectra (see Chapter 3.2.2.3). This is a hint for partial co-ligand exchange (chloro to aqua). The solid state spectrum (dashed line) shows bands at nearly the same wavelengths as in solution, only with completely different intensities. The most intense absorption is the oxo to iron CT transition at 400 nm and other bands appear as shoulders on this absorption. Also the Fe^{III} dd transition around 600 nm is clearly visible as a shoulder.

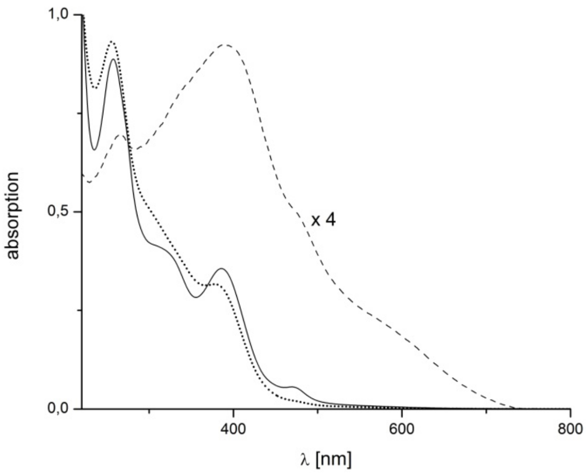

Figure 3.18: UV/vis spectra of **K**^{1} in MeCN (0.05 mM; dotted line), **14** in MeCN with 1% H_2O (0.05 mM; solid line) and in solid state in Al_2O_3 (dashed line).

EPR measurements of **14** in the solid state show only one not very intense signal at g_{eff} = 4.3, corresponding to high spin ferric ions. No other signal can be observed, which leads to the conclusion that the main species must be strongly coupled and therefore EPR-silent. This is in agreement with the postulated μ-oxo bridges between the complex units. Complex **14** was further examined by cyclic voltammetry (Figure 3.19). Again, 1% water had to be added to MeCN to make the solid dissolve. The obtained $E_{1/2}$ of 0.01 V vs. SCE is consistent with the value of -0.09 V measured with the *in situ* prepared complex solutions within experimental errors and due to the addition of water. This provides further support for the assumption that the precipitate forms the same species as the *in situ* prepared complexes when dissolved.

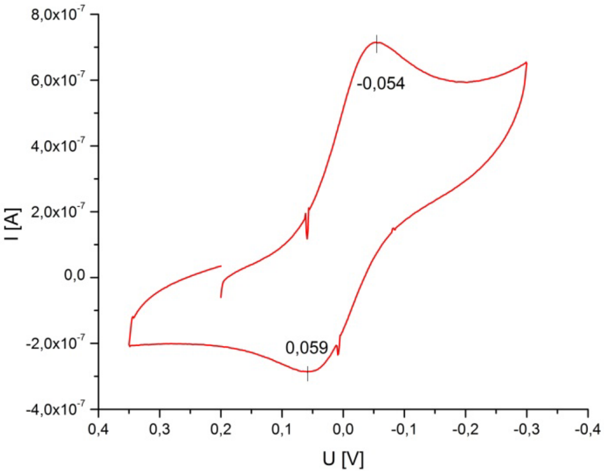

Figure 3.19: CV of **14**; recorded in MeCN with 1%H_2O and 0.1 M NBu_4ClO_4 vs. SCE.

Figure 3.20 shows a comparison of the ligand IR spectrum with that of **14**. The predominant ligand peak at 2787 cm^{-1} is a Bohlmann band arising from a C-H starching frequency where the C-H bond is in trans position to a nitrogen atom lone pair.[142] In our case, this type of bond is found in the cyclam part of the ligand. It vanishes when the complex forms, which can be explained by a loss of the nitrogen lone pair. This comes either from coordination of metals in the cyclam moiety or from protonation of the nitrogen atoms. The latter is more plausible in this case, as coordination to the cyclam part of **L**^{1} was excluded by various spectroscopic techniques. Another interesting band is the one at 1667 cm^{-1} in the ligand spectrum, which belongs to a C=N stretch vibration of the pyridines. Upon reaction with Fe^{III}, this band is shifted to 1627 cm^{-1}, which indicates coordination of the pyridines to the iron that causes weaker bonds and therefore vibrations at lower wave numbers. The band at 826 cm^{-1} in the **K^1** spectrum is assigned to the asymmetric Fe-O-Fe stretch vibration. It has a slightly higher frequency than other μ-oxo bridged diferric complexes (for comparison see Table 2.5 in Chapter 2.4). Only the last two entries in that table have similar values: These complexes have no additional bridge, like phosphate or similar co-ligands, and therefore the Fe-O-Fe angle is relatively large (between 160 and 180°).[108, 109] This is important structural information regarding **K^1**.

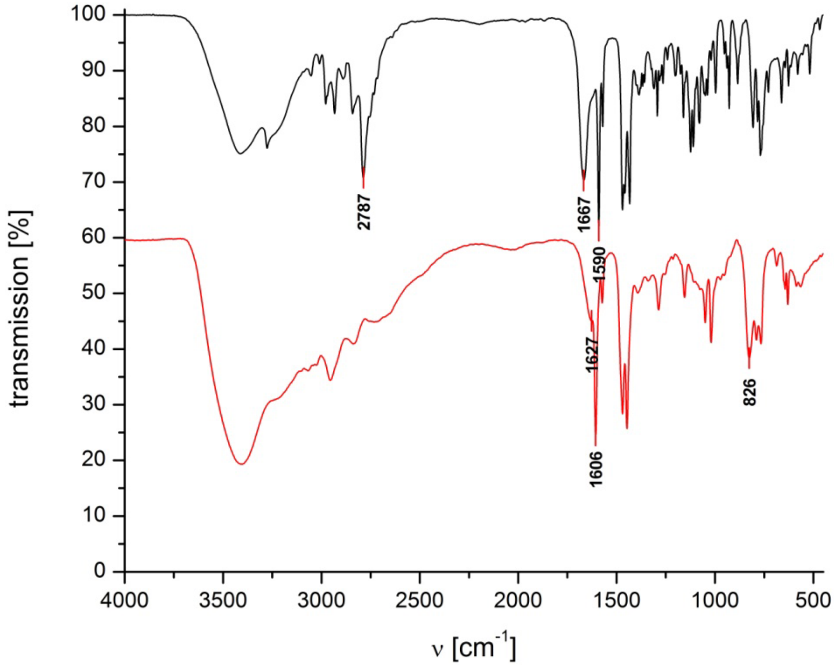

Figure 3.20: IR spectra of **L^1** (top) and **14** (bottom) in KBr.

3.2.3. *Coordination Chemistry of L^1 with Zn^{II} and Cu^{II}*

So far, only little work was done on **L^1** complexes with metals other than Fe^{III}. The main focus was on Zn^{II} and Cu^{II}. The idea was to block the cyclam moiety of **L^1** with a metal ion and leave the pyridine and amine functions free for Fe^{III} to build up “blocked” **K^1**. This should mimic the absence of the hydrogen bridge forming abilities of the cyclam part. Unfortunately, neither Zn^{II} nor Cu^{II} tend to go into the macrocycle, but rather are coordinated by the pyridine and amine site. This can be seen in the X-ray structures of the respective complexes **15** and **16** (Figure 3.21). The Cu^{II} complex **16** was further examined in solution by spectroscopic methods (UV/vis and EPR). The data resemble those for Cu^{II}(dipa)$_2^{2+}$ (dipa = di-2-pyridylmethylamine; see Table 3.7 for comparison).[121] Therefore, it can be concluded, that the coordination mode observed in the solid state is retained in solution.

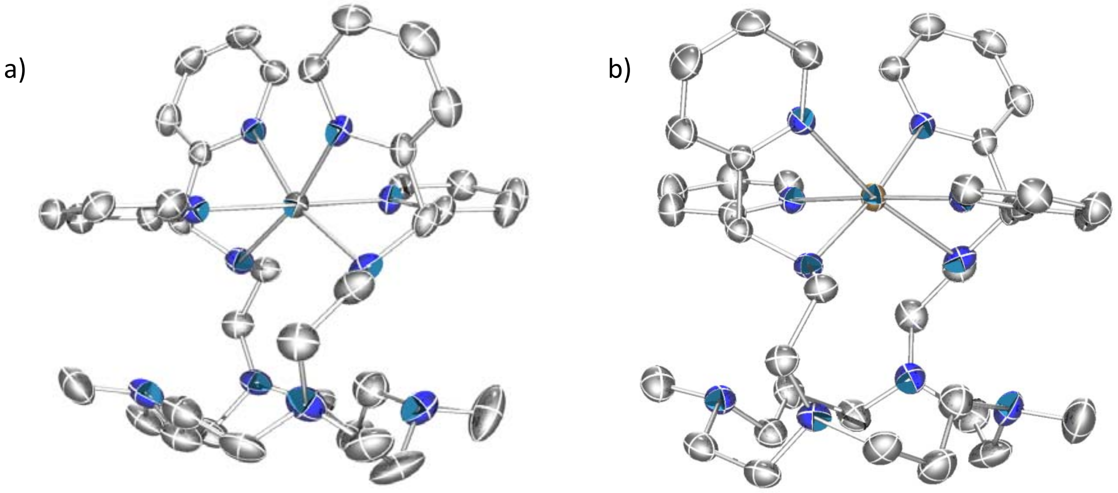

Figure 3.21: Ortep plots of the X-ray structures of a) [**L^1**Zn]$^{2+}$ (**15**) and b) [**L^1**Cu]$^{2+}$ (**16**) (hydrogen atoms are omitted for clarity; ellipsoids are drawn at 50% probability level).

Table 3.7: Comparison of spectroscopic parameters of [**L^1**Cu]$^{2+}$ **16** and [Cu(dipa)$_2$]$^{2+}$.

	λ_{max} (dd) [nm]	$g_{\parallel}$	$g_{\perp}$	$A_{\parallel}$ [*10^{-4} cm^{-1}]	$A_{\perp}$ [*10^{-4} cm^{-1}]
[**L^1**Cu]$^{2+}$	639	2.23	2.05	180	n.a.
[Cu(dipa)$_2$]$^{2+}$[121]	616	2.23	2.08	188	23

As the approach, to first block the cyclam site and subsequently form **K^1**, did not lead to the desired results, another route was taken by first mixing **L^1** and the iron salt to prepare **K^1** *in situ*, and afterwards adding $ZnCl_2$ or $CuCl_2$. Zn^{II} with its d^{10} configuration is not useful in terms of spectroscopic experiments, therefore only the **K^1**Cu mixture was used for UV/vis and EPR measurements, to determine whether the mixed metal complex was formed. The UV/vis spectrum of **K^1**Cu in MeCN (Figure 3.22 a) shows a band in the Cu^{II} dd region (dashed line), that is clearly different to that of **L^1**Cu (dotted line). The typical iron-oxo bands in the UV region are still present, but slightly shifted, which indicates a slightly different Fe-oxo-Fe structure. This might be interpreted as the presence of a mixed metal complex, where $\mathbf{K}^{\mathbf{1}}$ has an additional Cu^{II} ion coordinated in the cyclam moiety. It cannot be excluded, that the Cu^{II} center is only weakly attached to $\mathbf{K}^{\mathbf{1}}$. In contrast, the spectra in MeCN/buffer show some alterations (Figure 3.22 b): In the UV region, the iron-oxo bands become significantly more flat when going from $\mathbf{K}^{\mathbf{1}}$ to $\mathbf{K}^{\mathbf{1}}$Cu. Also, the dd band is dramatically changed so that it is hardly visible as a shoulder around 610 nm. A comparison with the dd band of $\mathbf{L}^{\mathbf{1}}$Cu shows some similarity. Therefore, it can be concluded that the previously formed mixed complex $\mathbf{K}^{\mathbf{1}}$Cu is destroyed when buffer is added. Most probably, the Cu^{II} displaces the ferric ions and is finally coordinated as shown in the X-ray structures above (Figure 3.21 b).

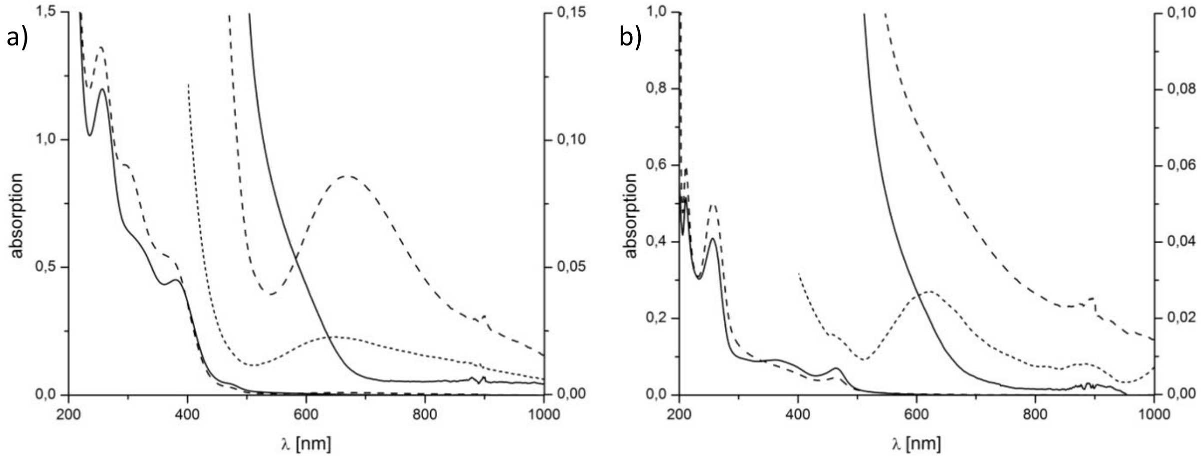

Figure 3.22: UV/vis spectra of $\mathbf{K}^{\mathbf{1}}$ (solid line), $\mathbf{K}^{\mathbf{1}}$Cu (dashed line) and $\mathbf{L}^{\mathbf{1}}$Cu (dotted line) in a) MeCN (0.05 mM for left and 0.5 mM for right axis) and b) MeCN/buffer pH 6 (0.025 mM for left and 0.25 mM for right axis).

Further comparison of $\mathbf{K}^{\mathbf{1}}$Cu and $\mathbf{L}^{\mathbf{1}}$Cu was made by EPR measurements. The spectra of $\mathbf{K}^{\mathbf{1}}$Cu (solid line) and $\mathbf{L}^{\mathbf{1}}$Cu (dashed line) are shown in Figure 3.23. Although the overall shape of the signals differs significantly, the g values are similar. The different form can be explained by the additional paramagnetic influence of the ferric ions present in the $\mathbf{K}^{\mathbf{1}}$Cu sample. This is in agreement with the interpretation that $\mathbf{K}^{\mathbf{1}}$ is slowly destroyed by addition of Cu^{II} in MeCN/buffer solution and replaced by $\mathbf{L}^{\mathbf{1}}$Cu.

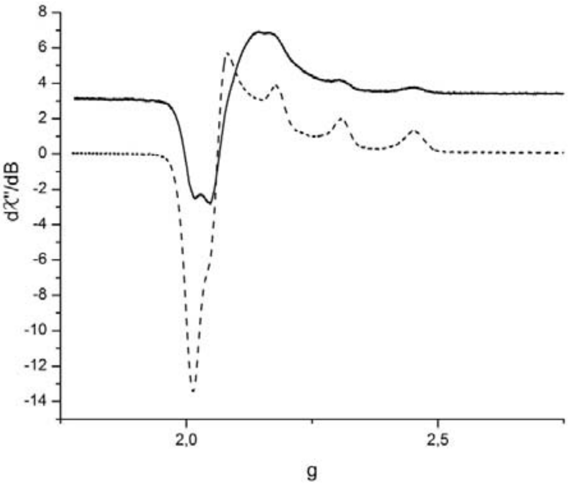

Figure 3.23: Comparison of X-band EPR spectra (in g space) of **K**^{1}Cu (0.625 mM; solid line) and **L**^{1}Cu (0.625 mM; dashed line); spectra were recorded at 9.457661 or 9.435719 GHz and 120 K in MeCN/buffer pH 6.

Our attempt, to eliminate the influence of a second coordination sphere of the cyclam moiety by adding another metal to **K**^{1}, failed. In MeCN solution, the desired complex is most probably formed, but under the conditions for the kinetic measurements (i.e. in MeCN/buffer 1:1), it is destroyed.

3.2.4. Summary L^1

Ligand **L**^{1} with its flexible cyclam spacer has unique properties in the coordination chemistry especially with ferric ions. An important observation for its intended function as mimic for PAPs is that it predominantly forms *in situ* μ-oxo bridged diferric complexes, even with less than two eq of Fe^{III}. A thorough characterization based on ^{1}H-NMR and UV/vis titrations, HR ESI mass spectrometry, Evans-NMR measurements and EPR spectroscopy, supports the assumed nature of the complex. The observed behavior is mainly due to the use of an appropriate precursor, tetrachloroferrate, in combination with the high basicity of the cyclam moiety, that results in the formation of a μ-oxo bridged diferric precursor with subsequent coordination of the pyridine and secondary amine parts of **L**^{1} to produce **K**^{1}. Cyclic voltammetry revealed the redox potential of **K**^{1} to be $E_{1/2} = -0.09$ V vs. SCE. Experiments with a one-electron reduction of **K^1** were only partly successful, as the resulting heterovalent Fe^{III}Fe^{II} complex is unstable over time, even under anaerobic conditions.

A further requirement for a suitable PAP mimic is the preservation of the observed structure in aqueous conditions, which are applied during kinetic measurements, and at different pH. This was also shown to be the case by EPR, Evans-NMR measurements and, to some extent, time-resolved UV/vis spectroscopy. The latter revealed that ligand exchange reactions after the addition of buffer to a solution **K^1** are relatively slow.

Importantly, phosphate and substrate mimics, like the phosphomonoesters pNPP and 1-NP, or the diester DPP, readily coordinate to **K^1**, as shown by HR ESI mass spectrometry, UV/vis and ^{31}P-NMR. The stoichometry differs from monoester to phosphate and the diester substrate mimic, being 1:2 for **K^1** with pNPP and 1:1 for **K^1** with phosphate and DPP at low pH. This is explained by the different coordination modes suggested by spectroscopic measurements. In combination with EPR measurements, spectra simulation and DFT calculations, structures for **K^1**pNPP$_2$ and **K^1**phosphate complexes were proposed. The weak antiferromagnetic coupling between the two metal ions (low J values) leads to the conclusion that the μ-oxo bridge is slowly hydrolyzed upon reaction of **K^1** with pNPP or phosphate, leading to a complex where the metal ions are bridged by the substrates alone. However, Evans NMR suggests that this applies only for a small fraction of the complex molecules, i.e. an equilibrium between an EPR-silent μ-oxo bridged species and a species with a hydrolyzed μ-oxo bridge is to be expected. This multitude of different structures with varying metal-metal distances reflects the high flexibility of the system.

Highly interesting with respect to the expected PAP mimicking abilities is the presence of two dd bands in the UV/vis spectrum of **K^1** with the diester DPP. In conjunction with the result from EPR experiments, where no signal is observed, this indicates a monodentate coordination mode, which is necessary for an efficient attack by a terminally bound hydroxide in a PAP like hydrolysis reaction. Unfortunately, no observation of this kind is made with monoester substrate mimics.

Another outstanding observation is the coordination of Cu^{II} and Zn^{II} in the pyridine and secondary amine part of **L^1**. Cyclam is a ligand which usually results in highly stable complexes, especially with Cu^{II}. Therefore, the preference for the dipa type coordination site and not for the cyclam moiety is rather surprising and should be studied in more detail.

3.3. The Phenolate-based Ligands HL^2 and H$_3$L^3

3.3.1. Synthesis and Structures of the Ligands HL^2 and H$_3$L^3

In analogy to the known literature model systems presented in Chapter 2.3, **HL^2** and **H$_3$L^3** were designed. The aim is to derivatize the ligand HBPMP[143] (see Chapter 2.3) in a way that coordinated substrates can interact with a second coordination sphere. The use of HBPMP as a basis for attaching a second coordination sphere has several advantages, namely that the synthetic pathways towards these type of ligands are well established.[79, 116, 143] On the other hand, extensive experimental and mechanistic studies have been performed with these systems, providing a basis for comparison.[55, 69, 92]

The retrosynthetic approach is shown in Scheme 3.13. The key step is the depicted twofold nucleophilic substitution of the primary chlorides in the *p*-cresol derivative by secondary amines.

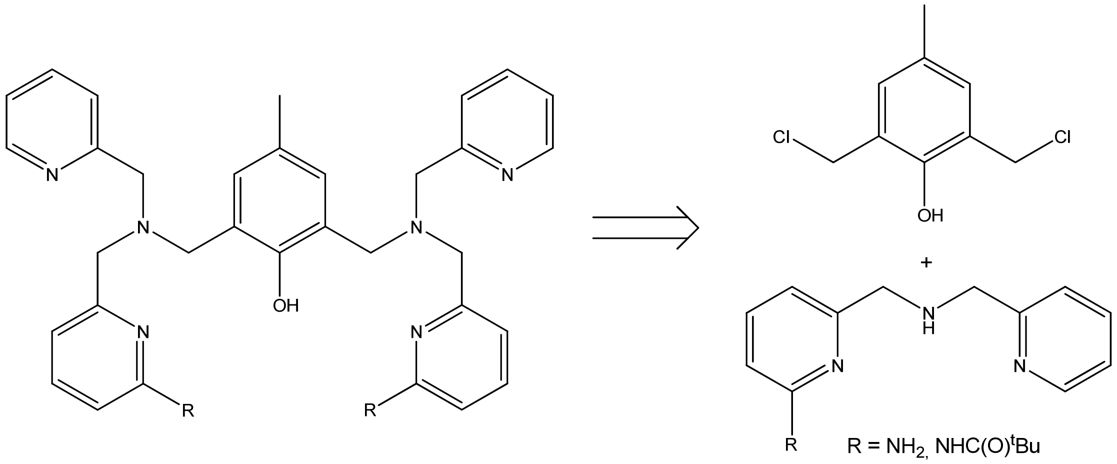

Scheme 3.13: Retrosynthetic approach to ligands **HL^2** and **H$_3$L^3**.

We chose the position ortho to the pyridine nitrogens for functionalization. Again, synthetic considerations were one reason for this decision, but also the obvious proximity to the first coordination sphere seemed promising. Preliminary modeling studies encouraged this idea, as well. The nature of the functional group was also important. In contrast to the cyclam part in **L^1**, which has a very high proton affinity, a less basic group should be used in this case to mimic the histidine residues in PAP enzymes more closely. The pK_a of imidazole is around 6, which means that at a physiological pH (7.4), 10 % of the histidines exist in a protonated form. The primary amine in 2-aminopyridine, which already has been used in similar ligands, has a pK_a of 6.8.[144] This is in sufficient agreement with the natural system. In order to keep the resulting positive charge small, only two of the available four pyridines are functionalized.

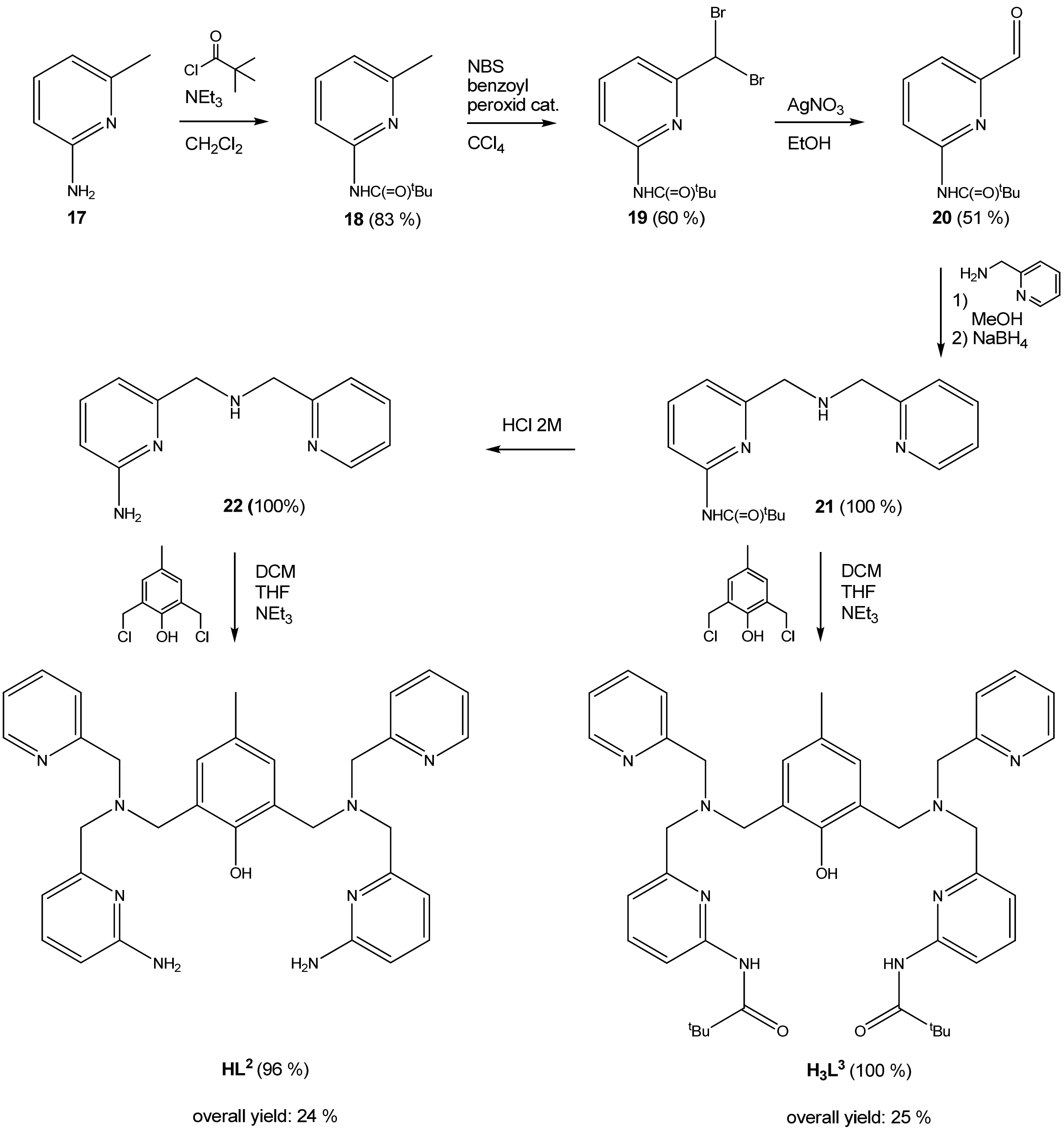

Scheme 3.14: Synthesis of ligands **HL^2** and **H_3L^3**.

Scheme 3.14 describes the full synthesis of both ligands. Starting from commercially available 2-amino-6-methylpyridine **17**, pivaloyl chloride is used to introduce a protecting group on the primary amine to give 2-pivaloylamino-6-methylpyridine **18** as white crystals in 83 % yield (lit. 84 %).[145] In the next step, the methyl group is doubly brominated with NBS in CCl_4 under reflux conditions. To achieve relatively high yields of dibromo- vs. monobromo product, NBS and benzoyl peroxide are added in small portions over 8h. Although small monobromide impurities are present at the end, **19** is used in the next step without further purification (60 % yield, lit. 55 %).[145] It is hydrolyzed by $AgNO_3$ in aqueous acetone under light shielding conditions to the corresponding aldehyde **20** in 51 % yield (lit. 89 %).[145] Subsequently, **20** is reacted with 2-picolylamine, forming the imine formation which is then reduced *in situ* with $NaBH_4$ to give the secondary amine **21** in quantitative yield. Ligand **H$_3$L^3** is directly accessible in quantitative yield from **21** and 2,6-bis(chloromethyl)-*p*-cresol **24**. The latter is synthesized in one step by stirring 2,6-bis(hydroxomethyl)-*p*-cresol **23** in conc. HCl in 97 %yield (lit. 94 %, see Scheme 3.15).[146, 147] Attempts to obtain **HL^2** from **H$_3$L^3** by cleaving off the protecting groups under reflux in 2M HCl failed. It seems that these conditions are too harsh for the ligand backbone, as only decomposition peaks were observed in ESI-MS of the raw reaction mixture. Therefore, an alternative approach was necessary: Amine **21** was refluxed in 2M HCl to deprotect the primary amine in quantitative yield. Subsequent reaction of the free amine **22** with 2,6-bis(chloromethyl)-*p*-cresol **24** resulted in exclusive formation of **HL^2** in 96 % yield. As expected, the secondary amine functionality turned out to be the more active nucleophile and the primary amine protecting group was not necessary in this reaction. The overall yields for **HL^2** and **H$_3$L^3** are 24 % (six steps) and 25 % (five steps), respectively.

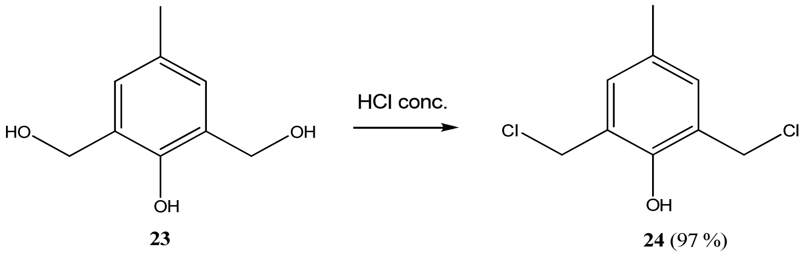

Scheme 3.15: Synthesis of 2,6-bis(chloromethyl)-*p*-cresol.[146, 147]

No crystals of **HL^2** and **H$_3$L^3** could be obtained that were suitable for X-ray analysis. To get insight into the structural properties of the ligands, a conformational search was performed in the same manner as for **L^1**. The lowest energy conformations of **HL^2** and **H$_3$L^3**, respectively, are shown in Figure 3.24. Various conformations were found within 10 kJ/mol for **HL^2** with the amine bearing pyridines either on one side (cisoid) or on different sides (transoid) of the central phenol group. This accounts for a high degree of flexibility, regarding the relative position of the coordinating groups. In the case of **H$_3$L^3**, up to 25 kJ/mol difference lies between the lowest energy cisoid structure and its transoid counterpart. Due to the more bulky amido groups, rotations around the C-C and C-N bonds of the methylene bridges become less favourable. Yet, this process is feasible. An additional effect can be observed in the lowest energy conformation shown in Figure 3.24 (right): The amido groups can form intramolecular hydrogen bonds and, by this, stabilize the molecule. This interaction is only observed in the shown conformation, not in any other obtained structure.

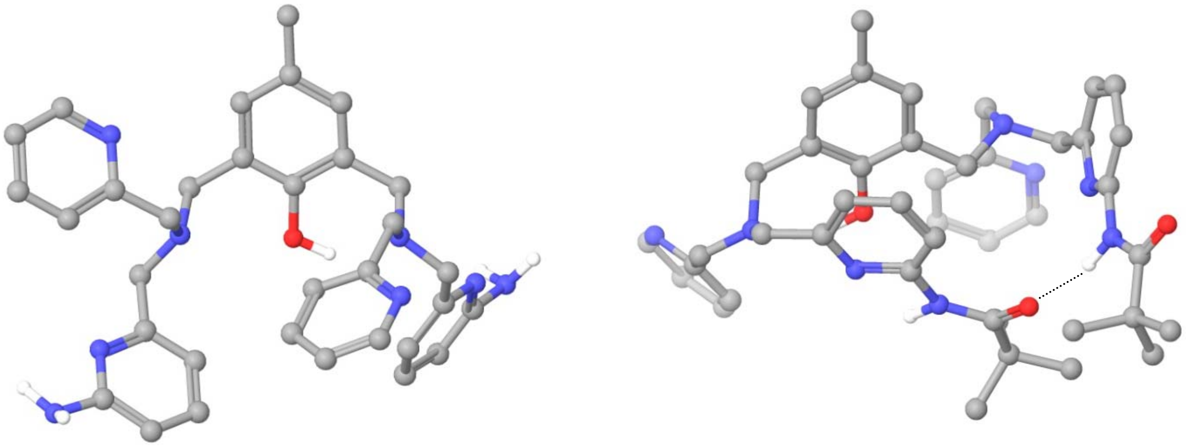

Figure 3.24: Lowest-energy conformers from a conformational search on **HL^2** (left) and **H$_3$L^3** (right).

3.3.2. *Fe^{III} Coordination Chemistry of HL^2 and H$_3$L^3*

3.3.2.1. *Solution Chemistry of In Situ Prepared K^2 and K^3 Complexes*

Due to the similarity of **HL^2** and **H$_3$L^3** to the well known PAP model systems based on ligand HBPMP, their coordination chemistry with Fe^{III} should be relatively easy to understand. Our expectation was that both ligands form dinuclear complexes, named **K^2** and **K^3**, when reacted with two equivalents of a ferric salt *in situ*. In order to investigate the coordination behavior in solution, various experiments were conducted, including UV/vis titrations, Evans-NMR measurements and ESI mass spectrometry. Tetraethylammonium tetrachloroferrate was used as the iron source in all experiments.

Ligand **HL^2** with its additional amino groups should result in a multiply charged species when two eq of Fe^{III} are added. Highly charged complexes are seldom seen in mass spectrometry. And in fact, only small signals of dinuclear complexes can be detected in ESI mass spectra of **HL^2** recorded in MeOH, regardless of one or two eq of Fe^{III} or additional base added (see Table 3.8). Due to the experimental setup, formic acid was automatically added to the measured solution, resulting in formates as counter ions in several cases.

Table 3.8: Results of ESI MS experiments with ligand **HL^2** in MeOH.

conditions	species	calc. m/z	exp. m/z	peak height
L^2 + 1 Fe^{III}	$[H_2L^2]^+$	561.31	561.49	67 %
“	$[HL^2Fe_2Cl(HCOO)_3]^+$	842.13	842.48	3 %
“	$[NaL^2Fe_2Cl(HCOO)_3]^+$	864.11	864.46	2 %
L^2 + 1 Fe^{III} + 1 NEt$_3$	$[H_2L^2]^+$	561.31	561.48	75 %
“	$[HL^2FeCl_2(HCOO)]$ x $HNEt_3^+$	833.30	833.49	6 %
“	$[HL^2Fe_2Cl(HCOO)_3]^+$	842.13	842.49	18 %
“	$[NaL^2Fe_2Cl(HCOO)_3]^+$	864.11	864.47	8 %
L^2 + 2 Fe^{III}	$[HL^2Fe_2Cl(HCOO)_3]^+$	842.13	842.50	18 %
“	$[NaL^2Fe_2Cl(HCOO)_3]^+$	864.11	864.46	23 %
L^2 + 2 Fe^{III} + 2 NEt$_3$	$[NaL^2Fe_2Cl(HCOO)_3]^+$	864.11	864.34	2 %

With only one eq of Fe^{III}, peaks attributable to mononuclear complexes and protonated ligand appear in the spectrum, which is not the case when two eq of Fe^{III} are added. This is a good indication for the formation of at least some dinuclear complexes with deficient Fe^{III}, as well as for full complexation of **HL^2** with two eq of Fe^{III}. If exclusively mononuclear complexes would be formed with one eq of Fe^{III}, no free ligand should be observed in the mass spectrum. It is as yet unknown if addition of triethylamine as base supports the formation of the complexes or only helps to make them visible in the mass spectra. Probably the latter case is more appropriate, as the ligand itself can already act as base in an intramolecular acid-base reaction.

In contrast, **H$_3$L^3** with its amido groups can be deprotonated up to three times, resulting in less positively charged diferric complexes. And indeed, ESI mass spectra of **H$_3$L^3** with two eq of Fe^{III} show dinuclear species. With additional formic acid, only mononuclear species can be seen. This is also the case when only one eq of Fe^{III} is added, regardless of the presence of additional acid or base. The obtained results (summarized in Table 3.9) indicate that the ligand **H$_3$L^3** preferably forms mononuclear complexes, when only one eq of Fe^{III} is added. The complexation seems to be incomplete, as there is some free ligand observable in the mass spectra with additional acid. Still, this observation might only be a consequence of the applied conditions, as addition of acid can shift the complexation equilibrium towards the reactants. Upon addition of a second eq of Fe^{III}, dinuclear complexes are formed, but some mononuclear complexes are still present. Unfortunately, the detection of these two classes of compounds requires different conditions (with and without formic acid, which protonates the amide functions). They never appear together in one spectrum. Therefore, it is impossible to directly compare their intensities. As in the case with only one eq of Fe^{III}, the addition of acid during the measurement might not only influence the visibility of different species in the spectra, but also the complexation equilibrium, leading to formation of mononuclear complexes instead of dinuclear. Other techniques are needed to clarify, if full complexation of ligand **H$_3$L^3** can be achieved *in situ*.

Table 3.9: Results of ESI MS experiments with ligand **H$_3$L^3** in MeOH.

conditions	species	calc. m/z	exp. m/z	peak height
L^3 + 1 Fe^{III}	[HL^{3}Fe]$^+$	782.34	782.52	100 %
“	[H$_2$L^{3}FeCl]$^+$	818.31	818.52	47 %
L^3 + 1 Fe^{III} w. acid	[H$_4$L^3]$^+$	729.42	729.64	100 %
“	[NaH$_3$L^3]$^+$	751.41	751.62	45 %
“	[NaH$_2$L^{3}Fe(HCOO)$_2$]$^+$	896.33	896.60	25 %
“	[H$_2$L^{3}FeCl]$^+$	818.31	818.57	7 %
L^3 + 1 Fe^{III} + 1 NEt$_3$	[HL^{3}Fe]$^+$	782.34	782.50	88 %
“	[H$_2$L^{3}FeCl]$^+$	818.31	818.54	7 %
L^3 + 1 Fe^{III} + 1 NEt$_3$ w. acid	[H$_4$L^3]$^+$	729.42	729.65	100 %
“	[NaH$_2$L^{3}Fe(HCOO)$_2$]$^+$	896.33	896.60	40 %
“	[NaH$_3$L^3]$^+$	751.41	751.64	38 %
“	[H$_2$L^{3}FeCl]$^+$	818.31	818.56	10 %
L^2 + 2 Fe^{III}	[L^{3}Fe$_2$Cl]$^{2+}$	436.12	436.24	100 %
“	[HL^{3}Fe$_2$Cl$_2$]$^{2+}$	454.10	454.24	5 %
L^2 + 2 Fe^{III} w. acid	[H$_2$L^{3}FeCl]$^+$	818.31	818.55	100 %
“	[NaH$_2$L^{3}Fe(HCOO)$_2$]$^+$	896.33	896.59	78 %
L^3 + 2 Fe^{III} + 2 NEt$_3$	[L^{3}Fe$_2$Cl]$^{2+}$	436.12	436.24	100 %
“	[HL^{3}Fe$_2$Cl$_2$]$^{2+}$	454.10	454.23	31 %
L^3 + 2 Fe^{III} + 2 NEt$_3$ w. acid	[NaH$_2$L^{3}Fe(HCOO)$_2$]$^+$	896.33	896.60	100 %
“	[H$_2$L^{3}FeCl]$^+$	818.31	818.56	75 %

More information was obtained by UV/vis titrations, where spectra of methanolic solutions with different ligand to metal ratios were recorded (spectra shown in Figure 3.25 and 3.26): Addition of Fe^{III} to **HL**^{2} results in the formation of a broad band in the visible region, which can be interpreted as phenolate-to-iron CT transition (see Figure 3.25 b). With substoichometric amounts of Fe^{III}, the maximum wavelength of this absorption is at λ = 558 nm and suddenly shifts to around λ = 650 nm when one or more than one equivalents are added. Yet, in the two spectra with 0.8 and 1 eq of Fe^{III}, (5th thin line and 1st bold line, respectively), small shoulders are visible, which indicate that a mixture of products is present in these cases. Therefore, a Gaussian analysis was performed on the absorptions, assuming two overlapping bands for 0.2 to 1.8 eq of Fe^{III}. The resulting spectra are shown in Appendix 6. They clearly show that, already starting from 0.2 eq of Fe^{III}, a small amount of dinuclear complex is present. The ration between mono- and dinuclear complex changes upon addition of more Fe^{III} towards a higher amount of the dinuclear one. With 2 eq of Fe^{III}, only one band with λ = 655 nm (1532 cm^{-1}M^{-1}) is visible, which belongs to the dinuclear complex **K^2**. In the UV region between 300 and 400 nm, two intense bands are observable, which can also be attributed to Fe-oxo type transitions (see Figure 3.25 a). The absorption at 300 nm is consecutively rising in intensity, when up to two equivalents of Fe^{III} are added, and hardly changes with further addition. In contrast, the band at 370 nm is getting even stronger with excess of Fe^{III} but also slightly shifts to lower wavelengths. No shoulder is visible at this band in the spectrum with two eq of Fe^{III} so that most probably all Fe^{III} is bound in the ligand under these conditions.

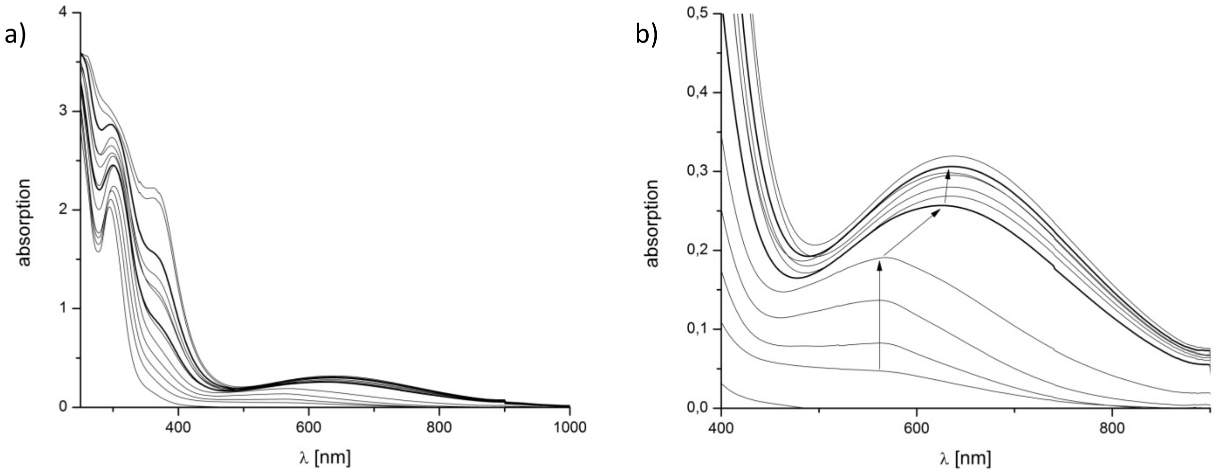

Figure 3.25: UV/vis titration of **HL**^{2} (0.2 mM) with [FeCl$_4$](NEt$_4$) in MeOH (in steps of 0.2 eq; bold lines indicate 1 and 2 eq of Fe^{III}, respectively); a) full spectrum, b) phenolate-to-iron CT band.

In summary, a mixture of mononuclear and dinuclear complexes is formed with substoichometric amounts of Fe^{III}. More dinuclear complexes are formed upon addition of up to two equivalents of Fe^{III} to reach full complexation of the ligand **HL^2**. These findings nicely support the results from the ESI MS experiments described above.

When **H$_3$L^3** is reacted with Fe^{III}, similar spectra to those with **HL^2** are obtained. The phenolate to ron CT band (Figure 3.26 b) shifts progressively from 533 to 629 nm with substoichometric amounts of Fe^{III} and stays at this value when more than one eq of Fe^{III} is added. Nevertheless, a shoulder on the lower wavelengths side of the band remains. In contrast to **HL^2**, the intensity increases almost linearly up to addition of 1.2 eq of Fe^{III}. These findings suggest that at small Fe^{III} concentrations a mixture of mono- and dinuclear complexes is formed (see Appendix 6 for Gaussian analysis of the bands), which is in contrast to the ESI MS results. Moreover, the formation of mononuclear complexes seems to be incomplete with an equimolar amount of Fe^{III}, as the intensity rises significantly from one to 1.2 eq of Fe^{III}. With two eq of Fe^{III}, complexation seems to be incomplete, due to a significant amount of mononuclear species in the Gaussian fitted spectra. This is in agreement with the ESI MS results.

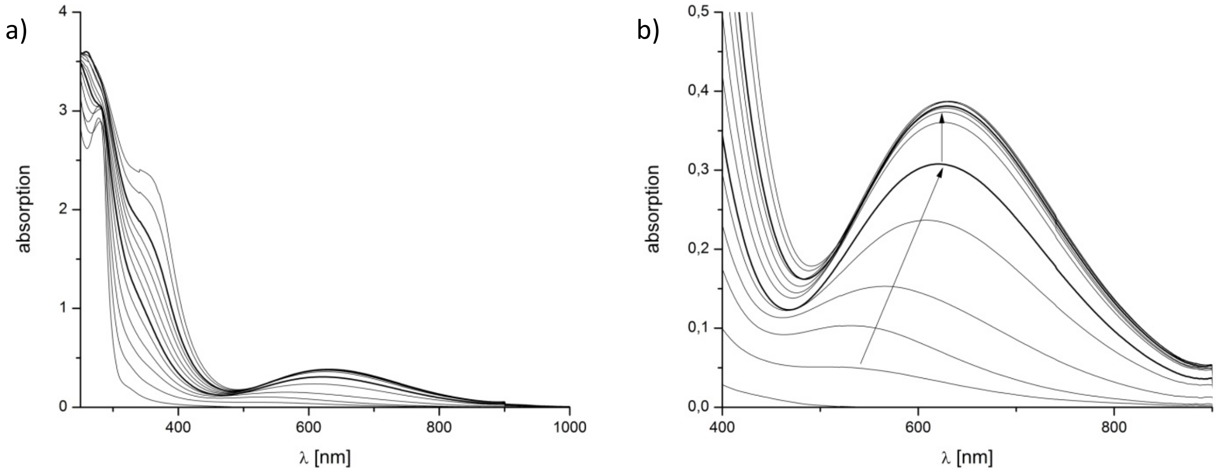

Figure 3.26: UV/vis titration of **H$_3$L^3** (0.2 mM) with [FeCl$_4$](NEt$_4$) in MeOH (in steps of 0.2 eq; bold lines indicate 1 and 2 eq of Fe^{III}, respectively); a) full spectrum, b) phenolate-to-iron CT band.

With respect to the addition of base to the *in situ* prepared complex solutions, **K^2** and **K^3** show a slightly different behavior. Addition of two equivalents of triethylamine to **K^2** causes a hypsochromic shift of about 40 nm and simultaneously a loss in intensity (Figure 3.27 a). Assuming that at first MeOH or methanolate was coordinated, a ligand exchange reaction seems plausible. By addition of base, hydroxo anions are formed due to water impurities and they can easily hydrolyze the complex. The result is the observed hypsochromic shift of the CT band, which cannot be interpreted in detail. The spectra of **K**^{3} on the other hand hardly change with up to two equivalents of base, which can be explained by the additional acidic amido functions of the ligand, which are deprotonated by two equivalents of triethylamine. When more base (four equivalents) is added, the same behavior as with **K**^{2} can be observed (Figure 3.27 b).

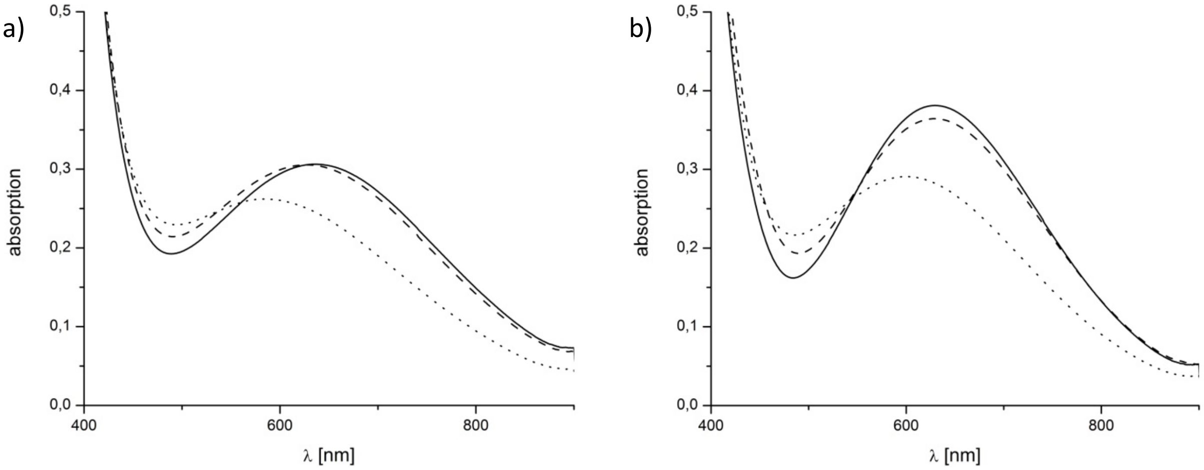

Figure 3.27: Changes of phenolate-to-iron CT band of a) **K**^{2} upon addition of one (dashed line) and two eq. (dotted line) of NEt$_3$ b) and **K**^{3} upon addition of two (dashed line) and four (dotted line) eq. of NEt$_3$ in MeOH.

In order to analyze the behavior of **K**^{2} and **K**^{3} in partly aqueous solution (MeOH/buffer 1:1), UV/vis spectra were recorded at pH 6 and pH 10 and compared to each other as well as to the original spectra in pure MeOH (Figure 3.28). And indeed, some differences can be seen with both complexes: The phenolate to iron CT band shifts to lower wavelengths, which again might be explained by ligand exchange (methanol(ate) vs. aqua/hydroxo). Another observation is the loss of the shoulder around 400 nm. Probably some free iron was still present and is now fully coordinated when buffer is added. Small differences are present between the pH 6 and pH 10 spectra, leading to the conclusion that a pH dependent equilibrium is present.

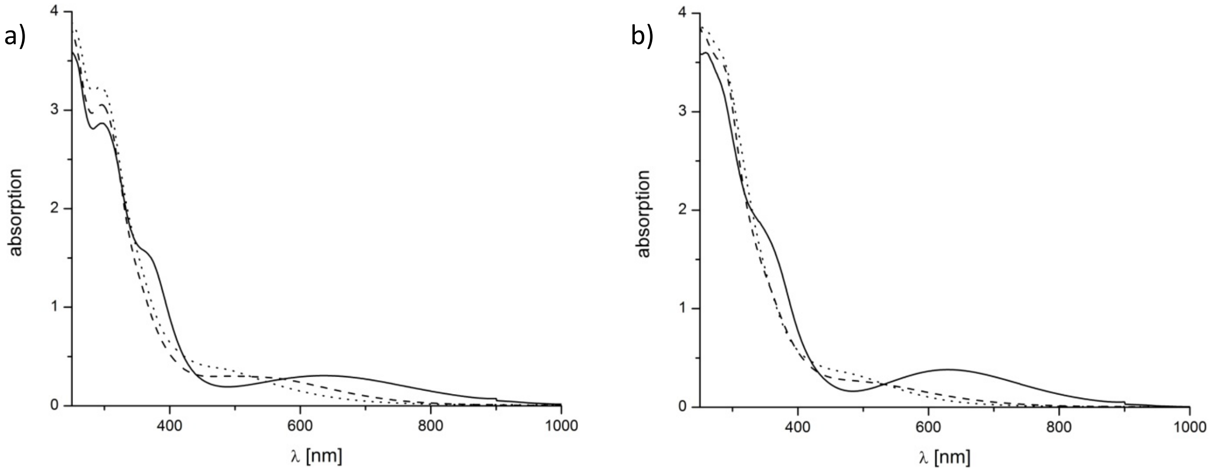

Figure 3.28: Comparison of UV/vis spectra of a) **K^2** and b) **K^3** in MeOH (solid line), MeOH/buffer pH 6 (dashed line) and MeOH/buffer pH 10 (dotted line); all 0.2 mM.

Encouraged by these results, a spectrophotometric pH-titration of the two complexes was performed to analyze their pH dependent equilibria. The spectra (Figure 3.29) were fitted with the program Specfit,[148] at first by assuming three species in the pH range between 4.6 and 11 and thus two protonation equilibria with single proton transfers, equivalent to the published schemes for similar systems (see Scheme 3.16). The additional μ-hydroxo group is based on X-ray structures of analogous complexes,[92] but there is no experimental evidence for that in our case. The resulting species distributions for a three-species-model are shown in Figure 3.30 (a and b) and Table 3.10 gives the associated pK$_a$ values.

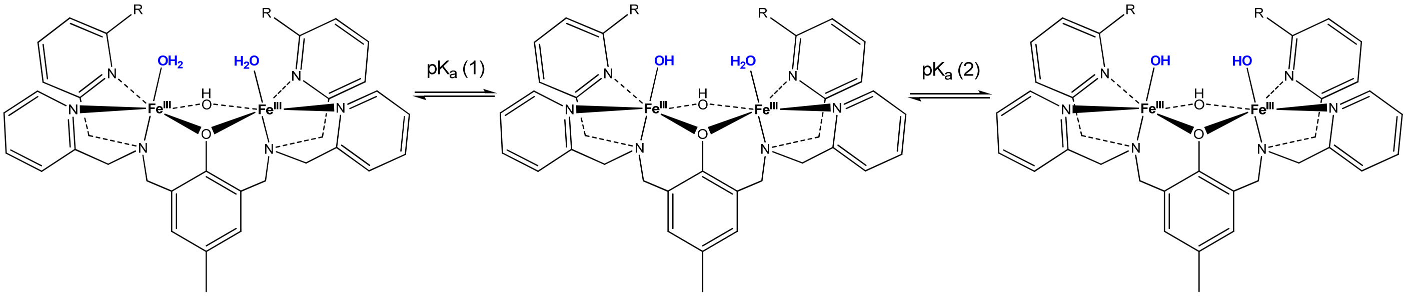

Scheme 3.16: Protonation equilibrium of **K^2** and **K^3** in a three-species-model.

Regarding the additional acid and base functionalities at **HL^2** and **H$_3$L^3**, further protonation equilibria become possible. At low pH, the pyridine-bound amines of **HL^2** are protonated (pK_a = 6.8 for 2-aminopyridine)[144] and should not be able to form hydrogen bonds to the Fe^{III} bound aqua ligands. The first deprotonation step leads to the possibility of an extended hydrogen bonding network, including the aqua/hydroxo ligands as well as the protonated amines. Their deprotonation will be the second step, probably with a simultaneous loss of two protons per complex unit. This fact was later included in the fitting procedure and resulted in only small changes with respect to the pK_a values. Nevertheless, the pK_a values for a four-species–model of **K^2** shown in Table 3.10 already represent the corrected fit. At last, another aqua ligand is deprotonated leading to a di-hydroxo species, which can still interact with the second coordination sphere amines. This equilibrium (Scheme 3.17) is more plausible for **K^2** than the simple three-species-model presented above.

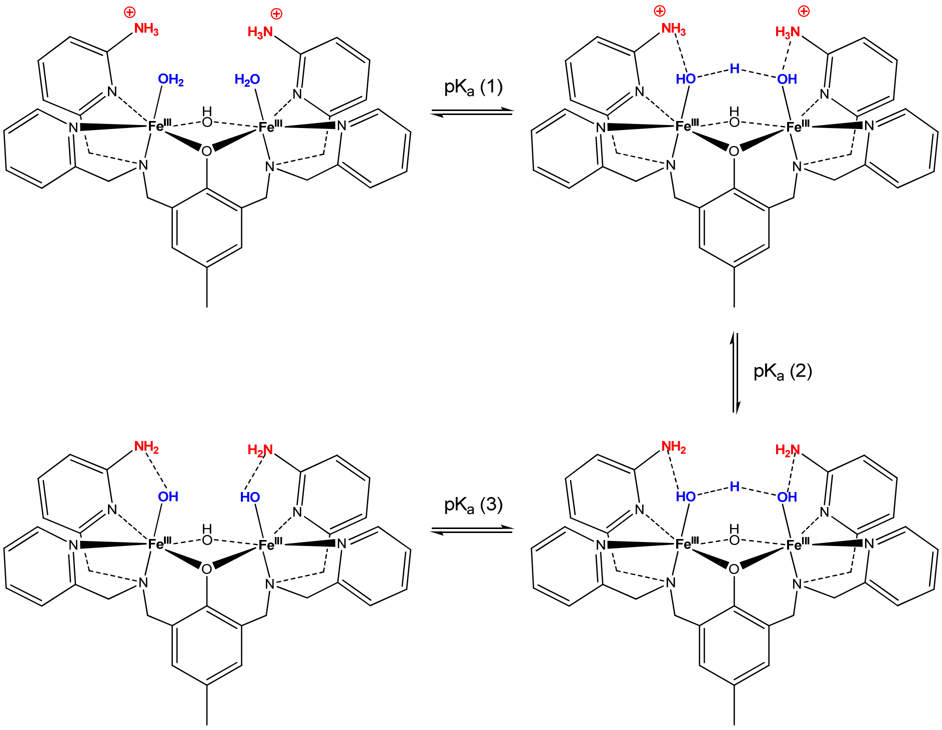

Scheme 3.17: Protonation equilibria of **K^2** in a four-species-model, incorporating interactions with the second coordination sphere amines.

In the case of **K^3**, the amides should coordinate to the ferric ions. This would result in only one free coordination site at each Fe^{III}. A μ-hydroxo bridge seems unlikely under these conditions because of steric strain arising from the tertiary butyl groups at the amides (see Appendix 7 for calculated structures). The first deprotonation step with pK_a (1) (Scheme 3.18) should occur at low pH due to the coordination mentioned above and not contribute to the observed spectral changes (for comparison: pK_a (acetamide in H_2O) = 0.63).[149] Therefore, a three-species model with pK_a (2) = 5.19 and pK_a (3) = 8.69 seems more likely for **K**^{3}.

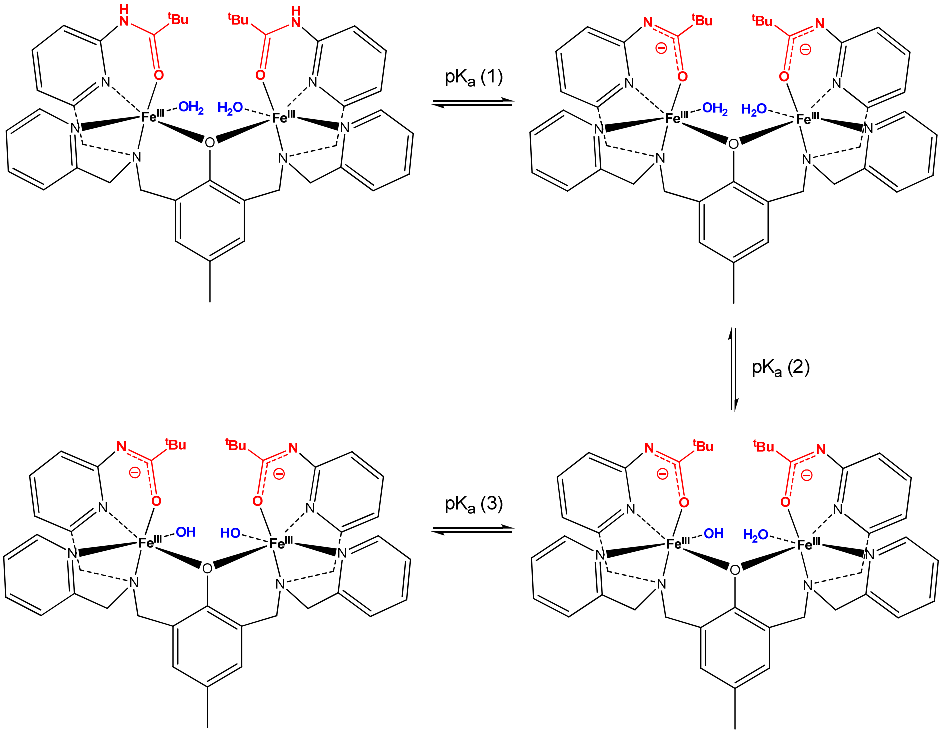

Scheme 3.18: Protonation equilibrium of **K**^{3} in a four-species-model with coordinated amide functions.

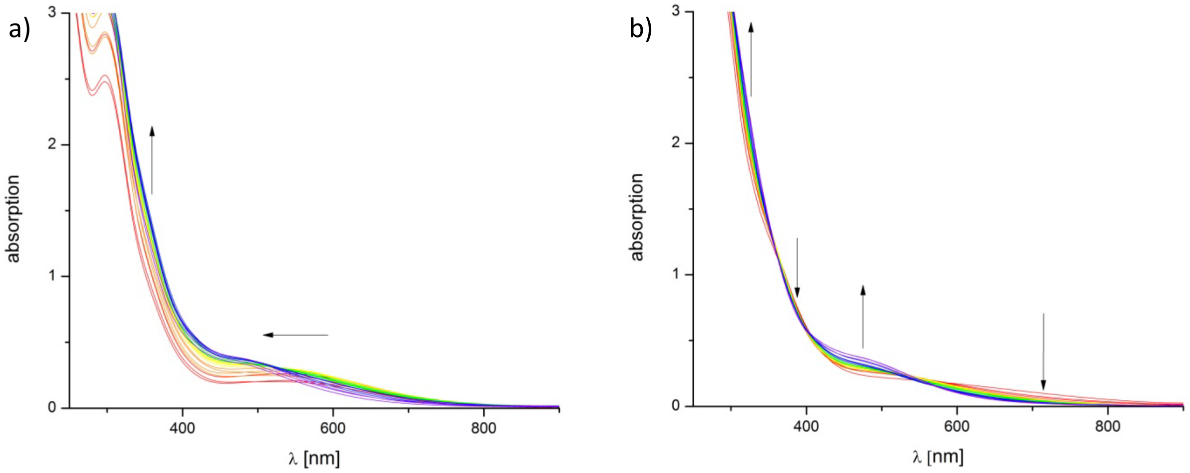

Figure 3.29: Spectrophotometric titration spectra of a) **K**^{2} and b) **K**^{3} in MeOH/buffer between pH 4.6 and 11 (arrows are indicating the changes from low to high pH) at 0.2 mM complex concentration.

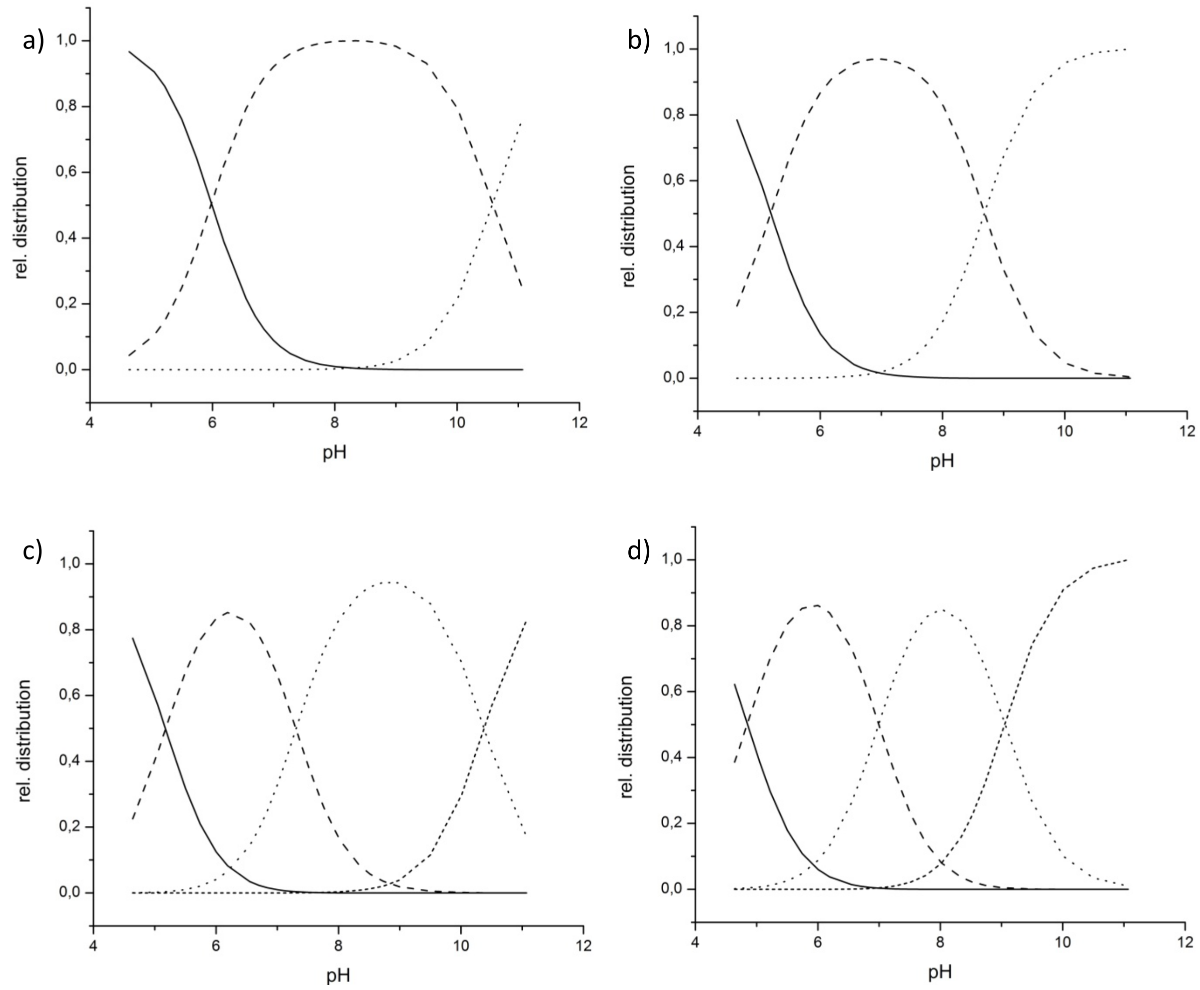

Figure 3.30: Species distribution for a three- and four-species-model, respectively for **K^2** (a, c) and **K^3** (b, d).

Table 3.10: Fitted pK$_a$ values from spectrophotometric titrations of **K^2** and **K^3**.

K^2		**K^3**	
3 species	*4 species*	*3 species*	*4 species*
5.98 ± 0.12	5.18 ± 0.19	5.19 ± 0.17	4.85 ± 0.22
	7.31 ± 0.25		6.99 ± 0.28
10.57 ± 0.57	10.38 ± 0.35	8.69 ± 0.14	9.05 ± 0.19

As in the case of **K^1**, the magnetic properties of **K^2** and **K^3** were examined by Evans-NMR,. Methanolic solutions of ligand and tetrachloroferrate were mixed in 1:1 or 1:2 ratios. The results are summarized in Table 3.11. In contrast to **K^1**, the 1:1 mixtures with both ligands, **HL^2** and **H$_3$L^3** have significantly larger μ_{eff} values than the 1:2 samples. This is consistent with uncoupled monomeric high spin Fe^{III} complexes, although the experimental values are higher than the expected spin-only value of 5.92. This is a usual observation, as contributions of spin-orbit coupling lead to higher values. Nevertheless, addition of base leads to a decrease of μ_{eff} which can be explained by formation of at least a small fraction of dinuclear complexes. With two eq of Fe^{III}, μ_{eff} takes values that correspond to dinuclear systems with relatively strong coupling. The expected spin state of S = 2 is the closest value corresponding to the experiment. Based on known complexes of this type, -J values between 5 and 15 cm^{-1} should be expected,[112, 113] originating from moderate coupling through the phenoxide bridge. This value would however lead to a larger μ_{eff}. Spin states of S = 3 or S = 4 can be populated at room temperature in this case. Thus, additional bridging ligands, like μ-oxo, might be present to increase the coupling. Assuming that no unbound Fe^{III} is present in the sample, coupling constants of larger than 30 cm^{-1} can be expected for both complexes.

Table 3.11: Results of Evans-NMR experiments with **HL^2** and **H$_3$L^3**.

sample	exp. μ_{eff} [B.M.] per complex unit	expected spin state S	calc. μ_{eff} [B.M.] for expected spin state
HL^2 + 1 Fe^{III}	6.77	5/2	5.92
HL^2 + 1 Fe^{III} + 1 NEt$_3$	6.16	5/2	5.92
HL^2 + 2 Fe^{III}	4.73	2	4.90
HL^2 + 2 Fe^{III} + 2 NEt$_3$	4.24	2	4.90
H$_3$L^3 + 1 Fe^{III}	6.52	5/2	5.92
H$_3$L^3 + 1 Fe^{III} + 1 NEt$_3$	6.03	5/2	5.92
H$_3$L^3 + 2 Fe^{III}	4.63	2	4.90
H$_3$L^3 + 2 Fe^{III} + 2 NEt$_3$	4.24	2	4.90

EPR spectra of **K^2** and **K^3** were recorded in MeCN and MeOH at 1.7 K. Only the high spin ferric ion g=4.3 signal can be observed in all cases, with a rather moderate intensity. This leads to the conclusion that mainly an EPR-silent species is present, i.e. a rather strongly coupled diferric complex. Again, coupling through the phenoxo bridge should lead to moderate coupling constants, what is in contradiction to the observed EPR silence of the samples. Nevertheless, these results support the data obtained by the Evans-NMR measurements.

3.3.2.2. Interactions of K^2 and K^3 with Phosphate and Phosphoesters

UV/vis and EPR experiments were performed to investigate the interactions of **K^2** and **K^3** with phosphate and phosphoesters as substrate mimics in MeCN/buffer mixtures. As in the case of **K^1**, 1-NP was used as a phosphomonoester and DPP as a diester in the UV/vis measurements, whereas the monoester pNPP was used in the EPR experiments (for substrate mimic structures see Scheme 3.9 in Chapter 3.2.2.4).

The UV/vis spectra of the phenolate to iron CT transition region around 500 nm are shown in Figure 3.31. In the case of phosphate as co-ligand (Figure 3.31 a and b), only small changes can be observed. λ_{max} is slightly shifted to higher wavelengths and the intensity of the transition is reduced. When 1-NP is added to **K^2** or **K^3**, there are also some changes observable (Figure 3.31 c and d): The phenolate to iron band of **K^2** is significantly shifted to higher wavelengths and broadened in comparison to the **K^2** spectrum. In the case of **K^3** with 1-NP, it shifts to lower wavelengths becoming a shoulder. The most interesting observation can be made in spectrum e, which is **K^2** in combination with the diester DPP. As indicated in the figure, a second shoulder at around 580 nm is developing in addition to the original one. This suggests a monodentate coordination mode for DPP, which causes two distinct ferric ions in the complex. As no such observation is made in the case of **K^3** with DPP (Figure 3.31 f), one might conclude that, due to hydrogen bonding interactions with the additional amines, **K^2** stabilizes the monodentate binding mode of the diester, whereas **K^3** does not.

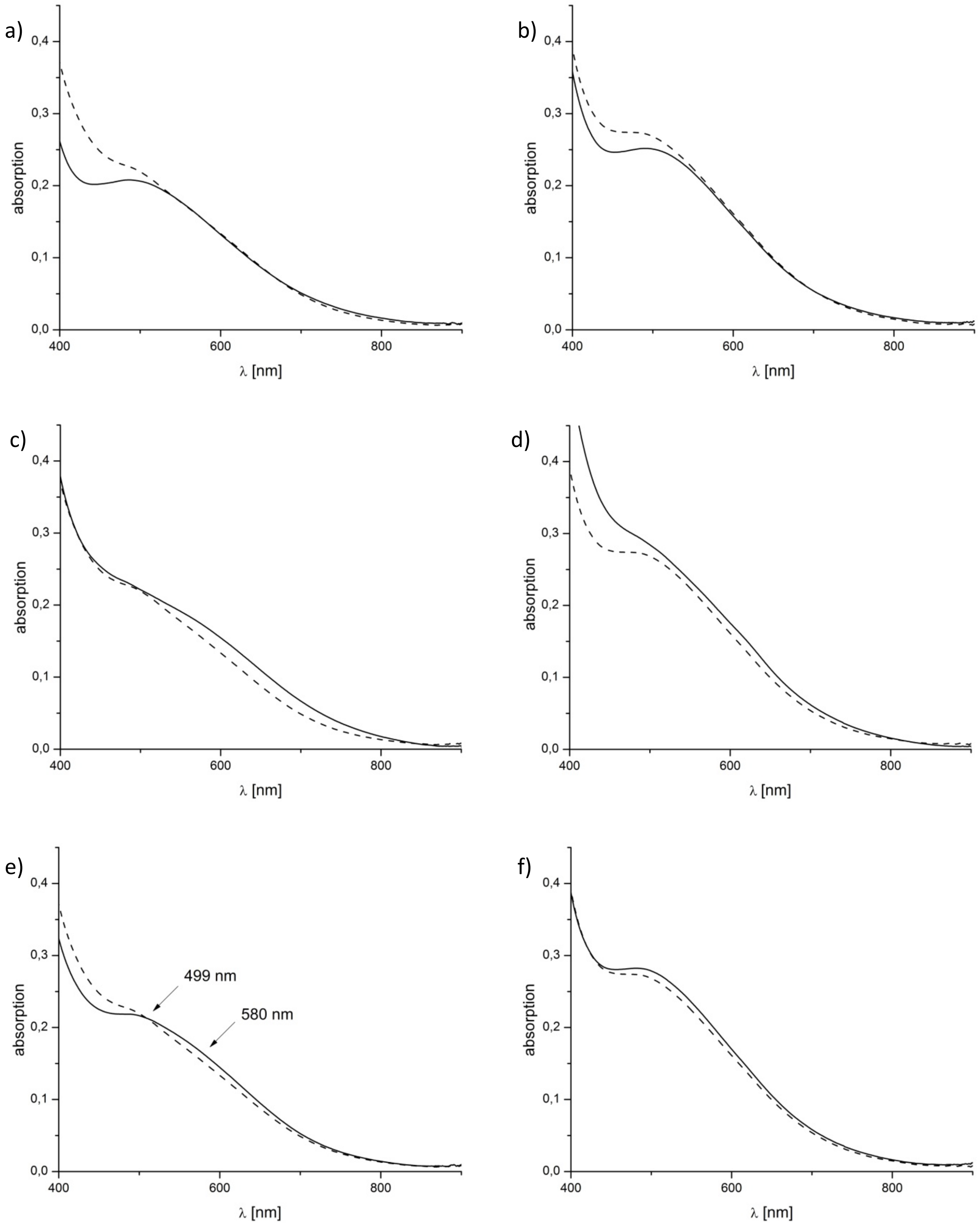

Figure 3.31: UV/vis spectra of a) **K**^{2} and b) **K**^{3} with phosphate, c) **K**^{2} and d) **K**^{3} with 1-NP and e) **K**^{2} and f) **K**^{3} with DPP in MeCN/buffer pH 6.5 at 0.15 mM complex and substrate concentration, i.e. 1:1 ratio (solid lines). The “free” complex spectra are shown as dashed lines.

EPR experiments on **K**^{2} and **K**^{3} with pNPP in MeCN/buffer pH 5 were performed at 1.6 to 20 K, showing rather complicated signals around $g_{eff} = 4.3$ and $g_{eff} = 2$. At first, simulations with MoSophe[137] were attempted by assuming an antiferromagnetically coupled diferric system. The metal-metal distance was taken from geometry-optimized structures and the J value was roughly estimated from temperature dependent measurements to be between 0 and -1.1 cm^{-1} (maximum of signal intensity is at temperatures lower than 1.6 K; see Figure 3.32 for temperature dependent spectra).

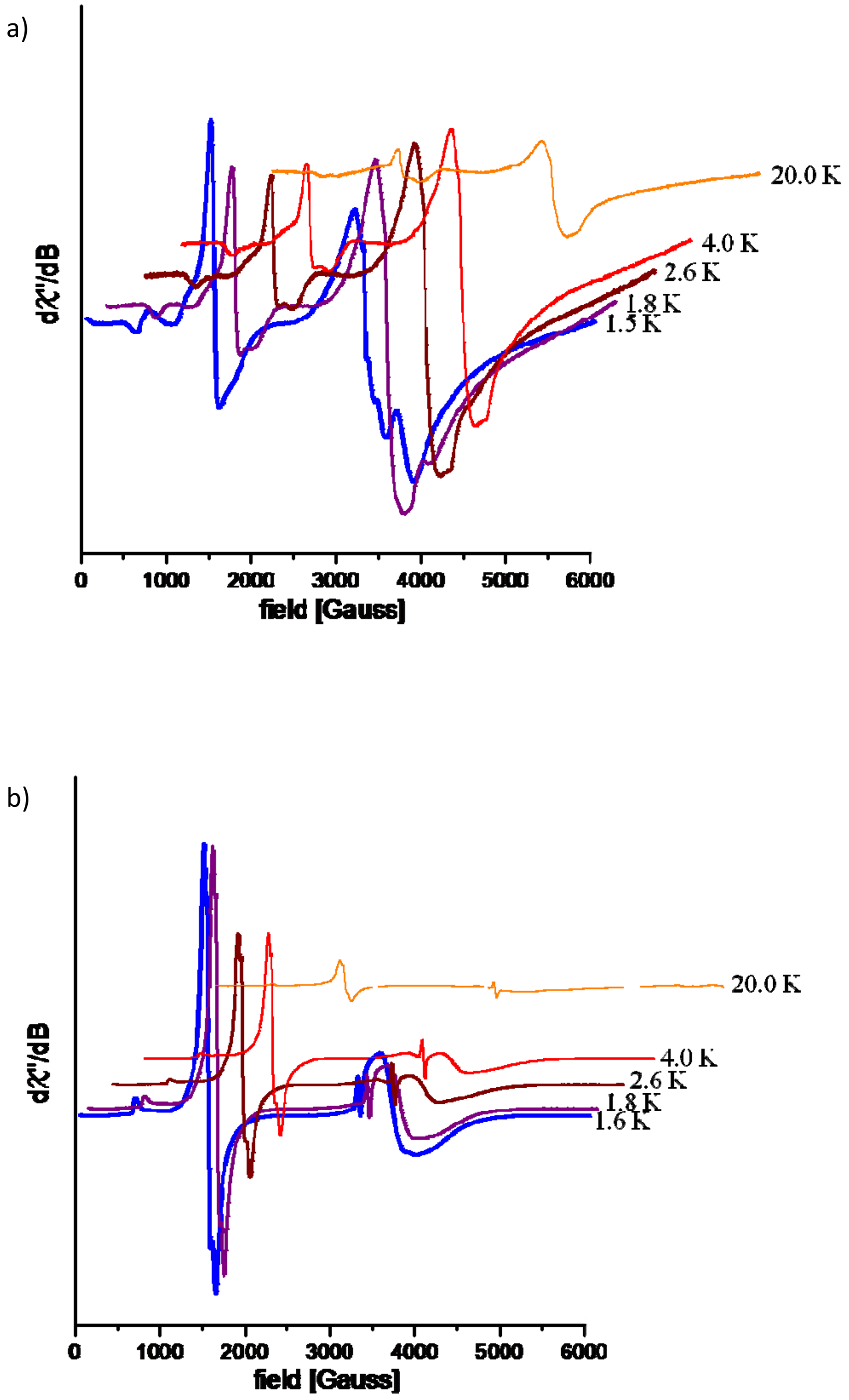

Figure 3.32: VT X-band EPR spectra of a) **K**^{2}pNPP (9.37863 GHz) and b) **K**^{3}pNPP (9.379757 GHz).

No acceptable agreement between the simulated and experimental spectra was found with this model. Only the proposal of a coupled heterovalent Fe^{III}Fe^{II} species with a resulting S = ½ spin state lead to better results in both cases. The initial parameter values for the g and D tensors were estimated by DFT calculations (see Chapter 4.5 for details). Based on equations 3.6 and 3.7, the individual values for the ferric and ferrous ion, respectively, were calculated from the total values g_S and D_S. Table 3.12 summarizes the calculated and simulated parameters for **K^2**pNPP and **K^3**pNPP. The resulting spectra and their preliminary simulations are shown in Figure 3.33.

$$g_S = c_1 g_1 + c_2 g_2{}^{[135]} \qquad \text{(eq. 3.6)}$$

$$D_S = d_1 D_1 + d_2 D_2 + d_{12} D_{12}{}^{[135]} \qquad \text{(eq. 3.7)}$$

The g tensor coefficients are c_1 = 7/3 and c_2 = -4/3 (for S = ½)[135]and the zero-field splitting coefficients are d_1 = 5/18 and d_2 = 1/6 (for S = 9/2)[150] in an S = 2 / S = 5/2 system. The dipole-dipole contributions d_{12} and D_{12} were calculated using the EPR calculator[137] with d(Fe-Fe) = 4.01 Å for **K^2**pNPP and d(Fe-Fe) = 3.90 Å for **K^3**pNPP. For additional help, the zero-field splitting for the ferric ions was approximately calculated by DFT by exchanging Fe^{II} with Zn^{II} in the geometry-optimized structure. This value was used for D_2 in eq. 3.7.

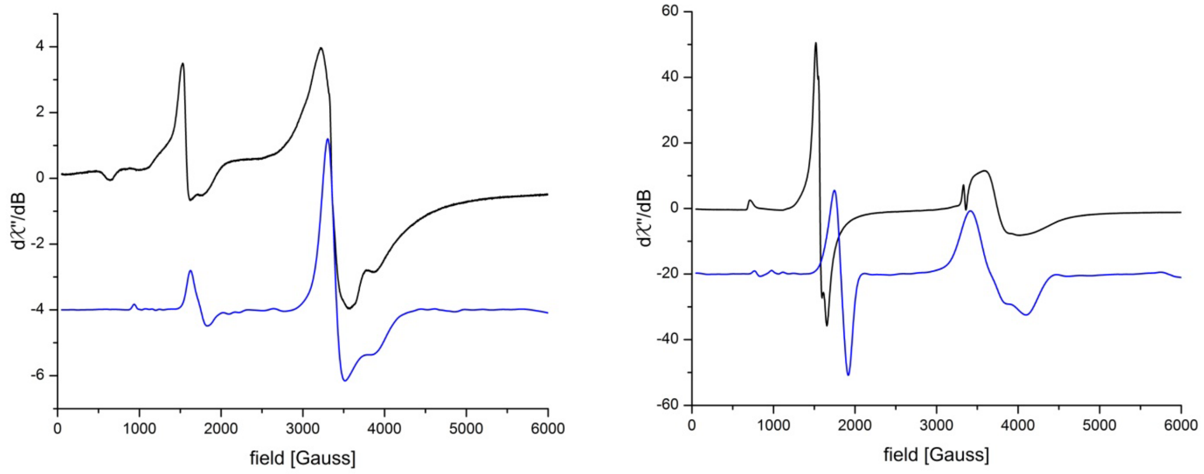

Figure 3.33: Experimental (black) and preliminary simulated (blue) X-band EPR spectra of a) **K^2** with pNPP and b) **K^3** with pNPP in MeCN/buffer pH 5 at 0.5 mM and 10 mM complex and substrate concentration, respectively; spectra were measured at a) 1.5 K and 9.37863 GHz and b) 1.6 K and 9.379757 GHz.

Table 3.12: Calculated and simulated parameters for **K^2** and **K^3** with pNPP (MoSophe).[a]

parameter	**K^2** + pNPP [b]		**K^3** + pNPP [c]	
	calc.	sim.	calc.	sim.
g_{iso} Fe^{III}	2.07	2.09	2.07	2.08
g_{iso} Fe^{II}	2.24	2.15	2.10	2.14
D_1 Fe^{III} [cm^{-1}]	-1.091	0.0012	1.161	0.021
E/D Fe^{III}	0.095	0.000	0.118	0.002
D_2 Fe^{II} [cm^{-1}]	-2.327	0.82	1.262	1.002
E/D Fe^{II} [d]	-	0.045	-	0.180
d (Fe-Fe) [Å]	4.012	3.900	3.904	3.900
J_{iso} [cm^{-1}][d]	-	-2.06	-	-1.84

[a] see Chapter 4.5 for details on calculation procedures; [b] D tensor orientation α/β/γ [°] = 20/-60/0 for Fe^{III} and -20/60/0 for Fe^{II}; [c] D tensor orientation α/β/γ [°] = 10/-50/0 for Fe^{III} and -10/50/0 for Fe^{II}; [d] no calculated values available.

The presented simulations (Figure 3.33 and Table 3.12) are not satisfying, as the signals of the simulation do not fully match to the experimental spectrum in both cases. Nevertheless, they support the interpretation of the the observed spectra as antiferromagnetically coupled $S = 5/2 + S = 2$ systems. In these kind of spin systems (see Appendix 5 b for the schematic energy diagram), the ground state is $S = 1/2$ and is populated at low temperatures. With increasing temperature, the $S = 3/2$ spin state will be populated as well, where the two Kramer doublets ± 1/2 and ± 3/2 lead to a second $S = 1/2$ like signal and a $\Delta M_s = \pm 3$ transition around $g_{eff} = 12$. A further increase in temperature populates the $S = 5/2$ spin state, giving rise to a typical $S = 5/2$ spectrum with $g_{eff} = 4.3$ (middle Kramer doublet) and additional resonances around $g_{eff} = 8.6$ and 5.2. All these signals are observable in the experimental and simulated spectra, although they are slightly shifted in the latter. This is probably due to non-accurate values for the zero-field splitting D and E/D. However, with MoSophe it has been unfeasible to simulate the spectra to a perfect state. The next approach will be to use an automatic optimizer in combination with simultaneous simulation of the VT spectra.

Since a ferric salt is used as a precursor under aerobic conditions and the results from the Evans-NMR experiments suggest that **K^2** and **K^3** are diferric complexes, it seems that the addition of pNPP alters the redox potential and the complexes are reduced *in situ*. The question arises about the nature of the reductant. In the low temperature spectra shown in Figure 3.32 and 3.33, a sharp signal is visible around $g_{eff} = 2.00$, which suggests the presence of a radical species. This might be the oxidized reaction partner. EPR spectra of the same sample were recorded in a more narrow field range at 5 K as well as at room temperature in order to have a closer look at this radical signal. At room temperature, a fine structure of the signal can be observed consisting of 24 equidistant lines (see Appendix 8). As pNPP is used in a large excess and pre-dissolved in buffer (pH 5), a substantial amount of the hydrolysis product, i.e *para*-nitrophenolate (p-NP), can be expected. It is known that phenolates with *para* substituents form relatively stable radicals, especially in the case of a nitro group which is electron withdrawing.[152] A simulation using the published coupling constants of the *para*-nitrophenoxy radical[151] did not match to the experimental spectrum. Another possible interpretation is that at room temperature, the *para*-nitrophenoxy radical reacts with the complex, **K^2** or **K^3**, and withdraws an electron from the ligand, leading to a ligand-based radical. The simulation of this signal, using couplings to the phenolate protons, the methyl protons and the protons at the methylene bridges between phenolate and the tertiary amines, as well as couplings to the two tertiary amine nitrogen atoms, is shown in Appendix 8. Interestingly, a direct reaction of **K^2** or **K^3** with p-NP did not lead to the previously observed signals, i.e. neither the sharp radical nor the $S = ½$ like signal at $g_{eff} < 2$ could be seen. The exact analysis of the obtained spectra is still under investigation.

The redox potential of p-NP is reported to be + 0.668 V (in MeCN) and around + 1.0 V (in H_2O) vs. SCE.[153] No redox potential measured in MeCN/buffer mixtures was found in literature, but we expect it to be in between. The redox potentials of pure **K^2** and **K^3** in MeCN or MeCN/buffer mixtures with or without pNPP could not be investigated by cyclic voltammetry, as the relatively low solubility of the ligands prevented the *in situ* prepararation of the complexes at high concentrations. Therefore, attempts were made to isolate complexes, which should be more soluble in the media mentioned above.

3.3.2.3. *Isolation and Characterization of Diferric Complexes of HL^2 and H$_3$L^3*

Solid diferric complexes of **HL^2** and **H$_3$L^3** were obtained by stirring the ligand with ferric perchlorate with and without sodium L-tartrate as an additional bridging ligand in hot methanol. Diffusion of diethylether into the complex solutions precipitated the complexes **25** to **28** (Scheme 3.19).

The use of the chiral anion tartrate as coligand is based on the idea that two possible isomers can be formed with ligands **HL^2** and **H$_3$L^3**, where the residues at the pyridines can be on one side of the complex (cisoid) or on opposite sides (transoid). In the latter case, a C_2 symmetric complex would result, whereas the cisoid structure would be asymmetric (see Scheme 3.20). The hope was to drive the complexation reaction to one or the other structure and, by this, facilitate crystal growth.

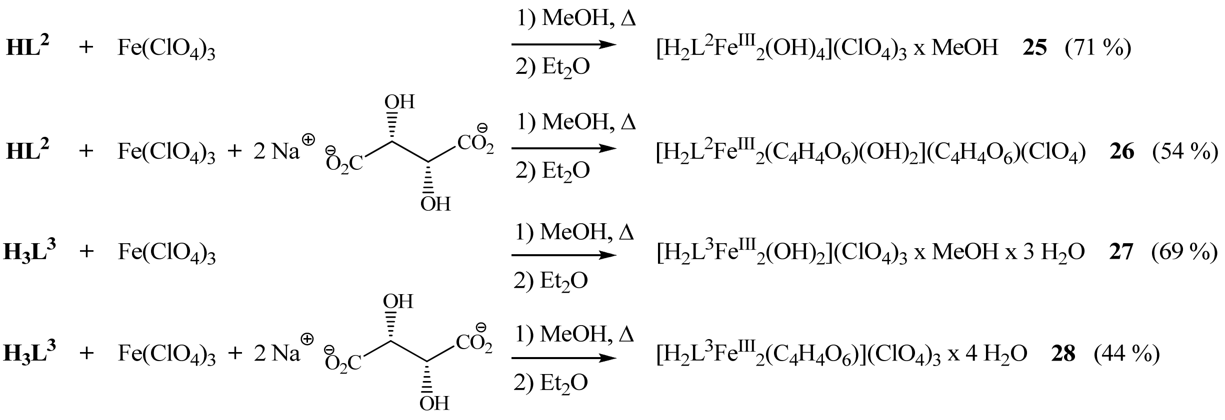

Scheme 3.19: Synthesis of diferric complexes of **HL^2** and **H$_3$L^3**.

Unfortunately, no X-ray quality crystals were obtained, so we focus on the results from analytic and spectroscopic studies as well as DFT calculations to describe the properties of the complexes. For clarity reasons, the complexes **25** and **27** without additional tartrate are called **K^2** and **K^3**, whereas **26** and **28** are called **K^2** tartrate and **K^3** tartrate. It should be noted that the complexes **K^2** and **K^3** do not necessarily have the same structure and composition as the *in situ* prepared complexes **K^2** and **K^3** described in the previous chapters.

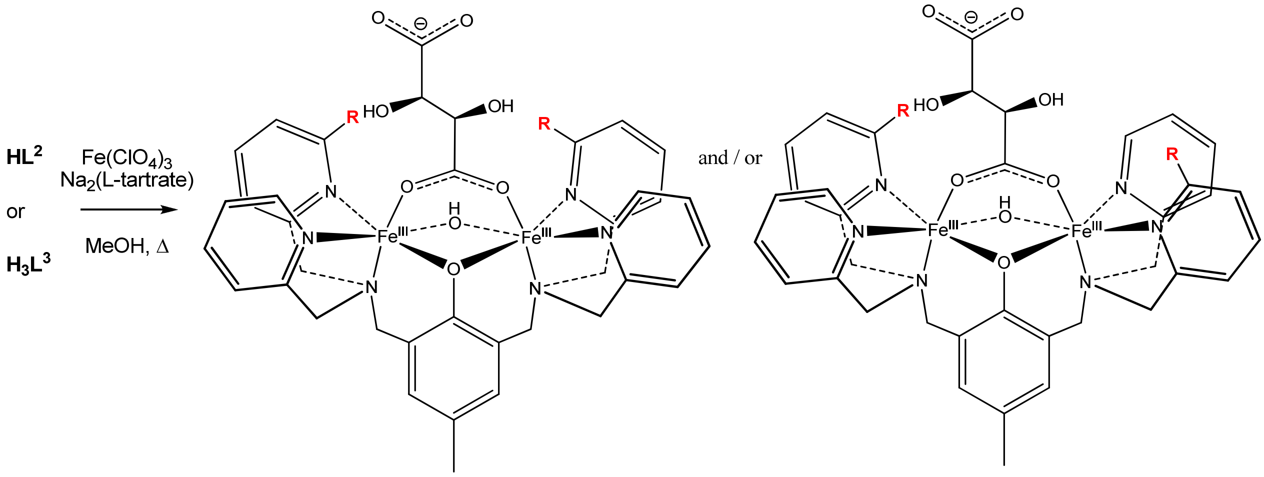

Scheme 3.20: Possible isomers of **K^2** and **K^3** with L-tartrate as coligand.

Elemental analysis fits to the presence of two ferric ions per complex unit in each case. The coordination sphere is assumed to be completed by a μ-hydroxo bridge and two terminal hydroxides in the case of **K^2** (based on structures of similar published complexes, see Chepter 2.3 for examples and references). The amide oxygen of **H$_3$L^3** most probably coordinate to the ferric ions, leaving one free site on each Fe^{III}, which can be occupied by terminal hydroxides as well. **K^2** tartrate contains two tartrate anions according to the elemental analysis. We assume that due to the sterical demand of the coligands, only one tartrate is coordinated. This should be also the case for **K^3** tartrate. Based on these data, different structures were geometry-optimized and their free energies were compared (see Table 3.13 for values and Chapter 4.5 for calculation details; structures are shown in Appendix 7): The tartrate-free complexes **K^2** and **K^3** do not show large energetic differences between the cisoid and transoid conformers. In the case of **K^2**, the cisoid conformer is slightly more favored when the amines are deprotonated (entry 1 in Table 3.13). In contrast, the transoid conformer of **K^3** is a little lower in energy than the cisoid one (entry 3). Yet, the energy differences are so small (1.5 kcal/mol) that the different structures can be seen as energetically equal within the accuracy of the method. For **K^2** with protonated amines, the transoid conformer is lower in energy, having a larger energy difference (almost 7 kcal/mol) than without the protons (entry 2). In the calculated structures (Appendix 7) one can see, that this should be mainly due to opening of the μ-OH bridge in the cisoid conformer.

Things become different when tartrate is coordinated to **K**^{2}. Now, even **K**^{2} with deprotonated amines shows significant energy differences between cisoid and transoid conformer (around 5 kcal/mol; entry 4). Protonation of the amines enables better interactions between tartrate and the ligand. Moreover, a cisoid arrangement, where all pyridines are coordinated would lead to a large steric strain due to the bulky ammonium groups. Therefore, only a structure, where one pyridine is rotated away from the metal ions converged to a minimum. In the transoid conformer, the ammonium group is located on the "backside" of the complex and not on the side where the tartrate is present, reducing the steric strain and enabling the coordination of all pyridines. These differences lead to a huge energy gap of more than 30 kcal/mol (entry 5). In the case of **K**^{3}, coordination of tartrate does not have an impact on favoring one conformer over the other, resulting in only a small energy difference of 1.17 kcal/mol. This can be explained by the missing hydrogen bonding interactions.

Table 3.13: Relative free energies of cisoid and transoid conformers of different **K**^{2}, **K**^{3}, **K**^{2} tartrate and **K**^{3} tartrate species.

entry	complex species	rel. free energy cisoid [kcal/mol]	rel. free energy transoid [kcal/mol]
1	**K**^{2}	1.54	0.00
2	**K**^{2} with prot. amines	0.00	6.98
3	**K**^{3}	0.00	1.56
4	**K**^{2} tartrate	5.16	0.00
5	**K**^{2} tartarte with prot. amines	33.44	0.00
6	**K**^{3} tartrate	0.00	1.17

UV/vis spectra were recorded in solution (MeCN and MeOH) as well as in solid state. The spectra of **K**^{2} and **K**^{3} (Figure 3.34 a and c) show some differences regarding the three media. In both cases, the λ_{max} values of the phenolate to iron transitions differ significantly (see also Table 3.14). The largest shift is observable with **K**^{3}, where a change from MeCN to MeOH causes a hypsochromic shift of 168 nm. Compared to the wavelengths in solid state, the wavelength difference in the MeCN spectra is a lot smaller than in MeOH, which indicates that in MeCN the solid state structure is hardly changed. MeOH is more likely to coordinate to the ferric ions than MeCN due to its more hard character. In the case of **K^2** tartrate and **K^3** tartrate (Figure 3.34 b and d), the spectra in MeCN and MeOH (solid and dashed line, respectively) look quite similar to each other, what is quite surprising at first. The wavelengths of the phenolate to iron CT transitions differ by only few nm in both cases, but the intensities are slightly different. There is a hypsochromic shift of nearly 100 nm from the solid state to the solution spectra. It seems that in these cases, the solid structure changes significantly when the complexes are dissolved. Probably, the L-tartrate anions are coordinated in solid state and dissociate in solution. The question remains why the resulting wavelengths are so similar, although in one case MeCN and in the other MeOH would be coordinated. One possibility is that the basic L-tartrate produces hydroxides in solution which are then bound to the ferric ions. The wavelengths of around 500 nm agree with this explanation, as they resemble those at high pH in the spectrophotometric titrations (Chapter 3.3.2.1).

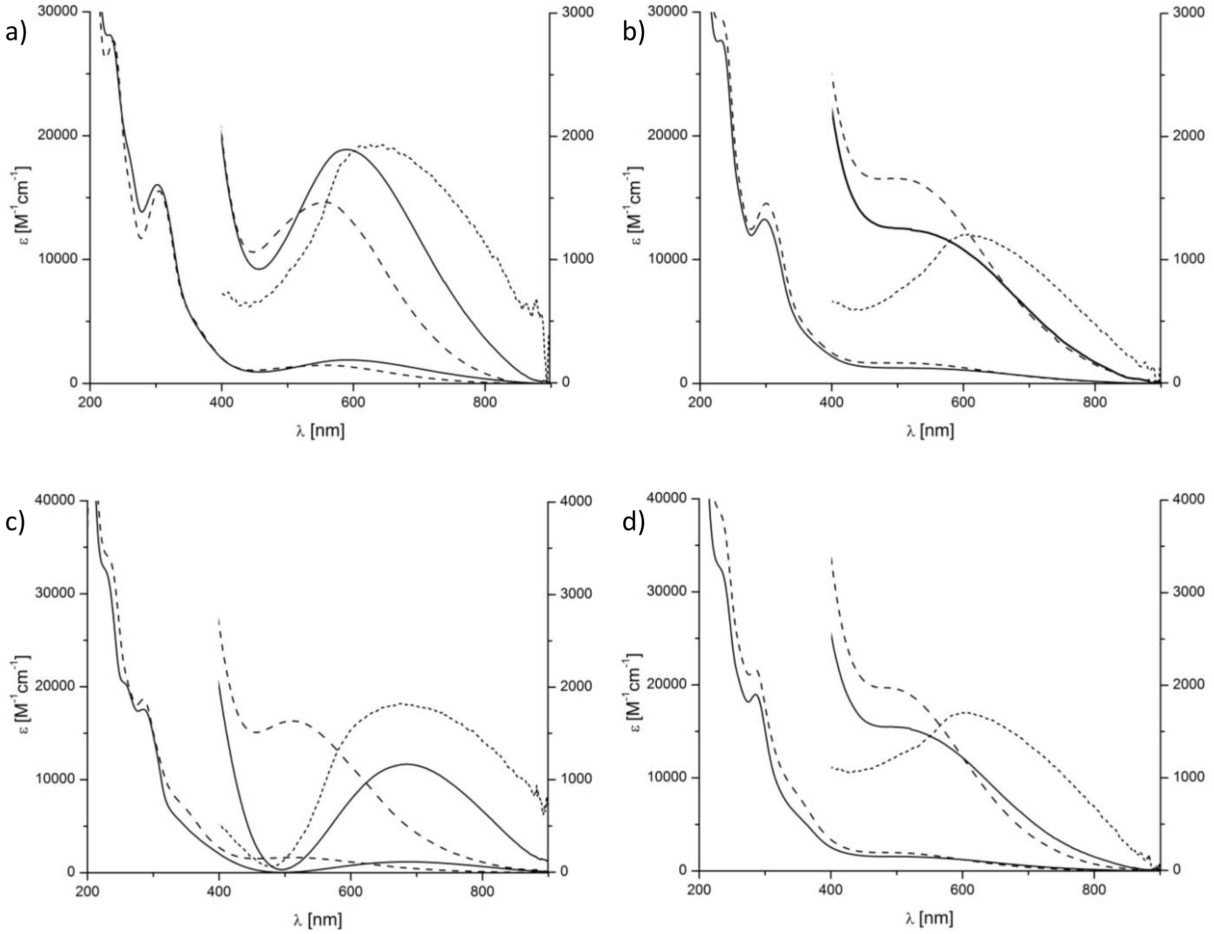

Figure 3.34: UV/vis spectra of a) **K^2**, b) **K^2** tartrate, c) **K^3** and d) **K^3** tartrate in MeCN (solid line), MeOH (dashed line) and as solid (dotted line in inset).

Table 3.14: Phenolate-to-iron CT transitions of the four complexes.

	K^2	**K^2** tartrate	**K^3**	**K^3** tartrate
λ_{MeCN} [nm] (ε [M^{-1}cm^{-1}])	589 (1892)	513 (1250)	685 (1166)	504 (1538)
λ_{MeOH} [nm] (ε [M^{-1}cm^{-1}])	560 (1465)	512 (1654)	517 (1630)	498 (1961)
λ_{solid} [nm]	630	615	681	612

Solid state IR spectra of all four complexes were measured and are compared to the free ligand spectra in Figure 3.35. The **HL^2** spectrum (black line in Figure 3.35 a) has three interesting regions. The two peaks at 792 and 760 cm^{-1} represent deformation vibrations of aromatic C-H groups. Almost the same values are obtained in the case of **H$_3$L^3** (black line in Figure 3.35 b). The absorptions at around 1500 cm^{-1} and 1600 cm^{-1} are C=N valence vibrations within the pyridines. In the region around 1600 cm^{-1}, also the NH_2 spreading vibration is present. Comparison of the free ligand spectrum with the spectra of the complexes enables the various vibrations to be assigned. A significant shift of the 1600 cm^{-1} region and the peaks at 1465 cm^{-1} towards higher wave numbers can be observed in the **K^2** spectrum (red line in Figure 3.35 a), which accounts for coordination of the pyridines. The peak at 1571 cm^{-1} is almost unchanged, only the relative intensity is decreased. It can be assigned to the NH_2 spreading vibration, and its loss can be interpreted as protonation of the amine group. In the **K^2** tartrate spectrum (blue line in Figure 3.35 a), the peaks are very similar to the signals in the **K^2** spectrum. An additional weak and broad band at 1748 cm^{-1} belongs to a valence vibration of the carboxylate part of the tartrate anion. In free tartrate, this vibration appears as broad peak at 1600 cm^{-1}. The observed shift accounts for coordination of the tartrate to the complex.

In contrast to **HL^2**, the spectrum of **H$_3$L^3** (black line in Figure 3.35 b) is much more complex, a consequence of the presence of amido groups in the ligand. The C=O stretching vibration is seen at 1690 cm^{-1} and is very typical. The N-H bending vibration comes at 1523 cm^{-1}. The pyridine bands are again in the region around 1600 cm^{-1} and 1500 cm^{-1}. Other intense absorptions can be seen at 1304 and 1152 cm^{-1}. They belong to the O-H deformation vibration and the C-OH valence vibration of the phenol moiety, respectively. Interestingly, these vibrations are not well resolved in the **HL^2** spectrum. Probably, the phenol is, at least partly, deprotonated in this case. In comparison, the spectra of **K^3** and **K^3** tartrate have a similar appearance as the **K^2** and **K^2** tartrate ones. The pyridine peaks are shifted towards higher wave numbers in all cases and the aromatic proton fingerprint bands are retained. The dominant C=O vibration in the $\mathbf{H_3L^3}$ spectrum at 1690 cm^{-1} is almost lost in the $\mathbf{K^3}$ and $\mathbf{K^3}$ tartrate cases, which accounts for coordination of the carbonyl oxygen to Fe^{III}. In contrast, the amido NH vibration at 1523 cm^{-1} is retained, i.e. the amide part is still protonated in the complexes. Similar to $\mathbf{K^2}$ tartrate, the broad weak band at 1741 cm^{-1} suggests coordination of the tartrate anion to the complex. The broad and intense signals around 1100 cm^{-1} as well as the sharp peak around 600 cm^{-1} in the complex spectra belong to perchlorate vibrations.

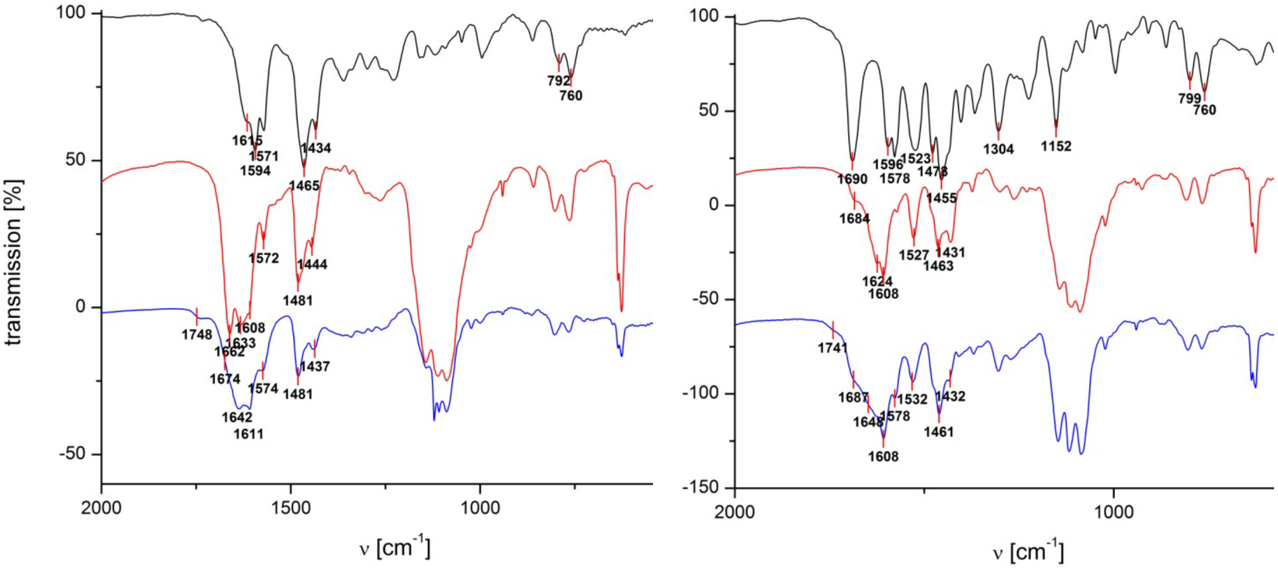

Figure 3.35: Comparison of IR spectra (fingerprint region) of a) $\mathbf{HL^2}$ with $\mathbf{K^2}$ and $\mathbf{K^2}$ tartrate and b) $\mathbf{H_3L^3}$ with $\mathbf{K^3}$ and $\mathbf{K^3}$ tartrate; ligands in black (top), complexes in red (middle) and tartrate complexes in blue (bottom).

X-band EPR spectra of $\mathbf{K^2}$ and $\mathbf{K^3}$ in solid state showed only moderate signals at $g_{eff} = 4.3$, which belong to high spin ferric ions. Most Fe^{III} ions seem to be antiferromagnetically coupled, leading to an EPR-silent complex. Assuming similar structures in the solid state and in the *in situ* prepared complexes described in Chapter 3.3.2.1, these results are consistent with the data from the Evans-NMR measurements.

The redox properties of $\mathbf{K^2}$ and $\mathbf{K^3}$ as well as the tartrate complexes were examined by cyclic voltammetry. Different chart speeds were applied, from 50 to 800 mV per second in each case, every time resulting in the same voltage for the oxidation and reduction peaks. The results for the four complexes are summarized in Table 3.15.

Table 3.15: Redox potentials[a] for **K**^{2}, **K**^{3}, **K**^{2} tartrate and **K**^{3} tartrate vs. $FeCp_2$ and SCE.

	K^2	**K**^{3}	**K**^{2} tartrate	**K**^{3} tartrate
$E_{1/2}$ vs. $FeCp_2$ [V]	-0.064	0,022	-0,293 / 0,382	-0,108
$E_{1/2}$ vs. SCE [V]	0,316	0,402	0,087 / 0,762	0,272

[a] recorded in MeCN with 0.1M NBu_4ClO_4 vs. Ag/Ag^+ with $E_{1/2}$ ($FeCp_2$) = 0.068 V.

The potentials most probably belong to an $Fe^{III}{}_2/Fe^{III}Fe^{II}$ couple and are in the range for reported values (see Table 2.6 in Chapter 2.4 for values and references). In comparison to literature-known complexes with tetra-pyridyl ligands, the redox potentials of **K**^{2} and **K**^{3} are slightly lower. This explains why **K**^{2} and **K**^{3} were obtained in their homovalent state. Nevertheless, a reduction to the heterovalent $Fe^{III}Fe^{II}$ complex should be feasible in both cases and result in stable species under anaerobic conditions. The tartrate complexes of **K**^{2} and **K**^{3} have redox potentials that are around 230 and 130 mV lower, respectively, than the tartrate-free complexes. Although we concluded from the UV/vis spectra that the tartrate anions are dissociated in solution, they strongly influence the redox behavior of **K**^{2} and **K**^{3}. This can be again explained by the coordination of hydroxides, which are produced by the basic tartrate anions. **K**^{2} tartrate has a second redox step at $E_{1/2}$ = 0.762 V vs. SCE, which is quasi-reversible. It belongs most probably to an oxidation to Fe^{IV}.

No signals were obtained for **K**^{2} or **K**^{3} in MeCN/buffer mixtures. Probably, the water is responsible for bad signals. Therefore, only the values in MeCN can be compared to the redox potential of *para*-nitrophenolate (see Chapter 3.3.2.1) to judge if the observed reduction of **K**^{2} and **K**^{3} with pNPP in MeCN/buffer is caused by the hydrolysis product *para*-nitrophenolate. In order to make this redox process possible, the reduced species, i.e. the complexes **K**^{2} or **K**^{3}, need to have a more positive redox potential than the reductant. This is not the case here. In conjunction with the result, that no radical and no S = ½ signal is visible in EPR upon reaction of **K**^{2} or **K**^{3} with *para*-nitrophenylphosphate, i.e. without pNPP, we conclude that coordination of pNPP alters the redox potentials of **K**^{2} and **K**^{3} towards more positive values.

3.3.3. Summary HL^2 and H_3L^3

The HBPMP derivatives **HL^2** and **H_3L^3** with additional amino and amido functions at two of the four pyridines, show some striking differences compared to ligand **L^1**. The most prominent distinction is their *in situ* coordination chemistry with Fe^{III}. HR ESI mass spectrometry in combination with UV/vis spectroscopy and Evans NMR measurements revealed that at low Fe^{III} concentrations mainly mononuclear complexes are formed and only a small fraction of dinuclear species is present. Only with two eq of Fe^{III}, dinuclear complexes are predominantly formed.

The redox potentials of the diferric complexes are slightly smaller compared to the values of HBPMP and HBIMP complexes bearing unsubstituted pyridine and imidazol donors.[76, 116] However, a one-electron reduction to the heterovalent complexes should be easier than with **K^1**, and moreover lead to stable complexes. This can be mainly attributed to the phenoxo linker included in the ligand backbone. **K^3** has a higher redox potential than **K^2**, which reflects differences in coordination due to the additional amido functions of **H_3L^3**.

A spectrophotometric analysis of **K^2** and **K^3** was performed in a pH range between 4.6 and 11. **K^2** with its basic amino groups most probably exists in four different species during the titration, including a di-aqua complex with protonated amines, an aqua-hydroxo species with protonated or deprotonated amines and finally a di-hydroxo complex. In the case of **K^3**, only three different species are observed in the mentioned pH range. The amides are probably already deprotonated at low pH values.

Concerning the structures of **K^2** and **K^3**, the main distinctive feature is the possibility of isomerism, with respect to the relative position of the functional amino and amido groups. A conformational search of the ligands showed them to be quite flexible with the cisoid and transoid isomers having similar energies. Also, the complexes without further co-ligands reveal only relatively small energetic differences between a cisoid and a transoid structure, as shown by DFT calculations. Coordination of the chiral anion L-tartrate to **K^2** leads to a differentiation of the structures in the calculations, producing larger energy gaps between cisoid and transoid complexes. With **K^3**, this is not the case due to the missing hydrogen bonding interactions. The predicted formation of only one possible conformer of **K^2** with chiral co-ligands should in principle make it easier to crystallize the complexes. Unfortunately, no crystals suitable for X-ray analysis could be obtained so far.

Phosphate and phosphoester substrate mimics coordinate in a similar way as seen with **K^1**. Whereas reactions with phosphate and the monoester 1-NP results in the formation of only one phenolate to iron CT transition at around 500 to 600 nm in the UV/vis spectra of **K^2**, indicating a bridging coordination mode, the diester DPP most probably coordinates monodentately and the UV/vis spectrum of this mixture shows two absorptions in this region. **K^3**, in contrast, does not show this behavior, what leads to the conclusion that the amines of **K^2** stabilize the monodentate coordination of DPP. This is important with respect to the envisioned activity of **K^2** in hydrolysis of phosphodiesters, and probably also monoesters, as a monodentately coordinated substrate represents the active conformation of the catalyst-substrate complex.

Addition of pNPP in a partly aqueous medium results in *in situ* reduction of both complexes, yielding heterovalent Fe^{III}Fe^{II} complexes. This is supported by EPR spectra of the mixtures at low temperatures, which show a broad signal at $g_{eff} < 2$ and an additional peak around $g_{eff} = 4.3$. This kind of spectrum is typical for antiferromagnetically coupled complexes with an S = ½ ground state and has been already observed in spectra of reduced mammalian PAP. A sharp peak at $g_{eff} = 2$ indicates the presence of a relatively stable radical, which is formed slowly over several hours. The fine structure and the g value suggest a phenoxo based radical. A *para*-nitrophenoxy radical coming from autohydrolysis of pNPP can be excluded, based on the simulation of the room temperature spectrum. The simulation rather suggests a ligand based radical, delocalized on the central phenolate part. The preliminary interpretation is that *para*-nitrophenolate still acts as reductant towards **K^2** and **K^3** that have a higher redox potential due to the coordination of pNPP. At room temperature, the radical character is transferred to the ligand backbone.

3.4. Phosphatase Activity of K^1, K^2 and K^3

The activity of all described complexes towards hydrolysis of the activated phosphoesters bis-(2,4-dinitrophenyl)-phosphate (BDNPP)[154] and 2,4-dinitrophenylphosphate (DNPP)[155] (see Scheme 3.21) was investigated by a spectrophotometrical assay. During hydrolysis, 2,4-dinitrophenolate is released as product with an intense absorption band at λ = 400 nm ($\varepsilon = 12100\ M^{-1}cm^{-1}$). BDNPP hydrolysis is a commonly used test reaction for PAP mimetics,[69, 92] although enzymes are known to almost exclusively hydrolyze monoesters.[55, 156] Nevertheless, the results provide important information about the catalytic activity and pK_a values of the complexes, which can be compared to other biomimetic systems.

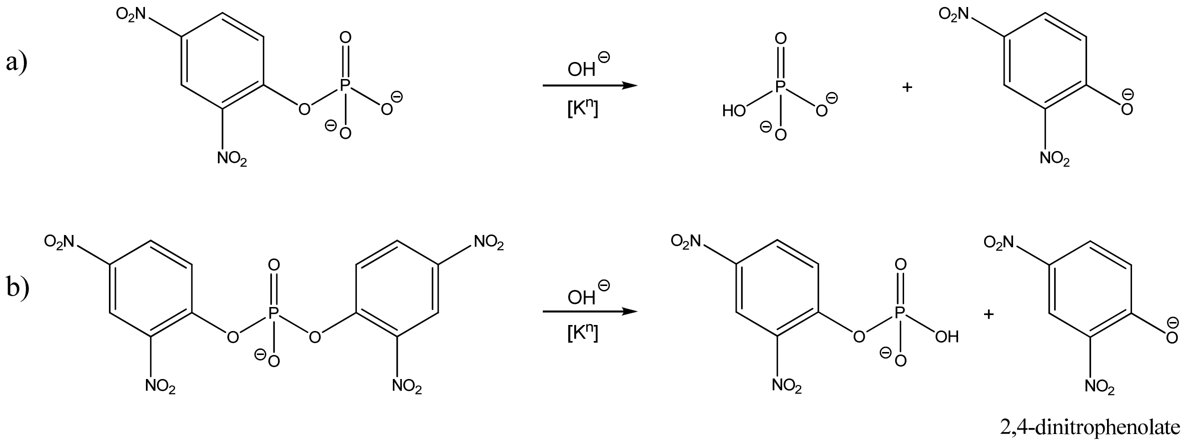

Scheme 3.21: Activated substrates a) DNPP and b) BDNPP and their hydrolysis reactions.

To characterize **K**^{1}, **K**^{2} and **K**^{3} as phosphatase catalysts, the activity at different pH values (4.6 to 10 or 11) was measured as well as with different substrate and catalyst concentrations. The measured pH profiles were fitted with equation 3.8, which is based on a model for a diprotic system with two active species.[157] The thus obtained K_a values are transformed to their negative logarithms (base 10) to give $pK_a(I)$ and $pK_a(II)$, i.e. the pK_a values of the deprotonation steps between the different active and inactive species (see Schemes 3.22 and 3.25). Factor γ describes how active the last species in the equilibria is in comparison to the most active one. $V_{0,max}$ is the maximum activity that can be reached at given conditions and optimum pH.

$$V_0 = V_{0,max} * \frac{\left(1+\frac{\gamma * K_a(II)}{[H^+]}\right)}{\left(1+\frac{[H^+]}{K_a(I)}+\frac{K_a(II)}{[H^+]}\right)} \qquad \text{(eq. 3.8)}$$

Substrate dependent measurements were treated according to Michaelis-Menten theory. The data are fitted using eq. 3.9. V_{max} is the maximum activity at saturation conditions; K_M is the Michaelis-Menten constant and can be seen as a measure of affinity of the substrate towards the catalyst.

$$V = \frac{V_{max} * [S]_0}{K_m + [S]_0} \qquad \text{(eq. 3.9)}$$

Additional information about catalyst activity and efficiency, respectively, can be obtained from eq. 3.10 and k_{cat}/K_M. These numbers are used to compare different catalysts as well as the activity of one catalyst towards different substrates.

$$k_{cat} = V_{max}/[K]_0 \qquad \text{(eq. 3.10)}$$

3.4.1. *Phosphatase Activity of K^1*

As described in Chapter 3.2.2.3, no information could be obtained by spectrophotometric titrations regarding species distribution of **K**^{1} at different pH values. The pH dependent UV/vis spectra of **K**^{1} do not show differences that are large enough to be fitted and therefore, no pK_a values could be obtained by this technique. Nevertheless, assuming a similar behavior of **K**^{1} to known model systems and taking into account the various results reported in Chapter 3.2.2.3., the following reaction scheme can be proposed (see Scheme 3.22): At low pH, a tetra-aqua form should be present, which lacks a suitable nucleophile and therefore remains inactive towards phosphoesters. Deprotonation of one water at each Fe^{III} leads to a di-aqua/di-hydroxo species, where the aqua ligands can be easily exchanged by the substrate and the hydroxides can act as nucleophiles. This species is supposed to be the active form of **K**^{1}.

Although the two Fe^{III} centers are strongly antiferromagnetically coupled, simultaneous deprotonation should be possible. Further deprotonation results in a tetra-hydroxo species, which might show some activity, provided that the hydroxo ligands can also be substituted by substrate molecules. The pK$_a$ values of these processes will be determined with the help of kinetic measurements. Coordinated substrate molecules should be able to interact with the protonated form of the cyclam moiety of **L**^{1}. This will also be discussed in the following chapters.

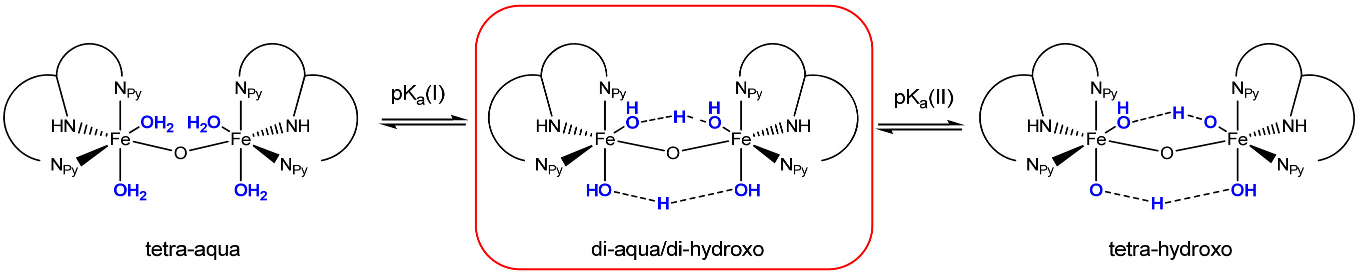

Scheme 3.22: Proposed species of **K**^{1} at different pH. The proposed active species is highlighted.

3.4.1.1. *Diesterase Activity of K^1*

Hydrolysis experiments with **K**^{1} and BDNPP (see Scheme 3.21 b) were conducted according to literature known procedures:[87-90] BDNPP (c_0 = 5 mM) and **K**^{1} (c_0 = 0.04 mM) were reacted in MeCN/buffer at 25°C. For the substrate and catalyst dependent measurements, their concentrations were varied. The resulting pH profiles of **K**^{1} as well as **L**^{1} with one eq of Fe^{III} and the Michaelis-Menten diagram of **K**^{1} are shown in Figure 3.36. Using equations 3.8, 3.9 and 3.10, respectively, the curves were fitted (red lines in the figures) giving the pK$_a$ values and the kinetic parameters presented in Table 3.16. Comparison of the two pH profiles shows an approximately halved activity with only one eq of Fe^{III} and very similar curve shapes. This supports again the suggested predominant formation of dinuclear complexes with **L**^{1}. Experiments with varying catalyst concentration showed a linear behavior, which excludes cooperativity or other effects.

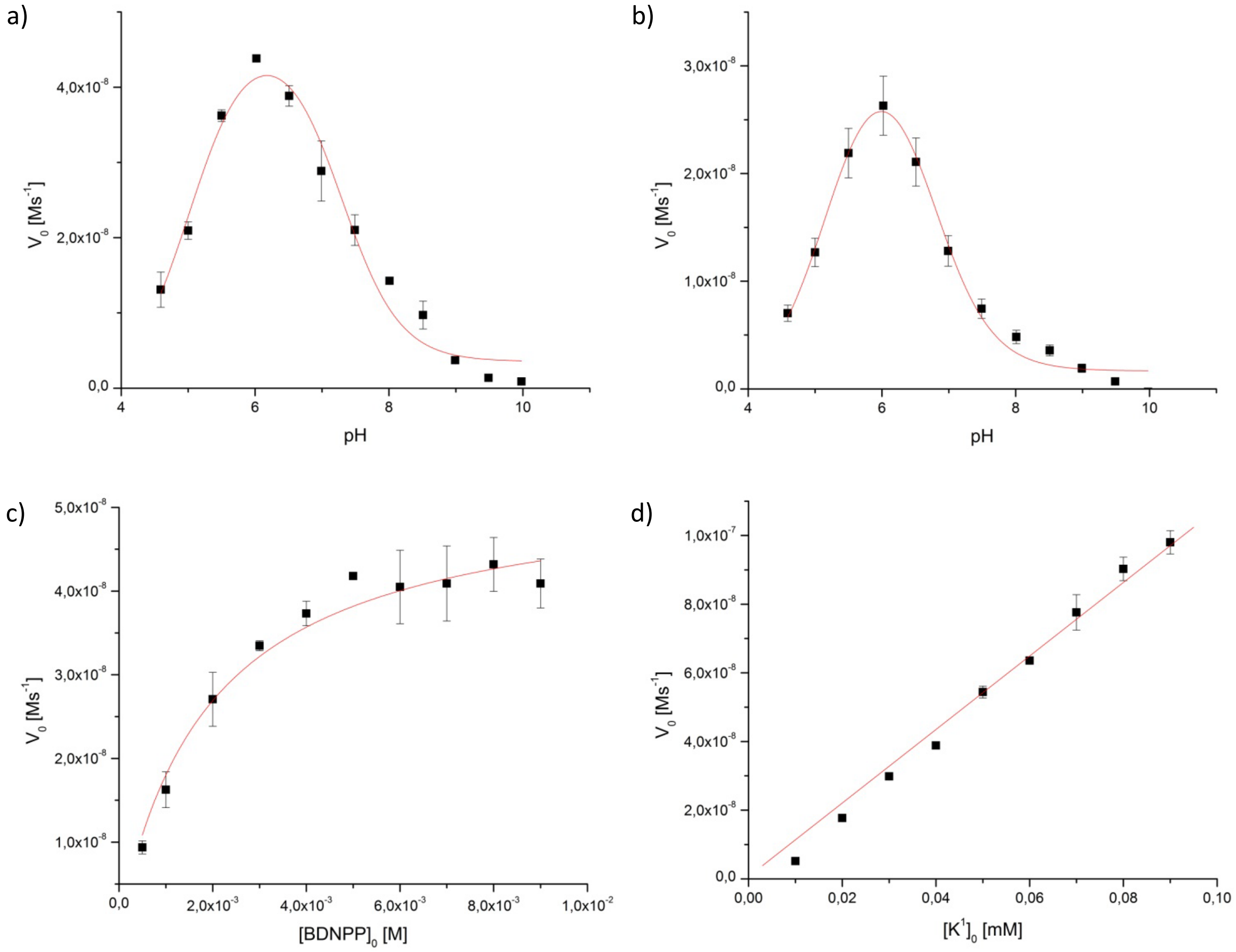

Figure 3.36: pH profiles of a) **K^1**, b) **L^1** with 1 eq of Fe^{III}, c) Michaelis-Menten diagram (pH 6) of **K^1** and d) **K^1** concentration dependence of BDNPP hydrolysis. The experimental data are shown as black squares, the red lines represent the fits using equations 3.8 and 3.9 for pH-profiles and Michaelis-Menten diagrams, respectively.

Table 3.16: Kinetic parameters of **K^1** and **L^1** with 1 eq of Fe^{III}.

catalyst	pH$_{max}$	pK$_a$(I)	pK$_a$(II)	k$_{cat}$ [s^{-1}] *10^{-3}	K$_M$ [M] *10^{-3}	k$_{cat}$/K$_M$ [M^{-1}s^{-1}]
K^1	6.17	5.03 ± 0.10	7.28 ± 0.12	1.33 ± 0.08	1.94 ± 0.37	0.68 ± 0.02
L^{1}Fe	6.01	5.21 ± 0.08	6.75 ± 0.09	n.a.	n.a.	n.a.

Stoichometric experiments were conducted and followed spectrophotometrically as well as via ^{31}P-NMR. No signal could be identified in the NMR experiment, although 2,4-dinitrophenol had been liberated from the phosphoester (as seen by UV/vis). Experiments with catalytic amounts of **K^1** did not show any product peaks either; only the reactant was visible. These findings suggests that after hydrolysis the product (DNPP or phosphate) remains bound to **K**^{1}, which is consistent with the observed inhibition, when phosphate containing buffer is used for kinetic assays. Most probably, this behavior is a result of the homovalency of **K**^{1}, leading to generally high affinity for bridging co-ligands. Analysis of the spectrophotometric experiment reveals the formation of only one equivalent of 2,4-dinitrophenol per BDNPP and **K**^{1}. Thus, only the first hydrolysis step, from BDNPP to DNPP, occurs and no formation of phosphate is observed.

3.4.1.2. *Monoesterase Activity of K*^{1}

So far, no PAP mimetics have been reported to hydrolyze monoester substrates.[55, 87, 88, 90, 92] Only the background reaction has been observed, independently of the substrate used (pNPP or DNPP). This was explained by a bridging coordination of the substrate, leading to a µ-OH bridge as the only possible nucleophile, which is proposed to be significantly less active than terminal hydroxides.[92]

A diferric system, like **K**^{1}, would normally be expected to coordinate phosphates or phosphoesters in a bridging mode. And indeed, as reported in Chapter 3.2.2.4., pNPP most probably coordinates in that way, even without any additional bridging nucleophile, and is not hydrolyzed by **K**^{1}. Nevertheless, our hope was to stabilize DNPP long enough in a monodentate coordination mode for a nucleophilic attack, as the discussed structure with two pNPP and the characteristic EPR spectrum slowly builds up over several hours.

Hydrolysis experiments were conducted in a similar way as for BDNPP (Scheme 3.21 a), only with 10-fold lower substrate concentration ($c_0 = 0.5$ mM). The substrate dependency measurement indicates why this was changed: At concentrations larger than 0.5 mM, saturation is observed, which is due to a relatively high autohydrolysis rate of DNPP (see Appendix 9 for data). The results are presented in Figure 3.37 and Table 3.17.

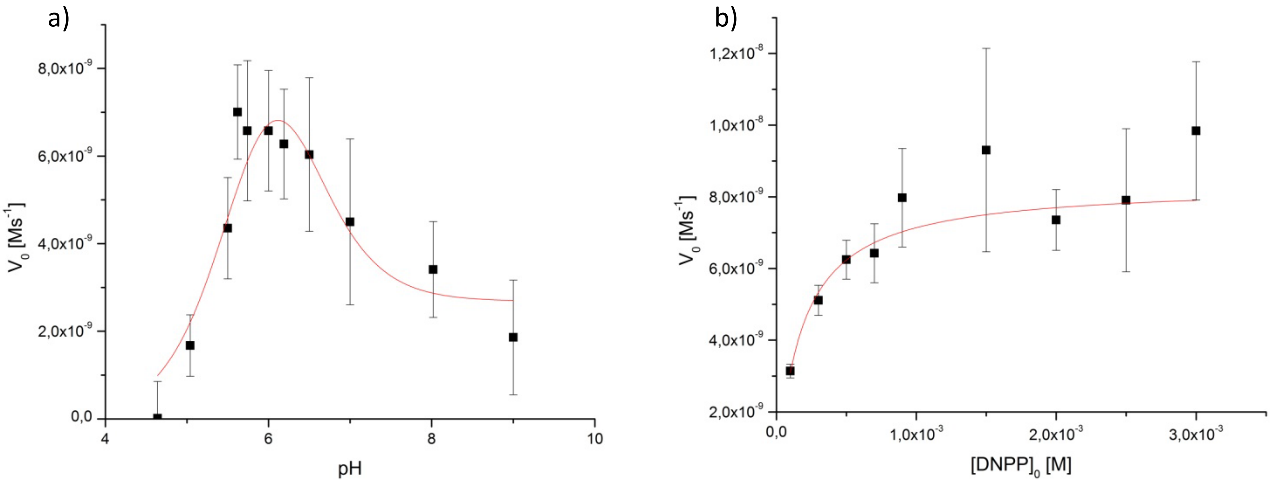

Figure 3.37: a) pH profile and b) Michaelis-Menten diagram (pH 6) of DNPP hydrolysis with **K**^{1}. The experimental data are shown as black squares, the red lines represent the fits using equations 3.8 and 3.9 for pH-profiles and Michaelis-Menten diagrams, respectively.

Table 3.17: Kinetic data for DNPP hydrolysis with **K**^{1}.

pH_{max}	pK_a(I)	pK_a(II)	k_{cat} [s^{-1}] *10^{-3}	K_M [mM]	k_{cat}/K_M [$M^{-1}s^{-1}$]
6.09	5.68 ± 0.27	6.33 ± 0.41	0.21 ± 0.01	0.17 ± 0.02	1.23 ± 0.14

The observed k_{cat} is not high, but significant; compared to the autohydrolytic rate, **K**^{1} accelerates the reaction only by a factor of 1.45 (at pH 6, with 0.5 mM DNPP). Nevertheless, the typical bell-shaped pH profile is observed and the resulting pH maximum and pK_a values indicate the same active species of **K**^{1} and a very similar mechanism as observed with BDNPP.

3.4.1.3. Mechanistic Suggestions

A comparison of the kinetic pH profiles for BDNPP and DNPP hydrolysis with **K**^{1} suggests that both reactions have a similar reaction mechanism. The main differences are the significantly lower values for k_{cat} and K_M for DNPP hydrolysis. In summary, DNPP hydrolysis is slower than BDNPP hydrolysis, but the affinity for the latter substrate is lower. One has to be careful in comparing these data as a tenfold lower substrate concentration is applied in the DNPP case. This is due to the high autohydrolysis rate of DNPP that also leads to a low K_M. Therefore, the efficiency k_{cat}/K_M is higher for DNPP than for BDNPP hydrolysis (1.23 vs. 0.68 $M^{-1}s^{-1}$). These findings suggest subtle differences for both reactions. Due to the high similarity of both substrates with the same leaving group (2,4-dinitrophenolate), no significant alterations in activation energy for the hydrolysis step would be expected. The following results highlight the differences between the two substrates.

Density functional theory calculations (see Chapter 4.5 for details) were used to elucidate the pathways and structures that contribute to the different reactivity of $\mathbf{K^1}$ towards DNPP and BDNPP. At first, the relative energies of substrates bound monodentately vs. bridging were calculated and compared (see Table 3.18), assuming an equilibrium between both structures. In the case of BDNPP, two different structures were geometry-optimized, where the P=O moiety is interacting with the protonated cyclam and an Fe^{III} bound water, respectively. The latter structure is the precursor for bridging coordination. From the difference in free energies, the equilibrium constant K can be obtained by using eq. 3.11 and 3.12.

$$\Delta G = -RT \bullet \ln K \qquad \text{(eq. 3.11)}$$

$$\text{with } K = \frac{[monodentate]}{[bridging]} \qquad \text{(eq. 3.12)}$$

Table 3.18: Relative energies for $\mathbf{K^1}$ with monodentately bound vs. bridging DNPP and BDNPP [kcal/mol].

	$\mathbf{K^1}$ + DNPP	$\mathbf{K^1}$ + BDNPP
monodentate coordination	3.08	0 / 4.94[a]
bridging coordination[b]	0	8.09
equilibrium constant *K*	$5.5*10^{-3}$	$8.5*10^{5}$

[a] Energies refer to the two different structures, where the P=O moiety is interacting with the protonated cyclam and an Fe^{III} bound water, respectively. [b] One pyridine belonging to $\mathbf{L^1}$ is dissociated upon bridging coordination of the substrate molecule.

The resulting relative free energies and equilibrium constants suggest that DNPP is more likely bound in a bridging way to **K**^{1}, whereas BDNPP is more stable when coordinated monodentately. A closer look at the geometry-optimized structures of the **K**^{1}BDNPP complexes reveals some interesting facts (see Appendix 10 for structures): The most stable structure is **K**^{1} with monodentate BDNPP, where an interaction between the P=O moiety and the protonated cyclam is possible. In this conformation, a direct reaction to the bridging arrangement is impossible due to the second phenolate residue. A rotation around the existing Fe^{III}-BDNPP bond results in a structure where the P=O moiety is situated in an appropriate position for coordination to the second Fe^{III}, forming hydrogen bonds to an Fe^{III} bound water. Yet, this structure is higher in energy than the previous one and the rotation provokes a loss of the hydrogen bond between BDNPP and the protonated cyclam, which suggests a high activation barrier for this process. Therefore, an equilibrium between the monodentate and bridging conformers seems unlikely. Only a minor fraction of the **K**^{1}BDNPP complex should be present in a bridging inactive form. In contrast, **K**^{1}DNPP can directly interchange between the monodentate and bridging coordination modes and the obtained equilibrium constant is reasonable.

In order to obtain kinetic information on the different pathways, DFT-based calculations on the two competing reactions, i.e. deactivation by formation of bridged structures vs. nucleophilic attack of a hydroxide at the phosphorous, were performed for **K**^{1} with DNPP. Starting from monodentately bound DNPP, the distance between the DNPP oxygen and the non-coordinated Fe^{III} was decreased stepwise for a relaxed scan potential surface towards the bridging DNPP (see Scheme 3.23 pathway a and Figure 3.38 a). Interestingly, the approach of the DNPP oxygen does not result in release of a bound aqua or hydroxo ligand, but a pyridine is displaced and finally rotated away from the coordination site. Pathway b is obtained by stepwise decreasing the distance between the terminal hydroxide at the second Fe^{III} and the phosphorous atom of the DNPP. The resulting energies are plotted in Figure 3.38 b. The black lines represent the energies of **K**^{1} with protonated cyclam. Hydrogen bonding interactions are found between the cyclam N-H group and the DNPP, as indicated in Scheme 3.23 and Figure 3.38 (bottom structure). In order to have a closer look on the effects of this interaction, an analogous scan was performed without the cyclam protons (grey lines). Obviously, no interactions between DNPP and the cyclam are possible in this case and a significantly different structure of the **K**^{1}DNPP complex is observed (Figure 3.38, top structure).

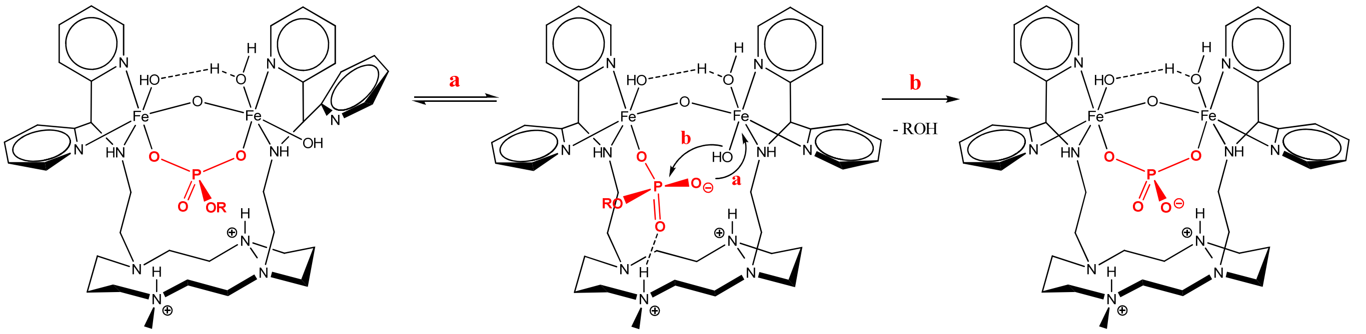

Scheme 3.23: Competing reaction pathways of DNPP coordinated to $\mathbf{K^1}$.

The resulting energy profiles give rise to the following conclusions. In both cases, the activation barrier for bridging coordination is considerably larger than the one for the hydrolysis reaction. However, the ratio is different: it is more favorable to hydrolysis in the protonated case. With the interaction between DNPP and cyclam, a nearly barrierless hydrolysis pathway is obtained. This result clearly supports the positive effects of the second coordination sphere on PAP like reactivity.

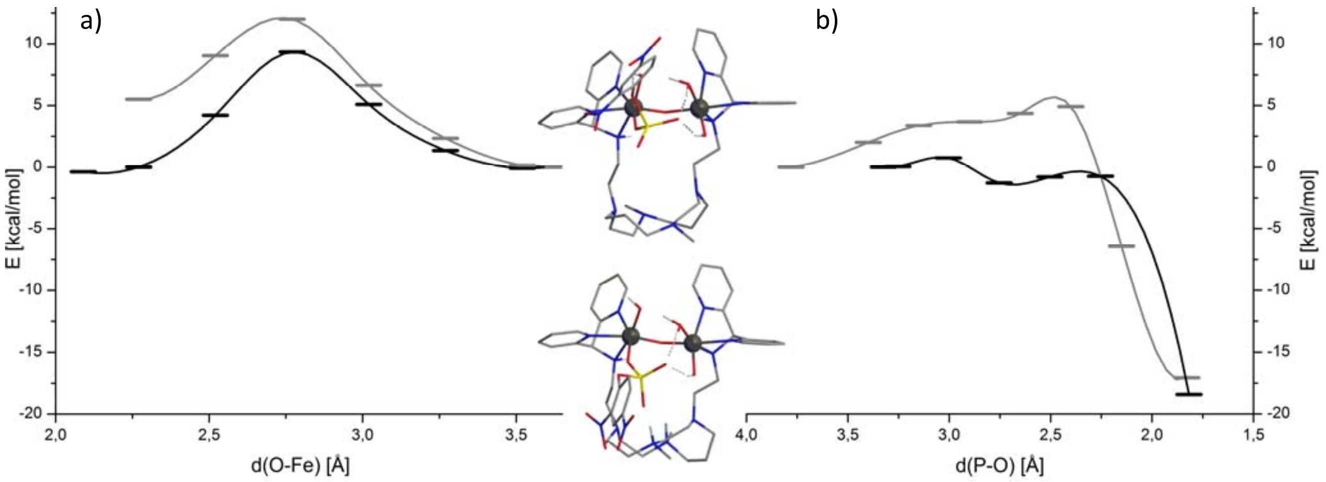

Figure 3.38: Energy profiles of a) bridging binding vs. b) hydrolysis of DNPP and $\mathbf{K^1}$ with protonated cyclam (black line) or $\mathbf{K^1}$ with deprotonated cyclam (grey line); the two structures shown in the middle are monodentately bound DNPP at $\mathbf{K^1}$ with protonated cyclam (bottom) and at $\mathbf{K^1}$ with deprotonated cyclam (top).

In combination with the results from experiments of $\mathbf{K^1}$ with the inactive substrate mimics 1-NP, pNPP and DPP (see Chapter 3.2.2.4), the following mechanistic suggestions for DNPP and BDNPP hydrolysis can be made (Scheme 3.24). The substrate is bound to one Fe^{III}

in a monodentate coordination mode, which is proposed to be the active conformation. An equilibrium between monodentately bound and bridging DNPP results in a smaller fraction of active species, as shown in Table 3.18, whereas no equilibrium is expected with BDNPP. This fact explains the observed difference in activities of **K**^{1} towards DNPP and BDNPP. Possible interactions with the protonated cyclam moiety can help to stabilize the active coordination mode. Subsequently, a hydroxide which is bound to the second Fe^{III} attacks the substrate and the leaving group 2,4-dinitrophenol is cleaved off. This process can either be concerted or stepwise as this question has yet to be addressed for **K**^{1} so far. The pentavalent phosphorous structure in Scheme 3.24 is then either a transition state or an intermediate. The product (phosphate or) DNPP stays bound in a bridging mode, which is suggested to be an inactive, inhibitory species. The only remaining nucleophiles are a μ-oxo group, which is not reactive enough to hydrolyze bound DNPP and the second hydroxide, which is too far away from the phosphorous atom. The diferric state of the complex results in tight binding of the product and prevents ligand exchange against water or another substrate molecule. Therefore, the reaction stops after one cycle.

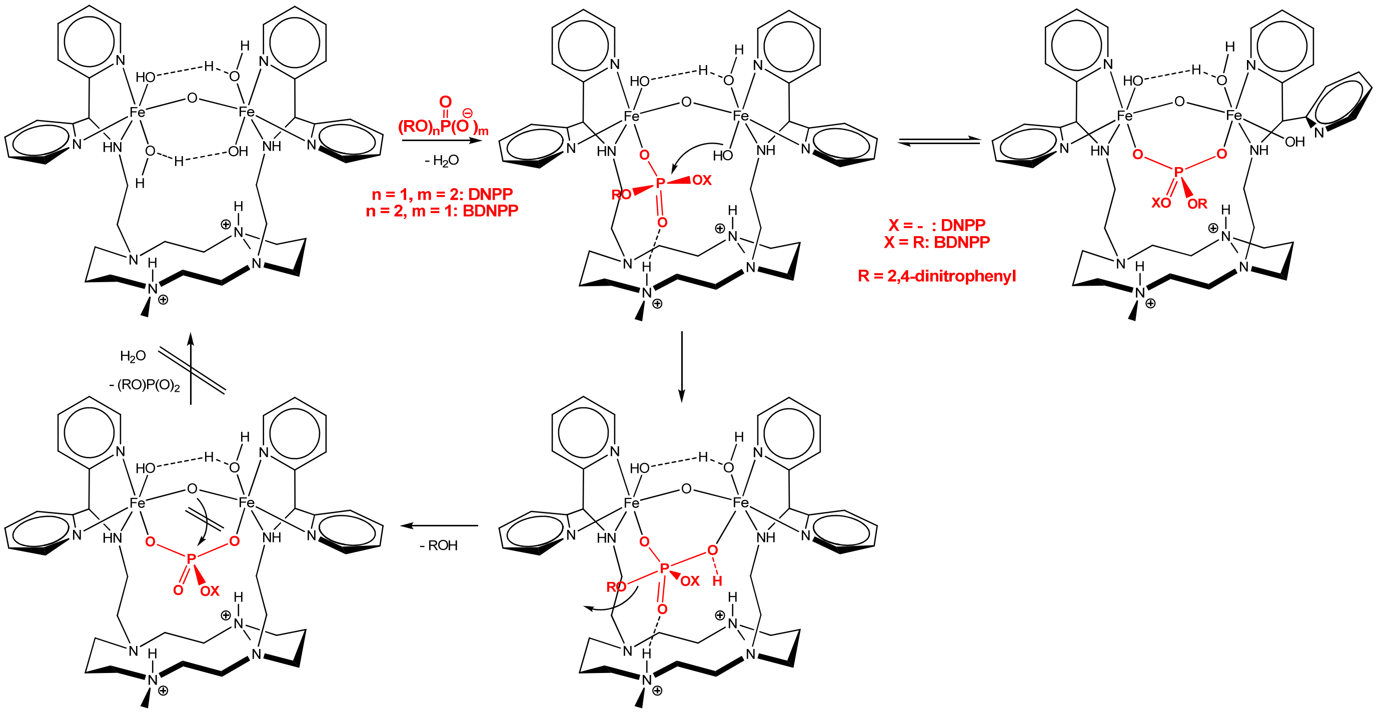

Scheme 3.24: Proposed reaction mechanism for BDNPP and DNPP hydrolysis with **K**^{1}.

The coordination of BDNPP and DPP to **K**^{1} in MeCN was monitored by stopped-flow UV/vis spectroscopy, as it was assumed that this is a very fast process. The use of

MeCN/buffer mixtures (like in the kinetic assays) was not possible in this case due to the experimental setup. The traces at 530 nm (ferric ion dd band) for **K**^{1} with BDNPP and DPP (1:1 ratio; 1 mM each) were compared to the trace of **K**^{1} and DPP at 400 nm (iron-oxo band; 0.04 mM **K**^{1} and 5 mM DPP; i.e. pseudo-first order conditions of the kinetic assays). No experiment with **K**^{1} and BDNPP could be made at the latter conditions due to the strong absorption of the 2,4-dinitrophenolate at 400 nm. Nevertheless, the trace with the inactive diester substrate mimic DPP and the one with BDNPP (Figure 3.39 b) show a very similar slope and shape. Therefore, we assume a similar kinetic behavior. The pseudo-first order reaction of **K**^{1} with DPP (Figure 3.39 a) was fitted with the first-order kinetic equation (eq. 3.13). The reaction rate for the formation of the **K**^{1}DPP complex was estimated to be $k = 3.21 \pm 0.09\ \text{s}^{-1}$, which is significantly faster than the observed reaction rate k_{cat} ($1.33 * 10^{-3}\ \text{s}^{-1}$) for BDNPP hydrolysis (see Figure 3.16 a for extinction coefficients of **K**^{1} and **K**^{1}DPP at 400 nm; A_0 is the absorption of **K**^{1}, A_∞ the final absorption of **K**^{1}DPP). Therefore, it can be concluded that the nucleophilic attack of an Fe^{III} bound hydroxide at the substrate is the rate determining step of the observed reaction.

$$A_t = A_\infty + (A_0 - A_\infty) * e^{-k*t} \qquad \text{(eq. 3.13)}$$

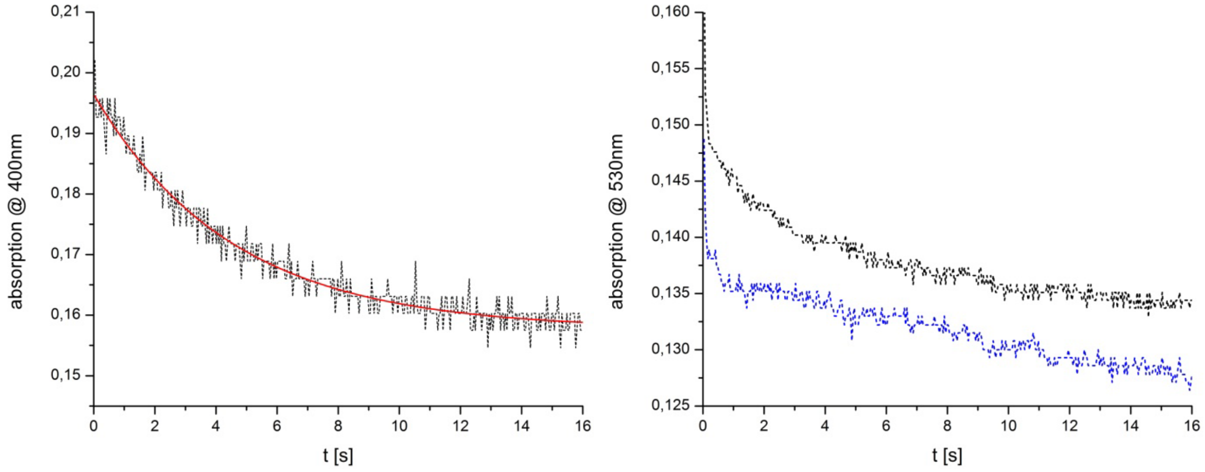

Figure 3.39: Kinetic traces of a) **K**^{1} + DPP (0.04 mM **K**^{1}, 5 mM DPP) at 400 nm with fitted curve (red line) and b) **K**^{1} + DPP (black line) and **K**^{1} + BDNPP (blue line) at 1 mM and 530 nm in MeCN.

Neither UV/vis nor EPR spectroscopy could give evidence for a monodentate coordination of phosphomonoesters to $\mathbf{K^1}$. Stopped-flow UV/vis spectra were recorded on a 1:1 mixture of $\mathbf{K^1}$ and the inactive monoester 1-NP in MeCN at 1mM concentration. Unfortunately, the region between 500 and 600 nm did not show two bands; only one weak band was observed independent of the time scale (0 to 0.5 or 16 seconds). These findings are in line with the obtained values for the equilibrium constant *K* between monodentately bound and bridging DNPP (Table 3.18).

3.4.2. Phosphatase Activity of K^2 and K^3

For simplicity reasons, the *in situ* prepared diferric complexes of $\mathbf{HL^2}$ and $\mathbf{H_3L^3}$ were used in the phosphatase activity assays. The different species of $\mathbf{K^2}$ and $\mathbf{K^3}$ were already described in detail in Chapter 3.3.2.1., based on spectrophotometric titrations. For $\mathbf{K^2}$, four species in the pH range between 4.6 and 11 were determined, whereby it is assumed that both aqua/hydroxo species, with and without protonated amino residues, are active catalysts. $\mathbf{K^3}$ revealed only two deprotonation steps over the pH range and therefore should have only one active species, similar to $\mathbf{K^1}$. The proposed active species of $\mathbf{K^2}$ and $\mathbf{K^3}$ are shown in Scheme 3.25.

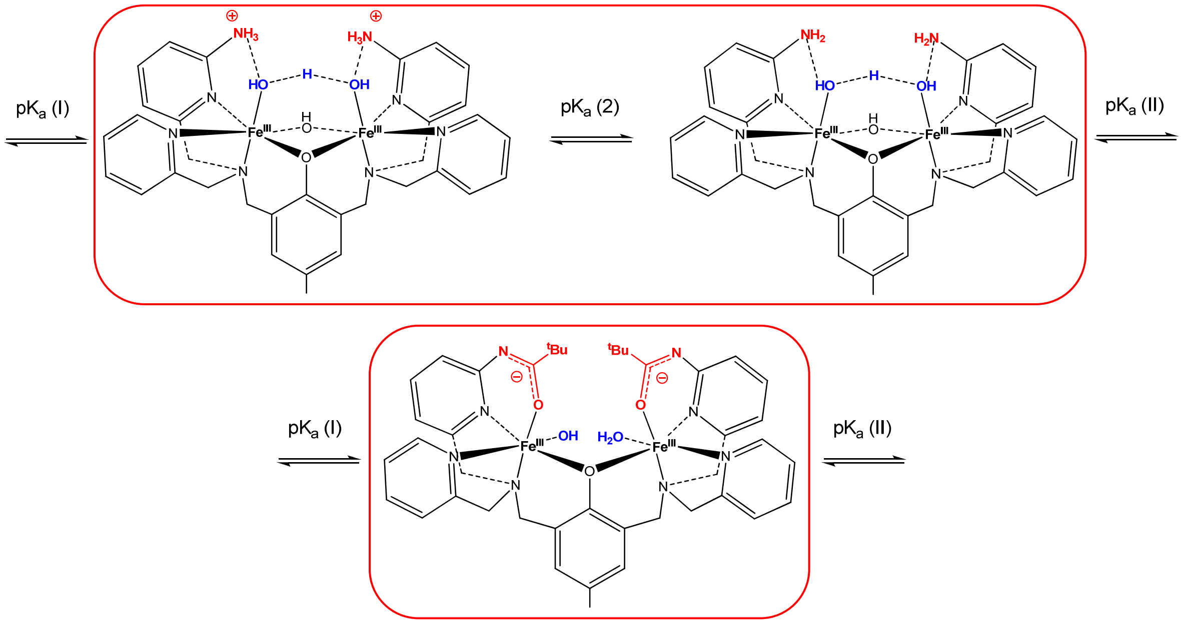

Scheme 3.25: Proposed active species of $\mathbf{K^2}$ and $\mathbf{K^3}$ (highlighted).

The heterovalent $Fe^{III}Fe^{II}$ complexes of $\mathbf{HL^2}$ and $\mathbf{H_3L^3}$ that are formed after reaction of $\mathbf{K^2}$ and $\mathbf{K^3}$ with excess pNPP (see Chapter 3.3.2.2.) are not considered in the kinetic analysis of phosphoester hydrolysis in this case. As it was previously shown, the diferric $\mathbf{K^2}$ and $\mathbf{K^3}$ complexes are only slowly reduced by *para*-nitrophenol. Therefore, no significant amounts of the $Fe^{III}Fe^{II}$ species are expected in the kinetic assays and only the diferric species have been taken into account.

3.4.2.1. Diesterase Activity of K^2 and K^3

In analogy to $\mathbf{K^1}$, the activity of $\mathbf{K^2}$ and $\mathbf{K^3}$ towards hydrolysis of the activated phosphodiester BDNPP was measured. The resulting pH profiles of $\mathbf{K^2}$ and $\mathbf{K^3}$ as well as $\mathbf{L^2}$ and $\mathbf{L^3}$ with one eq of Fe^{III} and the Michaelis-Menten diagrams of $\mathbf{K^2}$ and $\mathbf{K^3}$ are shown in Figure 3.40. From the fitted data, the important kinetic parameters are extracted and listed in Table 3.19. It is worth noting that $\mathbf{K^2}$ has a higher activity than $\mathbf{K^3}$, but also a slightly higher Michaelis-Menten constant, i.e. lower substrate affinity. Nevertheless, the efficiency k_{cat}/K_M is still higher for $\mathbf{K^2}$ than for $\mathbf{K^3}$. The pH profile of the experiment with $\mathbf{L^2}$ and one eq of Fe^{III} (Figure 3.40 c) reveals somewhat different parameters than the one with $\mathbf{K^2}$. This leads to the conclusion that with less than two eq of Fe^{III} dinuclear complexes are not predominantly formed. Otherwise one would expect the same pK_a values and pH_{max} as well as halved activity at this pH, like in the case with $\mathbf{K^1}$. Unfortunately, no suitable fit was obtained with $\mathbf{L^3}$ and one eq of Fe^{III} (Figure 3.40 d). The pH profile resembles that of a mononuclear complex or, in other words, a monoprotic system. These findings are in good agreement with the analytic results of *in situ* prepared complex solutions described in Chapter 3.3.2.1. Again, a linear behavior was observed in experiments with varying catalyst concentrations (the data are not shown).

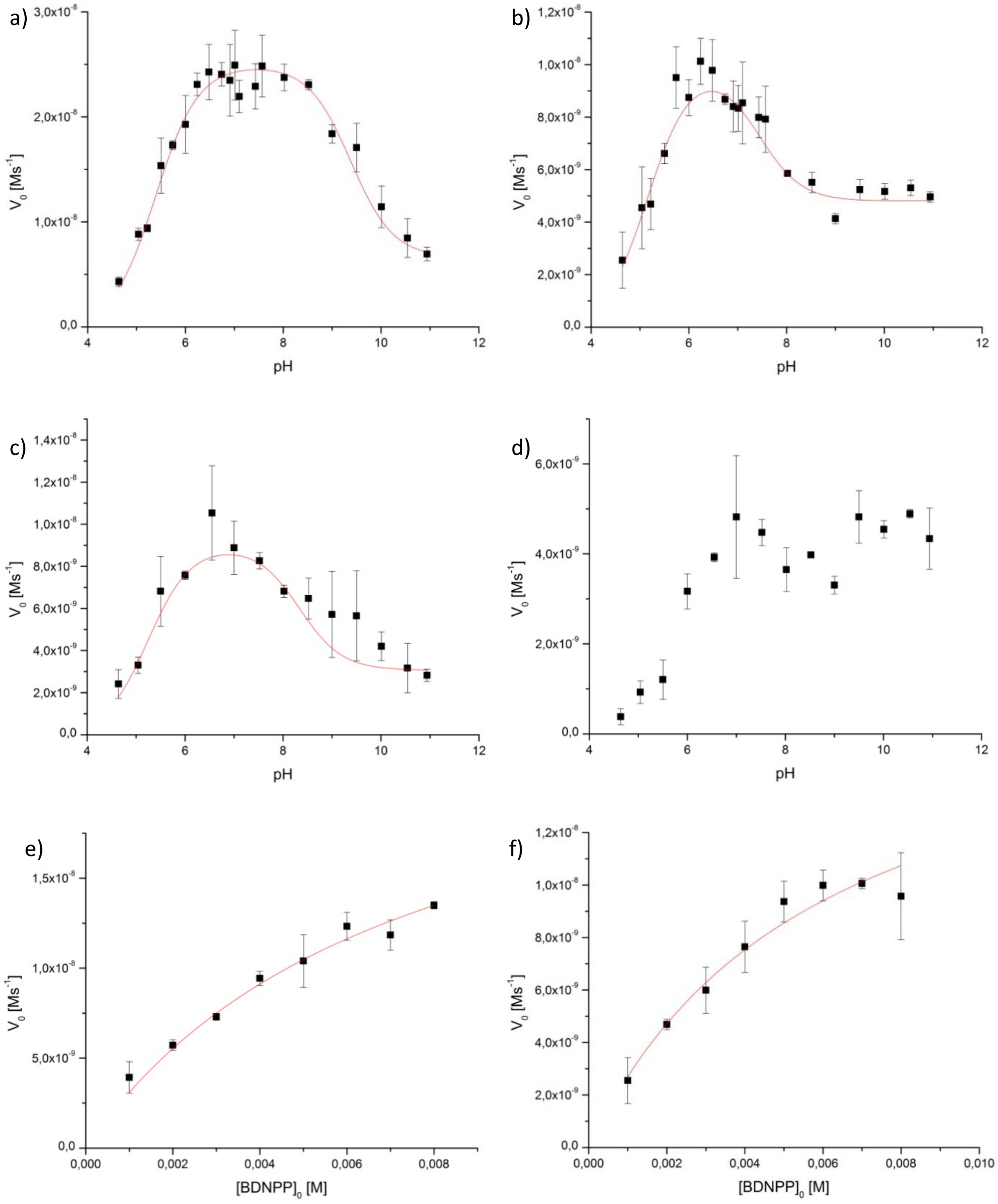

Figure 3.40: Results from kinetic analysis of BDNPP hydrolysis: pH profiles for a) $\mathbf{K^2}$, b) $\mathbf{K^3}$, c) $\mathbf{L^2}$ with 1 eq of Fe^{III}, d) $\mathbf{L^3}$ with 1 eq of Fe^{III} and Michaelis-Menten diagrams for e) $\mathbf{K^2}$ (pH 7.5) and f) $\mathbf{K^3}$ (pH 6.5). The experimental data are shown as black squares, the red lines represent the fits using equations 3.8 and 3.9 for pH-profiles and Michaelis-Menten diagrams, respectively.

Table 3.19: Kinetic parameters for BDNPP hydrolysis with $\mathbf{K^2}$ and $\mathbf{K^3}$ as well as $\mathbf{L^2}$ and $\mathbf{L^3}$ with 1 eq of Fe^{III}.

catalyst	pH_{max}	$pK_a(I)$	$pK_a(II)$	k_{cat} $[s^{-1}]$ *10^{-4}	K_M [M] *10^{-3}	k_{cat}/K_M $[M^{-1}s^{-1}]$ *10^{-2}
$\mathbf{K^2}$	7.44	5.39 ± 0.03	9.38 ± 0.10	6.48 ± 0.34	7.38 ± 0.69	8.79 ± 0.12
$\mathbf{L^2Fe}$	6.90	5.24 ± 0.08	8.34 ± 0.11	n.a.	n.a.	n.a.
$\mathbf{K^3}$	6.45	5.16 ± 0.10	7.43 ± 0.11	4.67 ± 0.26	5.92 ± 0.62	7.89 ± 0.09
$\mathbf{L^3Fe}$	n.a.	n.a.	n.a.	n.a.	n.a.	n.a.

The pH dependent activity profiles and pK_a values obtained can now be judged against the fitted data from the spectrophotometric titrations (Chapter 3.3.2.1). However, one must consider that these two experiments were performed in different media (MeCN/buffer vs. MeOH/buffer for kinetic and spectrophotometric assays, respectively). Therefore, some differences can be expected, although the pH should not change dramatically due to the use of buffered solutions. Furthermore, the kinetic data are obtained in the presence of substrate, which also might change the pH dependent properties of the complexes. As one can see in Figure 3.41, the pH profile of $\mathbf{K^2}$ fits better to the four-species-model fit (c) than to the one with only three species (a). In contrast, the profile of $\mathbf{K^3}$ resembles more the fit with three species only (b). These trends are also evident for the pK_a values compared in Table 3.20. In summary, this is a further support for the protonation equilibria depicted in Chapter 3.3.2.1.

Table 3.20: Comparison of pK_a values for $\mathbf{K^2}$ and $\mathbf{K^3}$ obtained by kinetic analysis and spectrophotometric titration (Chapter 3.3.2.1) with a three-species- or four-species-model, respectively.

	$\mathbf{K^2}$			$\mathbf{K^3}$		
	kinetic	*3 species*	*4 species*	*kinetic*	*3 species*	*4 species*
$pK_a(I)$	5.39 ± 0.03	5.98 ± 0.12	5.18 ± 0.19	5.16 ± 0.10	5.19 ± 0.17	4.85 ± 0.22
$pK_a(II)$	9.38 ± 0.10	10.57 ± 0.57	10.38 ± 0.35	7.43 ± 0.11	8.69 ± 0.14	9.05 ± 0.19

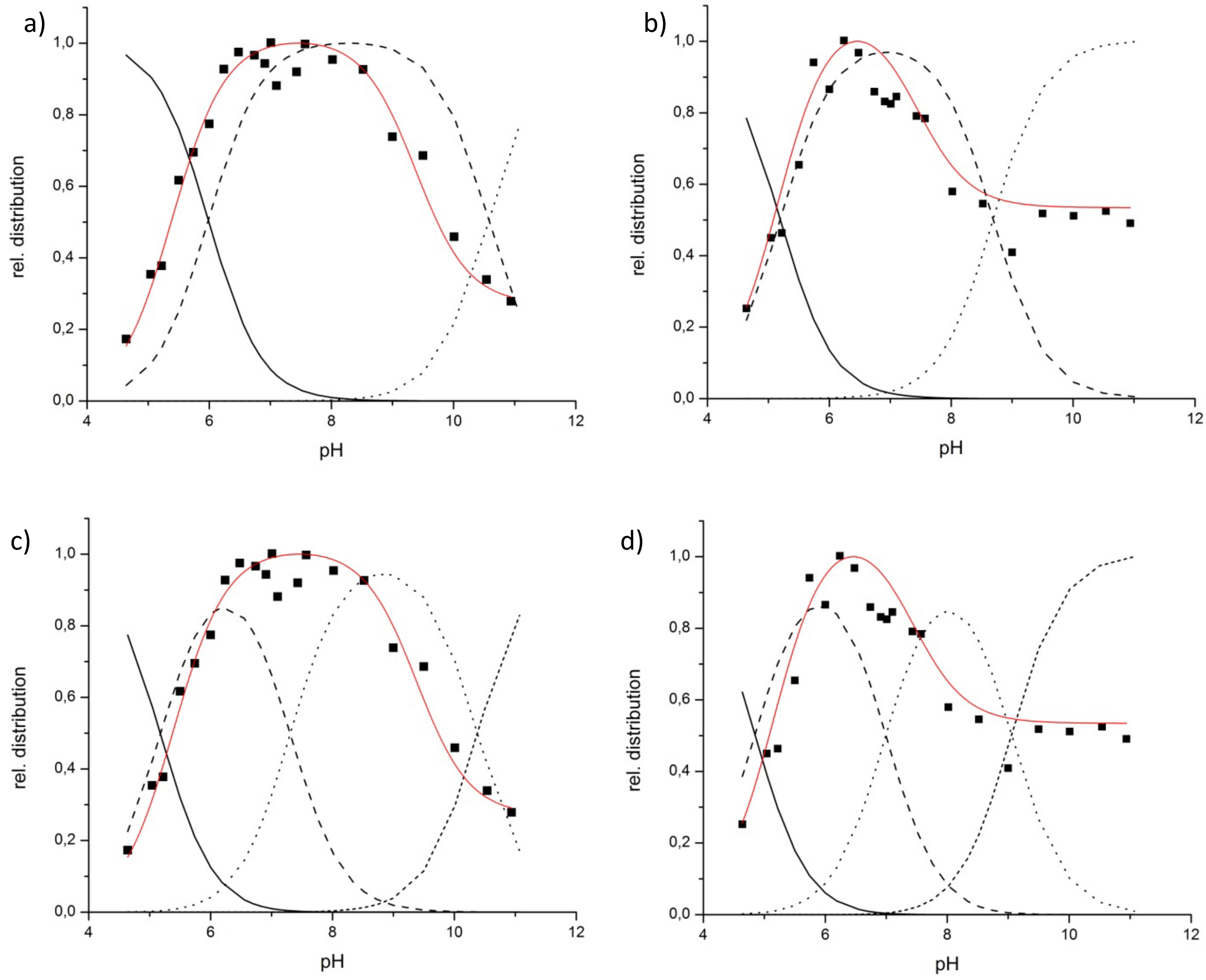

Figure 3.41: Overlays of species distribution (from spectrophotometric titrations) and kinetic pH profiles of BDNPP hydrolysis with a) **K**^{2} and b) **K**^{3} in the three-species-model as well as c) **K**^{2} and d) **K**^{3} in the four-species-model.

3.4.2.2. Monoesterase Activity of K^2 and K^3

Despite the relatively low activity of **K**^{2} and **K**^{3} towards hydrolysis of BDNPP, both complexes were tested for activity towards monoesters. DNPP was used as substrate with c_0 = 0.5 mM, as in the case with **K**^{1}. At first, quick tests were performed regarding activity at the pH which had maximum activity with BDNPP. **K**^{2} was tested at pH 7.5 and resulted in V_0 = $4.2*10^{-9}$ Ms^{-1}, which corresponds to an acceleration of only 20 % vs. the autohydrolysis reaction. **K**^{3} had its maximum activity at pH 6.5 and revealed a V_0 of only $2.4*10^{-9}$ Ms^{-1}

under these conditions (10 % acceleration). Due to the very low activity of $\mathbf{K}^3$ we decided to perform a full pH profile analysis only on $\mathbf{K}^2$ (Figure 3.42 a).

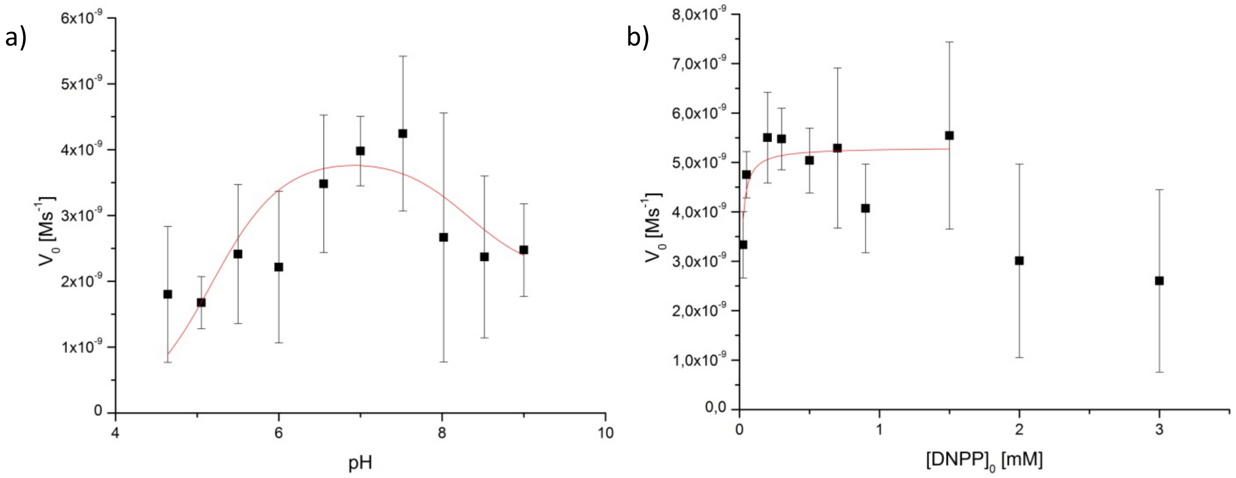

Figure 3.42: Results from kinetic analysis of DNPP hydrolysis by $\mathbf{K}^2$: a) pH profile and b) Michaelis-Menten diagram (pH 7). The experimental data are shown as black squares, the red lines represent the fits using equations 3.8 and 3.9 for pH-profiles and Michaelis-Menten diagrams, respectively.

The large errors and the flat curve make it difficult to fit the data properly. However, the pKa values of 5.17 ± 0.12 and 8.32 ± 0.59 and the maximum activity pH of 6.95 resemble in some way the values for BDNPP hydrolysis with $\mathbf{K}^2$. Substrate dependent measurements show that the plateau of the reaction rate is already reached at very low DNPP concentrations but also with a small value of V_0 ($K_M = 9.7 \pm 4.5$ µM; $V_{max} = 5.3 \pm 0.3 * 10^{-9}$ Ms^{-1}; Figure 3.42 b). One can even observe a decrease of the reaction rate at concentrations larger than 2 mM, which is certainly due to the high autohydrolysis rate of the DNPP molecule (see Appendix 9). The resulting k_{cat} is $1.33 \pm 0.08*10^{-4}$ s^{-1} and the catalytic efficiency k_{cat}/K_M is 13.6 ± 0.1.

3.4.3. Comparison of K^1, K^2 and K^3 in Hydrolysis of Phosphoesters

The presented PAP mimics **K**^{1}, **K**^{2} and **K**^{3} have quite different kinetic parameters, which is due to their completely different ligands. Nevertheless, these data are important to analyze the effects of alterations of the model systems, i.e. the incorporation of a second coordination sphere mimic in this case. Table 3.21 summarizes the results and compares them to literature known catalysts. Although PAP enzymes show no activity in the diferric state,[55, 156] some PAP mimetics containing a di-Fe^{III} core are reported to catalyze BDNPP hydrolysis.[97, 98, 100, 158] Unfortunately, only in one case the same experimental conditions (concentrations, temperature, buffer system) were applied (entry [a] in Table 3.20),[158] so only these results can be directly related to ours. In comparison to known PAP mimetics, **K**^{1} has the highest catalytic efficiency k_{cat}/K_M (last column in Table 3.21; see also Table 2.3 in Chapter 2.3 for heteronuclear systems), which is mainly due to the low K_M value, i.e. **K**^{1} has a high affinity for BDNPP. This is a result of the diferric state of the complex, as Fe^{III} is known to be more lewis-acidic than divalent metals and therefore more efficiently binds substrates.

Table 3.21: Kinetic parameters for BDNPP hydrolysis with **K**^{1}, **K**^{2} and **K**^{3} in comparison to literature-known complexes.

catalyst	pH_{max}	pK_a(I)	pK_a(II)	k_{cat} $[s^{-1}]$ $*10^{-4}$	K_M [M] $*10^{-3}$	k_{cat}/K_M $[M^{-1}s^{-1}]$ $*10^{-2}$
K^1	6.17	5.03 ± 0.10	7.28 ± 0.12	13.3 ± 0.8	1.94 ± 0.37	68.3 ± 2.2
K^2	7.44	5.39 ± 0.03	9.38 ± 0.10	6.48 ± 0.34	7.38 ± 0.69	8.79 ± 0.12
K^3	6.45	5.16 ± 0.10	7.43 ± 0.11	4.67 ± 0.26	5.92 ± 0.62	7.89 ± 0.09
[a]	n.a.	5.00	10.50	35.0 ± 2.0	8.70 ± 0.60	40.0 ± 6.0
[b]	6.00	4.74	7.54	30.0	13.0	23.0
[c]	6.35	5.00 ± 0.11	7.15 ± 0.14	1.69 ± 0.14	1.74 ± 0.35	9.71 ± 0.08

[a] $[LFe^{III}_2(\mu\text{-}OAc)_2]^{2+}$;[158] L = *N*-(2-hydroxybenzyl)-*N*-(2-hydroxy-5-methyl-3{[(pyridine-2-ylmethyl)amino]-methyl}benzyl)amino-acetic acid; [b] $[LFe^{III}(\mu\text{-}OAc)_2Fe^{II}]^+$;[86] L = 2-bis[{2-pyridyl-methyl)-aminomethyl}-6-{(2-hydroxy-benzyl)-(2-pyridyl-methyl)}-amino-methyl]-4-methylphenol; [c] = $[(BPMP)Fe^{III}_2]^{5+}$; n.a. = data not available.

The obtained pK_a values and pH maximum for **K**^{1} are quite different to the cited diferric complex [a] but similar to the data for the heterovalent di-iron complex [b] (see Table 3.21). The second pK_a of the heterovalent complex belongs to an aqua/hydroxo to di-hydroxo deprotonation step, where the reaction takes place at an Fe^{II} bound water molecule. It is unclear, what causes the high second pK_a of 10.50 with the diferric complex [b]; an Fe^{III} bound water can be excluded. In both complexes, [a] and [b], only one co-ligand can be bound in addition to the ligand and a bridging oxo group. In our case, two potentially free coordination sites are present. Therefore, the second pK_a of **K**^{1} should be attributed to water bound to a ferric ion already bearing a hydroxo ligand (see Scheme 3.26). The difference of nearly two between the first and second pK_a fits nicely to the difference between two deprotonation steps at Fe^{III} hexa-aqua ions.[159]

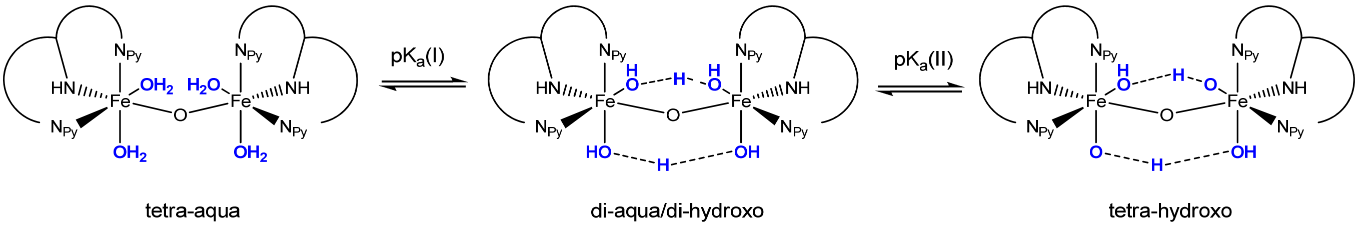

Scheme 3.26: Proposed deprotonation steps of **K**^{1}.

K^2 and **K**^{3} have an almost 10 fold lower catalytic efficiency k_{cat}/K_M in comparison to other diferric PAP mimetics. The substrate affinity K_M is in the same order of magnitude as catalyst [a], which is also based on a phenolate type ligand. In contrast, **K**^{1} has a significantly smaller K_M. Regarding the catalytic activity k_{cat}, catalyst [a] is ca. five times faster than **K**^{2} and **K**^{3}. This might be due to the different ligand setup with an additional acidic residue. No data are available in the literature regarding the catalytic abilities of the unsubstituted diferric HBPMP complex. Therefore, the ligand was synthesized, reacted with two eq of Fe^{III} *in situ* and tested for hydrolysis of BDNPP and DNPP under the same conditions as the other catalysts. The resulting k_{cat} is significantly smaller (ca. 4 times) than the one of **K**^{2}, but due to the low K_M of 1.74 mM the efficiency k_{cat}/K_M is in the same range as for **K**^{2} and **K**^{3}. Nevertheless, the higher activity k_{cat} in the **K**^{2} case accounts for a measurable effect of the additional amines.

Regarding the abilities of the different catalysts to hydrolyze monoester substrates, **K**^{2} is the most efficient catalyst so far, (k_{cat}/K_M in Table 3.22), whereas **K**^{1} has a slightly higher activity k_{cat}. The main difference between both systems is the large deviation of the K_M values. Interestingly, **K^2** has a higher affinity to DNPP than **K^1**, whereas in the case of BDNPP it is the other way round (see Table 3.21).

Table 3.22: Kinetic parameters for DNPP hydrolysis with **K^1** and **K^2**.

catalyst	pH_{max}	$pK_a(I)$	$pK_a(II)$	k_{cat} $[s^{-1}]$ $*10^{-4}$	K_M [µM]	k_{cat}/K_M $[M^{-1}s^{-1}]$
K^1	6.17	5.68 ± 0.27	6.33 ± 0.41	2.09 ± 0.09	170 ± 37	1.23 ± 0.14
K^2	6.95	5.17 ± 0.12	8.32 ± 0.59	1.33 ± 0.08	9.73 ± 4.48	13.60 ± 1.41

No other PAP mimic is known in the literature that can hydrolyze phosphomonoesters. Only bridging coordination of pNPP or DNPP is reported so far.[55, 92] **K^3** as well as the diferric complex of HBPMP show only minor acceleration of DNPP hydrolysis, which is in the range of the experimental error. We trace the observed activities of **K^1** and **K^2** back to the fact that both systems have an environment, which can act as a second coordination sphere mimic and favor hydrolysis over bridging binding of the monoester substrates. This was shown for **K^1** in Chapter 3.4.1.3. but is not yet proven in the case of **K^2**. Nevertheless, the large differences in K_M suggest that the influence of the second coordination sphere in both cases should be not identical.

3.5. *Summary and Outlook*

Purple acid phosphatases are versatile enzymes found in a large number of different species, including mammals, plants, fungi and bacteria. One of their roles is the hydrolysis of phosphoester substrates, more exactly phosphomonoesters. This function is for example used in plants for the mobilization of organic phosphates in soil, or bone resorption in mammals.

So far, no PAP mimetics with the ability to hydrolyze phosphomonoesters were reported in literature. Only the hydrolysis of activated phosphodiesters is possible with the known types of model compounds. Recent publications suggest that a) a monodentate coordination mode is necessary for hydrolytic activity and this is what takes place in the natural enzymes and b) in the PAP mimetics, a very fast reaction to bridging phosphomonoesters occurs, which produces a conformation that is inactive towards hydrolysis. In the enzymes, an extended hydrogen bonding network is responsible for perfect positioning of substrate and nucleophile. Also, it prevents the bridging coordination of substrates as well as products, which leads to a high activity. The new PAP mimetics presented in this work, $\mathbf{K^1}$, $\mathbf{K^2}$ and $\mathbf{K^3}$, are the first examples of diferric systems with additional functionalities that are designed to act as second coordination sphere mimic.

The μ-oxo bridged diferric complex $\mathbf{K^1}$ is readily formed from *in situ* reaction of the cyclam-based ligand $\mathbf{L^1}$ and tetrachloroferrate in MeCN. The high basicity of $\mathbf{L^1}$ is responsible for the formation of a μ-oxo bridged diferric precursor, which is then enclosed by the ligand´s coordinating units, leading to exclusive formation of dinuclear complexes. A thorough investigation of the coordination chemistry of $\mathbf{K^1}$ has been performed and the following conclusions can be drawn from the results: The *in situ* formed μ-oxo bridged character of $\mathbf{K^1}$ is retained under partly aqueous conditions, suggesting an inherent complex stability in the diferric state. Attempts to obtain the heterovalent $Fe^{III}Fe^{II}$ complex of $\mathbf{L^1}$ by bulk electrolysis of $\mathbf{K^1}$ were principally successful. Yet, the heterovalent complex cannot be isolated, even under anaerobic conditions. Most probably, a dispropotionation to the diferric and the diferrous state takes place. This behavior is typical for diferric complexes, where a direct ligand-based linker is missing. Experiments of $\mathbf{K^1}$ with different inactive phosphoesters gave interesting results regarding coordination modes and reaction equilibria. A clear distinction is drawn between phosphomono- and phosphodiesters. Whereas the results with monoesters suggest a bridging coordination mode of these substrate mimics, diesters are rather bound in a monodentate conformation. DFT calculations gave insight into the reasons for this observation: Hydrogen bonding interactions of the substrate BDNPP with the protonated cyclam moiety lead to the preference of a molecular structure, where the monodentately bound substrate is arranged in a way that disables direct coordination to the second metal ion. Therefore, the hydrolytically active monodentate coordination mode is retained. This is nicely reflected in a relatively high activity and efficiency of $\mathbf{K^1}$ towards BDNPP hydrolysis. In the case of the monoester analogue DNPP, the presence of only one 2,4-dinitrophenol group instead of two enables direct coordination to the second ferric ion without losing the energetically favorable interaction to the remote ligand parts. As a consequence, the inactive bridging coordination mode is preferred with monoesters. Nevertheless, the hydrogen bond to the protonated cyclam also influences the desired pathway, i.e. hydrolysis of the substrate by a terminal hydroxide bound to the second ferric ion. The calculated reaction profile shows an almost barrierless transition to the hydrolysis product. We therefore conclude that a certain part of the monoester will be hydrolyzed by $\mathbf{K^1}$ before reaching the inactive bridging mode. And in fact, a significant activity of $\mathbf{K^1}$ towards DNPP hydrolysis is observed – the first example of a truly functional PAP mimetic.

The two related complexes $\mathbf{K^2}$ and $\mathbf{K^3}$, synthesized from the phenolate based ligands $\mathbf{HL^2}$ and $\mathbf{H_3L^3}$, have a completely different structural setup compared to $\mathbf{K^1}$. They are designed in analogy to known model systems, like the symmetric ligand HBPMP, in order to directly compare the effects of a second coordination sphere mimic containing model in contrast to PAP mimetics without additional functionalities. $\mathbf{K^2}$ with its pendant amino groups represents a complex, where hydrogen bonding interactions between a coordinated substrate and the remote ligand parts are possible. In contrast, the pivaloylamido substitution of complex $\mathbf{K^3}$ leads to only one free coordination site per ferric ion, due to the coordination of the carbonyl oxygen atoms, and also induces a considerable steric strain onto the system. Reaction of $\mathbf{K^2}$ with phosphoesters shows similar results as seen with $\mathbf{K^1}$, namely bridging coordination of monoesters and monodentate coordination of diesters. This is rather unusual with these kinds of systems, as many crystal structures of phenolate based dinuclear complexes are known where a diester is bound in a bridging mode. Interestingly, $\mathbf{K^3}$ does not show signs of monodentate coordination of diesters, although one would expect steric interactions between their bulky residues and the ligand´s amido groups. These facts account for a significant effect of the amino groups in $\mathbf{K^2}$, suggesting interactions similar to those proposed for $\mathbf{K^1}$ and leading to a preference for monodentate binding of phosphodiesters. Regarding the phosphoester hydrolysis, this difference is nicely reflected by a significantly larger activity of

$\mathbf{K}^2$ towards hydrolysis of BDNPP as well as DNPP in contrast to $\mathbf{K}^3$ and the diferric complex of ligand HBPMP. Another exciting result regarding $\mathbf{K}^2$ and $\mathbf{K}^3$ is the observed formation of heterovalent complexes upon reaction with pNPP. This behavior is evocative of the proposed substrate driven *in vivo* redox regulation in mammalian PAP.

Many questions concerning both systems, $\mathbf{K}^1$ and $\mathbf{K}^2/\mathbf{K}^3$, remain under investigation. A direct proof for the positive influence of the cyclam and amino parts in $\mathbf{K}^1$ and $\mathbf{K}^2$ on phosphoester hydrolysis must be provided. So far, we base our suggestions on results from DFT calculations, which should be supported by experimental work. The main problem is how to knock out the proposed interactions selectively. In the case of $\mathbf{K}^2$ and $\mathbf{K}^3$, this problem is solved to some extent by the use of the pivaloyl protecting groups, which disable hydrogen bonding interactions. No successful experiments were performed so far regarding the interactions in $\mathbf{K}^1$.

An interesting experiment would be the use of Mössbauer spectroscopy. On one hand, this approach would further back up the proposed μ-oxo or μ-phenoxo bridged diferric nature of the complexes as well as the heterovalent state observed in $\mathbf{K}^2$pNPP and $\mathbf{K}^3$pNPP. On the other hand, we hope to gain a more detailed insight into the interactions of substrates and substrate mimics with the complexes and the influence on their electronic structure, especially in combination with Mössbauer parameters calculated by DFT methods.

Based on our results, the design and development of better and more realistic PAP mimetics should be continued. We have shown that the incorporation of a second coordination sphere into the model systems leads to a higher activity towards hydrolysis of phosphodiesters and, more importantly, allows hydrolysis of phosphomonoesters due to the stabilization of the active monodentate coordination mode.

Chapter 4:

Materials and Methods

4.1. Physical Measurements

NMR spectroscopy

NMR spectra were recorded at 399.89 MHz (^1H), 100.55 MHz (^{13}C) and 161.88 MHz (^{31}P) on a Bruker Avance II 400 instrument. For ^1H and ^{13}C spectra, the respective solvent peak and for ^{31}P spectra, 85% H_3PO_4 (0 ppm) was used as reference for the chemical shift δ. All reported coupling constants ^nJ are for ^1H-^1H couplings. The following abbreviations are used for signal multiplicities: s = singlet, bs = broad singlet, d = doublet, t = triplet, q = quartet, quin = quintet, dd = doublet of doublets, ddd = doublet of doublets of doublets, dt = doublet of triplets, tt = triplet of triplets, m = multiplet.

IR spectroscopy

IR measurements were performed with a Perkin Elmer 16 PC FT-IR spectrometer in KBr. Signal intensities are abbreviated as followed: b = broad, w = weak, m = medium, s = strong.

UV/vis spectroscopy

UV/vis spectra and time-course measurements at fixed wavelengths were recorded on a JASCO V-570 spectrophotometer equipped with a JASCO ETC-505T cryostat at 25°C. Time-dependent UV/vis measurements were performed by using a TIDAS II J&M spectrophotometer. The baseline was recorded prior to a measurement series using pure solvent and subtracted automatically. Fast processes were monitored by stopped-flow measurements using an Applied Photophysics PD.1 photodiode array stopped-flow spectrophotometer. A linear 256 element diode array APL xenon lamp served as the light source. For recording and handling the data, the software suite !XScan 1.09 by P.J. King (© AP Ltd. 1995) was used.

EPR spectroscopy

Liquid helium temperature X-band EPR spectra (ca. 9 GHz) were recorded on a Bruker Biospin ELEXSYS E580 spectrometer equipped with a Super High Q cavity and an Oxford Instruments ESR 910 cryostat with an ITC503 temperature controller at 1.8 to 16 K, located at the CAI (University of Queensland, Australia). The microwave frequency and magnetic field were calibrated with a Bruker frequency counter and an ER036 TM Tesla meter. Liquid nitrogen temperature and room temperature X-band EPR spectra (ca. 9 GHz) were recorded on a Bruker Biospin ELEXSYS E500 spectrometer with a Super High Q cavity located at the Institute of Inorganic Chemistry (University Heidelberg). In the case of liquid nitrogen cooling, an ITC4 temperature controller was used. Spin-Hamiltonian parameters were determined from computer simulation of the experimental spectra using MoSophe.[137] The simulated and experimental spectra were visualized with Xepr.[136]

Elemental analyses

Elemental analyses were performed in the analytical laboratories of the Chemical Institutes at the University of Heidelberg on an Elementar Vario EL machine.

Mass spectrometry

FAB mass spectra were measured on a Finnigan TSQ 700 instrument with nitrobenzylalcohol as matrix at the Institute of Inorganic Chemistry at the University of Heidelberg. ESI mass spectra were measured on a Micromass Q-TOF Ultima spectrometer at the Institute of Inorganic Chemistry at the University of Heidelberg. HR-ESI mass spectra were measured on a Bruker Apex-Qe hybrid 9.4 T FT-ICR instrument at the Institute of Organic Chemistry at the University of Heidelberg.

Cyclic voltammetry

CV measurements were performed on a CH Instruments CHI660D electrochemical workstation equipped with a faraday cage using a three-electrode setup consisting of a glassy carbon working electrode, a platinum wire as counterelectrode and a Ag/Ag^+ (0.1 mM in MeCN) reference electrode. The samples were prepared in degassed solvents with 0.1 M NBu_4ClO_4 as electrolyte. The redox potentials of the obtained signals were determinded by comparison to a $FeCp_2$ sample measured at the same conditions and referenced vs. SCE.

pH meter

pH values were adjusted at 25°C with a Metrohm 713 pH meter equipped with a KCl electrode and calibrated with pH standard solutions at pH 4, 7 and 9.

X-Ray Structure Analysis

The measurements were performed with a Stoe IPDS image plate and MoK_α radiation at low temperatures (200 K) in the laboratory of Prof. G. Linti at the Institute of Inorganic Chemistry, University of Heidelberg. The structures were solved and refined by Prof. G. Linti and Mr. T. Zessin using the software package SHELXTL 5.10.[160]

4.2. Chemicals

Solvents for organic synthesis were of standard quality and distilled prior to use. Solvents for complex synthesis and spectroscopy were of *p.a.* grade and used without further purification. Dry solvents were purchased form Sigma-Aldrich, stored over molecular sieves and used without further purification. For the kinetic assays, MilliQ water was used ($R > 18\ M\Omega$). Cyclam was purchased from ChemaTech, other chemicals from Sigma-Aldrich. All were used without purification, except 2,4-dinitrophenol, which was recrystallized, and phosphoryl chloride, which was distilled before use.

1,8-Dimethylcyclam,[119] *N*-tosylaziridine,[123, 124] di-(2-pyridyl)methyl chloride,[126] tetraethyl ammonium tetrachloroferrate,[128] 2,6-bis(chloromethyl)-4-methylphenol,[146, 147] 2-formyl-6-pivaloyl-amidopyridine,[145] BDNPP[154] and DNPP[155] were synthesized according to known literature procedures.

4.3. Syntheses

4.3.1. Synthesis of Ligand L^1

Di-(2-pyridyl)methyl chloride (12).

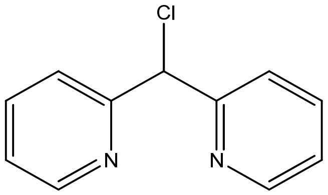

molecular formula:
$C_{11}H_9N_2Cl$
molecular weight:
204.66

Di-(2-pyridyl)ketone **10** (5.00 g, 27.10 mmol) is dissolved in dry MeOH (50 ml) and cooled to 0°C. $NaBH_4$ (1.30 g, 34.40 mmol) is added in small portions and the reaction mixture stirred over night at room temperature (rt). The solvent is removed *in vacuo*, the residue is taken up in water, acidified with 2M HCl and stirred for 10 min. The solution is made basic with diluted ammonia and extracted with DCM (3 x 50 ml). The organic phase is dried over Na_2SO_4 and the solvent is removed *in vacuo* to give di-2(pyridyl)methanol **11** as an orange oil (5.26 g, 100 %). It is dissolved in MeCN (60 ml) and cooled to 0°C. Triphenylphosphine (8.90 g, 22.9 mmol) in CCl_4 (50 ml) is added dropwise over 1.5h. The reaction mixture is stirred over night at rt, MeOH (5.5 ml) is added and after 15 min the reaction mixture is concentrated to ca. 1/3 original volume. Water (55 ml) is added and the mixture is brought to pH 1 with 2M HCl. It is washed with chloroform (2 x 55 ml), neutralized with K_2CO_3 and extracted with Et_2O (4 x 40 ml). The organic phase is dried over Na_2SO_4 and the solvent removed *in vacuo* to yield di-(2-pyridyl)methyl chloride **12** as a tan solid (4.32 g, 75 %).

^{1}*H-NMR* (400 MHz, $CDCl_3$): $\delta = 8.57$ (d, $^3J_{H,H} = 9.6$ Hz, 2H, N-CH_{ar}), 7.77 – 7.62 (m, 4H, CH_{ar}), 7.25 – 7.15 (m, 2H, CH_{ar}), 6.20 (s, 1H, Cl-C*H*).

^{13}*C-NMR* (100 MHz, $CDCl_3$): $\delta = 158.6$ (C_q), 149.3, 137.1, 123.0, 122.8 (C_{ar}H), 64.6 (Cl-CH).

N-Tosylaziridine (9).

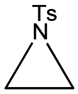

molecular formula:

$C_9H_{11}NO_2S$

molecular weight:

197.25

Tosylchloride (80.26 g, 0.42 mol) is dissolved in dry pyridine (50 ml) and cooled to -40°C. 2-Aminoethanol **7** (12.22 g, 0.20 mol) is added dropwise while maintaining the temperature and stiring. The reaction mixture is warmed up to -10°C, stirred for 1h, then warmed up to 0°C and stirred over night. Ice is added and the resulting precipitate is filtered off and washed with water. It is dissolved in chloroform, washed again with water and dried over Na_2SO_4. The solvent is removed *in vacuo*. The crude product is recrystallized in hot CCl_4 to give 2-tosylamidoethyltosylate **8** as white crystals (70.3 g, 95 %). In the next step, 2-tosylamidoethyltosylate (17.76 g, 48.10 mmol) is suspended in toluene and 3.5M KOH solution added dropwise. The resulting biphasic mixture is stirred vigorously for 2h, then the aqueous phase is removed. The organic phase is washed with water three times and dried over Na_2SO_4. The solvent is removed *in vacuo* to give *N*-tosylaziridine **9** as a brown oil, which solidifies upon standing (5.80 g, 61 %).

^{1}*H-NMR* (200 MHz, $CDCl_3$): $\delta = 7.83$ (d, $^3J_{H,H}$ = 8.2 Hz, 2H, CH_{ar}-CSO_2), 7.35 (d, $^3J_{H,H}$ = 8.2 Hz, 2H, CH_{ar}-CCH_3), 2.45 (s, 3H, CH_3), 2.36 (s, 4H, CH_2).

^{13}*C-NMR* (50 MHz, $CDCl_3$): $\delta = 144.6$ (C_q-SO_2), 134.8 (C_q-CH_3), 129.7 ($C_{ar}H$-CCH_3), 128.0 ($C_{ar}H$-CSO_2), 27.4 (CH_2), 21.6 (CH_3).

1,8-Dimethylcyclam (4).

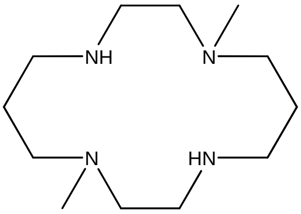

molecular formula:

$C_{12}H_{28}N_4$

molecular weight:

228.38

Cyclam **1** (1.65 g, 8.24 mmol) is dissolved in water (100 ml) and cooled to 0°C. Formalin (36 % in water, 1.50 ml) is added quickly and the reaction mixture stirred for 2h. The resulting white precipitate of 1,4,8,11-tetraazatricyclo[9.3.1.1^{4,8}]hexadecane **2** is filtered off, washed with water and dried *in vacuo* (1.65 g, 89 %). In the next step, it is dissolved in dry MeCN (50 ml) and methyl iodide (2.02 g, 14.23 mmol) is added quickly. After stirring for 2h, the white precipitate of 1,4,8,11-tetraazatricyclo[9.3.1.1^{4,8}]-1,8-dimethylhexadecanyl bis-iodide **3** is filtered off, washed with MeCN and dried *in vacuo* (3.51 g, 96 %). It is then stirred in 3M NaOH solution (750 ml) for 3h. After extraction with chloroform (5 x 200 ml), the organic phase is dried over Na_2SO_4 and the solvent is removed *in vacuo*. The product 1,8-dimethylcyclam **4** is obtained as a yellowish oil (1.60 g, 98 %).

^{1}H-NMR (400 MHz, $CDCl_3$): $\delta = 3.98$ (bs, 2H, NH_2), 2.71 – 2.62 (m, 8H, N-CH_2), 2.46 – 2.36 (m, 8H, N-CH_2), 2.17 (s, 6H, N-CH_3), 1.73 (quin, $^3J_{H,H} = 5.2$ Hz, 4H, C-CH_2-C).

^{13}C-NMR (100 MHz, $CDCl_3$): $\delta = 57.6$, 56.6, 49.8, 47.2 (N-CH$_2$), 41.8 (N-CH$_3$), 25.8 (C-CH$_2$-C).

1,8-Bis(2-tosylaminoethyl)-4,11-dimethylcyclam (5).

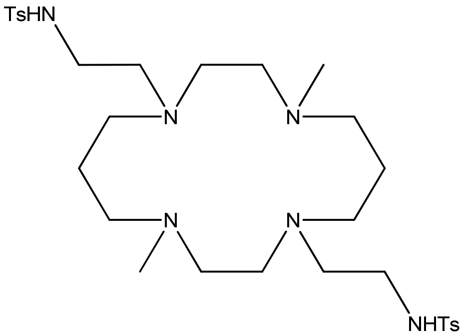

molecular formula:
$C_{30}H_{50}N_6O_4S_2$
molecular weight:
622.89

1,8-Dimethylcyclam **4** (1.00 g, 4.38 mmol) is dissolved in dry MeCN (30 ml). It is heated to reflux and *N*-tosylaziridine **9** (2.10 g, 10.66 mmol) in dry MeCN (30 ml) is added dropwise. The reaction mixture is refluxed for 6h. The solvent is removed *in vacuo* and the residue is recrystallized in hot DCM/EtOH (1:1) to yield **5** as a tan powder (1.80 g, 66 %).

^{1}H-NMR (400 MHz, $CDCl_3$): $\delta = 8.94$ (bs, 2H, NH), 7.72 (d, $^3J_{H,H} = 4.0$ Hz, 4H, CH_{ar}-CSO$_2$), 7.24 (d, $^3J_{H,H} = 4.0$ Hz, 4H, CH_{ar}-CCH$_3$), 2.88 (bt, $^3J_{H,H} = 5.2$ Hz, 4H, CH_2NH), 2.5-2.3 (m, 26H, Ph-CH_3 and all N-CH_2), 2.24 (s, 6H, N-CH_3), 1.65 (bs, 4H, C-CH_2-C).

^{13}C-NMR (100 MHz, $CDCl_3$): δ = 142.2 (C_q-SO_2), 138.3 (C_q-CH_3), 129.3 (C_{ar}H-CCH_3), 126.8 (C_{ar}H-CSO_2), 55.0, 54.1, 50.9, 50.7, 47.1 (all N-CH_2), 43.4 (N-CH_3), 42.3 (CH_2-NH), 24.8 (C-CH_2-C), 21.4 (CH_3-Ph).

FAB$^+$-MS (nibeol): *m/z* (%): 623.5 (91) $[M+H]^+$.

El. analysis (%):	calc. for $C_{30}H_{50}N_6O_4S_2$:	C: 57.85	H: 8.09	N: 13.49;
(Rep. No. 26336)	found:	C: 57.71	H: 8.12	N: 13.56.

1,8-Bis(2-aminoethyl)-4,11-dimethylcyclam (6).

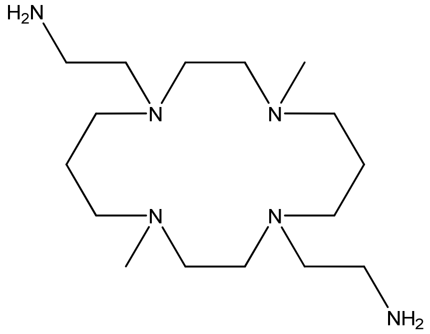

molecular formula:
$C_{16}H_{38}N_6$
molecular weight:
314.51

1,8-Bis(2-tosylaminoethyl)-4,11-dimethylcyclam **5** (1.00 g, 1.61 mmol) and conc. H_2SO_4 (7.5 ml) are heated to 100°C for 48h. The reaction mixture is added dropwise to diethylether. The resulting white precipitate is filtered off and washed with diethylether, dissolved in water (20 ml) and 3M NaOH solution is added until the solution reached pH 14. The product is extracted with chloroform (5 x 15 ml). The organic phase is dried over Na_2SO_4 and the solvent is removed *in vacuo* to yield **6** as a yellowish oil (0.50 g, 100 %).

^{1}H-NMR (400 MHz, $CDCl_3$): δ = 2.64 (t, $^3J_{H,H}$ = 5.6 Hz, 4H, CH_2-NH_2), 2.47-2.35 (m, 20H, all N-CH_2), 2.13 (s, 6H, N-CH_3), 1.85 (bs, 4H, NH_2), 1.55 (quin, $^3J_{H,H}$ = 6.8 Hz, 4H, C-CH_2-C).

^{13}C-NMR (100 MHz, $CDCl_3$): δ = 57.5, 54.6, 54.5, 51.5, 51.8 (N-CH_2), 43.2 (N-CH_3), 39.6 (CH_2-NH_2), 24.6 (C-CH_2-C).

FAB$^+$-MS (nibeol): *m/z* (%): 315.3 (100) $[M+H]^+$.

4,11-Dimethyl-1,8-bis[*N*-(2-di-(2-pyridyl)methyl)ethylamino]cyclam (L^1).

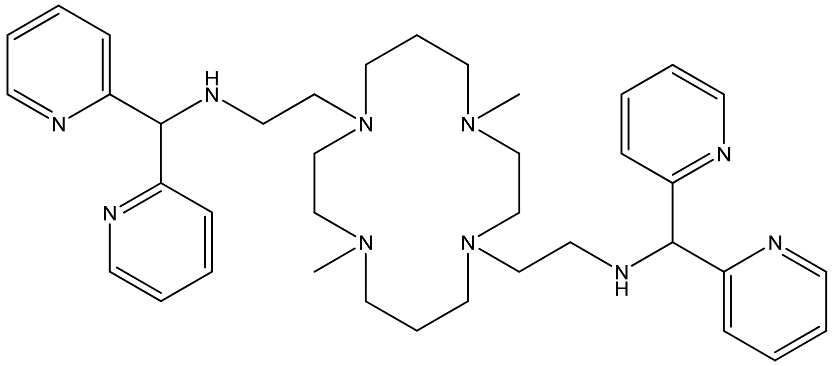

molecular formula:

$C_{38}H_{54}N_{10}$

molecular weight:

650.90

1,8-Bis(2-aminoethyl)-4,11-dimethylcyclam **6** (0.45 g, 1.43 mmol), di-(2-pyridyl)methylchloride **12** (0.60 g, 2.86 mmol) and potassium carbonate (0.41 g, 2.86 mmol) are dissolved in dry acetonitrile under argon and refluxed for 24h. After cooling down, the reaction mixture is poured into water (60 ml). Sodium hydroxide is added until the solution reached pH 14. The product is extracted with ethyl acetate (3 x 50 ml). The organic phase is dried over K_2CO_3 and the solvent is removed *in vacuo*. The crude product is purified by column chromatography (neutral alumina, chloroform/methanol 99:1 till 95:5). The resulting oil is recrystallized in hot hexane to yield **L^1** as pale yellowish crystals (0.24 g, 26 %).

^{1}H-NMR (400 MHz, $CDCl_3$): $\delta = 8.53$ (dd, $^3J_{H,H} = 4.8$ Hz, $^4J_{H,H} = 1.2$ Hz, 4H, CH_{ar}N), 7.60 (dt, $^3J_{H,H} = 8.0$ Hz, $^4J_{H,H} = 1.2$ Hz, 4H, CH_{ar} para to N), 7.48 (d, 4H, C$H_{ar}C_q$), 7.10 (ddd, 4H, $^3J_{H,H} = 8.0$ Hz, $^3J_{H,H} = 4.8$ Hz, $^4J_{H,H} = 1.2$ Hz, CH_{ar}CHN), 5.06 (s, 2H, C*H*Py_2), 3.12 (bs, 2H, N*H*), 2.7-2.2 (m, 24H, all N-CH_2), 2.11 (s, 6H, N-CH_3), 1.47 (quin, 4H, $^3J_{H,H} = 6.8$ Hz, 4H, C-CH_2-C).

^{13}C-NMR (100 MHz, $CDCl_3$): $\delta = 161.9$ ($C_{ar,q}$), 149.2, 136.5, 122.2, 122.0 (C_{ar}), 70.3 (*C*HPy_2), 54.5, 54.3, 53.9, 51.7, 50.8 (all N-*C*H_2), 45.7 (*C*H_2-NH), 43.5 (N-*C*H_3), 24.1 (C-*C*H_2-C).

IR (KBr): $\tilde{\nu}$ [cm^{-1}]= 3439 (b), 3282 (m), 2981 (m), 2937 (m), 2846 (m), 2792 (s), 1674 (s), 1565 (s), 1599 (m), 1473 (s), 1466 (s), 1435(s), 1294 (m), 1162 (m), 1125 (m), 1114 (m), 999 (w), 929 (m), 887 (w), 809 (m), 771 (m).

FAB$^+$-MS (nibeol): *m/z* (%): 651,6 (97) $[M+H]^+$.

El. analysis (%):	calc. for $C_{38}H_{54}N_{10} \times H_2O$:	C: 68.23	H: 8.44	N: 20.94;
(Rep. No. 26337)	found:	C: 68.69	H: 8.43	N: 21.05.

4.3.2. Synthesis of Complexes of L^1.

Tetraetylammonium tetrachloroferrate (13).

$[FeCl_4](NEt_4)$

molecular formula:
$C_8H_{20}NFeCl_4$
molecular weight:
327.91

Ferric chloride (779 mg, 4.80 mmol) and tetraethylammonium chloride (794 mg, 6.10 mmol) are dissolved separately in 10 ml EtOH each. The solutions are combined and the resulting yellow precipitate is filtered off, washed with EtOH and dried *in vacuo* (1.15 g, 73 %).

UV/vis (MeCN): λ_{max} [nm] (ε [$M^{-1}cm^{-1}$]) = 272 (4643), 315 (sh) (6943), 363 (7308).

El. analysis (%):	calc. for $C_8H_{20}NFeCl_4$ x 0.1 $FeCl_3$:	C: 27.95	H: 5.85	N: 4.10;
(Rep. No. 24914)	found:	C: 27.95	H: 5.92	N: 3.95.

$[H_2L^1Fe_2OCl_4](Cl)_2$ (14).

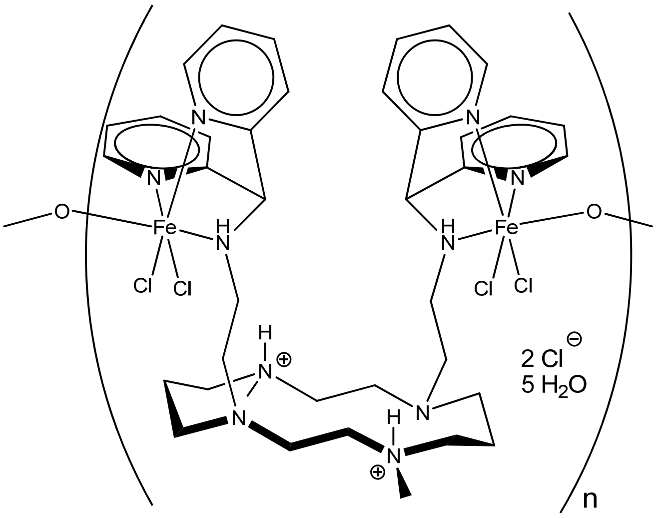

molecular formula:
$C_{38}H_{54}N_{10}OFe_2Cl_4$ x $5H_2O$ x 2HCl
molecular weight:
1083.40

Ligand **L^1** (195 mg, 0.30 mmol) and $[FeCl_4](NEt_4)$ (197 mg, 0.60 mmol) are separately dissolved in MeCN (30 and 3 ml, respectively) and the solutions are combined while stirring.

The resulting ochre precipitate is filtered off, washed with cold MeCN and dried *in vacuo* (215 mg, 67 %).

HR-ESI$^+$-MS (MeCN, 1% H_2O): *m/z* (%): 921.19821 (calc. 921.19838) (100) $[HLFe^{III}_2Cl_4O]^+$; 883.22483 (calc. 883.22439) (69) $[LFe^{III}_2Cl_3O]^+$; 741.35780 (calc. 741.35709) (14,6) $[LFe^{II}Cl]^+$.

UV/vis (MeCN, 1% H_2O): λ_{max} [nm] (ε [$M^{-1}cm^{-1}$]) = 256 (48470), 315 (sh) (23783), 378 (16450), 480 (sh) (900), 600 (143).

IR (KBr): $\tilde{\nu}$ [cm^{-1}] = 3439 (b), 2964 (w), 2859 (w), 1608 (s), 1593 (w), 1471 (s), 1449 (s), 1290 (w), 1158 (w), 1052 (w), 1022(m), 831 (m), 817 (m), 769 (m).

El. analysis (%):	calc. for $C_{38}H_{54}N_{10}OFe_2Cl_4$ x $5H_2O$ x 2HCl:				
(Rep. No. 26479)	C: 68.23	H: 8.44	N: 20.94	Cl: 19.63	Fe: 10.48;
found:	C: 68.69	H: 8.43	N: 21.05	Cl: 18.63	Fe: 10.51.

$[L^1Zn](OTf)_2$ (15).

$[\mathbf{L}^1Zn^{II}](OTf)_2$ x 1/3 $Zn(OH)_2$

molecular formula:
$C_{40}H_{54}N_{10}O_6S_2F_6Zn$ x 1/3 $Zn(OH)_2$
molecular weight:
1045.43

Ligand **L^1** (32.5 mg, 0.05 mmol) and Zn(II) triflate (18.2 mg, 0.05 mmol) are stirred in dry MeCN (9 ml) for one hour at rt. Diffusion of diethylether into the solution yields colourless crystals of **15** (0.05 g, 96 %).

HR-ESI$^+$-MS (MeCN): *m/z* (%): 357.19138 (calc. 357.19122) (87) $[LZn^{II}]^{2+}$; 863.33451 (863.33446) (61) $[LZn^{II}(OTf)_2]^+$.

El. analysis (%):	calc. for: $C_{40}H_{54}N_{10}O_6S_2F_6Zn$ x 1/3 $Zn(OH)_2$	C: 45.86 H: 5.26 N: 13.37;
(Rep. No. 26225)	found:	C: 45.90 H: 5.13 N: 13.00.

[$\mathbf{L^1}$Cu](OTf)$_2$ (16).

	molecular formula:
[$\mathbf{L^1}$Cu^{II}](OTf)$_2$ x MeCN	$C_{42}H_{57}N_{11}O_6S_2F_6Cu$
	molecular weight:
	1053.64

Ligand $\mathbf{L^1}$ (32.5 mg, 0.05 mmol) and Cu(II) triflate (18.1 mg, 0.05 mmol) are stirred in dry MeCN (4 ml) for one hour at rt. Diffusion of diethylether into the solution yields colourless crystals of **16** (50,0 mg, 95 %).

HR-ESI$^+$-MS (MeCN): *m/z* (%): 356.69148 (calc. 356.69145) (100) [LCu^{II}]$^{2+}$; 431.67117 (calc. 431.67137) (98) [HLCu^{II}(OTf)]$^{2+}$; 862.33687 (calc. 862.33492) (20) [LCu^{II}(OTf)]$^+$.

UV/vis (MeCN): λ_{max} [nm] (ε [M^{-1}cm^{-1}]) = 639 (45).

EPR (MeCN/buffer pH 6 1:1): $g_{\parallel} = 2.23$; $g_{\perp} = 2.05$; $A_{\parallel} = 180*10^{-4}$ cm^{-1}.

El. analysis (%):	calc. for: $C_{42}H_{57}N_{11}O_6S_2F_6Cu$	C: 47.88	H: 5.45	N: 14.62;
(Rep. No. 26226)	found:	C: 47.29	H: 5.47	N: 14.30.

4.3.3. Syntheses of Ligands HL^2 and H_3L^3

2,6-Bis(chloromethyl)-4-methylphenol (24).

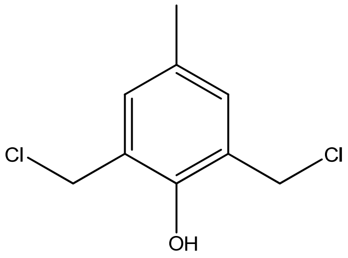

molecular formula:
$C_9H_{10}Cl_2O$
molecular weight:
205.08

2,6-Bis(hydroxymethyl)-4-methylphenol (16.50 g, 98.00 mmol) is stirred at rt in conc. HCl (200 ml) over night. After extraction with DCM (3 x 100 ml), the organic phases are dried over Na_2SO_4 and the solvent is removed in vacuo to give 2,6-bis(chloromethyl)-4-methylphenol as a yellow solid, which was stored at -20°C (19.49 g, 97 %).

^{1}*H-NMR* (400 MHz, $CDCl_3$): $\delta = 7.09$ (s, 2H, CH_{ar}), 4.66 (s, 4H, CH_2-Cl), 2.28 (s, 3H, CH_3).

^{13}*C-NMR* (100 MHz, $CDCl_3$): $\delta = 151.0$ (C_q-OH), 131.6 (CH_{ar}), 130.5 (C_q-CH_3), 124.7 (C_q-CH_2Cl), 42.4 (CH_2Cl), 20.3 (CH_3).

2-Formyl-6-pivaloylamidopyridine (20).

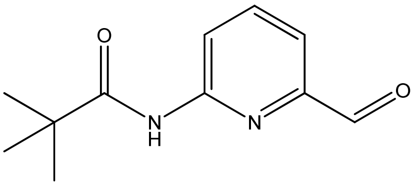

molecular formula:
$C_{11}H_{14}N_2O_2$
molecular weight:
206.24

2-Amino-6-methylpyridine **17** (54.07 g, 0.50 mol) is dissolved in a mixture of DCM (500 ml) and triethylamine (65.80 g, 0.65 mol). Pivaloylchloride (66.32 g, 0.55 mol) is added dropwise. The reaction is stirred at rt for 2h and quenched by adding water (100 ml). Phases are separated, the aq. phase is extracted with DCM (2 x 50 ml). The combined organic phases are dried over Na_2SO_4 and the solvent is removed *in vacuo*. The crude product is recrystallized from diethylether to give 2-methyl-6-pivaloylamidopyridine **18** as white crystals (79.84 g, 83 %). In the next step, **18** (9.62 g, 50.00 mmol) is dissolved in CCl_4 (130 ml). NBS (2.66 g, 15.00 mmol) and a catalytic amount of benzoylperoxide are addedand the mixture is refluxed (80°C). More portions of NBS (2.66 g, 15.00 mmol each) and benzoylperoxide are added after 2, 3, 4, 5, 6, 7 and 8h (i.e 120 mmol NBS, 2.4 eq). After the last addition, the solution is refluxed for a further hour and then cooled to rt over night. The next day, a 9th portion of NBS and benzoylperoxide is added and refluxed further 7h. After cooling to rt and filtering, the solvent is removed *in vacuo*. The resulting solid is dissolved in MeOH (70 ml) and KOH (5.20 g) in H_2O (30 ml) is added. The mixture is stirred at rt for 4h. The solvent is removed *in vacuo* and the residue dissolved in hexane (50 ml). The organic phase is washed with 6M HCl, then with $NaHCO_3$ solution and with brine, dried over Na_2SO_4. The solvent is removed *in vacuo* to yield 2-dibromomethyl-6-pivaloylamidopyridine **19** as an orange oil (10.25 g, 60%). **19** (8.00 g, 22.90 mmol) is dissolved in acetone (70 ml). $AgNO_3$ (11.65 g, 68.60 mmol) in H_2O (18 ml) is added and the mixture is stirred at rt over night in the dark. After filtration the solvent is removed *in vacuo*. The residue is dissolved in DCM (100 ml). The organic phase is washed with water, 0.5N $NaHCO_3$ and brine and dried over Na_2SO_4. The solvent is removed *in vacuo* to give 2-formyl-6-pivaloyamidopyridine **20** as clear oil (2.41 g, 51 %).

^{1}H-NMR (300 MHz, $CDCl_3$): $\delta = 9.86$ (s, 1H, C*H*=O), 8.44 (d, $^3J_{H,H} = 8.4$ Hz, NHC-CH_{ar}), 8.16 (bs, 1H, N*H*), 7.82 (t, $^3J_{H,H} = 8.4$ Hz, 1H, CH_{ar} para to N), 7.61 (dd, $^3J_{H,H} = 7.5$ Hz, $^4J_{H,H}$ = 0.9 Hz, 1H, HC(=O)C-CH_{ar}), 1.30 (s, 9H, CH_3).

^{13}C-NMR (75 MHz, $CDCl_3$): $\delta = 192.4$ (*C*H=O), 177.4 (*C*(=O)NH), 152.2 (N-C_q-NH), 150.9 (N-C_q-CHO), 139.4 (*C*H_{ar} para to N), 118.6, 118.4 (*C*H_{ar} meta to N), 40.4 ($C_{q,alkyl}$), 27.5 (*C*H_3).

N-(6-Pivaloylamido-2-pyridylmethyl)-*N*-(2-pyridylmethyl)amine (21).

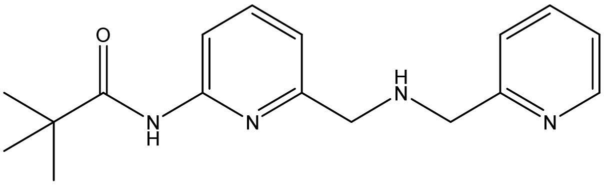

molecular formula:
$C_{17}H_{22}N_4O$
molecular weight:
298.38

2-Formyl-6-pivaloyamidopyridine **20** (2.20 g, 10.70 mmol) and picolylamine (1.27 g, 11.70 mmol) are dissolved in methanol (45 ml) and stirred for 2.5h at rt. The solution is cooled to 0°C and $NaBH_4$ (0.44 g, 11.70 mmol) is added in small portions. The mixture is stirred over night. H_2O (45 ml) is added and methanol is removed *in vacuo*. The aqueous phase is extracted with ethyl acetate (3 x 70 ml). The organic phase is dried over Na_2SO_4 and the solvent is removed in vacuo to give **21** as a yellow oil (3.52 g, 100 %).

^{1}H-NMR (300 MHz, $CDCl_3$): $\delta = 8.54$ (d, $^3J_{H,H} = 4.8$ Hz, 1H, N-CH_{ar}), 8.10 (d, $^3J_{H,H} = 8.0$ Hz, 1H, CH_{ar}), 7.68 – 7.56 (m, 2H, CH_{ar}), 7.34 (d, $^3J_{H,H} = 7.8$ Hz, 1H, CH_{ar}), 7.10 – 7.20 (m, 1H, CH_{ar}), 7.01 (d, $^3J_{H,H} = 7.4$ Hz, 1H, CH_{ar}), 4.00 (s, 2H, CH_2), 3.90 (s, 2H, CH_2), 3.50 (bs, 1H, NH_{aliph}), 1.31 (s, 9H, C(CH_3)$_3$).

^{13}C-NMR (100 MHz, $CDCl_3$): $\delta = 177.1$ (*C*=O), 158.4, 156.6, 151.2 ($C_{q,ar}$), 149.2, 138.8, 136.6, 122.5, 122.2, 118.0, 112.1 (CH_{ar}), 54.2, 53.7 (CH_2), 39.7 ($C(CH_3)_3$), 27.4 ($C(CH_3)_3$).

FAB$^+$-MS (nibeol): *m/z* (%): 299.2 (100) $[M+H]^+$.

N-(6-Amino-2-pyridylmethyl)-N-(2-pyridylmethyl)amine (22).

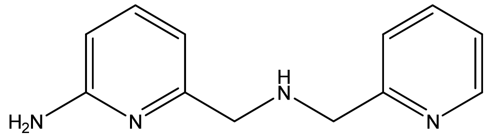

molecular formula:
$C_{12}H_{14}N_4$
molecular weight:
214.27

N-(6-Pivaloylamido-2-pyridylmethyl)-*N*-(2-pyridylmethyl)amine **21** (1.80 g, 6.00 mmol) is refluxed in 2M HCl (75 ml) for 48h. After cooling to rt, 1M NaOH solution is added until the pH reached 14. After extraction with DCM (3 x 200 ml), the organic phase is dried over Na_2SO_4 and the solvent is removed in vacuo to give **22** as a yellow oil (1.29 g, 100 %).

^{1}H-NMR (400 MHz, MeOH-d_4): $\delta = 8.55$ (d, $^3J_{H,H} = 4.8$ Hz, 1H, N-CH_{ar}), 7.82 (dt, $^3J_{H,H} = 7.8$ Hz, $^4J_{H,H} = 1.6$ Hz, 1H, CH_{ar}), 7.50 – 7.30 (m, 3H, CH_{ar}), 6.61 (d, $^3J_{H,H} = 7.2$ Hz, 1H, CH_{ar}), 6.49 (d, $^3J_{H,H} = 8.2$ Hz, 1H, arom. H), 4.12 (s, 2H, CH_2), 3.91 (s, 2H, CH_2).

^{13}C-NMR (100 MHz, $CDCl_3$): $\delta = 161.0$, 157.0, 154.3 ($C_{q,ar}$), 150.2, 139.8, 138.7, 124.3, 124.2, 112.4, 109.2 (CH_{ar}), 53.4 (2x) (CH_2).

FAB$^+$-MS (nibeol): *m/z* (%): 215.2 (100) $[M+H]^+$.

2,6-Bis[[[(6-pivaloylamido-2-pyridinyl)methyl](2-pyridinylmethyl)amino]methyl]-4-methylphenol (H_3L^3).

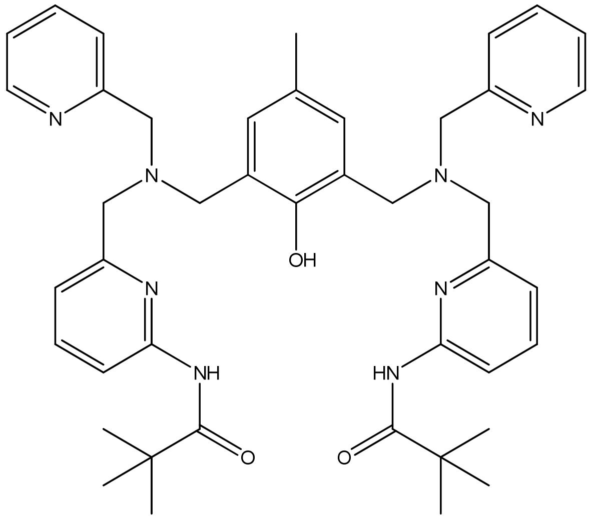

molecular formula:
$C_{43}H_{52}N_8O_3$
molecular weight:
728.92

2,6-Bis(chloromethyl)-p-cresol **24** (1.03 g, 5.00 mmol) is dissolved in DCM (8 ml) and cooled to 0°C. *N*-(6-Pivaloylamido-2-pyridylmethyl)-*N*-(2-pyridylmethyl)amine **21** (2.98 g, 10.00 mmol) and triethylamine (1.01 g, 10.00 mmol) are dissolved in THF (9 ml) and added dropwise. The solution is stirred at rt for 2d. It is filtered and the solvents are removed *in vacuo*. The residue is dissolved in DCM (75 ml), washed with brine, dried over Na_2SO_4 and the solvent is removed in vacuo to give **H_3L^3** as a pale-brown foam (3.64 g, 100 %).

^{1}H-NMR (500 MHz, $CDCl_3$): $\delta = 8.48$ (d, $^3J_{H,H}$ = 4.1 Hz, 2H, CH_{py}-N), 8.25 (bs, 2H, N*H*), 8.08 (d, $^3J_{H,H}$ = 9.0 Hz, 2H, HNC_q-CH_{py}), 7.61 (t, $^3J_{H,H}$ = 7.8 Hz, 2H, para to N), 7.56 (dt, $^3J_{H,H}$ = 7.6 Hz, $^4J_{H,H}$ = 1.8 Hz, 2H, CH_{py} para to N), 7.48 (d, $^3J_{H,H}$ = 7.8 Hz, 2H, CH_{py}), 7.14 – 7.06 (m, 4H, CH_{py}), 7.05 (s, 2H, CH_{phenol}), 3.86 (s, 4H, CH_2), 3.80 (s, 4H, CH_2), 3.77 (s, 4H, CH_2), 2.26 (s, 3H, phenol-CH_3), 1.31 (s, 18H, $C(CH_3)_3$).

^{13}C-NMR (125 MHz, $CDCl_3$): $\delta = 177.2$ (NH-*C*=O); 155.5 ($C_{q,py}$), 153.1 ($C_{q,py}$), 151.1 (C_q-OH), 148.8 (CH_{py}-N), 148.7 (C_q-NH), 138.9, 136.7 (CH_{py}), 136.6 (C_q-CH_3), 130.0 (CH_{phenol}), 127.8 (C_q-CH_2), 123.0, 122.0, 117.9, 111.8 (CH_{py}), 59.8, 58.7 (N-CH_2-py), 54.8 (N-CH_2-phenol), 39.8 ($C(CH_3)_3$), 28.0 ($C(CH_3)_3$), 20.6 (CH_3).

FAB$^+$-MS (nibeol): *m/z* (%): 729.4 (100) $[M+H]^+$.

IR (KBr): $\tilde{\nu}$ [cm^{-1}] = 3559 (b), 3396 (w) 3065 (w), 2964 (m), 2929 (m), 2870 (m), 2821 (m), 1690 (s), 1596 (s), 1578 (s), 1523 (s), 1478 (s), 1455 (s), 1403 (m), 1367 (m), 1304 (s), 1224 (m), 1152 (m), 1125 (w), 1082 (w), 996 (m), 861 (w), 799 (m), 760 (m), 623 (w), 577 (w).

El. analysis (%):	calc. for $C_{43}H_{52}N_8O_3$ x 0.33 DCM:	C: 68.73	H: 7.01	N: 14.80;
(Rep. No. 27951)	found:	C: 68.69	H: 7.07	N: 14.56.

2,6-Bis[[[(6-amino-2-pyridinyl)methyl](2-pyridinylmethyl)amino]methyl]-4-methyl-phenol (HL^2).

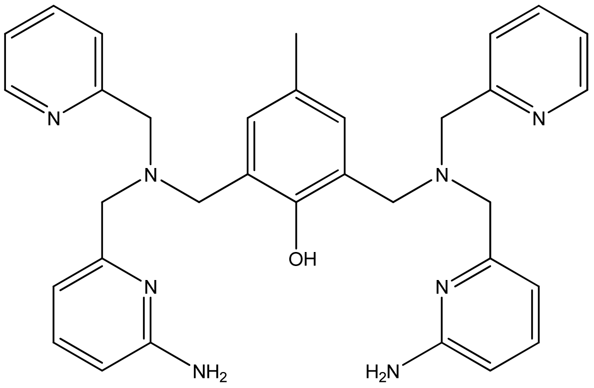

molecular formula:

$C_{33}H_{36}N_8O$

molecular weight:

560.69

2,6-Bis(chloromethyl)-p-cresol **24** (0.62 g, 3.00 mmol) is dissolved in DCM (5 ml) and cooled to 0°C. *N*-(6-Amino-2-pyridylmethyl)-*N*-(2-pyridylmethyl)amine **22** (1.29 g, 6.00 mmol) and tri-ethylamine (0.61 g, 6.00 mmol) are dissolved in THF (6 ml) and added dropwise. The solution is stirred at rt for 2d. It is filtered and the solvents are removed *in vacuo*. The residue is dissolved in DCM (50 ml), washed with brine, dried over Na_2SO_4 and the solvent is removed *in vacuo* to give **HL^2** as a pale-brown foam (1.62 g, 96 %).

^{1}H-NMR (500 MHz, $CDCl_3$): δ = 8.47 (d, $^3J_{H,H}$ = 4.4 Hz, 2H, CH_{py}-N), 7.56 (t, $^3J_{H,H}$ = 8.2 Hz, 2H, CH_{py} para to N), 7.35 (t, $^3J_{H,H}$ = 7.8 Hz, 2H, CH_{py} para to N), 7.08 (m, 4H, CH_{py}), 6.97 (s, 2H, CH_{phenol}), 6.78 (d, 2H, $^3J_{H,H}$ = 7.2 Hz, NH_2C_q-CH_{py}), 6.34 (d, 2H, $^3J_{H,H}$ = 8.0 Hz, CH_{py}), 4.50 (bs, 4H, NH_2), 3.84 (s, 4H, CH_2), 3.74 (s, 4H, CH_2), 3.69 (s, 4H, CH_2), 2.22 (s, 3H, CH_3).

^{13}C-NMR (125 MHz, $CDCl_3$): δ = 159.2 (C_q-NH_2), 157.9, 153.5 ($C_{q,py}$), 149.1 (C_q-OH), 148.6 (CH_{py}-N), 138.5, 136.5, 130.1 (CH_{phenol}), 127.2 (C_q-CH_3), 123.0 (CH_{py}), 122.4 (C_q-CH_2), 121.9, 112.5, 107.2 (CH_{py}), 59.7, 58.9 (N-CH_2-py), 55.0 (N-CH_2-phenol), 20.6 (CH_3).

FAB$^+$-MS (nibeol): *m/z* (%): 561.3 (100) $[M+H]^+$.

IR (KBr): $\tilde{\nu}$ [cm^{-1}] = 3454 (b), 3380 (b), 3342 (b), 3187 (w), 2915 (w), 2814 (w), 1615 (s), 1594 (s), 1571 (s), 1465 (s), 1434 (s), 1361 (m), 1298 (m), 1229 (m), 1159 (w), 1119 (w), 1092 (w), 1045 (w), 996 (m), 864 (w), 790 (m), 760 (m).

El. analysis (%):	calc. for $C_{33}H_{36}N_8O$ x 0.33 DCM:	C: 67.97	H: 6.27	N: 19.02;
(Rep. No. 24914)	found:	C: 68.11	H: 6.28	N: 17.51.

4.3.4. Syntheses of Diferric Complexes of HL^2 and H$_3$L^3

[H$_2$L^{2}Fe$_2$(OH)$_3$](ClO$_4$)$_3$(OH) (25).

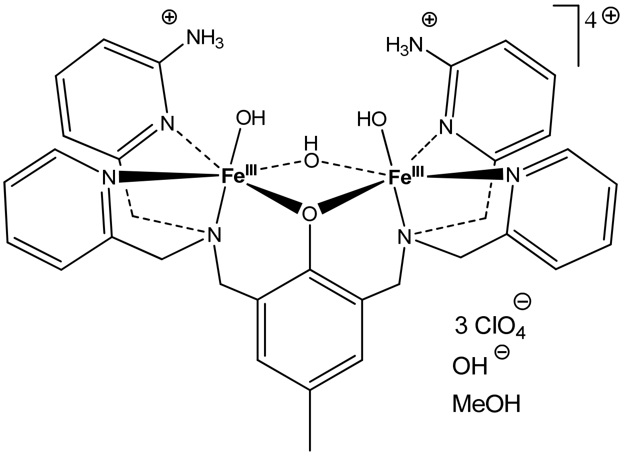

molecular formula:

$C_{33}H_{40}N_8Cl_3Fe_2O_{16}$ x MeOH x OH^-

molecular weight:

1071.81

Ligand **HL^2** (200 mg, 0.35 mmol) is dissolved in 50 ml MeOH and heated to 50°C. Ferric perchlorate hydrate (250 mg, 0.70 mmol) is added in 5 ml MeOH while stirring. The solution immediately turns dark blue and is heated at 50°C for 1h. The solvent is removed *in vacuo* and the residue is taken up in a small volume of MeCN. The complex is precipitated by diffusion of diethylether into the solution. The product is filtered off and dried *in vacuo* to yield **25** as a very dark blue powder (0.29 g, 77 %).

HR-ESI$^+$-MS (MeOH): not detectable.

UV/vis (MeCN): λ_{max} [nm] (ε [M^{-1}cm^{-1}]) = 232 (28065), 256 (sh) (19297), 302 (16044), 365 (sh) (4374), 593 (1893).

IR (KBr): $\tilde{\nu}$ [cm^{-1}] = 3370 (b), 3201 (b), 3094 (w), 2940 (w), 2865 (w), 2022 (w), 1661 (s), 1634 (s), 1572 (m), 1480 (m), 1445 (m), 1298 (w), 1265 (w), 1144 (s), 1111 (s), 1088 (s), 1025 (w), 1008 (w), 855 (w), 802 (m), 763 (m), 636 (m), 627 (m).

El. analysis (%):	calc. for $C_{33}H_{36}N_8Cl_4Fe_2O_{18}$ x Et_2O:		
(Rep. No. 28451)	C: 38.30	H: 4.00	N: 9.66;
found:	C: 38.47	H: 4.25	N: 9.97.

$[H_2L^2Fe_2(C_4H_4O_6)(OH)_2](ClO_4)$ (26).

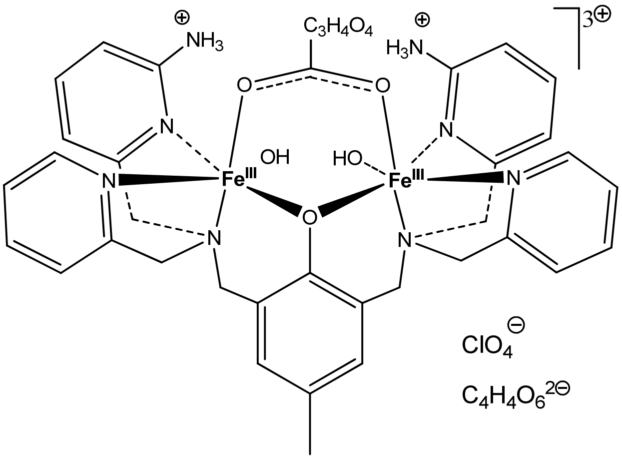

molecular formula:

$C_{41}H_{43}N_8O_{17}Fe_2Cl \times 2\ H_2O$

molecular weight:

1103.00

Ligand **HL**^{2} (200 mg, 0.35 mmol) is dissolved in 35 ml MeOH and heated to 50°C. Ferric perchlorate hydrate (250 mg, 0.70 mmol) in 5 ml MeOH and sodium tartrate (140 mg, 0.70 mmol) in 15 ml MeOH are added while stirring. The solution immediately turns dark blue and is heated at 50°C for 1h. The complex is precipitated by diffusion of diethylether into the solution. The product is filtered off and dried *in vacuo* to yield **26** as a very dark blue powder (0.21 g, 54 %).

HR-ESI$^+$-MS (MeCN): *m/z* (%): 817.14752 (calc. 817.14840) (53.5) $[LFe^{III}_2(C_4H_2O_6)]^+$.

UV/vis (MeCN): λ_{max} [nm] (ε [$M^{-1}cm^{-1}$]) = 232 (27710), 299 (13241), 374 (sh) (3278), 522 (1239).

IR (KBr): $\tilde{\nu}$ [cm^{-1}] = 3419 (b), 3217 (b), 3071 (w), 2925 (w), 2858 (w), 2022 (w), 1730 (w), 1636 (s), 1609 (s), 1580 (m), 1480 (m), 1441 (m), 1262 (w), 1340 (w), 1311 (w), 1286 (w), 1142 (m), 1121(s), 1109 (s), 1089 (s), 1018 (w), 803 (w), 765 (w), 636 (m), 626 (m).

El. analysis (%):	calc. for $C_{41}H_{43}N_8O_{17}Fe_2Cl \times 2\ H_2O$:		
(Rep. No. 28412)	C: 44.65	H: 4.29	N: 10.16;
found:	C: 44.64	H: 4.33	N: 10.07.

$[L^3Fe_2](ClO_4)_3$ (27).

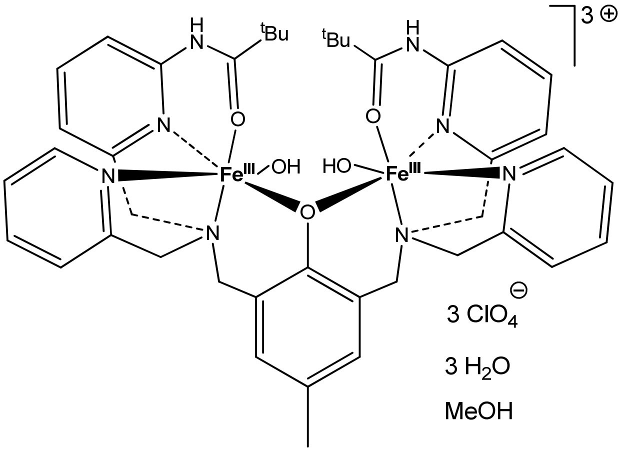

molecular formula:

$C_{43}H_{53}N_8O_{17}Fe_2Cl_3$ x MeOH x 3 H_2O

molecular weight:

1257.05

Ligand **H_3L^3** (110 mg, 0.15 mmol) is dissolved in 10 ml MeOH and heated to 50°C. Ferric perchlorate hydrate (100 mg, 0.30 mmol) is added in 2 ml MeOH while stirring. The solution immediately turns dark green and is heated at 50°C for 1h. The complex is precipitated by diffusion of diethylether into the solution. The product is filtered off and dried *in vacuo* to yield **27** as a very dark green powder (0.13 g, 69 %).

HR-ESI$^+$-MS (MeOH): *m/z* (%): 882.29171 (calc. 882.29187) (100) $[H_2LFe^{III}(ClO_4)]^+$; 896.32903 (calc. 896.32843) (49) $[NaH_2LFe^{III}(HCO_2)_2]^+$; 934.22315 (calc. 934.22220) (38) $[LFe^{III}{}_2SO_4]^+$.

UV/vis (MeCN): λ_{max} [nm] (ε [$M^{-1}cm^{-1}$]) = 228 (sh) (32473), 258 (sh) (20290), 284 (17562), 361 (sh) (4134), 687 (1166).

IR (KBr): $\tilde{\nu}$ [cm^{-1}] = 3430 (b), 3085 (w), 2975 (w), 2936 (w), 2875 (w), 2016 (w), 1679 (w), 1624 (s), 1608 (s), 1573 (w), 1528 (m), 1463 (m), 1431 (m), 1371 (w), 1263 (w), 1143 (s); 1111 (s), 1089 (s), 1023 (m), 922 (w), 809 (w), 767 (w), 636 (m), 626 (m).

El. analysis (%):	calc. for $C_{43}H_{53}N_8O_{17}Fe_2Cl_3$ x MeOH x 3 H_2O:		
(Rep. No. 28453)	C: 42.04	H: 4.97	N: 8.91;
found:	C: 41.78	H: 4.86	N: 8.71.

$[H_2L^3Fe_2(C_4H_4O_6)](ClO_4)_3$ (28).

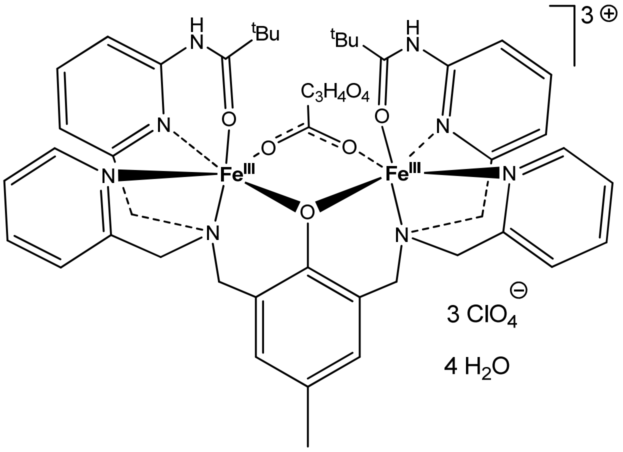

molecular formula:

$C_{47}H_{55}N_8O_{21}Fe_2Cl_3$ x 4 H_2O

molecular weight:

1357.08

Ligand H_3L^3 (110 mg, 0.15 mmol) is dissolved in 15 ml MeOH and heated to 50°C. Ferric perchlorate hydrate (100 mg, 0.30 mmol) in 2 ml MeOH and sodium tartrate (60 mg, 0.3 mmol) in 10 ml MeOH are added while stirring. The solution immediately turns dark blue and is heated at 50°C for 1h and the solvent is removed *in vacuo*. The residue is taken up in a small volume of MeCN and the complex is precipitated by diffusion of diethylether into the solution. The product is filtered off and dried *in vacuo* to yield **28** as a very dark blue powder (0.09 g, 44 %).

HR-ESI$^+$-MS (MeOH): *m/z* (%): 985.26368 (calc. 985.26343) (100) $[LFe^{III}{}_2(C_4H_4O_6)]^+$.

UV/vis (MeCN): λ_{max} [nm] (ε [$M^{-1}cm^{-1}$]) = 234 (sh) (32329), 286 (18963), 354 (sh) (5646), 515 (1537).

IR (KBr): $\tilde{\nu}$ [cm^{-1}] = 3432 (b), 3075 (w), 2971 (w), 2933 (w), 2869 (w), 2033 (w), 1608 (s), 1578 (m), 1530 (m), 1461 (s) 1436 (m), 1409 (w), 1370 /w), 1251 (w), 1304 (m), 1271 (w), 1147 (s), 1117 (s), 1086 (s), 1022 (w), 943 (w), 804 (m), 767 (m), 637 (m), 626 (m).

El. analysis (%):	calc. for $C_{47}H_{55}N_8O_{21}Fe_2Cl_3$ x 4 H_2O:		
(Rep. No. 28452)	C: 41.60	H: 4.60	N: 8.26;
found:	C: 41.37	H: 4.58	N: 8.21.

4.3.5. Syntheses of Phosphoester Substrates

Bis-(2,4-dinitrophenyl)phosphate (BDNPP) pyridinium salt (29).

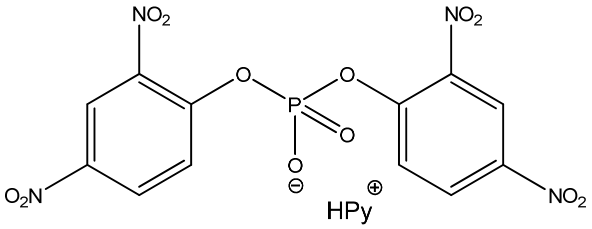

molecular formula:
$C_{17}H_{12}N_5O_{12}P$
molecular weight:
509.28

2,6-Dinitrophenol (2.76 g, 15.00 mmol) is dissolved in dry acetonitrile (30 ml). Dry pyridine (2.5 ml) is added and the solution is cooled to 0°C. Freshly distilled $POCl_3$ (0.5 ml) is added and the reaction is stirred for 15 min. It is poured onto ice/water (200 ml) and the turbid mixture is cooled to 0°C over night. The resulting precipitate is filtered off, washed with a small amount of cold water and dried *in vacuo*. The crude product is recrystallized twice from acetone/Et_2O (1:1) to give BDNPP pyridinium salt **29** as a yellowish powder (0.68 g, 24 %).

^{1}H-NMR (400 MHz, acetone-d_6): $\delta = 9.03$ (dd, $^3J_{H,H} = 6.8$ Hz, $^4J_{H,H} = 1.6$ Hz, 2H, N-CH_{py}), 8.78 (tt, $^3J_{H,H} = 7.6$ Hz, $^4J_{H,H} = 1.2$ Hz, 1H, CH_{py} para to N), 8.71 (d, $^3J_{H,H} = 2.8$ Hz, 2H, NO_2C-CH_{ar}-CNO_2), 8.50 (dd, $^3J_{H,H} = 9.2$ Hz, $^4J_{H,H} = 2.8$ Hz, 2H, CH_{py} meta to N), 8.25 (dd, $^3J_{H,H} = 7.2$ Hz, $^4J_{H,H} = 6.8$ Hz, 2H, CH_{ar}-CNO_2), 8.12 (d, $^3J_{H,H} = 9.2$ Hz, 2H, POC-CH_{ar}).

^{31}P-NMR (162 MHz, acetone-d_6): $\delta = -14.16$

El. analysis (%):	calc. for $C_{17}H_{12}N_5O_{12}P$:	C: 40.09	H: 2.37	N: 13.75;
(Rep. No. 27589)	found:	C: 40.19	H: 2.46	N: 13.66.

2,4-Dinitrophenylphosphate (DNPP) lutidinium salt (30).

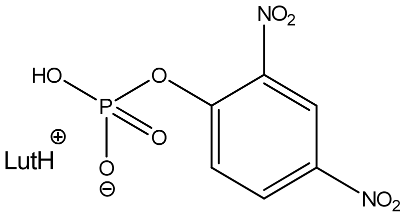

molecular formula:
$C_{13}H_{14}N_3O_8P$
molecular weight:
371.24

BDNPP pyridinium salt **29** (1.28 g, 2.50 mmol) in MeOH (100 ml) is passed through a DOWEX 50 WX2 ion exchange column (Na^+ form) and the pyridinium ion exchanged for Na^+. The solvent is removed *in vacuo* (T < 30°C) and the resulting Na^+-BDNPP is stirred in 0.3M NaOH solution (50 ml) at 25°C for 1h. 5M HCl (ca. 15 ml) is added at 0°C until the pH reaches 0 and the resulting precipitate of 2,4-dinitrophenol is removed by filtration. The solvent is removed *in vacuo* (T < 40°C). The residue is taken up in Et_2O, undissolved NaCl is filtered off and 2,6-lutidine is added dropwise while stirring until the solution becomes slightly yellow. The white precipitate is filtered off and recrystallized in hot EtOH to give the DNPP lutidinium salt **30** as white crystals (0.46 g, 50 %).

^{1}H-NMR (400 MHz, acetone-d_6): $\delta = 8.67$ (d, $^3J_{H,H}$ = 2.0 Hz, 1H, NO_2C-CH_{ar}-CNO_2), 8.46 (dd, $^3J_{H,H}$ = 6.0 Hz, $^4J_{H,H}$ = 1.8 Hz, 1H, CH_{ar}-CNO_2), 8.08 (d, $^3J_{H,H}$ = 6.0 Hz, 1H, CH_{lut} para to N), 8.04 (m, 1H, POC-CH_{ar}), 7.46 (d, $^3J_{H,H}$ = 5.2 Hz, 2H, CH_{lut} meta to N), 2.66 (s, 6H, CH_3).

^{31}P-NMR (100 MHz, acetone-d_6): $\delta = -5.69$

El. analysis (%):	calc. for $C_{13}H_{14}N_3O_8P$:	C: 42.06	H: 3.80	N: 11.32;
(Rep. No. 24914)	found:	C: 41.90	H: 3.79	N: 11.25.

4.4. General Procedures

General Procedure 1: Preparation of Complex Solutions

For **L^1**, **H_3L^3** and HBPMP, 2 mM ligand solution in MeCN or MeOH was mixed with 4 mM tetraethylammonium tetrachloroferrate solution in MeCN or MeOH The resulting complex solutions were 1 mM in MeCN or MeOH. In the case of **HL^2**, the solubility of the ligand in MeCN is low. Therefore, 0.8 mM ligand solution was prepared and mixed with 1.6 mM tetraethylammonium tetrachloroferrate solution to give 0.4 mM solution of **K^2**.

General Procedure 2: Phosphoester Hydrolysis Experiments with BDNPP[87-90]

Phosphatase activity for the activated diester substrate BDNPP was determined in acetonitrile/buffer (1:1) at 25°C between pH 4.6 and 10. The product formation (2,4-dinitrophenolate) was observed spectrophotometrically at 400 nm. To obtain the starting activity, the time between 30 and 240 sec was analyzed by linear regression. A multicomponent buffer was used containing MES; HEPES and CHES (all 50 mM) and $LiClO_4$ (250 mM) in MilliQ water. The desired pH was adjusted with aq. NaOH. The complex and substrate solutions were prepared separately in MeCN and their final concentrations in the cuvette were 0.04 mM and 5 mM, respectively. This was varied for complex-and substrate-dependency measurements. The resulting pH profiles were fitted in Origin 8.1G using the following equation for a diprotic system with two active species:[157]

$$V_0 = V_{0,\max} \frac{\left(1 + \frac{\gamma \cdot K_a(2)}{[H^+]}\right)}{\left(1 + \frac{[H^+]}{K_a(1)} + \frac{K_a(2)}{[H^+]}\right)}$$

The substrate-dependency data were fitted using the Michaelis-Menten equation:

$$V = \frac{V_{\max}[S]_0}{K_M + [S]_0}$$

General Procedure 3: Phosphoester Hydrolysis Experiments with DNPP

Phosphatase activity for the activated monoester substrate DNPP was determined in a similar way as the BDNPP assays, with the following alterations: DNPP was dissolved in buffer of the desired pH. The final concentration in the cuvette was 0.5 mM. Autohydrolysis rates were determined prior to as well as directly after the two catalytic measurements for each pH. Spectral changes that affected the rates due to ligand exchange at the complex were also recorded and subtracted at the end.

4.5. Details on DFT and Force Field Calculations

DFT geometry optimizations were performed with Gaussian 03, rev. E.01[161] (**K**^{1}) or Gaussian 09, rev. A.02[162] (**K**^{2} and **K**^{3}) with the B3LYP[163, 164] functional, the TZVP[165, 166] basis set on Fe and P, and the SVP[165, 166] basis set on C, H, N and O. The optimized structures were confirmed by frequency calculations as minima on the PES and reported energies are zero-point corrected.

J values, g values and zero-field splitting tensors[167] of the geometry-optimized **K**^{1}, **K**^{2} and **K**^{3} complexes were estimated in Orca 2.6, rev. 04 with the same functional and basis set as before, except using TZVP[165, 166] on O instead of SVP, [165, 166] J values were calculated using the broken symmetry method implemented in Orca.[141]

The potential surface scans on **K**^{1}DNPP as well as the equilibrium calculations on **K**^{1}BDNPP and **K**^{1}DNPP were performed in Gaussian 09, rev. A.02[162] with the B3LYP[163, 164] functional and the lanl2dz[168] basis set and the PCM solvation model[169] with acetonitrile as solvent. The minimum structures of the latter were confirmed by frequency calculations and reported energies are zero-point corrected.

Conformational searches on **L**^{1}, **HL**^{2} and **H$_3$L**^{3} were done in the program package Maestro 8.5.111 with the application Macromodel 9.6.[127] Torsional sampling (monte carlo multiple minimum) with 1000 steps is used to produce between 50 and 200 different structures, which are subsequently geometry-optimized in up to 50000 iterations (MM3* force field,[170] steepest descent method, gradient convergence threshold = 0.01).

References

[1] Fischer, E. *Berichte der Deutschen Chemischen Gesellschaft* **1894**, *27*, 3479-3483.

[2] Pauling, L. *Nature* **1948**, *161*, 707-709.

[3] Polanyi, M. *Zeitschrift für Electrochemie* **1921**, *27*, 142.

[4] Vallee, B. L. and Williams, R. J. P. *Proceedings of the National Academy of Sciences of the United States of America* **1968**, *59*, 498-505.

[5] McNaught, A. D. and Wilkinson, A. In *IUPAC. Compendium of Chemical Terminology.*; 2nd ed. (the "Gold Book") ed.; Blackwell Scientific Publications: Oxford, **1997**.

[6] Williams, R. J. P. In *Hematin Enzymes*; Falk, J. E., Lemberg, R. and Morton, R. K., Eds.; Pergamon Press: Oxford, **1961**, p 41.

[7] Lemberg, R., Ehrenberg, A. and Williams, R. J. P. In *Hemes and Hemeproteins*; Chance, B., Estabrook, R. and Yonetani, T., Eds.; Academic Press: New York, **1966**, p 79 pp., 331 pp., 462 pp., 552 pp.

[8] Coleman, J. E. and Vallee, B. L. *Journal of Biological Chemistry* **1960**, *235*, 390-395.

[9] Lindskog, S. *Journal of Biological Chemistry* **1963**, *238*, 945-951.

[10] Jiang, L., Althoff, E. A., Clemente, F. R., Doyle, L., Rothlisberger, D., Zanghellini, A., Gallaher, J. L., Betker, J., Tanaka, F., Barbas III, C. F., Hilvert, D., Houk, K. N., Stoddard, B. L. and Baker, D. *Science* **2008**, *319*, 1387-1391.

[11] Rothlisberger, D., Khersonsky, O., Wollacott, A. M., Jiang, L., DeChancie, J., Betker, J., Gallaher, J. L., Althoff, E. A., Zanghellini, A., Dym, O., Albeck, S., Houk, K. N., Tawfik, D. S. and Baker, D. *Nature* **2008**, *453*, 190-195.

[12] Simon, L. and Goodman, J. M. *Journal of Organic Chemistry* **2010**, *75*, 1831-1840.

[13] Mitic, N., Smith, S. J., Neves, A., Guddat, L. W., Gahan, L. R. and Schenk, G. *Chemical Reviews* **2006**, *106*, 3338-3363.

[14] Moss, D. W., Raymond, F. D. and Wile, D. B. *Critical Reviews in Clinical Laboratory Sciences* **1995**, *32*, 431-467.

[15] Angel, N. Z., Walsh, N., Forwood, M. R., Ostrowski, M. C., Cassady, A. I. and Hume, D. A. *Journal of Bone and Mineral Research* **2000**, *15*, 103-110.

[16] Hayman, A. R., Jones, S. J., Boyde, A., Foster, D., Colledge, W. H., Carlton, M. B., Evans, M. J. and Cox, T. M. *Development* **1996**, *122*, 3151-3162.

[17] Oddie, G. W., Schenk, G., Angel, N. Z., Walsh, N., Guddat, L. W., De Jersey, J., Cassady, A. I., Hamilton, S. E. and Hume, D. A. *Bone* **2000**, *27*, 575-584.

[18] Valizadeh, M., Schenk, G., Nash, K., Oddie, G. W., Guddat, L. W., Hume, D. A., de Jersey, J., Burke, T. R. and Hamilton, S. *Archives of Biochemistry and Biophysics* **2004**, *424*, 154-162.

[19] Nuttleman, P. R. and Roberts, R. M. *Journal of Biological Chemistry* **1990**, *265*, 12192-12199.

[20] Sibille, J. C., Doi, K. and Aisen, P. *Journal of Biological Chemistry* **1987**, *262*, 59-62.

[21] Kaija, H., Alatalo, S. L., Halleen, J. M., Lindqvist, Y., Schneider, G., Vaananen, H. K. and Vihko, P. *Biochemical and Biophysical Research Communications* **2002**, *292*, 128-132.

[22] Raisanen, S. R., Alatalo, S. L., Ylipahkala, H., Halleen, J. M., Cassady, A. I., Hume, D. A. and Vaananen, H. K. *Biochemical and Biophysical Research Communications* **2005**, *331*, 120-126.

[23] Cashikar, A. G., Kumaresan, R. and Rao, N. M. *Plant Physiology* **1997**, *114*, 907-915.

[24] Bozzo, G. G., Raghothama, K. G. and Plaxton, W. C. *Biochemical Journal* **2004**, *377*, 419-428.

[25] Schenk, G., Guddat, L. T., Ge, Y., Carrington, L. E., Hume, D. A., Hamilton, S. and de Jersey, J. *Gene* **2000**, *250*, 117-125.

[26] Twitchett, M. B. and Sykes, A. G. *European Journal of Inorganic Chemistry* **1999**, 2105-2115.

[27] Allen, S. H., Nuttleman, P. R., Ketcham, C. M. and Roberts, R. M. *Journal of Bone and Mineral Research* **1989**, *4*, 47-55.

[28] Hayman, A. R., Warburton, M. J., Pringle, J. A. S., Coles, B. and Chambers, T. J. *Biochemical Journal* **1989**, *261*, 601-609.

[29] Janckila, A. J., Woodford, T. A., Lam, K. W., Li, C. Y. and Tam, L. T. *Leukemia* **1992**, *6*, 199-203.

[30] Nakazato, H., Okamoto, T., Nishikoori, M., Washio, K., Morita, N., Haraguchi, K., Thompson, G. A. and Okuyama, H. *Plant Physiology* **1998**, *118*, 1015-1020.

[31] Durmus, A., Eicken, C., Sift, B. H., Kratel, A., Kappl, R., Huttermann, J. and Krebs, B. *European Journal of Biochemistry* **1999**, *260*, 709-716.

[32] Schenk, G., Ge, Y. B., Carrington, L. E., Wynne, C. J., Searle, I. R., Carroll, B. J., Hamilton, S. and de Jersey, J. *Archives of Biochemistry and Biophysics* **1999**, *370*, 183-189.

[33] Schenk, G., Boutchard, C. L., Carrington, L. E., Noble, C. J., Moubaraki, B., Murray, K. S., de Jersey, J., Hanson, G. R. and Hamilton, S. *Journal of Biological Chemistry* **2001**, *276*, 19084-19088.

[34] Ullah, A. H. J. and Cummins, B. J. *Preparative Biochemistry* **1988**, *18*, 473-481.

[35] Ullah, A. H. J. and Cummins, B. J. *Preparative Biochemistry* **1988**, *18*, 37-65.

[36] Schenk, G., Korsinczky, M. L. J., Hume, D. A., Hamilton, S. and DeJersey, J. *Gene* **2000**, *255*, 419-424.

[37] Schenk, G., Elliott, T. W., Leung, E., Carrington, L. E., Mitic, N., Gahan, L. R. and Guddat, L. W. *BMC Structural Biology* **2008**, *8*:6.

[38] Wang, X. D., Randall, C. R., True, A. E. and Que, L. *Biochemistry* **1996**, *35*, 13946-13954.

[39] Wang, X. D. and Que, L. *Biochemistry* **1998**, *37*, 7813-7821.

[40] Day, E. P., David, S. S., Peterson, J., Dunham, W. R., Bonvoisin, J. J., Sands, R. H. and Que, L. *Journal of Biological Chemistry* **1988**, *263*, 15561-15567.

[41] Dietrich, M., Münstermann, D., Suerbaum, H. and Witzel, H. *European Journal of Biochemistry* **1991**, *199*, 105-113.

[42] Suerbaum, H., Körner, M., Witzel, H., Althaus, E., Mosel, B. D. and Müller-Warmuth, W. *European Journal of Biochemistry* **1993**, *214*, 313-321.

[43] Aquino, M. A. S., Lim, J. S. and Sykes, A. G. *Journal of the Chemical Society-Dalton Transactions* **1994**, 429-436.

[44] Strater, N., Klabunde, T., Tucker, P., Witzel, H. and Krebs, B. *Science* **1995**, *268*, 1489-1492.

[45] Klabunde, T., Strater, N., Frohlich, R., Witzel, H. and Krebs, B. *Journal of Molecular Biology* **1996**, *259*, 737-748.

[46] Guddat, L. W., McAlpine, A. S., Hume, D., Hamilton, S., de Jersey, J. and Martin, J. L. *Structure with Folding & Design* **1999**, *7*, 757-767.

[47] Youngme, S., Chaichit, N., Kongsaeree, P., van Albada, G. A. and Reedijk, J. *Inorganica Chimica Acta* **2001**, *324*, 232-240.

[48] Doi, K., McCracken, J., Peisach, J. and Aisen, P. *Journal of Biological Chemistry* **1988**, *263*, 5757-5763.

[49] Klabunde, T. and Krebs, B. *Metal Sites in Proteins and Models* **1997**, *89*, 177-198.

[50] Antanaitis, B. C., Aisen, P. and Lilienthal, H. R. *Journal of Biological Chemistry* **1983**, *258*, 3166-3172.

[51] Averill, B. A., Davis, J. C., Burman, S., Zirino, T., Sandersloehr, J., Loehr, T. M., Sage, J. T. and Debrunner, P. G. *Journal of the American Chemical Society* **1987**, *109*, 3760-3767.

[52] Yang, Y. S., McCormick, J. M. and Solomon, E. I. *Journal of the American Chemical Society* **1997**, *119*, 11832-11842.

[53] Wang, D. L., Holz, R. C., David, S. S., Que, L. and Stankovich, M. T. *Biochemistry* **1991**, *30*, 8187-8194.

[54] Bernhardt, P. V., Schenk, G. and Wilson, G. J. *Biochemistry* **2004**, *43*, 10387-10392.

[55] Cox, R. S., Schenk, G., Mitic, N., Gahan, L. R. and Hengge, A. C. *Journal of the American Chemical Society* **2007**, *129*, 9550-9551.

[56] Merkx, M. and Averill, B. A. *Journal of the American Chemical Society* **1999**, *121*, 6683-6689.

[57] Merkx, M., Pinkse, M. W. H. and Averill, B. A. *Biochemistry* **1999**, *38*, 9914-9925.

[58] Wynne, C. J., Hamilton, S. E., Dionysius, D. A., Beck, J. L. and Dejersey, J. *Archives of Biochemistry and Biophysics* **1995**, *319*, 133-141.

[59] Mitic, N., Hadler, K. S., Gahan, L. R., Hengge, A. C. and Schenk, G. *Journal of the American Chemical Society* **2010**, *132*, 7049-7054.

[60] Smith, S. J., Casellato, A., Hadler, K. S., Mitic, N., Riley, M. J., Bortoluzzi, A. J., Szpoganicz, B., Schenk, G., Neves, A. and Gahan, L. R. *Journal of Biological Inorganic Chemistry* **2007**, *12*, 1207-1220.

[61] Rogers, M. S., Tyler, E. M., Akyumani, N., Kurtis, C. R., Spooner, R. K., Deacon, S. E., Tamber, S., Firbank, S. J., Mahmoud, K., Knowles, P. F., Phillips, S. E. V., McPherson, M. J. and Dooley, D. M. *Biochemistry* **2007**, *46*, 4606-4618.

[62] Singh, S., Madzelan, P., Stasser, J., Weeks, C. L., Becker, D., Spiro, T. G., Penner-Hahn, J. and Banerjee, R. *Journal of Inorganic Biochemistry* **2009**, *103*, 689-697.

[63] Hakkim, V. and Subramanian, V. *Journal of Physical Chemistry A* **2010**, *114*, 7952-7959.

[64] Funhoff, E. G., Wang, W. L., Andersson, G. and Averill, B. A. *Febs Journal* **2005**, *272*, 2968-2977.

[65] Breslow, R. *Chemical Society Reviews* **1972**, *1*, 553-580.

[66] McLoughlin, S. Y., Jackson, C., Liu, J. W. and Ollis, D. L. *Applied and Environmental Microbiology* **2004**, *70*, 404-412.

[67] Ghanem, E., Li, Y. C., Xu, C. F. and Raushel, F. M. *Biochemistry* **2007**, *46*, 9032-9040.

[68] Jarenmark, M., Carlsson, H. and Nordlander, E. *Comptes Rendus Chimie* **2007**, *10*, 433-462.

[69] Gahan, L. R., Smith, S. J., Neves, A. and Schenk, G. *European Journal of Inorganic Chemistry* **2009**, 2745-2758.

[70] Than, R., Feldmann, A. A. and Krebs, B. *Coordination Chemistry Reviews* **1999**, *182*, 211-241.

[71] Norman, R. E., Yan, S. P., Que, L., Backes, G., Ling, J. S., Sanders-Loehr, J., Zhang, J. H. and O´Connor, C. J. *Journal of the American Chemical Society* **1990**, *112*, 1554-1562.

[72] Hartman, J. A. R., Rardin, R. L., Chaudhuri, P., Pohl, K., Wieghardt, K., Nuber, B., Weiss, J., Papaefthymiou, G. C., Frankel, R. B. and Lippard, S. J. *Journal of the American Chemical Society* **1987**, *109*, 7387-7396.

[73] Armstrong, W. H. and Lippard, S. J. *Journal of the American Chemical Society* **1984**, *106*, 4632-4633.

[74] Gomez-Romero, P., Casan-Pastor, N., Ben-Hussein, A. and Jameson, G. B. *Journal of the American Chemical Society* **1988**, *110*, 1988-1990.

[75] Yan, S. P., Que, L., Taylor, L. F. and Anderson, O. P. *Journal of the American Chemical Society* **1988**, *110*, 5222-5224.

[76] Mashuta, M. S., Webb, R. J., Oberhausen, K. J., Richardson, J. F., Buchanan, R. M. and Hendrickson, D. N. *Journal of the American Chemical Society* **1989**, *111*, 2745-2746.

[77] Suzuki, M., Uehara, A. and Endo, K. *Inorganica Chimica Acta* **1986**, *123*, L9-L10.

[78] Borovik, A. S., Murch, B. P., Que, L., Papaefthymiou, V. and Munck, E. *Journal of the American Chemical Society* **1987**, *109*, 7190-7191.

[79] Borovik, A. S., Papaefthymiou, V., Taylor, L. F., Anderson, O. P. and Que, L. *Journal of the American Chemical Society* **1989**, *111*, 6183-6195.

[80] Schepers, K., Bremer, B., Krebs, B., Henkel, G., Althaus, E., Mosel, B. and Müller-Warmuth, W. *Angewandte Chemie-International Edition in English* **1990**, *29*, 531-533.

[81] Borovik, A. S., Que, L., Papaefthymiou, V., Munck, E., Taylor, L. F. and Anderson, O. P. *Journal of the American Chemical Society* **1988**, *110*, 1986-1988.

[82] Holman, T. R., Andersen, K. A., Anderson, O. P., Hendrich, M. P., Juarez-Garcia, C., Munck, E. and Que, L. *Angewandte Chemie-International Edition in English* **1990**, *29*, 921-923.

[83] Ghiladi, M., McKenzie, C. J., Meier, A., Powell, A. K., Ulstrup, J. and Wocadlo, S. *Journal of the Chemical Society-Dalton Transactions* **1997**, 4011-4018.

[84] Bernard, E., Moneta, W., Laugier, J., Chardon-Noblat, S., Deronzier, A., Tuchagues, J. P. and Latour, J. M. *Angewandte Chemie-International Edition in English* **1994**, *33*, 887-889.

[85] Bernard, E., Chardon-Noblat, S., Deronzier, A. and Latour, J. M. *Inorganic Chemistry* **1999**, *38*, 190-193.

[86] Neves, A., Debrito, M. A., Drago, V., Griesar, K. and Haase, W. *Inorganica Chimica Acta* **1995**, *237*, 131-135.

[87] Lanznaster, M., Neves, A., Bortoluzzi, A. J., Szpoganicz, B. and Schwingel, E. *Inorganic Chemistry* **2002**, *41*, 5641-5643.

[88] Karsten, P., Neves, A., Bortoluzzi, A. J., Lanznaster, M. and Drago, V. *Inorganic Chemistry* **2002**, *41*, 4624-4626.

[89] Lanznaster, M., Neves, A., Bortoluzzi, A. J., Aires, V. V. E., Szpoganicz, B., Terenzi, H., Severino, P. C., Fuller, J. M., Drew, S. C., Gahan, L. R., Hanson, G. R., Riley, M. J. and Schenk, G. *Journal of Biological Inorganic Chemistry* **2005**, *10*, 319-332.

[90] Batista, S. C., Neves, A., Bortoluzzi, A. J., Vencato, I., Peralta, R. A., Szpoganicz, B., Aires, V. V. E., Terenzi, H. and Severino, P. C. *Inorganic Chemistry Communications* **2003**, *6*, 1161-1165.

[91] Xavier, F. R., Neves, A., Casellato, A., Peralta, R. A., Bortoluzzi, A. J., Szpoganicz, B., Severino, P. C., Terenzi, H., Tomkowicz, Z., Ostrovsky, S., Haase, W., Ozarowski, A., Krzystek, J., Telser, J., Schenk, G. and Gahan, L. R. *Inorganic Chemistry* **2009**, *48*, 7905-7921.

[92] Neves, A., Lanznaster, M., Bortoluzzi, A. J., Peralta, R. A., Casellato, A., Castellano, E. E., Herrald, P., Riley, M. J. and Schenk, G. *Journal of the American Chemical Society* **2007**, *129*, 7486-7488.

[93] Ferreira, D. E. C., De Almeida, W. B., Neves, A. and Rocha, W. R. *Physical Chemistry Chemical Physics* **2008**, *10*, 7039-7046.

[94] Arii, H., Funahashi, Y., Jitsukawa, K. and Masuda, H. *Dalton Transactions* **2003**, 2115-2116.

[95] Feng, G. Q., Natale, D., Prabaharan, R., Mareque-Rivas, J. C. and Williams, N. H. *Angewandte Chemie-International Edition* **2006**, *45*, 7056-7059.

[96] Merkx, M. and Averill, B. A. *Biochemistry* **1998**, *37*, 11223-11231.

[97] Duboc-Toia, C., Menage, S., Vincent, J. M., Averbuch-Pouchot, M. T. and Fontecave, M. *Inorganic Chemistry* **1997**, *36*, 6148-6149.

[98] Verge, F., Lebrun, C., Fontecave, M. and Menage, S. *Inorganic Chemistry* **2003**, *42*, 499-507.

[99] Horn, A., Vencato, I., Bortoluzzi, A. J., Horner, R., Silva, R. A. N., Spoganicz, B., Drago, V., Terenzi, H., de Oliveira, M. C. B., Werner, R., Haase, W. and Neves, A. *Inorganica Chimica Acta* **2005**, *358*, 339-351.

[100] Longhinotti, E., Domingos, J. B., Szpoganicz, B., Neves, A. and Nome, F. *Inorganica Chimica Acta* **2005**, *358*, 2089-2092.

[101] Parrilha, G. L., Fernandes, C., Bortoluzzi, A. J., Szpoganicz, B., Silva, M. D., Pich, C. T., Terenzi, H. and Horn, A. *Inorganic Chemistry Communications* **2008**, *11*, 643-647.

[102] Drueke, S., Wieghardt, K., Nuber, B. and Weiss, J. *Inorganic Chemistry* **1989**, *28*, 1414-1417.

[103] Norman, R. E., Holz, R. C., Menage, S., O´Connor, C. J., Zhang, J. H. and Que, L. *Inorganic Chemistry* **1990**, *29*, 4629-4637.

[104] Drueke, S., Wieghardt, K., Nuber, B., Weiss, J., Fleischhauer, H. P., Gehring, S. and Haase, W. *Journal of the American Chemical Society* **1989**, *111*, 8622-8631.

[105] Turowski, P. N., Armstrong, W. H., Roth, M. E. and Lippard, S. J. *Journal of the American Chemical Society* **1990**, *112*, 681-690.

[106] Turowski, P. N., Armstrong, W. H., Liu, S. C., Brown, S. N. and Lippard, S. J. *Inorganic Chemistry* **1994**, *33*, 636-645.

[107] Yan, S. P., Pan, X. Y., Taylor, L. F., Zhang, J. H., OConnor, C. J., Britton, D., Anderson, O. P. and Que, L. *Inorganica Chimica Acta* **1996**, *243*, 1-8.

[108] Hazell, A., Jensen, K. B., McKenzie, C. J. and Toftlund, H. *Inorganic Chemistry* **1994**, *33*, 3127-3134.

[109] Schugar, H. J., Rossman, G. R., Barraclough, C. G. and Gray, H. B. *Journal of the American Chemical Society* **1972**, *94*, 2683-2690.

[110] Picraux, L. B., Smeigh, A. L., Guo, D. and McCusker, J. K. *Inorganic Chemistry* **2005**, *44*, 7846-7859.

[111] Holz, R. C., Elgren, T. E., Pearce, L. L., Zhang, J. H., O´Connor, C. J. and Que, L. *Inorganic Chemistry* **1993**, *32*, 5844-5850.

[112] Krebs, B., Schepers, K., Bremer, B., Henkel, G., Althaus, E., Müller-Warmuth, W., Griesar, K. and Haase, W. *Inorganic Chemistry* **1994**, *33*, 1907-1914.

[113] Nie, H. L., Aubin, S. M. J., Mashuta, M. S., Wu, C. C., Richardson, J. F., Hendrickson, D. N. and Buchanan, R. M. *Inorganic Chemistry* **1995**, *34*, 2382-2388.

[114] Neves, A., Erthal, S. M. D., Drago, V., Griesar, K. and Haase, W. *Inorganica Chimica Acta* **1992**, *197*, 121-124.

[115] Neves, A., deBrito, M. A., Vencato, I., Drago, V., Griesar, K. and Haase, W. *Inorganic Chemistry* **1996**, *35*, 2360-2368.

[116] Borovik, A. S. and Que, L. *Journal of the American Chemical Society* **1988**, *110*, 2345-2347.

[117] Lindqvist, Y., Johansson, E., Kaija, H., Vihko, P. and Schneider, G. *Journal of Molecular Biology* **1999**, *291*, 135-147.

[118] Uppenberg, J., Lindqvist, F., Svensson, C., Ek-Rylander, B. and Andersson, G. *Journal of Molecular Biology* **1999**, *290*, 201-211.

[119] Royal, G., Dahaoui-Gindrey, V., Dahaoui, S., Tabard, A., Guilard, R., Pullumbi, P. and Lecomte, C. *European Journal of Organic Chemistry* **1998**, 1971-1975.

[120] Bianchi, A., Micheloni, M. and Paoletti, P. *Coordination Chemistry Reviews* **1991**, *110*, 17-113.

[121] Bernhardt, P. V., Comba, P., Mahu-Rickenbach, A., Stebler, S., Steiner, S., Varnagy, K. and Zehnder, M. *Inorganic Chemistry* **1992**, *31*, 4194-4200.

[122] Renz, M., Hemmert, C., Gornitzka, H. and Meunier, B. *New Journal of Chemistry* **1999**, *23*, 773-776.

[123] Hope, D. B. and Horncastle, K. C. *Journal of the Chemical Society C* **1966**, 1098-1101.

[124] Martin, A. E., Ford, T. M. and Bulkowski, J. E. *The Journal of Organic Chemistry* **1982**, *47*, 412-415.

[125] Murase, I., Mikuriya, M., Sonoda, H. and Kida, S. *Journal of the Chemical Society, Chemical Communications* **1984**, 692-694.

[126] Roelfes, G., Vrajmasu, V., Chen, K., Ho, R. Y. N., Rohde, J. U., Zondervan, C., la Crois, R. M., Schudde, E. P., Lutz, M., Spek, A. L., Hage, R., Feringa, B. L., Munck, E. and Que, L. *Inorganic Chemistry* **2003**, *42*, 2639-2653.

[127] MacroModel, version 9.6, *Schrödinger*, New York, **2005**.

[128] Gill, N. S. *Journal of the Chemical Society* **1961**, 3512-3515.

[129] Reem, R. C., McCormick, J. M., Richardson, D. E., Devlin, F. J., Stephens, P. J., Musselman, R. L. and Solomon, E. I. *Journal of the American Chemical Society* **1989**, *111*, 4688-4704.

[130] Armstrong, W. H. and Lippard, S. J. *Inorganic Chemistry* **1985**, *24*, 981-982.

[131] Evans, D. F. *Journal of the Chemical Society* **1959**, 2003-2005.

[132] Wilkinson, E. C., Dong, Y. H. and Que, L. *Journal of the American Chemical Society* **1994**, *116*, 8394-8395.

[133] Chin, J. *Accounts of Chemical Research* **1991**, *24*, 145-152.

[134] Frey, S. T., Murthy, N. N., Weintraub, S. T., Thompson, L. K. and Karlin, K. D. *Inorganic Chemistry* **1997**, *36*, 956-&.

[135] Bencini, A. and Gatteschi, D., *EPR of Exchange Coupled Systems*, Springer-Verlag, Berlin, **1990**.

[136] Hanson, G. R., Gates, K. E., Noble, C. J., Griffin, M., Mitchell, A. and Benson, S. *Journal of Inorganic Biochemistry* **2004**, *98*, 903-916.

[137] Hanson, G. R., Noble, C. J. and Benson, S. In *High Resolution EPR: Applications to Metalloenzymes and Metals in Medicine*; Hanson, G. R. and Berliner, L. J., Eds. **2009**; Vol. 28, p 105-173.

[138] Mabbs, F. E. and Collison, D. C., *Electron Paramagnetic Resonance of Transition Metal Compounds.*, Elsevier, Amsterdam, **1992**.

[139] Smith, T. D. and Pilbrow, J. R. *Coordination Chemistry Reviews* **1974**, *13*, 173-278.

[140] Taylor, P. C., Baugher, J. F. and Kriz, H. M. *Chemical Reviews* **1975**, *75*, 203-240.

[141] Neese, F. *Journal of Physics and Chemistry in Solids* **2004**, *65*, 781-785.

[142] Bohlmann, F. *Chemische Berichte* **1958**, *91*, 2157-2167.

[143] Suzuki, M., Kanatomi, H. and Murase, I. *Chemistry Letters* **1981**, 1745-1748.

[144] Kaljurand, I., Kutt, A., Soovali, L., Rodima, T., Maemets, V., Leito, I. and Koppel, I. A. *Journal of Organic Chemistry* **2005**, *70*, 1019-1028.

[145] Inomata, T., Shinozaki, K., Hayashi, Y., Arii, H., Funahashi, Y., Ozawa, T. and Masuda, H. *Chemical Communications* **2008**, 392-394.

[146] Tan, Y. C., Gan, X. M., Stanchfield, J. L., Duesler, E. N. and Paine, R. T. *Inorganic Chemistry* **2001**, *40*, 2910-2913.

[147] Liu, Q. and Rovis, T. *Journal of the American Chemical Society* **2006**, *128*, 2552-2553.

[148] Kriss, G. A. In *Astronomical Data Analysis Software & Systems III*; Crabtree, D. R., Hanisch, R. J. and Barnes, J., Eds.; Astronomical Society of the Pacific: San Francisco, **1994**; Vol. 61.

[149] Weast, R. C., Astle, M. J. and Beyer, W. H., *CRC Handbook of Chemistry and Physics, 67th Ed.*, CRC Press, Inc., Boca Raton, Florida, **1986-1987**.

[150] Personal communication with Noble, C. J. (*CAI, University of Queensland, Brisbane, Australia* **2010**).

[151] Holton, D. M. and Murphy, D. *Journal of the Chemical Society, Faraday Transactions 2* **1979**, *75*, 1637-1642.

[152] Bordwell, F. G. and Cheng, J. P. *Journal of the American Chemical Society* **1991**, *113*, 1736-1743.

[153] Grampp, G., Landgraf, S. and Muresanu, C. *Electrochimica Acta* **2004**, *49*, 537-544.

[154] Bunton, C. A. and Farber, S. J. *The Journal of Organic Chemistry* **1969**, *34*, 767-772.

[155] Rawji, G. and Milburn, R. M. *The Journal of Organic Chemistry* **1981**, *46*, 1205-1206.

[156] Schlossnagle, D. C., Bazer, F. W., Tsibris, J. C. and Roberts, R. M. *Journal of Biological Chemistry* **1974**, *249*, 7574-7579.

[157] Segel, I. H., *Enzyme Kinetics - Behavior and Analysis of Rapid Equilibrium and Steady-State Enzyme Systems.*, Wiley, New York, **1975**.

[158] Smith, S. J., Schenk, G. and Gahan, L. R., unpublished results, **2009**.

[159] Perera, W. N. and Hefter, G. *Inorganic Chemistry* **2003**, *42*, 5917-5923.

[160] Sheldrick, G. M., *SHELXTL User´s Manual*, Siemens Analytical X-Ray Instruments Inc., **1994**.

[161] Gaussian 03, Revision E.01, Frisch, M. J., Trucks, G. W., Schlegel, H. B., Scuseria, G. E., Robb, M. A., Cheeseman, J. R., Montgomery, J., J. A. , Vreven, T., Kudin, K. N., Burant, J. C., Millam, J. M., Iyengar, S. S., Tomasi, J., Barone, V., Mennucci, B., Cossi, M., Scalmani, G., Rega, N., Petersson, G. A., Nakatsuji, H., Hada, M., Ehara, M., Toyota, K., Fukuda, R., Hasegawa, J., Ishida, M., Nakajima, T., Honda, Y., Kitao, O., Nakai, H., Klene, M., Li, X., Knox, J. E., Hratchian, H. P., Cross, J. B., Bakken, V., Adamo, C., Jaramillo, J., Gomperts, R., Stratmann, R. E., Yazyev, O., Austin, A. J., Cammi, R., Pomelli, C., Ochterski, J. W., Ayala, P. Y., Morokuma, K., Voth, G. A., Salvador, P., Dannenberg, J. J., Zakrzewski, V. G., Dapprich, S., Daniels, A. D., Strain, M. C., Farkas, O., Malick, D. K., Rabuck, A. D., Raghavachari, K., Foresman, J. B., Ortiz, J. V., Cui, Q., Baboul, A. G., Clifford, S., Cioslowski, J., Stefanov, B. B., Liu, G., Liashenko, A., Piskorz, P., Komaromi, I., Martin, R. L., Fox, D. J., Keith, T., Al-Laham, M. A., Peng, C. Y., Nanayakkara, A., Challacombe, M., Gill, P. M. W., Johnson, B., Chen, W., Wong, M. W., Gonzalez, C. and Pople, J. A., *Gaussian Inc.*, Wallingford CT, **2004**.

[162] Gaussian 09, Revision A.02, Frisch, M. J., Trucks, G. W., Schlegel, H. B., Scuseria, G. E., Robb, M. A., Cheeseman, J. R., Scalmani, G., Barone, V., Mennucci, B., Petersson, G. A., Nakatsuji, H., Caricato,

M., Li, X., Hratchian, H. P., Izmaylov, A. F., Bloino, J., Zheng, G., Sonnenberg, J. L., Hada, M., Ehara, M., Toyota, K., Fukuda, R., Hasegawa, J., Ishida, M., Nakajima, T., Honda, Y., Kitao, O., Nakai, H., Vreven, T., Montgomery, J., J. A. , Peralta, J. E., Ogliaro, F., Bearpark, M., Heyd, J. J., Brothers, E., Kudin, K. N., Staroverov, V. N., Kobayashi, R., Normand, J., Raghavachari, K., Rendell, A., Burant, J. C., Iyengar, S. S., Tomasi, J., Cossi, M., Rega, N., Millam, J. M., Klene, M., Knox, J. E., Cross, J. B., Bakken, V., Adamo, C., Jaramillo, J., Gomperts, R., Stratmann, R. E., Yazyev, O., Austin, A. J., Cammi, R., Pomelli, C., Ochterski, J. W., Martin, R. L., Morokuma, K., Zakrzewski, V. G., Voth, G. A., Salvador, P., Dannenberg, J. J., Dapprich, S., Daniels, A. D., Farkas, O., Foresman, J. B., Ortiz, J. V., Cioslowski, J. and Fox, D. J., *Gaussian Inc.*, Wallingford CT, **2009**.

[163] Becke, A. D. *Physical Review A* **1988**, *38*, 3098-3100.

[164] Lee, C. T., Yang, W. T. and Parr, R. G. *Physical Review B* **1988**, *37*, 785-789.

[165] Schafer, A., Horn, H. and Ahlrichs, R. *Journal of Chemical Physics* **1992**, *97*, 2571-2577.

[166] Schafer, A., Huber, C. and Ahlrichs, R. *Journal of Chemical Physics* **1994**, *100*, 5829-5835.

[167] Neese, F. and Solomon, E. I. *Inorganic Chemistry* **1998**, *37*, 6568-6582.

[168] Dunning, J., T. H. and Hay, P. J. In *Modern Theoretical Chemistry*; Schaefer III, H. F., Ed.; Plenum: New York, **1976**, p 1-28.

[169] Tomasi, J., Mennucci, B. and Cammi, R. *Chemical Reviews* **2005**, *105*, 2999-3093.

[170] Allinger, N. L., Yuh, Y. H. and Lii, J. H. *Journal of the American Chemical Society* **1989**, *111*, 8551-8566.

Appendices:

Appendix 1: Abbreviations

1-NP	1-naphthyl phosphate
BDNPP	bis-(2,4-dinitrophenyl)phosphate
B.M.	Bohr magnetons
$(BzO)_2$	dibenzoyl peroxide
CD	circular dichroism
CHES	2-(*N*-cyclohexylamino)ethanesulfonic acid
CT	charge transfer
CV	cyclovoltammetry
CW	continuous wave
D	zero field splitting
Δ	reflux temperature
DCM	dichloromethane
DFT	density functional theory
dipa	di-(2-pyridyl)methylamine
DMF	*N*,*N*´-dimethylformamide
DMP	dimethyl phosphate
DNPP	(2,4-dinitrophenyl)phosphate
DPP	diphenyl phosphate
E	rhombicity parameter of zero field splitting
eq	equivalents
eq.	equation
ESI	electron spray ionisation
EPR	electron paramagnetic resonance
Et_2O	diethylether
EtOH	ethanol

FAB	fast atom bombardment
$FeCp_2$	ferrocene
h	hour
HBPMP	2,6-bis[(bis-pyridin-2-ylmethyl-amino]-methyl]-4-methylphenol
HEPES	4-(2-hydroxyethyl)-1-piperazinylethanesulfonic acid
HL^2	2,6-bis[[[(6-amino-2-pyridinyl)methyl](2-pyridinylmethyl)amino]methyl]-4-methylphenol
H_3L^3	2,6-bis[[[(6-pivaloylamido-2-pyridinyl)methyl](2-pyridinylmethyl)amino]-methyl]-4-methylphenol
HR	high resolution
HSAB	hard and soft acids and bases
IR	infra red
K^1	diferric complex of **L^1**, formed *in situ*
K^2	diferric complex of **HL^2**
K^3	diferric complex of **H_3L^3**
L^1	4,11-dimethyl-1,8-bis[*N*-(2-di-(2-pyridyl)methyl)ethylamino]cyclam
LMCT	ligand metal charge transfer
M	molar, [mol/L]
MCD	magnetic circular dichroism
MeCN	acetonitrile
MeOH	methanol
MES	2-(*N*-morpholino)ethanesulfonic acid
min	minutes
MS	mass spectrometry
mV	millivolt
NBS	*N*-bromosuccinimide
NHE	normal hydrogen electrode
nibeol	4-nitrobenzylalcohol

NMR	nuclear magnetic resonance
PAP	purple acid phosphatase
PCM	point charge model
pNPP	*para*-nitrophenyl phosphate
ppm	parts per million
py	pyridine
ROS	reactive oxygen species
rt	room temperature
SCE	saturated calomel electrode
Ts	tosyl
UV/vis	ultraviolet/visible
VT	variable temperature

Appendix 2: EPR spectra of [$FeCl_4$](NEt_4), K^1 in MeCN and MeCN/buffer.

X-band EPR spectra (1.7 K) of [$FeCl_4$](NEt_4) 0.2 mM in MeCN (black line) at 9.376422 GHz, $\mathbf{K^1}$ 0.1 mM in MeCN (blue line) at 9.376783 GHz and $\mathbf{K^1}$ 0.1 mM in MeCN/buffer pH 5 1:1 (orange line) at 9.377746 GHz.

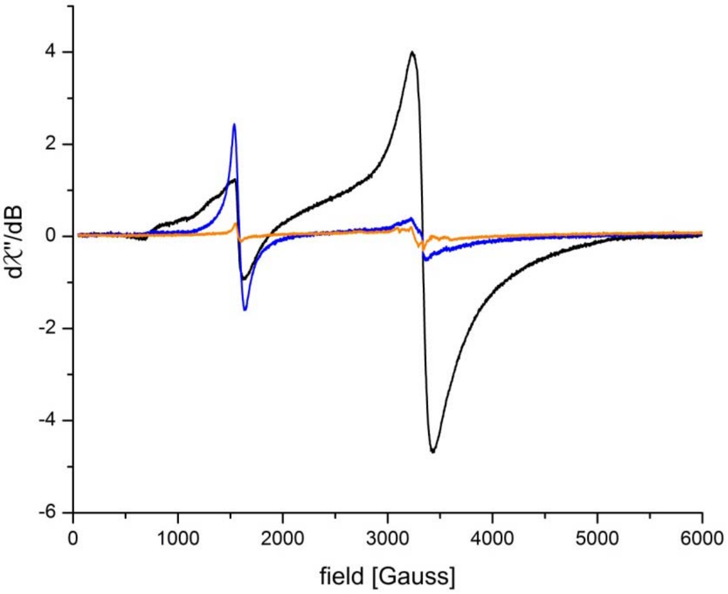

Appendix 3: EPR spectra of K^1 and reduced K^1 in MeCN.

X-band EPR spectra (140 K) of $\mathbf{K^1}$ 0.5 mM in MeCN (black line) at 9.432774 GHz and $\mathbf{K^1}$ after bulk electrolysis (1h at -0.3 V) 0.5 mM in MeCN (blue line) at 9.431626 GHz.

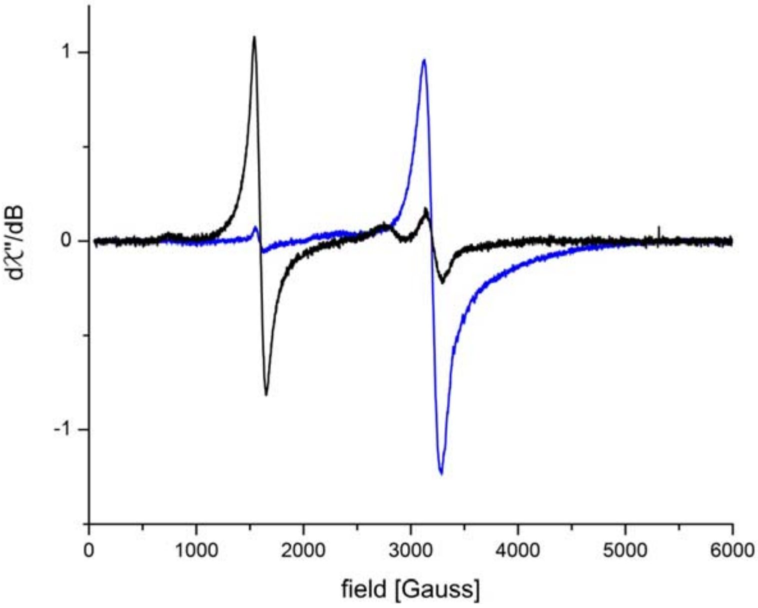

Appendix 4: UV/vis spectrum of K^1 with acetamide.

Time dependent UV/vis spectrum of $\mathbf{K^1}$ (0.05 mM) with acetamide (1 mM) in MeCN/buffer pH 5; spectra were recorded over 30 min with one scan each minute.

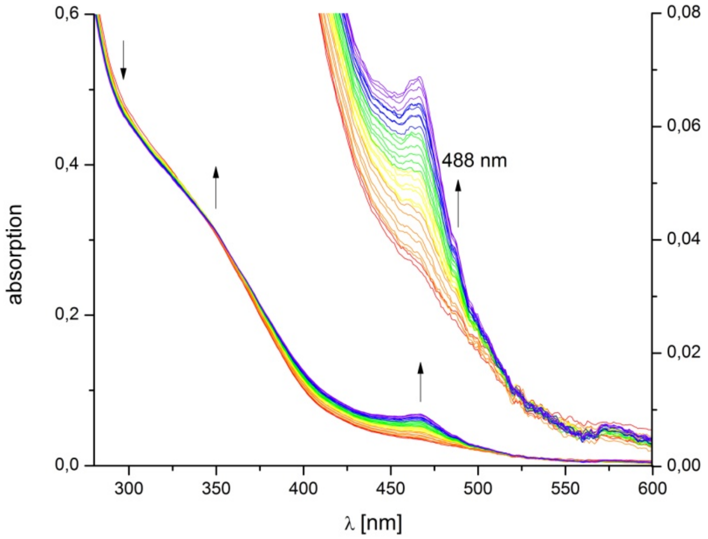

Appendix 5: Schematic energy diagrams of exchange coupled systems.

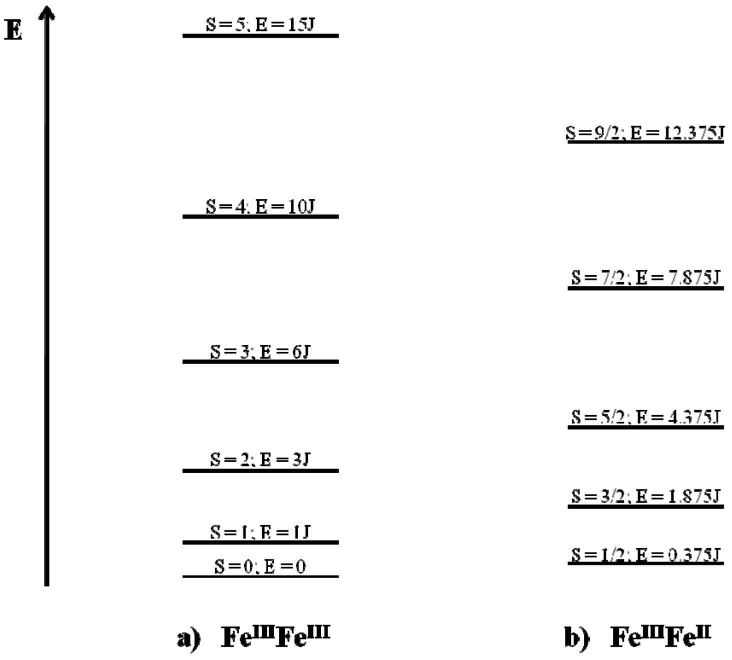

Appendix 6: Gaussian analysis of UV/vis spectra of K^2 and K^3.

- **K^2**:

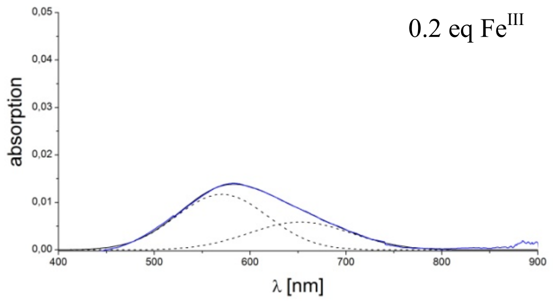

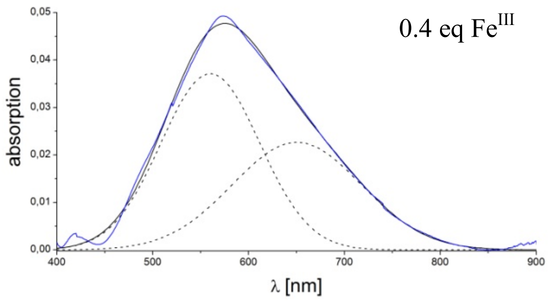

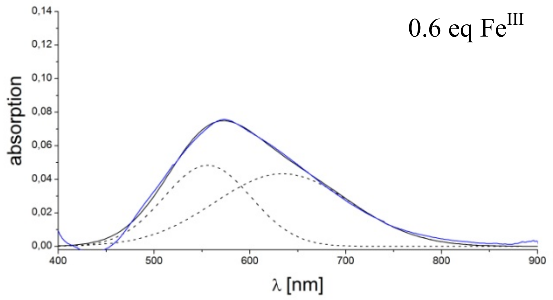

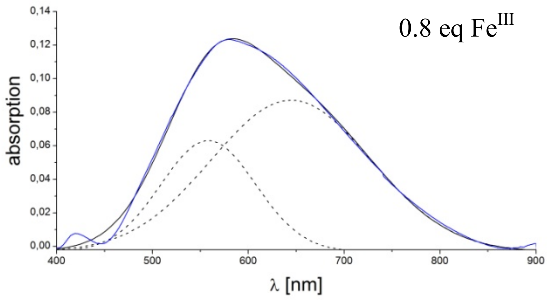

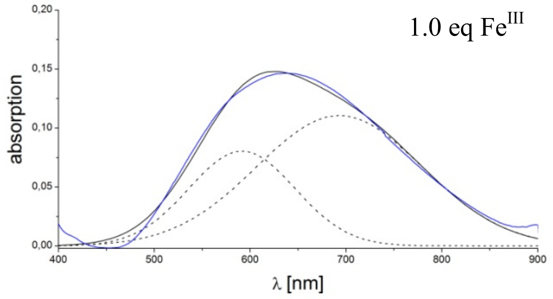

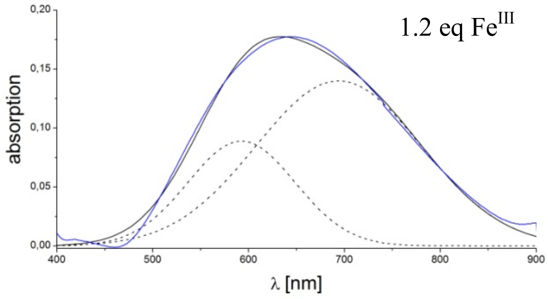

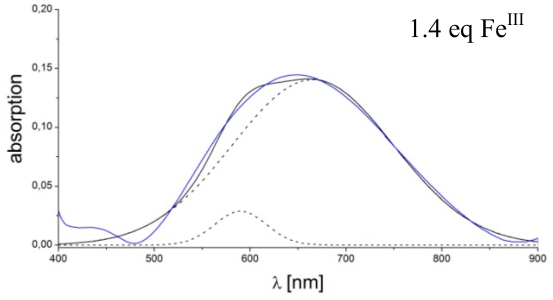

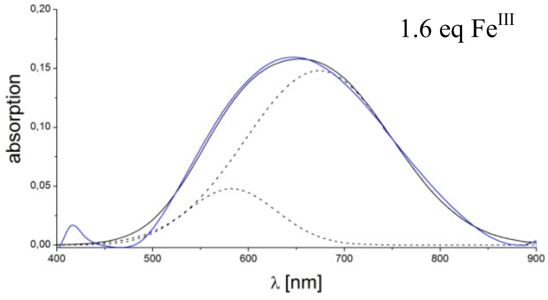

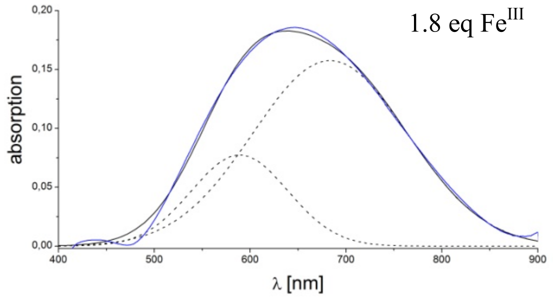

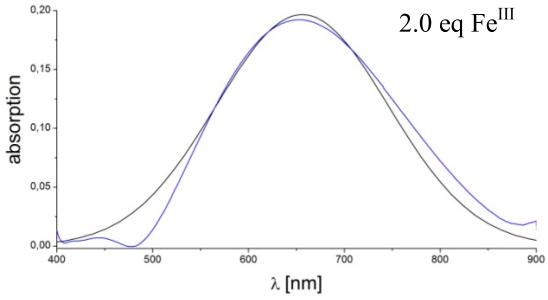

- **K**^{3}:

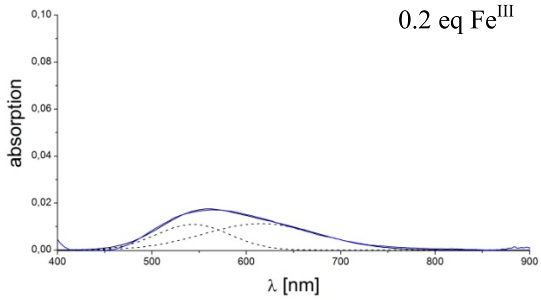
0.2 eq Fe^{III}
absorption
0,10
0,08
0,06
0,04
0,02
0,00
400
500
600
700
800
900
λ [nm]

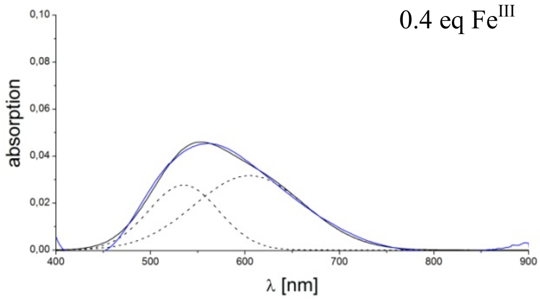
0.4 eq Fe^{III}
absorption
0,10
0,08
0,06
0,04
0,02
0,00
400
500
600
700
800
900
λ [nm]

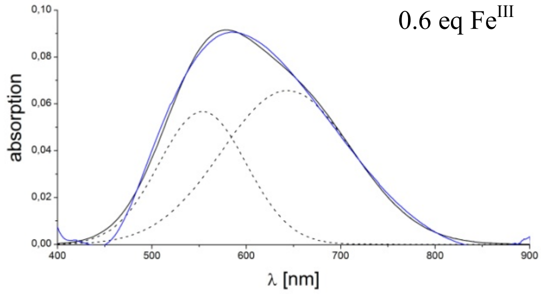
0.6 eq Fe^{III}
absorption
0,10
0,08
0,06
0,04
0,02
0,00
400
500
600
700
800
900
λ [nm]

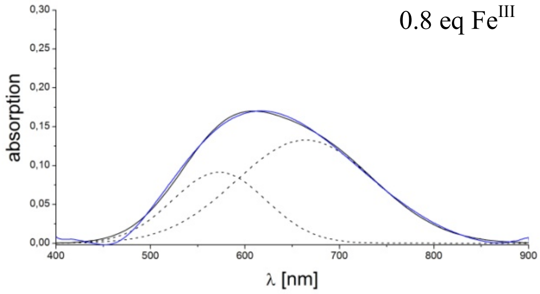
0.8 eq Fe^{III}
absorption
0,30
0,25
0,20
0,15
0,10
0,05
0,00
400
500
600
700
800
900
λ [nm]

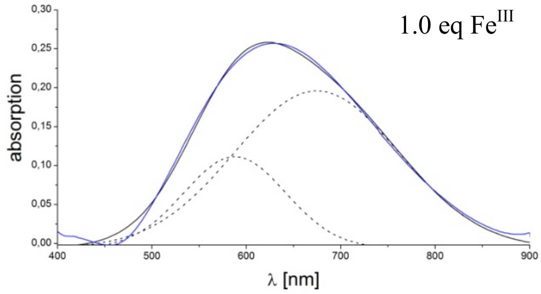
1.0 eq Fe^{III}
absorption
0,30
0,25
0,20
0,15
0,10
0,05
0,00
400
500
600
700
800
900
λ [nm]

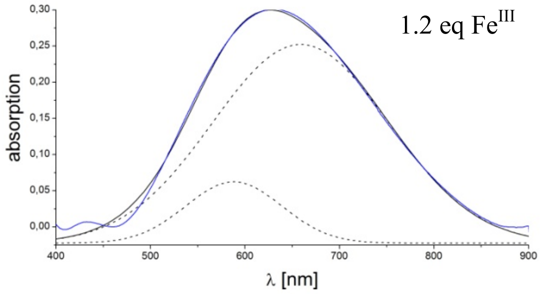
1.2 eq Fe^{III}
absorption
0,30
0,25
0,20
0,15
0,10
0,05
0,00
400
500
600
700
800
900
λ [nm]

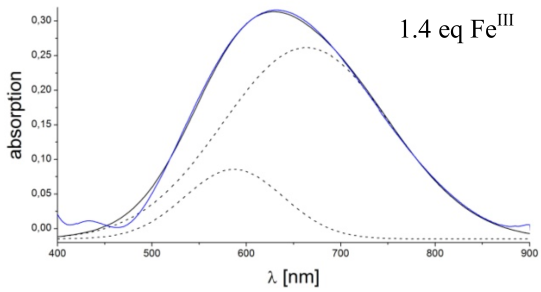
1.4 eq Fe^{III}
absorption
0,30
0,25
0,20
0,15
0,10
0,05
0,00
400
500
600
700
800
900
λ [nm]

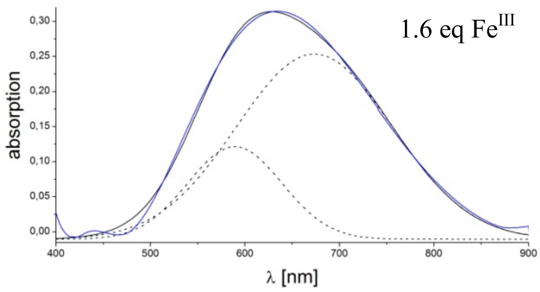
1.6 eq Fe^{III}
absorption
0,30
0,25
0,20
0,15
0,10
0,05
0,00
400
500
600
700
800
900
λ [nm]

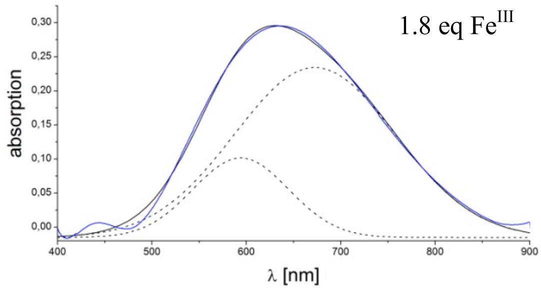
1.8 eq Fe^{III}
absorption
0,30
0,25
0,20
0,15
0,10
0,05
0,00
400
500
600
700
800
900
λ [nm]

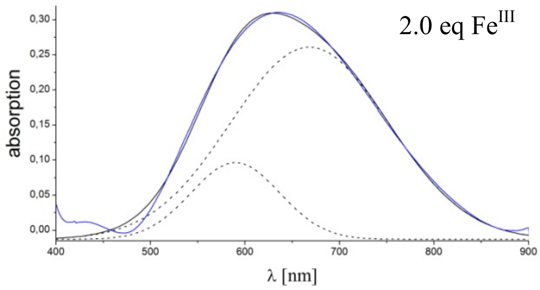
2.0 eq Fe^{III}
absorption
0,30
0,25
0,20
0,15
0,10
0,05
0,00
400
500
600
700
800
900
λ [nm]

Appendix 7: Calculated structures of K^2, K^2 tartrate, K^3 and K^3 tartrate.

K^2 cisoid

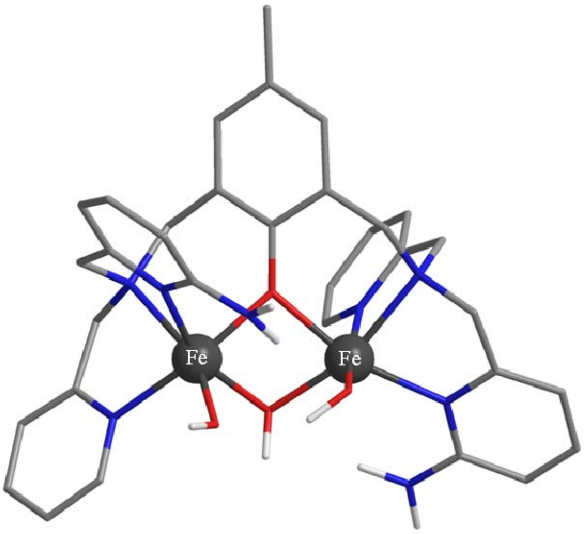

K^2 transoid

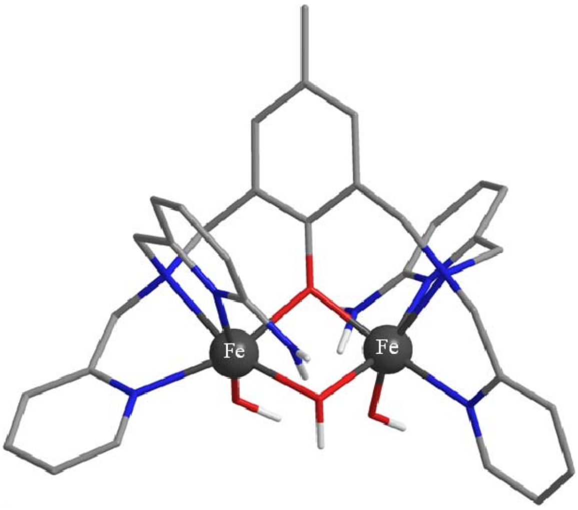

K^2 cisoid with prot. amines

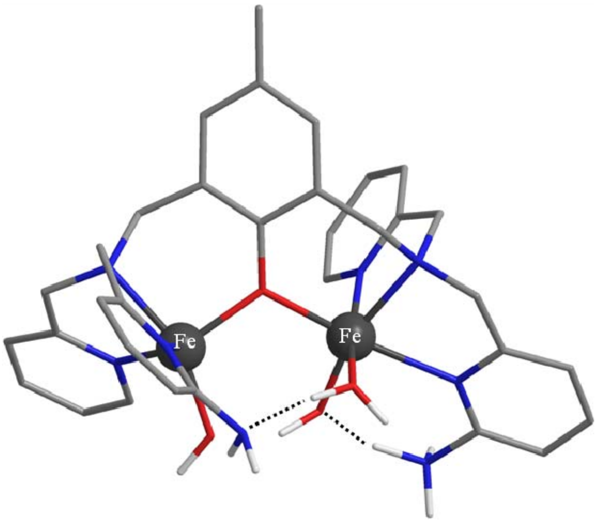

K^2 transoid with prot. amines

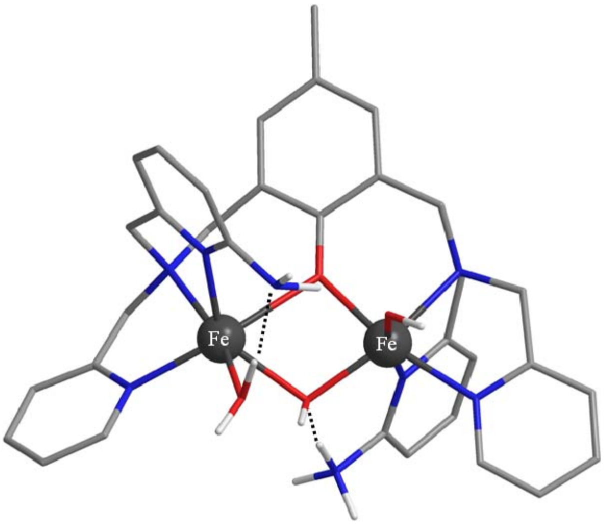

K^3 cisoid

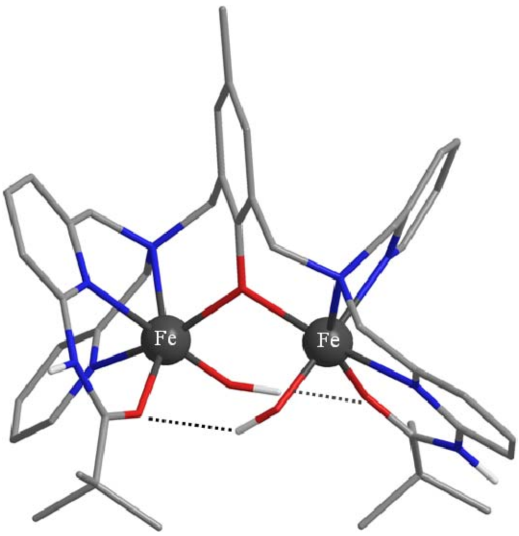

K^3 transoid

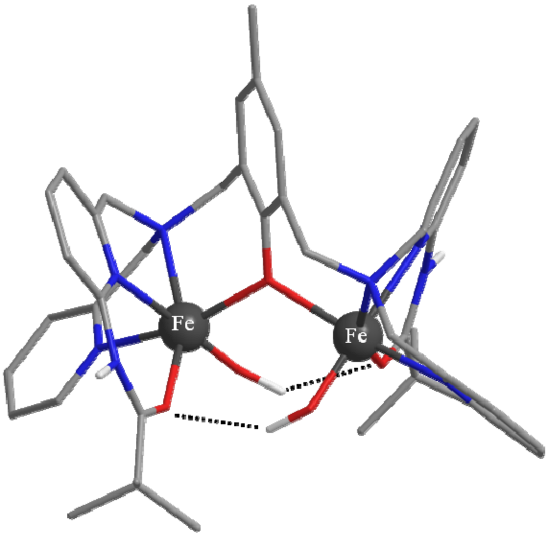

K^{2}tartrate cisoid

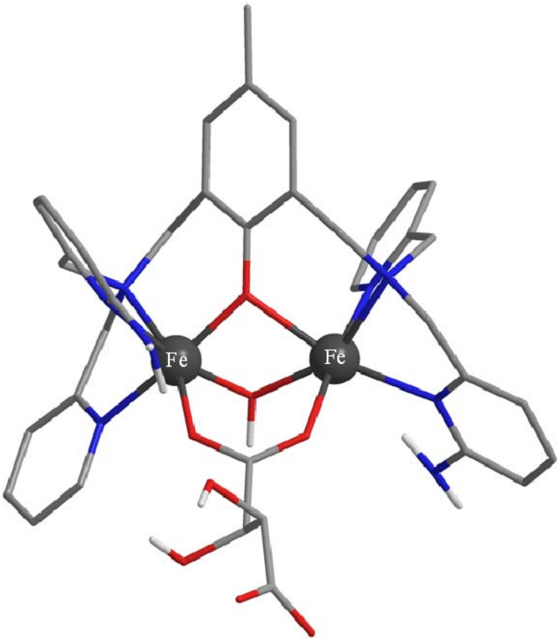

K^{2}tartrate transoid

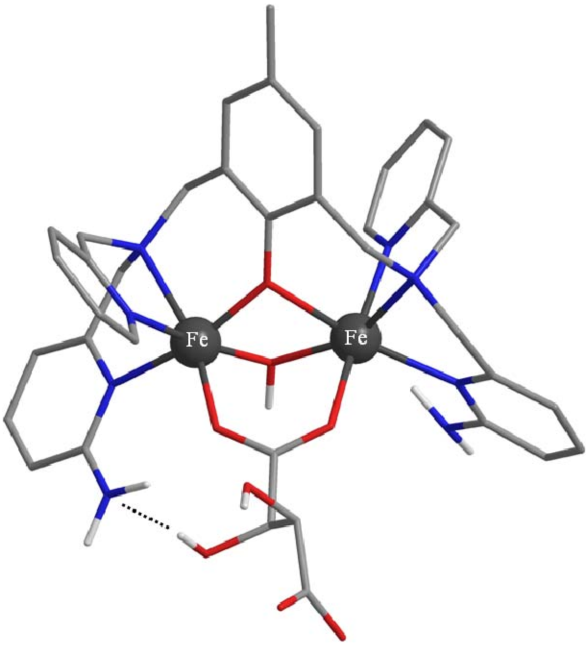

K^{2}tartrate cisoid with prot. amines

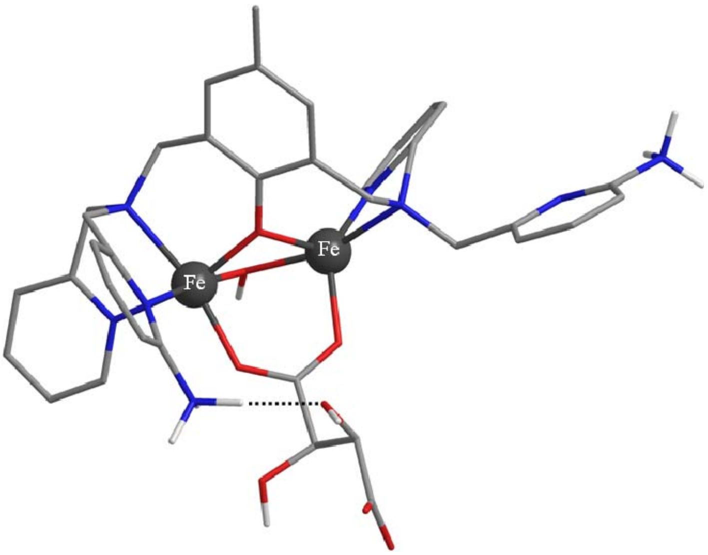

K^{2}tartrate transoid with prot. amines

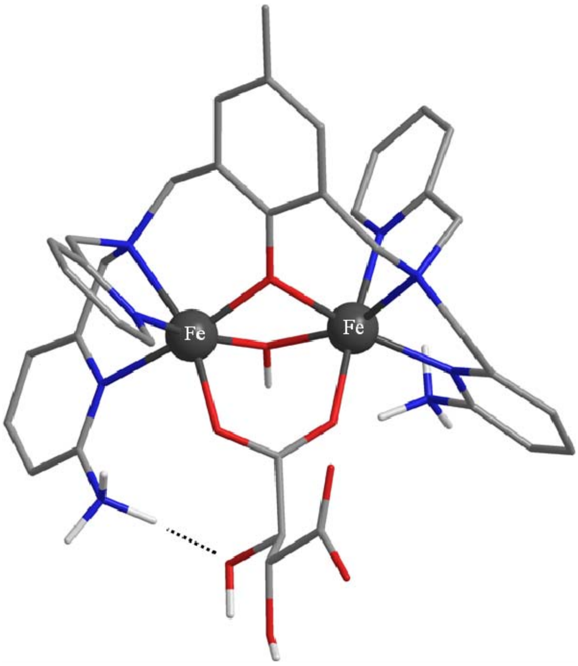

K^{3}tartrate cisoid

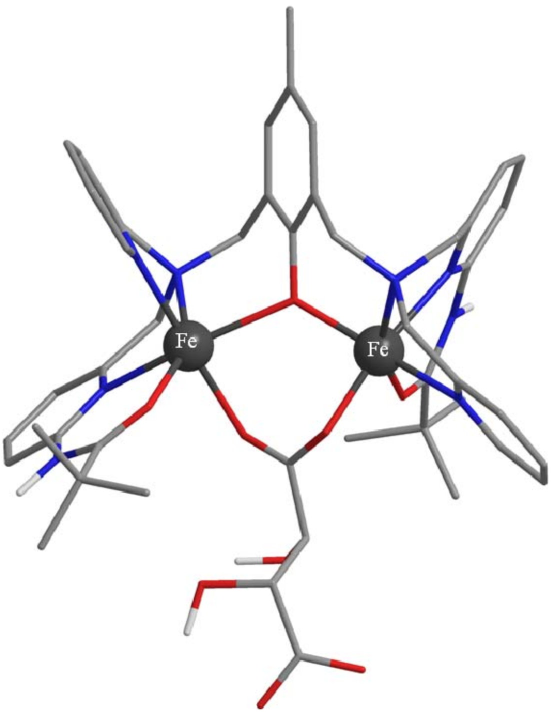

K^{3}tartrate transoid

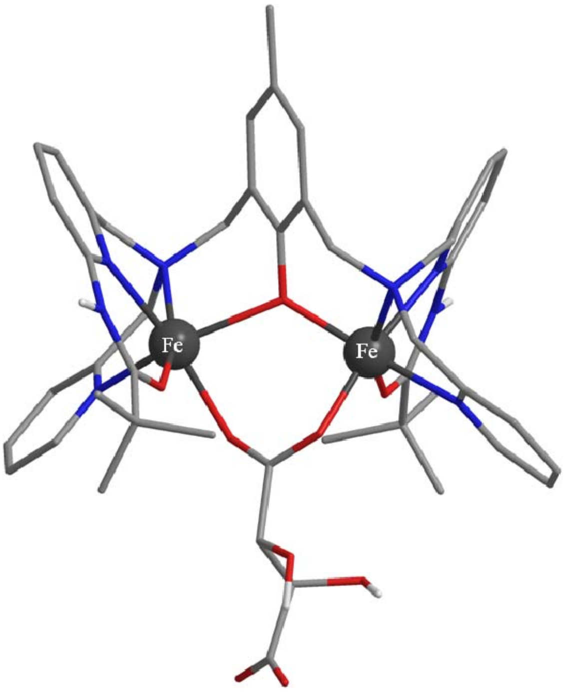

Appendix 8: EPR spectrum of the radical generated by K^{3}pNPP.

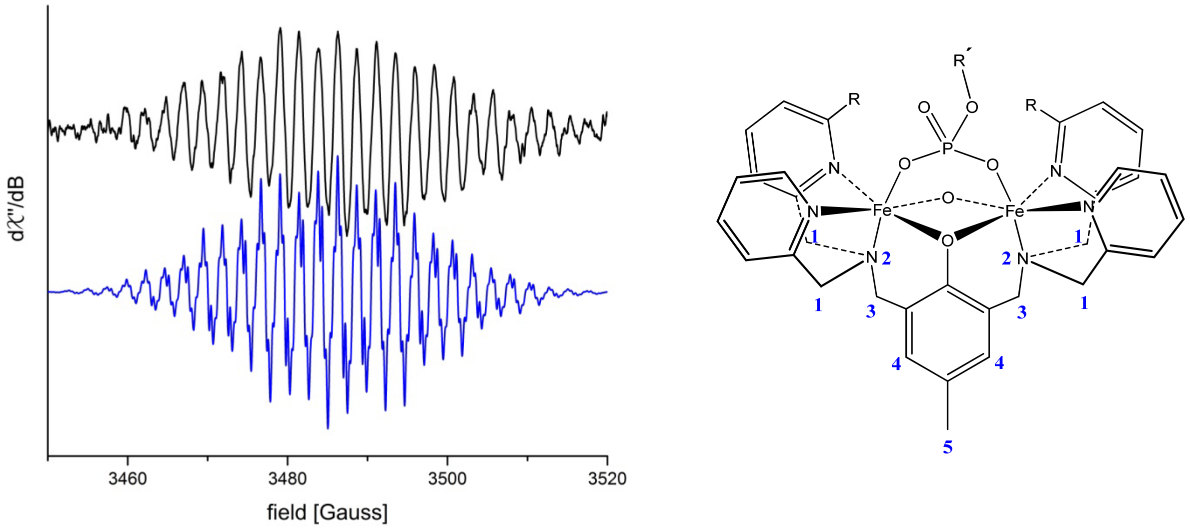

Experimental (black) and simulated (blue) X-band EPR spectrum of the radial generated by **K^3**pNPP in MeCN/buffer pH 5 (0.5 mM **K^3**, 10 mM pNPP) measured at 9.788782 GHz, 298 K and 1.0 Gauss modulation amplitude. The simulated coupling constants are (in mT): 0.045 (8 x, CH_2 **1**), 0.72 (2 x, N **2**), 0.72 (4 x, CH_2 **3**), 0.24 (2 x, CH **4**), -0.24 (3 x, CH_3 **5**).

Appendix 9: Autohydrolysis rates of DNPP.

concentration dependency at pH 6

c_0(DNPP) [mM]	V_0 [10^{-8} M/s]	ΔV_0 [10^{-8} M/s]
0,10	0,60	0,02
0,30	1,07	0,04
0,50	1,91	0,01
0,70	2,17	0,01
0,90	2,92	0,08
1,50	4,64	0,28
2,00	5,86	0,04
2,50	7,55	0,15
3,00	8,72	0,15

pH dependency at c_0 = 0.5 mM

pH	V_0 [10^{-8} M/s]	ΔV_0 [10^{-8} M/s]
4,64	0,31	0,07
5,04	0,77	0,02
5,50	1,16	0,11
5,62	1,49	0,03
5,74	1,57	0,07
6,00	1,85	0,14
6,19	1,99	0,12
6,50	1,98	0,18
7,00	2,13	0,04
8,02	2,46	0,11
9,00	2,34	0,04

Appendix 10: Calculated structures of K^{1}DNPP and K^{1}BDNPP.

K^{1}DNPP monodentate, front view

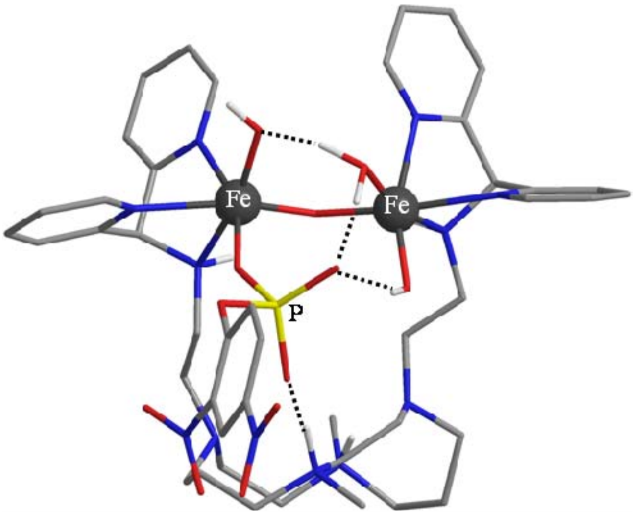

K^{1}DNPP monondentate, side view

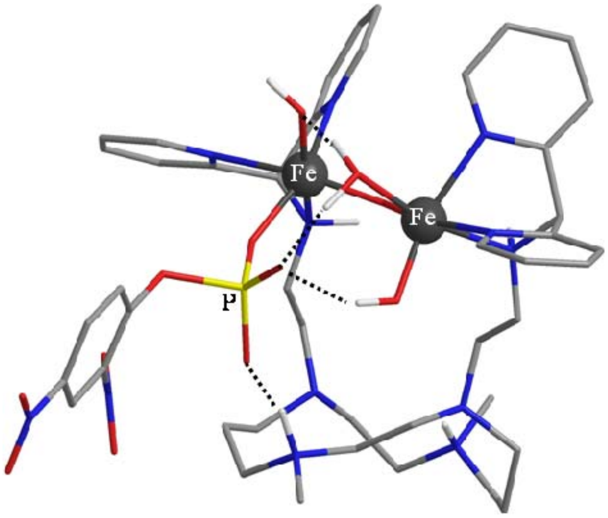

K^{1}DNPP monodentate deprotonated, front view

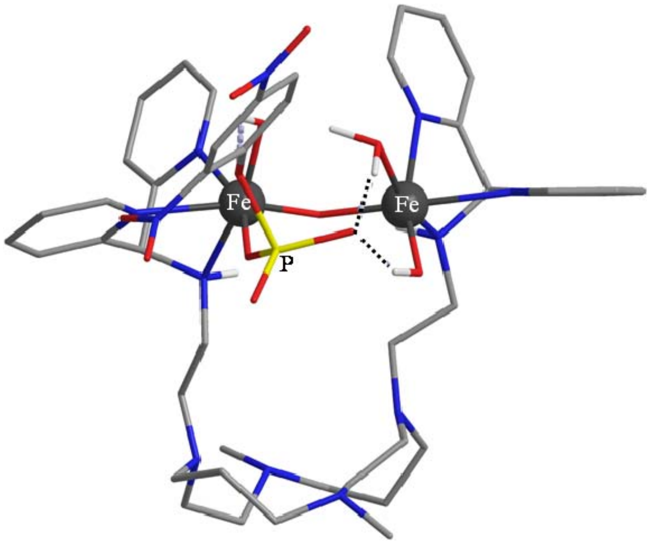

K^{1}DNPP monodentate deprotonated, side view

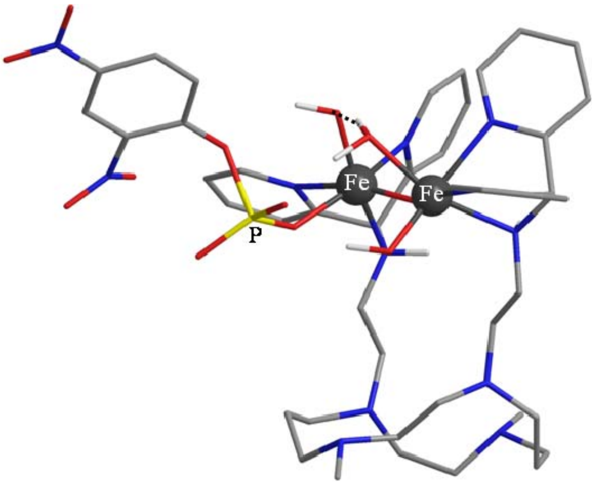

K^{1}DNPP bidentate, front view

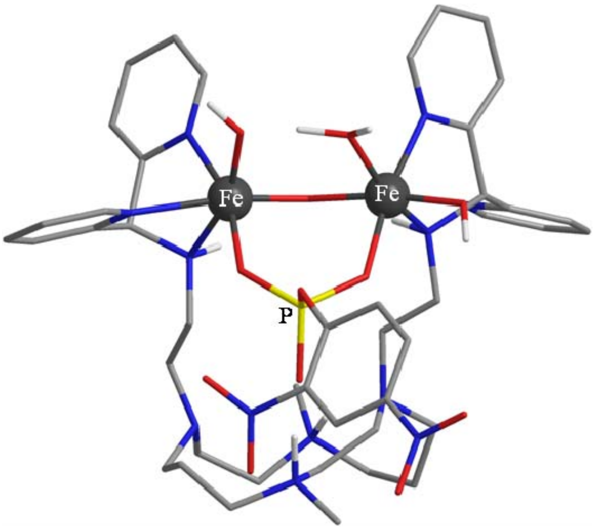

K^{1}DNPP bidentate, side view

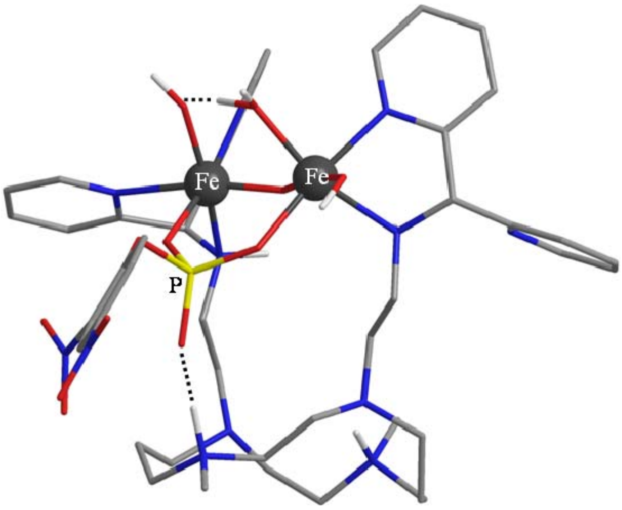

K^{1}DNPP bidentate deprotonated, front view

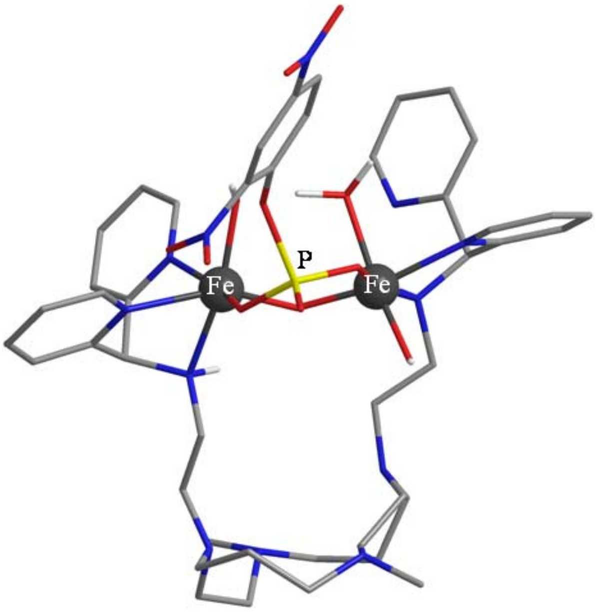

K^{1}DNPP bidentate deprotonated, side view

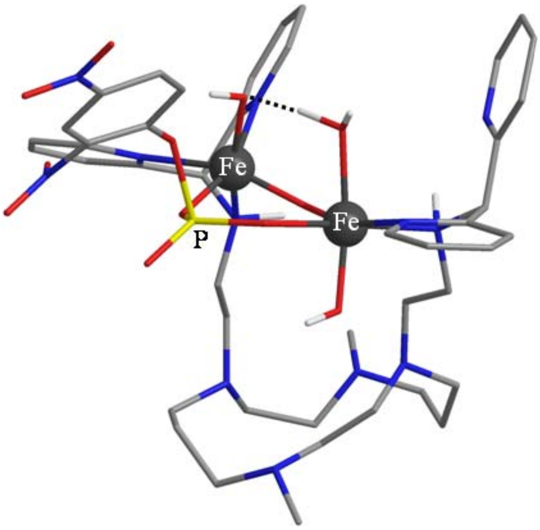

K^{1}BDNPP monodentate, front view

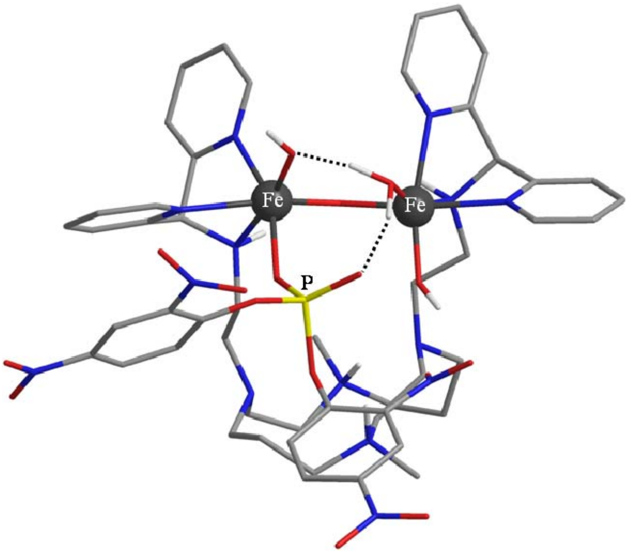

K^{1}BDNPP monodentate, side view

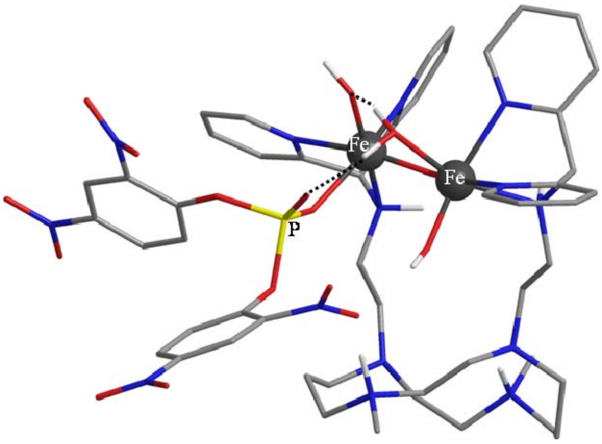

K^{1}BDNPP monodentate rotated, front view

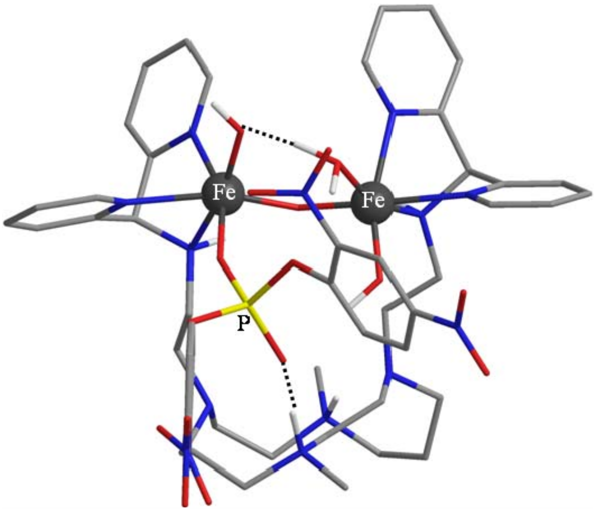

K^{1}BDNPP monodentate rotated, side view

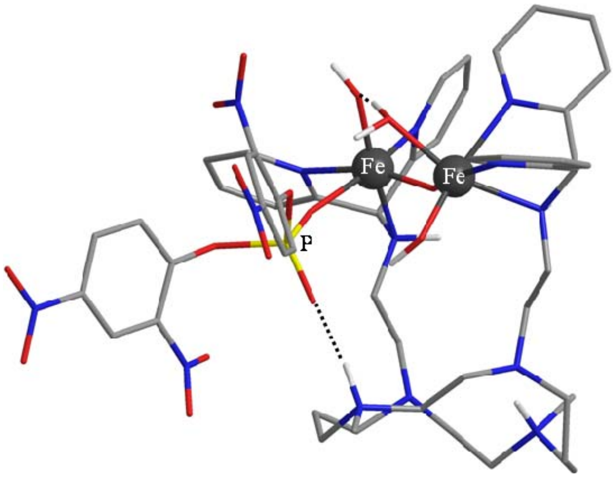

K^{1}BDNPP bidentate, front view

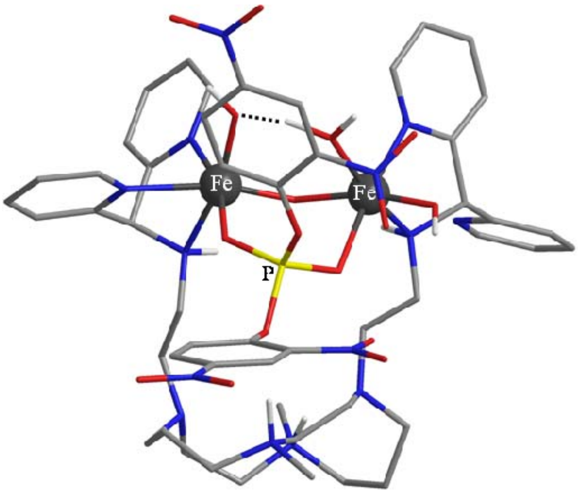

K^{1}BDNPP bidentate, side view

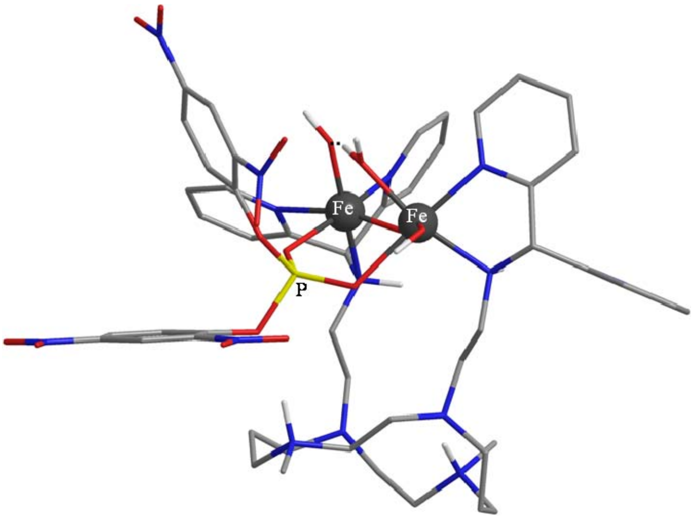

Appendix 11: Crystal Structure Data

Data for L^1 x 2 H_2O:

Identification code	mz5abs	
Empirical formula	C38 H58 N10 O2	
Formula weight	686.94	
Temperature	200(2) K	
Wavelength	0.71073 Å	
Crystal system	Triclinic	
Space group	P -1	
Unit cell dimensions	a = 8.4924(17) Å	α = 102.85(3) °
	b = 10.681(2) Å	β = 93.32(3) °
	c = 11.126(2) Å	γ = 108.57(3) °
Volume	923.6(3) $Å^3$	
Z	1	
Absorption coefficient	0.079 mm^{-1}	
F_{000}	372	
Crystal size	0.235 · 0.228 · 0.100 mm^3	
θ range for data collection	1.90 to 22.47 °	
Index ranges	$-9 <= h <= 9, -11 <= k <= 11, -11 <= l <= 11$	
Reflections collected	2274	
Independent reflections	1033 [R_{int} = 0.1036]	
Completeness to θ = 25.68 °	94.5 %	
Absorption correction	Numerical	
Max. and min. transmission	0.9918 and 0.9812	
Refinement method	Full-matrix least-squares on F^2	
Data / restraints / parameters	2274 / 0 / 238	
Goodness-of-fit on F^2	0.829	
Final R indices [$I > 2\sigma(I)$]	$R1$ = 0.1323, w$R2$ = 0.1704	
R indices (all data)	$R1$ = 0.0663, w$R2$ = 0.1502	
RMS residual density, largest diff. peak and hole	0.088, 0.340 and -0.265 e·$Å^{-3}$	

Data for $[H_2L^1](ClO_4)_2$ x 2 MeCN:

Identification code	mz2m	
Empirical formula	C42 H62 N12 Cl2 O8	
Formula weight	933.94	
Temperature	200(2) K	
Wavelength	0.71073 Å	
Crystal system	Monoclinic	
Space group	P 21/c	
Unit cell dimensions	a = 14.210(3) Å	α = 90.00 °
	b = 8.8923(18) Å	β = 101.59(3) °
	c = 18.919(4) Å	γ = 90.00 °
Volume	2341.9(8) $Å^3$	

Z	2
Absorption coefficient	0.203 mm^{-1}
F_{000}	992
Crystal size	0.37 · 0.26 · 0.14 mm^3
θ range for data collection	2.20 to 26.12 °
Index ranges	-17 <= h <= 17, -10 <= k <= 10, -23 <= l <= 22
Reflections collected	4614
Independent reflections	2324 [$R_{\text{int}} = 0.0579$]
Completeness to $\theta = 25.68$ °	99.2 %
Absorption correction	none
Max. and min. transmission	n.a.
Refinement method	Full-matrix least-squares on F^2
Data / restraints / parameters	4614 / 21 / 334
Goodness-of-fit on F^2	0.688
Final R indices [$I > 2\sigma(I)$]	$R1 = 0.0967$, w$R2 = 0.1346$
R indices (all data)	$R1 = 0.0478$, w$R2 = 0.1180$
RMS residual density, largest diff. peak and hole	0.046, 0.450 and -0.445 e·Å^{-3}

Data for [L^{1}Zn](OTf)$_2$:

Identification code	mz9a	
Empirical formula	C40 H54 F6 N10 Zn O6 S2	
Formula weight	1014.42	
Temperature	200(2) K	
Wavelength	0.71073 Å	
Crystal system	Monoclinic	
Space group	P 21/c	
Unit cell dimensions	$a = 13.873(3)$ Å	$\alpha = 90.00$ °
	$b = 17.163(3)$ Å	$\beta = 104.08(3)$ °
	$c = 19.895(4)$ Å	$\gamma = 90.00$ °
Volume	4594.8(16) Å^3	
Z	4	
Absorption coefficient	0.707 mm^{-1}	
F_{000}	2112	
Crystal size	0.674 · 0.285 · 0.256 mm^3	
θ range for data collection	2.28 to 28.22 °	
Index ranges	-18 <= h <= 18, -22 <= k <= 22, -26 <= l <= 24	
Reflections collected	10518	
Independent reflections	5522 [$R_{\text{int}} = 0.0708$]	
Completeness to $\theta = 25.68$ °	92.8 %	
Absorption correction	Numerical	
Max. and min. transmission	0.8577 and 0.7596	
Refinement method	Full-matrix least-squares on F^2	
Data / restraints / parameters	10518 / 0 / 594	
Goodness-of-fit on F^2	0.970	
Final R indices [$I > 2\sigma(I)$]	$R1 = 0.1352$, w$R2 = 0.0798$	
R indices (all data)	$R1 = 0.2400$, w$R2 = 0.2126$	
RMS residual density, largest diff. peak and hole	0.107, 3.082 and -1.972 e·Å^{-3}	

Data for [L^{1}Cu](OTf)$_2$:

Identification code	mz10a	
Empirical formula	C42 H57 F6 N11 Cu O6 S2	
Formula weight	1053.65	
Temperature	200(2) K	
Wavelength	0.71073 Å	
Crystal system	Monoclinic	
Space group	P 21/c	
Unit cell dimensions	a = 11.157(2) Å	α = 90.00 °
	b = 30.396(6) Å	β = 92.15(3) °
	c = 14.021(3) Å	γ = 90.00 °
Volume	4751.4(16) Å^3	
Z	4	
Absorption coefficient	0.630 mm^{-1}	
F_{000}	2196	
Crystal size	0.501 · 0.355 · 0.219 mm^3	
θ range for data collection	1.95 to 26.15 °	
Index ranges	$-13 <= h <= 13, -37 <= k <= 37, -17 <= l <= 17$	
Reflections collected	9345	
Independent reflections	4651 [R_{int} = 0.0975]	
Completeness to θ = 25.68 °	98.3 %	
Absorption correction	Numerical	
Max. and min. transmission	0.8981 and 0.8033	
Refinement method	Full-matrix least-squares on F^2	
Data / restraints / parameters	9345 / 0 / 622	
Goodness-of-fit on F^2	0.970	
Final R indices [$I > 2\sigma(I)$]	$R1$ = 0.1015, w$R2$ = 0.0979	
R indices (all data)	$R1$ = 0.0470, w$R2$ = 0.0885	
RMS residual density, largest diff. peak and hole	0.066, 0.526 and -0.303 e·Å^{-3}	

Erklärungen gemäß § 8 (3) b) und c) der Prüfungsordnung:

a) Ich erkläre hiermit an Eides statt, dass ich die vorliegende Arbeit selbst verfasst habe und mich dabei keiner anderen als der von mir bezeichneten Quellen und Hilfen bedient habe.

b) Ich erkläre hiermit an Eides statt, dass ich an keiner anderen Stelle, außer an der University of Queensland, Brisbane, Australia im Rahmen eines „dual PhD“ Abkommens, ein Prüfungsverfahren beantragt bzw. diese Dissertation in dieser oder anderer Form bereits anderweitig als Prüfungsarbeit verwendet oder einer anderen Fakultät als Dissertation vorgelegt habe.

Heidelberg, 09. September 2010

(Marta Zajaczkowski-Fischer)